ALMA MATER STUDIORUM
UNIVERSITÀ DI BOLOGNA

DOTTORATO DI RICERCA IN

Fisica

Ciclo XXXVII

Settore Concorsuale: 02/A1 Fisica Sperimentale delle Interazioni Fondamentali
Settore Scientifico Disciplinare: FIS/01 Fisica Sperimentale

The luminosity measurement at the LHC with the ATLAS experiment: upgrade for the LUCID detector for High Luminosity-LHC and Z cross section measurement with early Run3-data for luminosity validation

Presentata da: Davide Cremonini

Coordinatore Dottorato
Prof. Alessandro Gabrielli

Supervisore
Prof.ssa Sara Valentinetti
Cosupervisore
Dott. Federico Lasagni Manghi
Prof.ssa Laura Fabbri

Esame finale anno 2025

Abstract

The knowledge of the luminosity is crucial for measuring the cross sections of all physical processes and provides real-time information about the performance of the accelerator. In this thesis, luminosity will be discussed both from a technical point of view and as one of the main systematic uncertainties in physics analysis.

In the first part of this thesis, the measurement of luminosity is discussed, starting with a theoretical overview and introducing various experimental techniques. The focus then shifts to the LUCID detector, the primary luminometer of the ATLAS experiment, used during LHC Run-2 (2015–2018) and Run-3 (2022–present). Given the challenging conditions expected in the High-Luminosity LHC, LUCID requires a complete redesign. Three prototypes of the future LUCID have been installed and are currently under tests to evaluate the performances of the new LUCID using data collected in Run-3.

In the second part of the thesis, the measurement of the inclusive Z-boson production cross section at a center-of-mass energy of $\sqrt{s} = 13.6$ TeV is presented, along with its ratio to the W and $t\bar{t}$ production cross sections, using early ATLAS Run-3 data. This analysis is among the first conducted at the start of each data-taking period, as it allows for checks on detector calibration, alignment, and luminosity measurement via the Z-counting technique and, in this case, testing theoretical predictions at a new center-of-mass energy.

Contents

List of Figures

List of Tables

Introduction

This thesis focuses on luminosity, covering both the techniques for its measurement and its impact on physics analyses, where it is one of the main sources of systematic uncertainty.

The first part of this thesis focuses on luminosity, a fundamental parameter in accelerator physics. Luminosity is crucial for measuring the cross sections of all physical processes and provides real-time information about the performance of the accelerator. Therefore, a detector capable of measuring luminosity both online and offline with high precision is essential. LUCID-2 (LUminosity Cherenkov Integrating Detector) was the main ATLAS luminometer for Run-2, consisting of 16 PMTs placed around the beampipe, 17 meters from the interaction point. It achieved a total uncertainty of 0.8% on the full Run-2 dataset. Similar performances are expected for Run-3, but at the High-Luminosity LHC (HL-LHC), the current detector will not be able to deliver the same precision. Thus, a new detector (LUCID-3) is necessary to maintain high offline precision under the challenging HL-LHC conditions.

One major issue the current LUCID might face during HL-LHC operation is the saturation of the luminosity algorithms. To address this, the detector's acceptance must be reduced. Two PMT-based prototypes have been developed: one placed farther from the beampipe and another positioned behind one of the forward shieldings. In this thesis, their linearity with respect to pileup and their long-term stability will be discussed, using data collected in 2023 and 2024. Another prototype, using quartz fiber coupled with PMTs for readout, was also developed. In this design, particles passing through the fibers emit Cherenkov light, which is collected by the PMTs. The key advantages of this type of detector are:

- PMTs are placed in a lower radiation area.
- Luminosity algorithms do not saturate.
- It is expected to be perfectly linear as function of the pileup.

A fiber detector was installed during Run-2, but its long-term stability was poor due to unmonitored fiber degradation caused by radiation damage. The new fiber detector features larger PMTs, monitored using ^{207}Bi (as in LUCID-2), and employs a new type

of radiation-hard fiber monitored by LED signals. Characterizing this prototype will be more complex than for the PMT prototypes. It will include studies of fiber degradation as a function of absorbed radiation dose in a dedicated γ-irradiation session, and a beam test to study Cherenkov light production in the fiber as a function of incident particle direction. Finally, the detector's linearity and long-term stability will be analyzed.

The second part of the thesis focuses on the study of Z boson physics, a fundamental component of the Standard Model of particle physics. To provide context, this section begins with an introduction to the Standard Model. This is followed by a brief overview of the mechanisms by which proton-proton interactions occur, as well as the methods used to simulate these processes in Monte Carlo simulations.

After discussing the properties and characteristics of the Z boson, including its discovery, production and decay modes, the analysis strategy will be outlined in detail. In this analysis, after reconstructing all physics objects, a selection process is applied to reduce the background. Correction factors are applied to account for detector inefficiencies. An inconsistency was identified in the transverse momentum (p_t) distribution of the Z boson. To address this, an additional correction factor was computed to take into account higher-order effects. This correction enhances the precision of the measurement and aligns the theoretical predictions more closely with results.

Two distinct methods are employed to extract the cross section of the Z boson production: an event-counting approach, which relies on counting events that pass the selection criteria, and a profile likelihood fit, a statistical method that maximizes the likelihood of observing the data under different hypotheses. Finally, the cross sections of the Z, W, and $t\bar{t}$ processes are combined. This combined measurement strategy helps to cancel out certain systematic uncertainties, such as luminosity. Due to the clear signature of the decay of the Z boson into two leptons, coupled with the very low background contamination, the Z boson can also be effectively used to measure luminosity using the Z-counting technique. A preliminary Z-counting using the data collected in 2022 is presented.

Chapter 1

Beam Dynamics and Luminosity

1.1 Introduction

Luminosity is a fundamental parameter in accelerators physics because it is essential for the measurement of the cross section of every physics process and gives us information about the performance of the accelerator (in this case LHC) in real time. To understand properly luminosity, an overview on some basic concept of beam dynamics is given. Then, the concept of luminosity is discussed.

Although many topics would have a general validity, the main focus will be the ATLAS experiment at LHC at CERN, Geneva. Being a collider, in LHC there are 2 circulating beams rotating in opposite directions. Beams are divided into packets, called bunches, since the accelerator system (that will be explained later) is not able to accelerate continuous beams. This means that the collisions will happen only in certain time frames called Bunch crossing ID (BCID). Although the beam can be made by ions, in this thesis we will consider only proton beams.

1.2 Beam dynamics

In order to properly understand what is luminosity and how to measure it, an introduction on beam dynamics is necessary.

1.2.1 Electric and magnetic fields

A charged particle with charge q, momentum $\vec{p}$ and velocity $\vec{v}$ in the electromagnetic field ($\vec{E}$,$\vec{B}$) experiences the Lorentz's force $\vec{F}$

$$\vec{F} = q(\vec{E} + \vec{v} \times \vec{B}) \tag{1.1}$$

In an accelerator, the charged particles gain energy by their interaction with the electric field $\vec{E}$. The magnetic force $\vec{v} \times \vec{B}$ is perpendicular to both $\vec{v}$ and $\vec{B}$. The trajectory of a charged particle will be curved when it passes through a dipole magnet. At relativistic velocities an electric field E and a magnetic field B have the same effect for E = cB. A magnetic field of 1 T would then be the equivalent of an electric field of $3 \cdot 10^8$ V·m^{-1}. Producing such an electric field is far beyond technical limits for current technology; as a result magnetic fields are used to steer the beams. The effects of a magnetic field are first analyzed followed by the effects of the electric one.

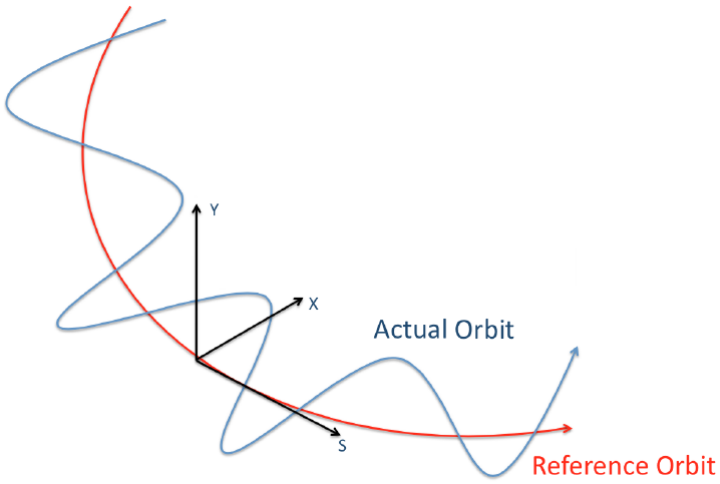

Figure 1.1: Coordinate system used to describe beam dynamics. The reference orbit is drawn in red while the effective orbit is drawn in blue.

A typical coordinate system (x, y, s) used to describe the particle's motion is shown in Fig. 1.1. In order to describe the path of the particles, s is the longitudinal direction along the reference orbit, while x and y are the transversal coordinates which define the transverse plane. We call $\vec{r_0}$ the reference trajectory with null x and y coordinates for every s. The particle trajectory around the reference orbit can be expressed as:

$$\vec{r} = \vec{r_0} + x\hat{x}(s) + y\hat{y}(s), \tag{1.2}$$

where $\hat{x}(s)$ and $\hat{y}(s)$ are the versors along x and y axis. The $\vec{B}$ field components can be expressed as a function of a dipolar and quadrupolar term. Dipole magnets guide the charged particles along the closed orbit and the Lorentz force bends the trajectory with a bending angle θ

$$\theta = \frac{q}{p}\int_{s_1}^{s_2} Bdl = \frac{1}{B\rho}\int_{s_1}^{s_2} Bdl \tag{1.3}$$

where p and q are the momentum and the charge of the particle, respectively, while ρ is the bending radius and s_1 and s_2 are 2 points along the orbit. Knowing that the total

bending angle of a circular accelerator is 2π, the total dipole field is

$$\oint Bdl = \frac{2\pi p}{q} = 2\pi B\rho \tag{1.4}$$

from which we obtain the bending radius ρ

$$\rho = \frac{p}{qB} = \frac{mv}{qB}. \tag{1.5}$$

While dipole magnets are used to bend the particle's trajectory, quadrupole magnets are used to focus or defocus the beam in order to control the beam size. A focusing quadrupole in the horizontal plane corresponds to a defocusing one on the vertical plane and viceversa.

The task of the electric fields is to accelerate the charged particles. There are various technologies that can be used and the choice depends on the scale of energy. At high energies, radio frequencies (RF) are used to generate a longitudinal electric field. The passage through a RF cavity induce a variation of energy of $\Delta E = q\Delta V$ where q is the charge and $\Delta V = V_0 \sin(\omega_{RF} t + \phi)$ is the effective gap voltage, ω_{RF} is the RF frequency, V_0 is the effective peak accelerating voltage and ϕ is a phase. To be properly accelerated, particles must be in phase with the accelerating voltage. Thus, the RF frequency must be an integer (h) multiple of the revolution frequency. In that way, the particle crosses the electric field every turn at a constant phase and so experiences a constant force.

$$f_{RF} = h \cdot f_{rev}. \tag{1.6}$$

A particle with a speed β (in units of c) circulates in the accelerator with a period $T_{rev} = \frac{2\pi R}{\beta c}$ and a frequency $f_{rev} = \frac{\beta c}{2\pi R}$ (in LHC, $f_{rev} = 11$kHz).

1.2.2 Betatron Motion and Transverse Emittance

The betatron motion describes the motion of the particle in the transverse plane, around the reference orbit. The equation describing this motion is derived from the Lorentz force. Knowing that $\vec{B}$ is non-null only on the transverse plane xy, the Hill's equations [1] can be written as:

$$x'' + K_x(s)x = 0 \tag{1.7}$$

$$y'' + K_y(s)y = 0 \tag{1.8}$$

$$K_x = \frac{1}{\rho^2} \mp K_1(s) \tag{1.9}$$

$$K_y = \mp K_1(s) \tag{1.10}$$

where $K_1(s) = \frac{B_1(s)}{B\rho}$ is the effective focusing function which sign depends on the charge of the particle and $B_1(s)$ is the magnetic field evaluated at the center of the quadrupole.

$K_x(s)$ and $K_y(s)$ are periodic functions and can be assumed constant because in the accelerator magnetic field components are nearly uniform.

Considering only the y axis and imposing the periodic condition $K(s+L) = K(s)$, where L is the distance between two successive quadrupole stations, the solution to Hill's equation can be written as:

$$y(s) = \begin{cases} A\cos(\sqrt{K}s + b) & \text{per} K > 0 \\ As + b & \text{per} K = 0 \\ A\cosh(\sqrt{-K}s + b) & \text{per} K < 0 \end{cases} \tag{1.11}$$

An alternative expression can be expanded in terms of the betatron state vector and the betatron transfer matrix M[2]:

$$\mathbf{y}(s) = \begin{pmatrix} y(s) \\ y'(s) \end{pmatrix} \tag{1.12}$$

$$\mathbf{y}(s) = M(s|s_0)\mathbf{y}(s_0) \tag{1.13}$$

Eq 1.13 is the solution of the Hills equations as a function of the betatron state vector and the transfer matrix, where $M(s|s_0)$ has the following expression, depending on $K(l = s - s_0)$ and in the case of $K > 0$ (focusing quadrupole):

- $K > 0$ (focusing quadrupole)

$$M = \begin{pmatrix} \cos\sqrt{|K|}l & \frac{1}{\sqrt{k}}\sin\sqrt{K}l \\ -\sqrt{K}\sin\sqrt{K}l & \cos\sqrt{|K|}l \end{pmatrix} \tag{1.14}$$

- $K = 0$ (drift space)

$$M = \begin{pmatrix} 1 & l \\ 0 & 1 \end{pmatrix} \tag{1.15}$$

- $K < 0$ (defocusing quadrupole)

$$M = \begin{pmatrix} \cosh\sqrt{|K|}l & \frac{1}{\sqrt{k}}\sinh\sqrt{K}l \\ -\sqrt{K}\sinh\sqrt{K}l & \cosh\sqrt{|K|}l \end{pmatrix} \tag{1.16}$$

Eq 1.13, in the case of $K > 0$, can be interpreted as an harmonic oscillator:

$$y(s) = A\omega(s)\cos(\Phi(s) - \Phi_0) \tag{1.17}$$

where $\omega(s)$ is a periodic function with periodicity L, $\Phi(s) = \sqrt{K}s$, A and Φ_0 are the integration constants. Substituting eq 1.17 into Hill's equations we can define a new set of variables, called Courant-Snyder functions or Twiss parameters:

$$\beta(s) = \frac{\omega^2(s)}{K} \tag{1.18}$$

$$\alpha(s) = -\frac{1}{2}\frac{\partial\beta(s)}{\partial s} \tag{1.19}$$

$$\gamma(s) = \frac{1+\alpha^2(s)}{\beta(s)}. \tag{1.20}$$

$\beta(s)$ is also called betatron amplitude function. Using eqs. 1.18, 1.19 and 1.20 we can parametrize the transfer matrix that describes a complete turn around the ring as

$$\mathbf{M} = \begin{pmatrix} \cos\Phi + \alpha\sin\Phi & \beta\sin\Phi \\ -\gamma\sin\Phi & \cos\Phi - \alpha\sin\Phi \end{pmatrix} \tag{1.21}$$

where Φ is the betatron phase advance, defined as:

$$\Phi = \int_{s_0}^{s_0+L} \frac{ds}{\beta(s)} \tag{1.22}$$

where L is the length of the periodic beam line for which the K function is periodic. For an accelerator of circumference $C = NL$ with N identical superperiods, $N\Phi$ is the phase change per revolution. We can also derive two characteristic quantities, Q_x and Q_y, called betatron tunes which indicates the number of betatron oscillations per revolution

$$Q_i = \frac{N\Phi_i}{2\pi} = \frac{1}{2\pi}\int_s^{s+C} \frac{ds}{\beta_i(s)} \tag{1.23}$$

where $i = x, y$. The betatron oscillation frequency is given by $Q_i f_0$, where f_0 is the revolution frequency. The general solution of the Hills equations along the y-axis can be written as

$$y(s) = a\sqrt{\beta_y(s)}\cos[\Phi_y(s) + \Phi_0], \tag{1.24}$$

where

$$\Phi_y(s) = \int_0^s \frac{ds}{\beta_y(s)}. \tag{1.25}$$

Therefore, we will have pseudo-harmonic oscillation with variable amplitude of $\sqrt{\beta_y(s)}$.

1.2.3 Beam Emittance

The particle distribution is generally described by a six dimensional density function ρ in which x, y and s represent the variables that define the coordinate system. In linear dynamics the transverse and longitudinal distributions are often considered as uncorrelated, so the six dimension can therefore be factorized into three independent phase-space (x, x') (y, y') and (s, E).

Replacing $\Phi_y(s) + \Phi_0$ by $\theta(s)$ in Eq. 1.24 we obtain

$$y(s) = a\sqrt{\beta_y(s)}\cos\theta(s) \tag{1.26}$$

and deriving

$$y'(s) = -\frac{a}{\sqrt{\beta_y(s)}}[\sin\theta(s) + \alpha(s)\cos\theta(s)]. \tag{1.27}$$

Combining eq 1.26 with eq 1.27 together we obtain the following equation

$$\gamma y^2 + 2\alpha y y' + \beta y'^2 = a^2 \tag{1.28}$$

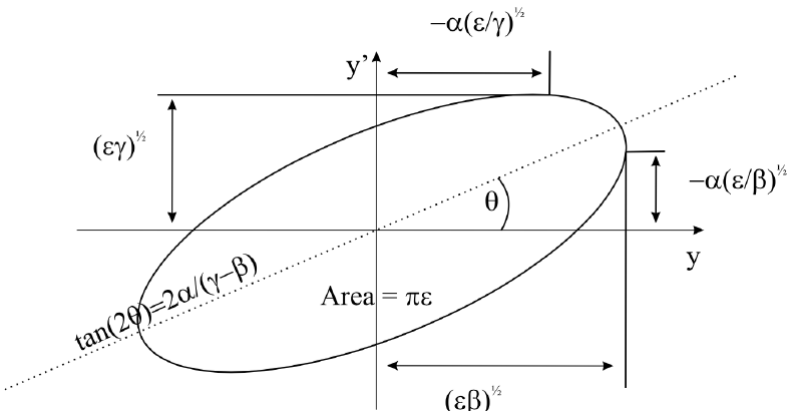

Figure 1.2: Scheme of the motion of the particle in the phase space. Typically, it represents an ellipse parametrized through Courant-Snyder parameters α, β and γ.

which is the Courant-Snyder invariant, which remains constant along a particle trajectory and describes an ellipse (Fig 1.2), in the phase-space (y, y'). a^2 is called emittance of a single particle following its individual trajectory:

$$\epsilon = a^2 = \frac{Ellipse\,area}{\pi}. \tag{1.29}$$

The emittance is the area of the ellipse which contains a certain percentage of particles.

A beam is composed by particles centered around the reference orbit, so for any distribution of particles, it's possible to define a region in phase space occupied by all of them. Taking a normalized distribution function $\rho(y, y')$, the moments of the beam distribution are

$$\langle y \rangle = \int\int y\,\rho(y, y')\,dydy' \tag{1.30}$$

$$\langle y' \rangle = \int\int y'\,\rho(y, y')\,dydy' \tag{1.31}$$

$$\sigma_y^2 = \int\int (y - \langle y \rangle)^2 \rho(y, y')\, dy dy' \tag{1.32}$$

$$\sigma_{y'}^2 = \int\int (y' - \langle y' \rangle)^2 \rho(y, y')\, dy dy' \tag{1.33}$$

$$\sigma_{yy'} = \int\int (y - \langle y \rangle)(y' - \langle y' \rangle) \rho(y, y')\, dy dy' = r\sigma_y \sigma_{y'} \tag{1.34}$$

where σ_y and $\sigma_{y'}$ are the RMS beam widths, $\sigma_{yy'}$ is the correlation and r is the correlation coefficient.

The RMS beam emittance is defined as:

$$\epsilon_{rms} = \sqrt{\sigma_y^2 \sigma_{y'}^2 - \sigma_{yy'}^2} = \sigma_y \sigma_{y'} \sqrt{1 - r^2} \tag{1.35}$$

and it is equal to the phase space area enclosed by the Courant-Snyder ellipse of the RMS particle. It can be shown that for a beam with RMS emittance $\pi\epsilon$, the RMS beam width is

$$\sigma_y = \sqrt{\beta\epsilon}. \tag{1.36}$$

1.3 Luminosity

The general definition of the luminosity $\mathscr{L}$ is given by the formula:

$$\mathscr{L} = \frac{R}{\sigma}, \tag{1.37}$$

where R is the rate of a generic physical process and σ is its cross section. A precise absolute luminosity measurement is necessary for every cross section measurement, although the required precision can vary from analysis to analysis.

We can define two different types of luminosities:

- the instantaneous luminosity $\mathscr{L}$ [$\mathrm{cm}^{-2}\mathrm{s}^{-1}$], defined by Eq 1.37, is related to the instantaneous performance of the collider, the time interval where it is measured may fluctuate from tens of nanoseconds to minutes, depending on the type of collider (bunched or continuous beams). $\mathscr{L}$ typically decays with time constants of hours or even days. It is mainly used in accelerator performance monitoring.

- the integrated luminosity, denoted by $\int \mathscr{L} dt$ refers to the instantaneous luminosity accumulated over a certain time interval and is typically quoted in units of cm^{-2}, or equivalently in inverse barns (b^{-1}), microbarns (μb^{-1}), picobarns (pb^{-1}), etc. It is mainly used to refer to the accumulated statistic.

The experimental technique implemented at LHC to measure both the integrated and the instantaneous luminosity are described in the following sections. These techniques can be divided in direct and indirect. In direct measurements, such as the so-called Van der Meer scans or the beam gas interaction scans, the absolute luminosity is inferred from bunch properties. In indirect measurements, information on physics processes like measured rates are used. The measured rate is in fact only proportional to the absolute luminosity and it is referred to as relative luminosity.

Both absolute and relative luminosity are important to measure the cross section of a process from its rate. The absolute luminosity scale directly affects the reported cross-sections, and so it must be calibrated as accurately as possible; the stability and long-term internal consistency of the instantaneous luminosity measurements are essential to evaluate the time integral correctly.

Also, real-time instantaneous-luminosity monitoring is crucial for beam tuning and collision optimization; the absolute specific luminosity, defined as the luminosity per bunch and per unit bunch intensity, provides information on beam emittances and collider optics that cannot be obtained reliably otherwise; and the long-term evolution of the integrated luminosity directly quantifies, in a global way, the overall performance of the collider.

1.4 Luminosity from beam parameters

The absolute luminosity can be obtained starting from the parameters of an accelerator. For simplicity, we make some assumption on the beams and on the collisions [3]:

- the transverse and longitudinal beam densities are Gaussian;
- linear x–y coupling is small enough to be neglected (i.e. the motion on the x axis is independent of the motion on y axis);
- dispersion at Interaction Point (IP) and angular dispersion are negligible;
- beam–beam-induced effects are negligible.

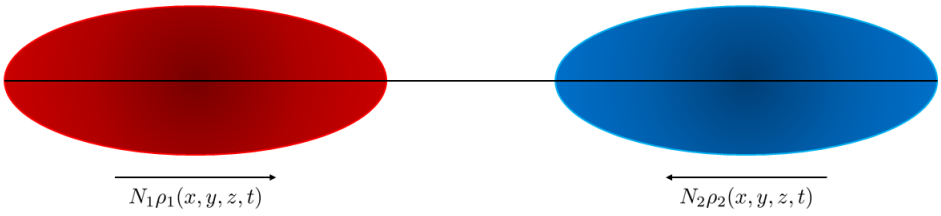

Figure 1.3: Scheme of the collision between 2 bunches with a zero crossing angle.

The bunch luminosity $\mathcal{L}_b$ produced by one colliding-bunch pair (Fig. 1.3), with time- and position-dependent density functions $\rho_1(x,y,z,t)$ and $\rho_2(x,y,z,t)$ is given by:

$$\mathcal{L}_b = f_r n_1 n_2 K \int \rho_1(x,y,z,t)\rho_2(x,y,z,t)\, dx\, dy\, dz\, dt \tag{1.38}$$

where 1 refers to bunch 1 and 2 refers to bunch 2, f_r is the revolution frequency, n_1 and n_2 are the number of protons in each bunch and the densities are normalized such that their spatial integral is equal to 1 for each time. K is a kinematic factor given by

$$K = \sqrt{(\vec{v_1} - \vec{v_2})^2 - \frac{(\vec{v_1} \times \vec{v_2})^2}{c^2}} \tag{1.39}$$

where $\vec{v_1}$ and $\vec{v_2}$ are the velocities of each beam. Supposing that $\vec{v_1}$ and $\vec{v_2}$ have the same module, the lab frame is defined in the following way: x-axis points in the direction of $\vec{v_1} + \vec{v_2}$, y-axis in that of $\vec{v_1} \times \vec{v_2}$ and the z-axis is parallel to $\vec{v_1} - \vec{v_2}$. The crossing angle lies in the xz plane.

Assuming that $v_1 = v_2 = c$, the bunch luminosity simplifies to

$$\mathcal{L}_b = f_r\, n_1\, n_2\, 2c \cos\theta_c \int \rho_1(x,y,z,t)\rho_2(x,y,z,t)\, dx\, dy\, dz\, dt \tag{1.40}$$

The beam density is defined

$$\rho_B = \frac{1}{\sqrt{(2\pi)^3}\sigma_{xB}\sigma_{yB}\sigma_{zB}} \times exp\left[-\frac{(x-x_B)^2}{2\sigma_{xB}^2} - \frac{(y-y_B)^2}{2\sigma_{yB}^2} - \frac{(z-ct)^2}{2\sigma_{zB}^2}\right] \tag{1.41}$$

where $B = 1, 2$ indicates the two beams, σ_{jB} $(j = x, y, z)$ is the dimension of the beam. For head on collisions, the bunch luminosity becomes

$$\mathcal{L}_b = f_r\, n_1\, n_2\, 2c \int \rho_1(x,y,z,t)\rho_2(x,y,z,t)\, dx\, dy\, dz\, dt\ = \frac{f_r\, n_1\, n_2}{2\pi\, \Sigma_x\, \Sigma_y} \tag{1.42}$$

where

$$\Sigma_j = \sqrt{\sigma_{j1}^2 + \sigma_{j2}^2}.$$

If the two beams have the same dimensions ($\sigma_{x1} = \sigma_{x2}$ and $\sigma_{y1} = \sigma_{y2}$) $\mathcal{L}_b$ can thus be rewritten as

$$\mathcal{L}_b = \frac{f_r\, n_1\, n_2}{4\pi\, \sigma_x\, \sigma_y} \tag{1.43}$$

If in addition $\epsilon_x = \epsilon_y$ and $\beta_x^* = \beta_y^*$, then the beans are round ($\sigma_x = \sigma_y$) and

$$\mathcal{L}_b = \frac{f_r\, n_1\, n_2}{4\pi\, \sigma^2} = \frac{f_r\, n_1\, n_2\, \gamma}{4\pi\, \epsilon_N\, \beta^*} \tag{1.44}$$

where $\epsilon_N = \gamma\,\beta\,\epsilon$ is called the normalized emittance, γ is the relativistic Lorentz factor and β is the velocity. The total instantaneous luminosity is given by

$$\mathscr{L} = \sum_b \mathcal{L}_b \tag{1.45}$$

There are some effects that reduce the luminosity as defined so far: crossing angle, offset collision and hourglass effect. These will be discussed in the following paragraphs. Other effects that have an impact on the maximum obtainable luminosity are related to dispersion effects and beam-beam interactions. The analysis of these effects is outside the scope of this thesis and therefore won't be treated.

1.4.1 Crossing angle

The crossing angle (Fig. 1.4) is introduced in order to restrict collisions only to the IP and to avoid unwanted parasitic-collisions at the other positions in the ring where the two beams are not separated. Due to the crossing angle θ_c, the luminosity is reduced by a factor:

$$F_c = \sqrt{1 + \left(\frac{\theta_c \sigma_s}{2\theta^*}\right)^2} \tag{1.46}$$

where σ_s is the longitudinal (s) bunch length and σ^* the transverse R.M.S. beam size at the interaction point.

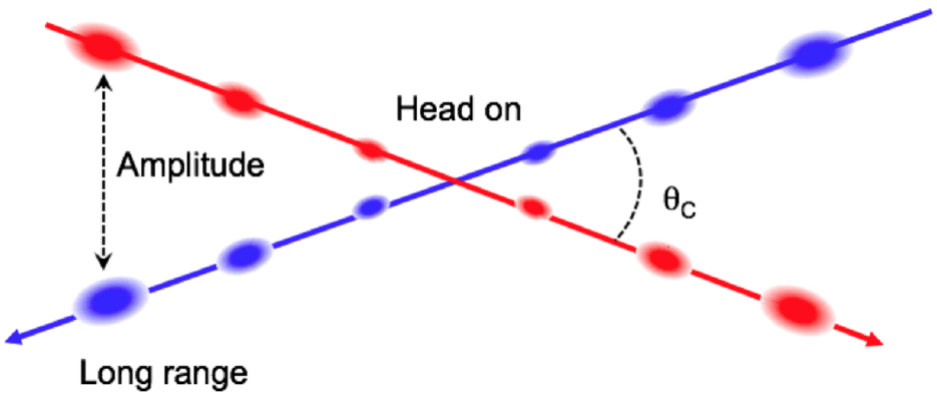

Figure 1.4: Scheme of the collision between 2 bunches with a non-zero crossing angle(θ_c).

1.4.2 Offset collisions

The two beams do not always collide head-on, actually they can be shifted in the horizontal and vertical directions by arbitrary displacements x_i and y_i ($i = 1, 2$). The beam

density has to be rewritten in the following way:

$$\rho_{i,x} = \frac{1}{\sigma_{ix}\sqrt{2\pi}} e^{-\left(\frac{(x-x_i)^2}{2\sigma_{ix}^2}\right)} \tag{1.47}$$

$$\rho_{i,y} = \frac{1}{\sigma_{iy}\sqrt{2\pi}} e^{-\left(\frac{(y-y_i)^2}{2\sigma_{iy}^2}\right)} \tag{1.48}$$

The luminosity will be

$$\mathcal{L} = \mathcal{L}_{MAX} e^{\left[-\frac{(\delta_x)^2}{2(\sigma_{1x}^2+\sigma_{2x}^2)} - \frac{(\delta_y)^2}{2(\sigma_{1y}^2+\sigma_{2y}^2)}\right]} \tag{1.49}$$

where $\mathcal{L}_{MAX}$ is the luminosity in head-on collision case and δ_x and δ_y are the two displacements of the centroids in the transverse plane.

1.4.3 Hourglass effect

The beam size $\sigma(s)$ is related to the betatron function and emittance:

$$\sigma(s) = \sqrt{\epsilon\beta(s)}. \tag{1.50}$$

At the interaction point, $\beta(s)$ is typically adjusted to have a local minimum in order to minimize the beam size and consequently maximize the interaction rate. The value of $\beta(s)$ at the IP is known as β^*.

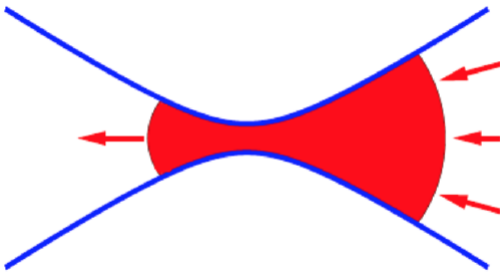

Figure 1.5: Pictorial view of Hourglass Effect. The bunch shape at the IP is drawn in red and the blue line indicates the parabolic shape of the β function. The bunch has a minimum in transverse size at the IP and grows moving away from it.

The assumption of the previous discussion is that the beam density functions are uncorrelated in the transverse and longitudinal planes and that the beam sizes are constant in the collision region. Actually, for low β^*, this is not a good approximation. The β-function varies around the minimum value as:

$$\beta(s) = \beta^*\left(1 + \frac{s^2}{\beta^{*2}}\right) \tag{1.51}$$

and the transverse beam size $\sigma(s)$ will be:

$$\sigma(s) = \sigma^* \sqrt{1 + \frac{s^2}{\beta^{*2}}} \tag{1.52}$$

The effect is known as hourglass effect because of the shape of the function (Fig. 1.5). The maximum luminosity is obtained for collisions occurring exactly at the IP, while away from the IP the beam size increases and the luminosity decreases. This effect becomes relevant if β^* is small compared to the bunch length, in particular if the ratio $r = \frac{\beta^*}{\sigma_s}$ is of the order of 1 or less.

1.5 Relative-luminosity monitoring methods

The bunch luminosity can be written as [4]:

$$\mathcal{L}_b = \frac{R_{ref,b}}{\sigma_{ref}} \tag{1.53}$$

where $R_{ref,b}$ is the rate of a reference collision process in a bunch crossing and σ_{ref} is the corresponding cross-section. The reference process can in principle be chosen arbitrarily; choosing inelastic *pp* collisions as a typical one, the above equation can be rewritten as

$$\mathcal{L}_b = \frac{\mu_b f_r}{\sigma_{inel}} \tag{1.54}$$

where μ_b is the average number of inelastic interactions per bunch crossing (BC), also called pile-up parameter, f_r is the bunch revolution frequency, and σ_{inel} is the inelastic pp cross-section. Therefore, the instantaneous luminosity can be determined using any method that measures the ratio μ_b/σ_{inel}.

There are several methods to determine this ratio, the main ones are [5]:

- *Event counting*: the fraction of bunch crossings in which a specified detector registers an "event" satisfying a given selection requirement is counted. For instance, a bunch crossing can be said to contain an "event" if at least one *pp* interaction in that crossing induces at least one observed hit in the detector being considered.

- *Hit counting*: determine the number of hits (for example the number of electronic channels or energy clusters above a specified threshold) per bunch crossing in a given detector.

- *Particle counting* : luminosity is proportional to the distribution of the number of particles per bunch crossing (or its mean) inferred from reconstructed quantities such as calorimeter-energy distributions, or from other observables that reflect the instantaneous particle flux traversing the detector.

A summary with the main pros and cons of each algorithm is given in Table 1.1

Eq. (1.54) can be rewritten as:

$$\mathcal{L}_b = \frac{\mu_b f_r}{\sigma_{inel}} = \frac{\mu_{vis} f_r}{\epsilon \sigma_{inel}} = \frac{\mu_{vis} f_r}{\sigma_{vis}} \tag{1.55}$$

where ϵ is the efficiency for one inelastic *pp* collision to satisfy the event-selection criteria, and $\mu_{vis} = \epsilon\mu$ is the average number of visible inelastic interactions per BC. The visible cross-section $\sigma_{vis} = \epsilon\sigma_{inel}$ is the calibration constant that relates the measurable quantity μ_{vis} to the absolute bunch luminosity $\mathcal{L}_b$.

If the probability of more than one interaction to occur within a bunch crossing is low enough, the relative luminosity can be monitored simply using an arbitrary physics process with sufficiently high rate and low enough background:

$$\mathcal{L}_b = \frac{R_{vis}}{\sigma_{vis}} \tag{1.56}$$

In this case, the mean number of visible interaction is:

$$\mu_{vis} = \frac{N}{N_{BC}} \tag{1.57}$$

where N is the (background-subtracted) number of events passing the selection criteria that are observed during a given time interval, and N_{BC} the number of bunch crossings in that same interval. When μ increases, the probability that two or more *pp* interactions occur in the same bunch crossing is no longer negligible, and μ_{vis} is no longer linearly related to the raw event count N. Instead μ_{vis} must be calculated taking into account Poisson statistics and instrumental or pile-up-related effects, as discussed below.

1.5.1 Event counting

In order to determine the value of μ_{vis} some assumptions are made:

- the number of pp interactions follows the Poisson statistics;
- the efficiency to detect a single inelastic *pp* interaction is constant even if several interactions occur in the same bunch crossing. This is equivalent to assuming that the efficiency ϵ_n for detecting one event associated with n interactions occurring in the same crossing is given by

  $$\epsilon_n = 1 - (1 - \epsilon_1)^n \tag{1.58}$$

  where ϵ_1 is the detection efficiency corresponding to a single inelastic interaction in a bunch crossing.

Thus, the absolute bunch luminosity is given by:

$$\mathcal{L}_b = \frac{\mu_{vis} f_r}{\sigma_{vis}} \tag{1.59}$$

using the value of σ_{vis} measured, for instance, by the Van der Meer method. To measure the value of μ_{vis} different algorithms like OR-algorithm and AND-algorithm can be used.

OR-algorithm

The majority of ATLAS luminometers is made of 2 symmetrical elements with respect to the interaction point called side-A and side-C. In an Event-OR algorithm, a bunch crossing is counted as containing an "event" if there is at least one hit on either the A or the C side of the detector. Since the Poisson probability for observing zero events in a given bunch crossing is $P_0(\mu_{vis}) = e^{-\mu_{vis}} = e^{-\mu\epsilon^{OR}}$, the probability of observing at least one event is

$$P_{OR}(\mu_{vis}) = \frac{N_{OR}}{N_{BC}} = 1 - P_0 = 1 - e^{-\mu_{vis}} \tag{1.60}$$

where N_{OR} is the number of bunch in which happened at least one interaction that satisfies the selection criteria and N_{BC} is the total number of colliding bunches. Solving for μ_{vis}:

$$\mu_{vis} = -\ln\left(1 - \frac{N_{OR}}{N_{BC}}\right) \tag{1.61}$$

AND-algorithm

In this case, a bunch crossing is counted if there is at least one hit in each of the two detector arms. This coincidence condition can be satisfied either from a single pp interaction or from individual hits on either side of the detector from different pp interactions in the same bunch crossing. Therefore, the event-counting probability no longer depends on a single efficiency: it must be written in terms of ϵ^A, ϵ^C and ϵ^{AND}, the efficiencies for observing an event with, respectively, at least one hit on the A-side, at least one hit on the C-side and at least one hit on both sides simultaneously. These efficiencies are related to the $P_{OR}(\mu_{vis})$ by the formula $\epsilon^{OR} = \epsilon^A + \epsilon^C - \epsilon^{AND}$.

The probability $P_{AND}(\mu)$ of observing at least one hit on both sides is one minus the probability P_0^{OR} of observing no hit on at least one side. The latter, in turn, equals the probability of no hits on at least side A ($P_{0A} = e^{-\mu\epsilon^A}$), plus the probability that there be no hit on at least side C ($P_{0C} = e^{-\mu\epsilon^C}$), minus the probability of no hits on either

side ($P_0 = e^{-\mu\epsilon^{OR}}$):

$$\begin{aligned} P_{AND}(\mu) = \frac{N_{AND}}{N_{BC}} &= 1 - P_0^{OR} \\ &= 1 - (e^{-\mu\epsilon^A} + e^{-\mu\epsilon^C} + e^{-\mu\epsilon^{OR}}) \\ &= 1 - e^{-\mu\epsilon^A} - e^{-\mu\epsilon^C} - e^{-\mu\epsilon^{OR}} \end{aligned} \tag{1.62}$$

This equation cannot be inverted analytically, and the best approach depends on the values of ϵ^A, ϵ^C and ϵ^{AND}.

If the layouts, geometries and efficiencies of the forward and backward luminometers are sufficiently similar, the above equation can be simplified under the assumption that $\epsilon^A \approx \epsilon^C$. The efficiencies ϵ^{AND} and ϵ^{OR} are defined as, respectively, $\epsilon^{AND} \equiv \sigma_{vis}^{AND}/\sigma_{inel}$ and $\epsilon^{OR} \equiv \sigma_{vis}^{OR}/\sigma_{inel}$. The average number of visible inelastic interactions per BC is computed as $\mu_{vis} \equiv \epsilon^{AND}\mu$. The previous equation can be thus rewritten as:

$$\begin{aligned} \frac{N_{AND}}{N_{BC}} &= 1 - 2e^{-\mu(\epsilon^{AND}+\epsilon^{OR})} + e^{-\mu\epsilon^{OR}} \\ &= 1 - 2e^{-\mu_{vis}(\sigma_{vis}^{AND}/\sigma_{inel}+\sigma_{vis}^{OR}/\sigma_{inel})/2} + e^{-\mu_{vis}\sigma_{vis}^{OR}/\sigma_{inel}} \end{aligned} \tag{1.63}$$

If the efficiency is high and $\epsilon^{AND} \approx \epsilon^A \approx \epsilon^C$, Eq.(1.62) can be approximated by

$$\mu_{vis} \approx -ln\left(1 - \frac{N_{AND}}{N_{BC}}\right) \tag{1.64}$$

1.5.2 Hit counting

When $\mu_{vis} \gg 1$, event-counting algorithms lose sensitivity as fewer and fewer bunch crossings in a given time interval report zero observed interactions: this is known as saturation or zero starvation. In the limit where $N/N_{BC} = 1$, it is no longer possible to use event counting to determine the interaction rate μ_{vis}, and more sophisticated techniques must be used. One example is hit counting, where the number of hits in a given detector is counted rather than just the total number of events. This provides more information about the interaction rate per event, and raises the luminosity at which the algorithm saturates.

Under the assumption that the number of hits in one *pp* interaction follows a binomial distribution[1] and that the number of interactions per bunch crossing follows a Poisson distribution, the average probability to have a hit per bunch crossing in one of the detector channels can be calculated as

$$P_{HIT}(\mu_{vis}^{HIT}) = \frac{N_{HIT}}{N_{BC}N_{CH}} = 1 - e^{\mu_{vis}^{HIT}} \tag{1.65}$$

[1]This is true only if the probability to register a signal is independent on the number of signals in the other channels

where N_{HIT} is the total numbers of hits, N_{BC} is the total numbers of bunch crossings and N_{CH} is the number of detector channels. μ_{vis}^{HIT} can be calculate as:

$$\mu_{vis}^{HIT} = -ln\left(1 - \frac{N_{HIT}}{N_{BC}N_{CH}}\right) \tag{1.66}$$

Therefore, the bunch luminosity becomes

$$\mathcal{L}_b = \frac{\mu_{vis}^{HIT} f_r}{\sigma_{vis}^{HIT}} \tag{1.67}$$

Hit counting algorithms are typically more sensitive than event-counting methods to instrumental imperfections such as threshold effects, instrumental noise, channel-to-channel efficiency variations and long-term gain drifts. Even so, such algorithms have been used successfully in the hostile experimental environment of the LHC, where very high values of the pile-up parameter μ render event counting impractical for large-acceptance luminometers.

Pile-up Effects and Non-Linearity

The intrinsic non-linearity of the counting methods, which is a direct consequence of Poisson statistics violation, has fundamental implications for luminometers meant to operate in a regime where the probability of detecting more than one inelastic pp interaction per bunch crossing cannot be neglected.

Firstly, and fundamentally because of the lack of synchrotron-radiation damping, bunch-to-bunch intensity and emittance fluctuations of 10%–20% are not uncommon in proton colliders. The resulting fluctuations in bunch luminosity L_b, coupled with the non-linearities apparent in Eqs. 1.61, 1.62 and 1.66, are often violent enough that bunch-averaged luminosity measurements become impractical. For large enough values of μ_{vis}, a naive procedure that averages the event probabilities (P_{OR}, P_{AND}, P_{HIT} ...) over all colliding bunch pairs and only then applies the Poisson combinatorial formalism above, can bias the measurement by tens of percent compared to the correct procedure of computing first the bunch luminosity L_b for each bunch separately, and then summing over all colliding bunch pairs. It is therefore essential, at least in an LHC-like environment, that the front-end electronics and dedicated data-acquisition (DAQ) systems associated with luminometers are specially designed from the start to cope with bunch-by-bunch luminosity determination.

Moreover, the applicability of the Poisson formalism depends on the validity of the assumption expressed by Eq.1.58: the efficiency for detecting an elastic pp interaction is independent of the number of interactions that occur in each bunch crossing or equivalently, from the detector's point of view, the interactions are independent from other. This latter assumption is intrinsically not true when a threshold is set to define a hit

(and consequently an event), which is exactly the way in which event and hit counting work. If, for example, two pp interactions happen in the same bunch crossing, both producing signals in the detector which are individually below the threshold (i.e. they would not be individually detected), but whose sum is above the threshold, then this assumption is clearly violated. The same holds if background not related to the pp interaction add up to produce a hit in addition or even without signals from collisions. The result is that the Poisson assumption is violated and non-linearities appear in the luminosity measurement with increasing pile-up. This effect is called migration and can be reduced, but not eliminated, by lowering as much as possible the thresholds. Only in the impossible limit of zero-threshold, the effect disappears. Migration becomes more important as the pile-up parameter increases. An in depth study of this effect will be discussed in Chapter 2.12.

1.5.3 Particle counting

A related strategy is the use of particle-counting algorithms, where some observable is directly proportional to the rate of particles interacting in the detector. These should be the most linear algorithms, since the visible interaction rate is directly proportional to the particle flux. These algorithms can involve detectors like trackers and calorimeters.

The advent of large-acceptance, high-precision silicon trackers at the LHC has enabled the development of additional algorithms that are based on reconstructing charged-particle tracks and, from these, pp interaction vertices.

Track-based event counting consists in measuring the fraction of bunch crossings with a minimum number of tracks (typically 1 or 2) reconstructed in the silicon trackers. Track counting is conceptually similar to hit counting and is more robust for background subtraction. In these algorithms, the number of well-reconstructed tracks per bunch crossing are counted with the track quality ensured by tight selection criteria.

In vertex-counting algorithms, the average number of visible interactions per bunch crossing is determined by counting the number of reconstructed vertices found in each bunch crossing. In its principle, the method is intrinsically linear and is applicable to much higher μ regimes than vertex-based event counting. But it suffers from nonlinear behavior with increasing pile-up parameter, primarily due to two effects: vertex masking and fake vertices. Vertex masking occurs when the vertex reconstruction algorithm fails to resolve nearby vertices from separate interactions, decreasing the vertex reconstruction efficiency as the interaction rate increases. Fake vertices result from a vertex that would normally fail the requirement on the minimum number of tracks, but additional tracks from a second nearby interaction are erroneously assigned to it so that the resulting reconstructed vertex satisfies the selection criteria.

Energy deposited in calorimeter is also proportional to particle flux. In ATLAS, the best approach is to measure the particle flux as reflected by the total ionization current flowing through a well-chosen set of liquid-argon calorimeter cells, or the current drawn by

the photomultipliers (PMTs) of an iron-scintillator hadronic calorimeter. Although such measurements do not, strictly speaking, count individual particles, the recorded currents depend linearly on the luminosity to sub-percent accuracy. The biggest drawback of this approach is that they can not provide bunch by bunch luminosity. LUCID has been able to measure luminosity bunch by bunch by measuring the charge produced by its PMTs every bunch crossing. The biggest challenge in measuring luminosity with this method, called charge counting, is keeping the PMT gain stable since it may vary inside a run due to PMT ageing and between runs.

Algorithm	**Pros**	**Cons**
Event counting	• Simple observable (signal in a detector).	• Saturation at low μ. • Intrinsic non linear.
Hit counting	• Simple observable (number of hits in a detector). • Applicable at higher pilepup compared to event counting.	• Intrinsic non linear. • Suffer from saturation.
Particle counting	• Perfectly linear. • Does not suffer from saturation.	• May be computationally intensive. • May not be able to achieve bunch-by-bunch luminosity. • May be limited by resolution or acceptance.

Table 1.1: Pros and Cons of Event, Hit, and Particle counting luminosity algorithms

1.6 Absolute luminosity calibration

To measure luminosity starting from μ_{vis} it is necessary to calibrate detectors and algorithms determining the visible cross section σ_{vis}[6].

The simplest method is to compare the visible interaction rate μ_{vis} to the absolute luminosity computed, in the same time interval, with measured beam parameters. For example, far from the IP, the parameters of the two beams can be separately estimated and then extrapolated to the collision point. Unfortunately this technique has a limited precision. A more accurate technique is the determination of the beam-overlap area directly at the IP using the beam-separation scans. A different approach is to measure, in dedicated runs, the elastic *pp* cross section at small angle and, using the optical theorem, to extract both the total cross section and the luminosity and relate it with the rate measured by the luminosity detectors. Finally well known physics processes for which not only the cross section, but also the total acceptance and efficiency are known with sufficient precision can be used. In the following paragraphs only the first two methods will be discussed since they are both used by the ATLAS experiment. An example of how the absolute luminosity is measured in ATLAS will be discussed in Chap. 2.6.

1.6.1 Measurement of beam parameters

The bunch luminosity (eqs 1.42, 1.43) can be calculated from the population of the two bunches n_B and from their transversal section σ_{iB} (i=x,y; B=1,2). Although the measurement of the population has reached a precision of 1%, a precise measurement of the transversal section of the bunches at IP is very difficult due to the experimental resolution and spatial limitations. The beam-profile monitoring is based on wire scanners or synchrotron light telescope methods. The monitors are installed in diagnostic regions away from the IP and they usually reports the projected horizontal and vertical RMS beam sizes, which can be extrapolated to the interaction point using an optical model of the collider lattice. Nevertheless, this technique has some limitation that has to be taken into account.

- Instrumental systematics (such as wire scanning speed, beam-induced heating, distortion of optical mirrors, resolution effects, etc.) make the precise determination of the absolute transverse beam size at the monitor rather challenging.
- The determination of the single-beam sizes to the IP requires the knowledge of a certain set of parameters, such as the betatron functions and betatron phases, both at the monitor points and at the IP. These parameters must be determined in separated sessions and their combination typically contribute with significant amount to the uncertainty to each of the four IP single-beam sizes σ_{iB}.

- Extrapolation becomes challenging if transverse coupling, dispersion and dynamic-β effects play a significant role.
- The assumption of Gaussian beams, factorisable in x and y, may demonstrate itself as an incorrect hypothesis, because of instrumental limitations.

Typical precision obtained with such methods are not better than 10-15%.

1.6.2 Van der Meer scan at LHC

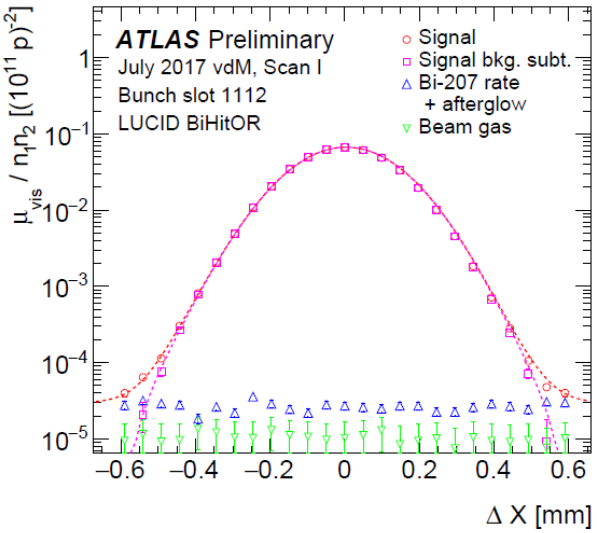

Figure 1.6: Visible interaction rate per unit bunch population vs beam separation as measured by LUCID for bunch 1112 in scan 1 of the July 2017 VdM session

At LHC, the primary technique to determine the absolute luminosity scale is based on dedicated beam-separation scans. The underlying idea is to measure the parameters of the colliding bunches, namely the transverse dimensions of the beams, by varying the distance between the colliding beams in dedicated 'scan sessions'. By comparing the known luminosity delivered at the peak of the Van der Meer (VdM)[7] (fig 1.6) scan to the visible interaction rate μ_{vis}, the visible cross-section of inelastic pp collisions can be determined. To achieve the desired accuracy on the absolute luminosity, these scans are usually performed not during normal physics operations, but under carefully controlled conditions and with beam parameters optimized for the purpose (low number of filled bunches, null crossing angle and a β^* equal to 19.2 m instead of 0.25-0.8 m). The bunch luminosity is given by

$$\mathcal{L}_b = \frac{f_r \, n_1 \, n_2}{2\pi \, \Sigma_x \, \Sigma_y} \tag{1.68}$$

Σ_x (and in an analogous way Σ_y) can be determined using the instantaneous luminosity $R(\Delta x)$ measured as a function of the distance Δx between the two beams along the trasversal direction x.

$$\Sigma_x = \frac{1}{\sqrt{2\pi}} \frac{\int R(\Delta x) d\Delta x}{R(0)} \tag{1.69}$$

If $R(\Delta x)$ is Gaussian, Σ_x will be the RMS of the distribution. Since $R(\Delta x)$ is normalized, it is possible to use every quantity that is proportional to luminosity to determine the calibration curve. Combining 1.42 and 1.69, it is possible to calculate the visible cross section as

$$\sigma_{vis} = \mu_{vis}^{MAX} \frac{2\pi \, \Sigma_x \, \Sigma_y}{n_1 \, n_2} \tag{1.70}$$

where μ_{vis}^{MAX} is the maximum number of visible interaction per bunch crossing calculated in the peak of the scan curve.

Chapter 2

Luminosity Measurement in ATLAS

2.1 Introduction

This chapter focuses on the measurement of luminosity in the ATLAS experiment. It begins with a brief overview of the accelerator complex and the LUCID-1 detector, followed by a detailed description of LUCID-2. Since LUCID-2 is not the only luminometer used in ATLAS, the other luminometers will also be briefly introduced. The discussion then addresses the main sources of systematic uncertainties in luminosity measurements, using the analysis of Run-2 data (2015-2018) as an example. Preliminary results from the 2022 luminosity measurements will be presented, followed by a discussion of new studies conducted on LUCID-2 to evaluate the detector's performance for 2023 and 2024.

2.2 The Large Hadron Collider

The Large Hadron Collider (LHC) is currently the largest accelerator in the world, located at CERN in Geneva. It was built to extend the discovery potential of the LEP (the previous CERN accelerator) and the Tevatron (Fermilab accelerator), enabling the investigation of events with energy thresholds exceeding 10 TeV. The LHC consists of a 27 km ring of superconducting magnets that accelerate the particle beams. However, the LHC is only the final stage of a larger accelerator chain (see Fig. 2.1) [8], which includes several older accelerators previously used at CERN. The chain includes:

- **LINAC2**: A linear accelerator that takes protons from the source and accelerates them to 50 MeV;
- **Proton Synchrotron Booster (PSB)**: Accelerates protons from LINAC2 up to 1.4 GeV;
- **Proton Synchrotron (PS)**: Accelerates particles up to 28 GeV and divides them into 25 ns bunches;

- **Super Proton Synchrotron (SPS)**: The final stage before the LHC, raising the energy to 450 GeV.

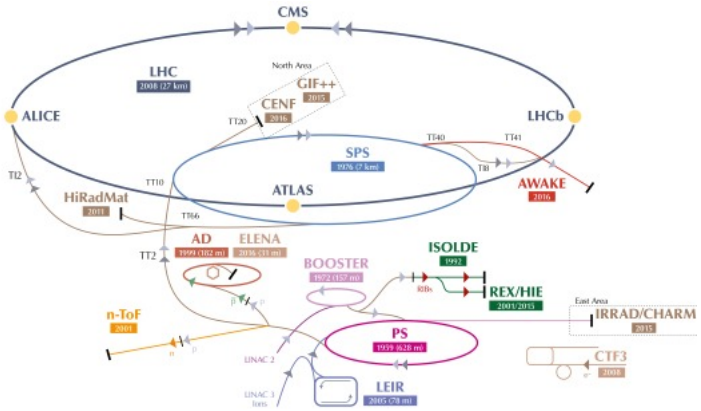

Figure 2.1: Schematic of the LHC accelerator chain, showing the integration of older CERN accelerators, now used as pre-accelerators for the LHC beams before injection.

Two beams circulate in opposite directions within the LHC. They can be made up of either protons or ions. The points where the beams collide are called interaction points (IPs). The beams are divided into 3564 packets (bunches) because the acceleration system was not designed to accelerate continuous beams. Only 2808 of the available bunches can be filled. During physics runs, a bunch crossing occurs every 25 ns. The maximum design center-of-mass energy is 14 TeV, but during Run 2, a center-of-mass energy of 13 TeV was reached, and in 2022, 13.6 TeV was achieved. The parameters of the beams are shown in Table 2.1.

Parameter	2024	Design value
Beam energy [TeV]	6.8	7
β^* at IP 1[m]	0.30	0.55
Bunch spacing [ns]	25	25
Maximum number of bunches	2544	2808
Mean bunch intensity [protons/bunch]	1.1×10^{11}	1.5×10^{11}
Peak luminosity [$\mathrm{cm}^{-2}\mathrm{s}^{-1}$]	2.33×10^{34}	1×10^{34}
Maximum number of events per BCID	65	19

Table 2.1: Current LHC performance compared to design values.

The four experiments located at the LHC are placed at the interaction points: ATLAS, CMS, ALICE, and LHCb.

- **ATLAS** (A Toroidal LHC Apparatus): Focuses on studying the Higgs boson, making precision measurements of the Standard Model, and searching for signs of physics beyond the Standard Model;
- **CMS** (Compact Muon Solenoid): Uses different and complementary detector technologies with similar goals to those of ATLAS;
- **ALICE** (A Large Ion Collider Experiment): Studies the behavior of quarks under conditions of high temperature and high energy density. It is the only experiment at the LHC focused on heavy-ion collisions;
- **LHCb** (LHC beauty): Investigates the physics of b-flavor particles and the violation of symmetries, such as CP violation.

2.3 LUCID-1

LUCID-1 (LUminosity measurement using a Cherenkov Integrating Detector) was the luminometer used by ATLAS during Run-1 (2009–2013). It consisted of two symmetric arms installed around the beam pipe, 17 meters from the IP. Each arm contained 20 aluminum cylinders filled with a Cherenkov radiator gas, all pointing towards the IP. When a charged particle entered a cylinders, it produced Cherenkov light, which was collected by photomultiplier tubes (PMTs) located at the end of the tubes. The design of this detector was quite similar to the CLC luminometer, which successfully operated in the CDF experiment at Fermilab [9].

Sixteen of the aluminum cylinders had PMTs directly attached, while in the remaining four cylinders, the light was first collected by optical quartz fibers and then sent to PMTs placed in a low-radiation area. LUCID-1 was designed to measure luminosity with a 5% precision at μ-values up to about 7, but it provided accurate measurements even at higher μ-values. However, as the μ-value exceeded 20 in 2011, it was observed that small signals from secondary particles passing through only part of the gas volume would add up and exceed the discriminator thresholds, a phenomenon known as "migration". This caused the number of counts from the detector to deviate from Poisson statistics, thereby compromising the luminosity calculation.

Interestingly, it was discovered that particles passing only through the 1.2 mm thick quartz window of the PMTs produced enough Cherenkov photons to generate a sizable signal, and these signals were less affected by the migration problem. As a result, the detectors were operated without gas for a large portion of 2011 and the entirety of 2012. Furthermore, it was observed that the current drawn by the PMTs during physics runs was proportional to the luminosity. Due to the low precision in current measurement and the inability to measure luminosity with BCID granularity, new electronics were

developed not only to discriminate signal but also to integrate them and perform charge algorithm.

The high particle density at the LUCID location caused the anode current in the PMTs to reach twice the recommended limit, leading to PMT aging. To address this issue, a system was implemented to inject LED light through optical quartz fibers into the front of the aluminum Cherenkov tubes. The LED light enabled accurate gain measurements by detecting the single photoelectron peak. However, at higher luminosities, these measurements were affected by background noise from the activation of materials surrounding LUCID.

Another challenge at high luminosities was the phenomenon of zero-starvation. During a typical 60-second ATLAS luminosity measurement period, known as a Luminosity Block (LB, or lumiblock), some LUCID luminosity algorithms registered hits during every bunch crossing. This was mitigated by reducing the detector's acceptance. In light of these challenges and to improve the accuracy of luminosity measurements, LUCID-2 was developed.

2.4 LUCID-2

LUCID-2, the primary ATLAS luminometer for Run 2, was designed in 2013, installed in 2014, and commissioned in 2015. It consists of several small Cherenkov detectors used for luminosity measurement and monitoring. The key improvements of LUCID-2, compared to LUCID-1, include the use of the thin quartz windows of the PMTs as the sole Cherenkov medium, and the deposition of small amounts of radioactive ^{207}Bi sources onto these windows to monitor the gain stability of the PMTs. The result is a fast and accurate luminosity detector that remains stable throughout data collection.

Measuring luminosity at the LHC is challenging due to the multiple interactions that occur during each bunch crossing. Therefore, determining luminosity at the LHC requires evaluating the average number of interactions (μ) that occur when two bunches collide in the experiment. In 2011, a maximum of 20 pp-interactions per bunch crossing was observed. This number doubled in 2012 and doubled again during LHC Run 2. Luminosity measurements at the LHC must, therefore, function effectively in scenarios with high pile-up. The LUCID-2 detector measures luminosity not only by counting hits (signals exceeding a threshold) in the detector but also by integrating these signals. This latter method is advantageous because it can operate effectively even in high pile-up conditions, such as those seen and anticipated during LHC Runs 2 and 3 (2022-2026).

The LHC can fill up to 2808 different colliding bunch pairs, each separated by 25 ns, and luminosity must be measured for each bunch individually. This posed several design challenges for both the detector and its readout electronics.

In the early phase of each fill during Run-3, the LHC maintains a constant μ level that is sustainable for the detectors (known as *luminosity leveling*). This stability is achieved

by adjusting parameters such as beam separation, crossing angle, or both together. Currently, the target μ value is set at an average of 62, though differences between bunches can vary by up to 40%. This approach aims to maximize integrated luminosity while keeping peak luminosity and pile-up at manageable levels. Therefore, it is essential for LUCID to provide rapid feedback. LUCID-2 was designed to provide the LHC fast updates on both luminosity and beam background information at a rate of approximately 1 Hz.

2.4.1 LUCID-2 Design

The goal of LUCID-2 is to provide precise luminosity measurements with a total uncertainty of approximately 1%, conducted on a bunch-by-bunch basis. To achieve this objective, LUCID-2 must utilize very short signal durations (less than 25 ns). Another challenge it faces is the range of pileup conditions: it must be capable of measuring from $\mu \approx 60$ during normal physics runs to $\mu \ll 1$ during specific runs, such as the van der Meer scan (vdM). This requirement impacts the acceptance of the detector, which must be sufficiently high to be sensitive during vdM runs, yet low enough to avoid saturating the algorithms used in physics runs.

LUCID-2 consists of two modules (Fig 2.2), located on sides A and C of the ATLAS experiment, placed symmetrically 17 m from the interaction point.

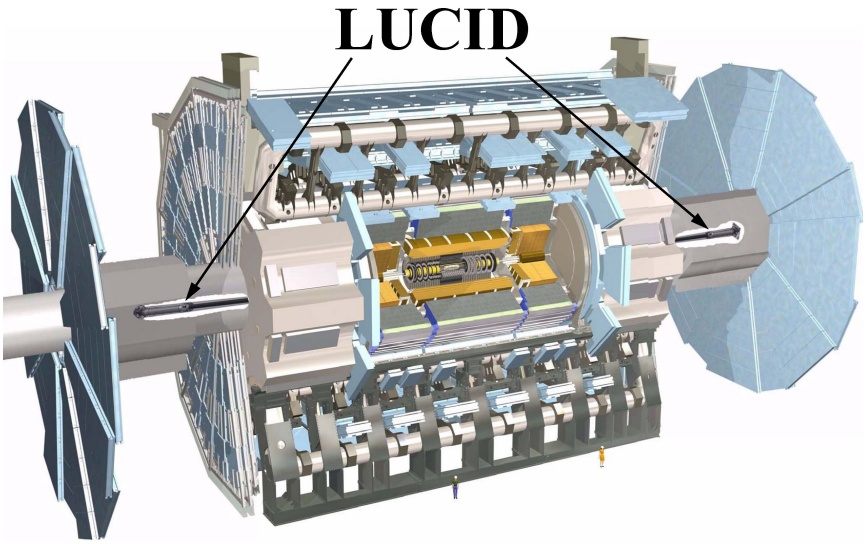

Figure 2.2: Position of LUCID within the ATLAS detector.

Each module comprises 16 photomultiplier tubes (PMTs), arranged in 4 blocks with 4 PMTs each (see Fig 2.3). The placement and dimensions of the PMT windows are optimized to achieve the best acceptance. The PMTs are mounted to the beam pipe using

a carbon fiber support structure, which also houses sensors for monitoring temperature and the cooling system. The cooling system is activated only during a very specific phase of the beampipe preparation at the start of a data-taking period: the beampipe bake-out [1].

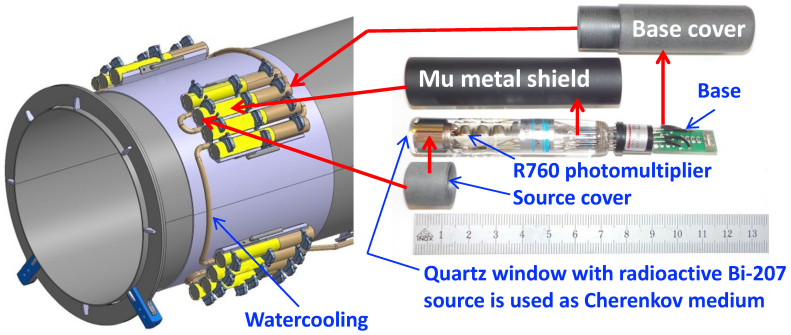

Figure 2.3: Schematic representation of LUCID-2 during Run-3.

Each PMT features a quartz window that serves as a Cherenkov radiator. Behind this window, a photoelectric material converts the Cherenkov photons into photoelectrons. This electron signal is then amplified by a chain of dynodes, achieving a gain of up to 10^6. The amplified signal is read out by the LUCID ReadOut Driver (LUCROD), a custom VME board designed to amplify, digitize, discriminate, and integrate the signals.

During Run-2, four different types of PMTs were utilized:

- Bi: four Hamamatsu R760 PMTs with a diameter of 10 mm, coated with ^{207}Bi on the quartz window for calibration;
- Bi2: another set of four PMTs similar to the Bi type, used for cross-checks and redundancy;
- BiM (Bi-MOD): four Hamamatsu R760 PMTs featuring an aluminum foil between the quartz window and the photocathode to partially mask the photocathode itself and reduce acceptance to an effective 7 mm diameter. The quartz window is also coated with ^{207}Bi for calibration;
- Spare: a set of four PMTs similar to the Bi type, kept as replacements in case of malfunction of the primary PMTs.

[1] The beam pipe bake-out refers to a process used in particle accelerators and similar vacuum systems to achieve and maintain ultra-high vacuum (UHV) conditions inside the beam pipe. This process involves heating the beam pipe to a specific elevated temperature to remove adsorbed gases and contaminants from the interior surfaces of the pipe

PMT types alternate to ensure uniform coverage of with all algorithms.

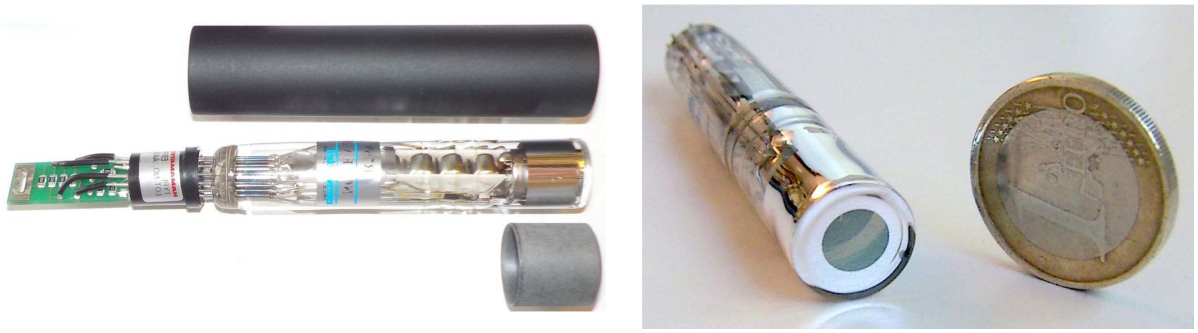

Figure 2.4: Left: Hamamatsu R760 photomultiplier with its base, mu-metal magnetic shield, and a peek cap that seals the ^{207}Bi source. Right: Modified PMT with a white aluminum ring deposited on the inside of the PMT window.

The Bi-MODs (Fig. 2.4 right) were developed by Hamamatsu, based on the standard R760, at the request of the LUCID group. This modification aimed to reduce the detector acceptance by approximately half. These photomultipliers feature a ring of aluminum deposited on the inside of their windows, which diminishes the acceptance. However, Monte Carlo simulations indicated that this reduced acceptance resulted in a greater dependence on μ, a trend that was confirmed in data (see Fig 2.5). The Bi-MODs were replaced with new PMTs (Hamamatsu R1635) during the year-end technical stop in 2023. The new PMTs are smaller than the R760, maintaining the same acceptance as the BiM while exploiting a nonlinearity with respect to μ similar to that of the standard R760.

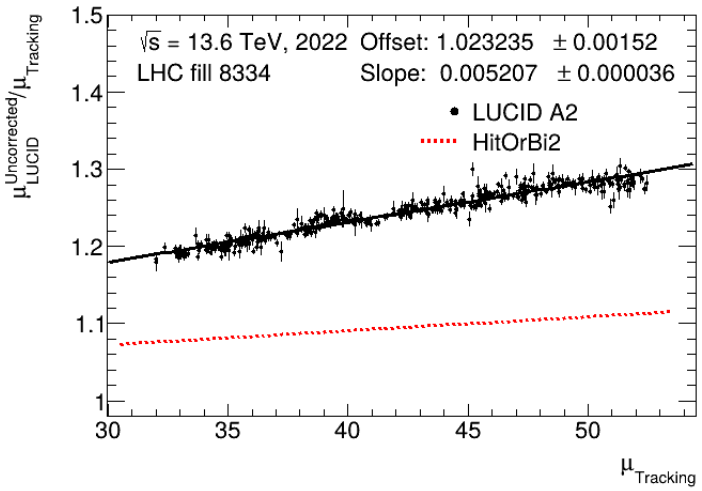

Figure 2.5: μ-dependence fit for a BiM PMT in 2023. The red dotted line shows the μ-dependence fit of standard LUCID-2 PMTs

In Run-2, four optical fibers coupled with a PMT for readout were also installed. These fibers serve a dual purpose: they act both as Cherenkov radiators and as transmission mediums to convey Cherenkov light to the PMT situated in a less radioactive area. However, they were removed between Run 2 and Run 3 due to stability issues over the long term (see Fig 2.6).

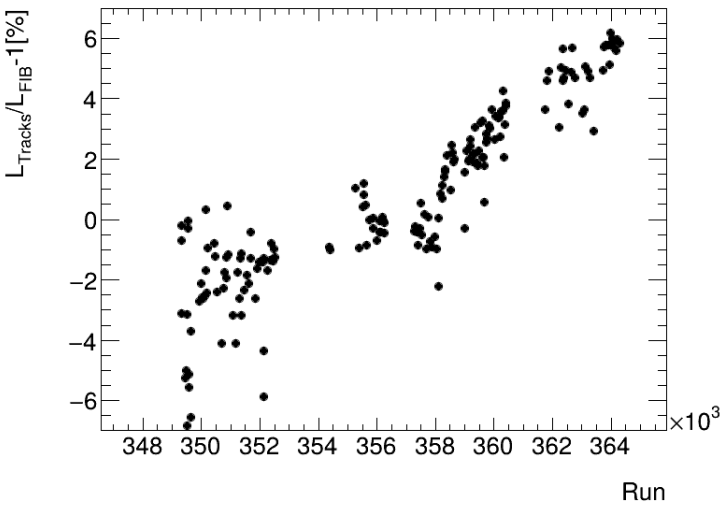

Figure 2.6: Long-term stability of the LUCID-2 fibers as a function of the run number.

2.4.2 LUCID-2 Electronics

A completely new electronic system was developed for LUCID-2. This new electronics can not only count discriminator hits from the photomultipliers but also integrate signals. The advantage of measuring integrated pulses is that it is proportional to the number of particles passing through the detector, thus mitigating the previously mentioned migration problem. The main challenge of this technique is maintaining a perfectly constant PMT gain both during a run and between runs. Part of the LUCID electronics is situated close to the detector, approximately 15 m away from the photomultipliers, to avoid distortions of the signal along the cable and not contaminating the signal in the next BCID.

Figure 2.7 illustrates the block diagram of the LUCID-2 electronics. The photomultiplier pulses are routed to four LUCROD [10] boards, a custom 9U VME board designed by the Electronics Lab of the Bologna INFN unit. These boards amplify, digitize, discriminate, and integrate the signals. The LUCRODs are also capable of providing luminosity algorithms for individual PMTs or combining the PMTs on the same side into OR or AND algorithms (see Chapter 1.5). Hit patterns corresponding to all possible bunch crossings (25 ns time slots) are transmitted to two custom VME boards known as LUMAT (LUMinosity And Trigger monitoring), located about 100 m away, via optical links. The LUMAT boards collect hits from the LUCRODs on both sides of the detector to generate combinatorial algorithms that involve PMTs from both sides.

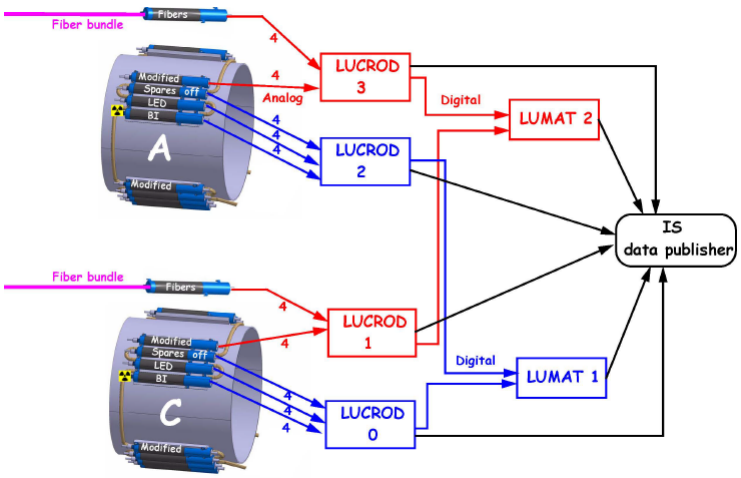

Figure 2.7: Block diagram of the electronics for the LUCID-2 detector.

The LUCROD board is schematically represented in Fig 2.8 and shown in a photograph in Fig 2.9. The board includes 16 LEMO analog inputs, 16 LEMO analog outputs (which are amplified copies of the inputs), and four LEMO digital I/O channels for triggering and debugging purposes. It also features JTAG and optical-link connectors.

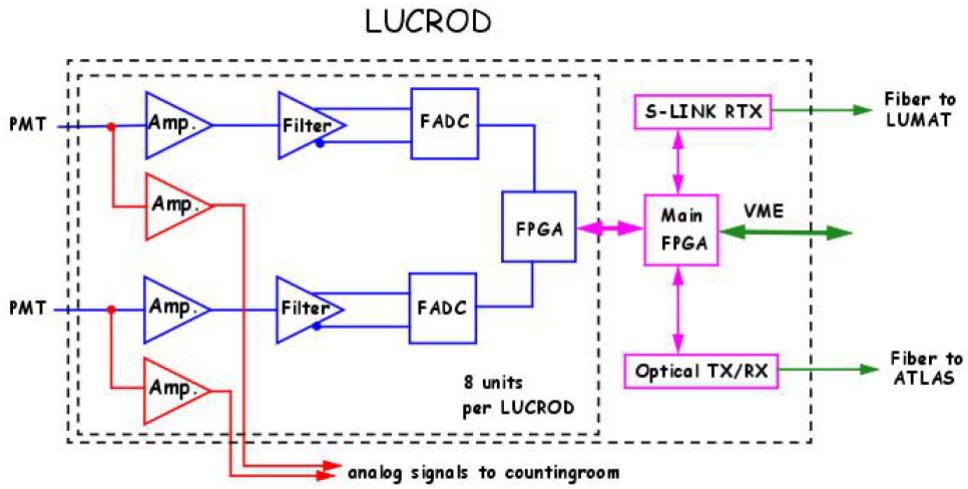

Figure 2.8: Block diagram of the LUCROD board.

Additionally, it houses a TTCrq[2] to receive external synchronization signals, along with optical transceivers to transmit digital information. The board implements several internal clocks that can be synchronized with the ATLAS 40 MHz main clock via the TTCrq, including a 40 MHz clock, 320/480 MHz clocks used by the FADC, and a 50 MHz clock utilized by the transceiver and its communication block.

Each LUCROD input channel is equipped with two independent and programmable amplifiers (with a gain of up to a factor of 16), one serving the analog output and the other supplying a 320/480 MHz FADC with 12-bit resolution and a 1.5 V dynamic range. The zero level of the signals is adjustable using dedicated Digital-to-Analog Converters (DACs).

Each LUCROD board hosts eight FPGAs directly connected to the FADCs, referred to as channel FPGAs, which receive the digitized data from two Flash Analog-to-Digital Converters (FADCs). Additionally, it is equipped with two other FPGAs, known as the main FPGAs, that receive data from the channel FPGAs, combine them in single side luminosity algorithm and interface with the optical transceivers to send hit pattern to LUMATs.

In the channel FPGAs, the digitized inputs are summed over each Bunch Crossing ID (BCID) period (25 ns or 8 clock samples) to provide charge information, and the maximum pulse height is compared to a programmable threshold to define hits within the same time windows. Hits and charge information are accumulated in 3564-slot FIFOs (the depth corresponding to an LHC orbit). When a trigger occurs, 64 samples of the digitized waveforms are made available for VME readout, selectable between a pro-

[2]A mezzanine card developed by the CERN microelectronics group to manage Timing, Trigger, and Control systems for the LHC (\http://ttc.web.cern.ch/TTC/).

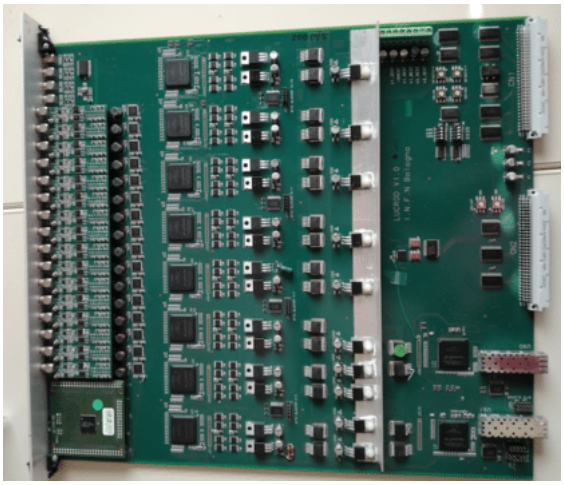

Figure 2.9: Photograph of the LUCROD board.

grammable portion of the LHC orbit (BCID trigger) or the presence of a hit (self-trigger). This slow VME readout provides a monitoring data stream containing hardware samples of each PMT waveform (Fig 2.10).

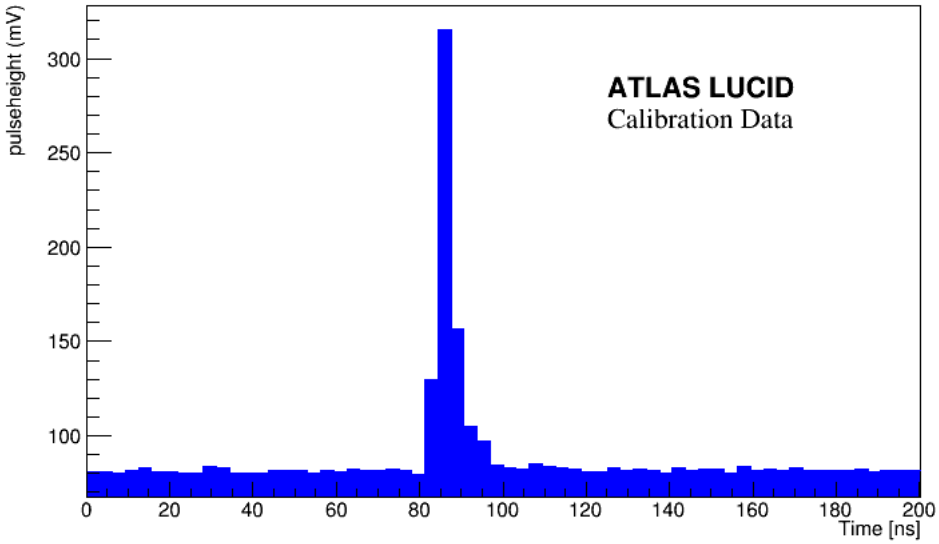

Figure 2.10: Example of a signal generated by the Bismuth calibration source as read by the LUCROD.

The main FPGAs receive charge and hit data from programmable combinations of the channel FPGAs, providing charge sums, hit sums, and event sums (indicating at least one hit in one of the selected inputs) with BCID granularity. Furthermore, the main FPGA routes hits to the output transceiver, which feeds optical fibers connected to a LUMAT board. The hit pattern data sent from the LUCROD also include an orbit signal that marks the beginning of the the bunch crossing sequence (the Bunch Counter Reset signal received by the TTCrq) and an internally generated counter. These signals are utilized on the LUMAT board to synchronize the signals from side A and side C and to check for data loss.

Since the LUCROD boards are positioned near the PMTs in an area that cannot be accessed during LHC running periods, a dedicated firmware was developed to allow for loading and updating the firmware to recover from Single Event Upsets (SEUs).

In LUCID-2, given that hits are generated close to the detector, the LUMAT boards are equipped with Fast TracKer Input Mezzanines (FTK IM) [11], capable of receiving optical data from up to four S-link connections that carry both hit and synchronization data. The FTK IM, which houses two Spartan IV FPGAs, is programmed to receive two

streams of hit data from the two LUCROD boards assigned to sides A and C. These two streams of hits are then appropriately synchronized before being transmitted to the main FPGA of the LUMAT board, a Stratix II from Altera, where the main bunch-by-bunch luminosity algorithms are implemented.

Both the LUCROD and LUMAT boards accumulate hits and events (with the LUCROD also integrating charges) over lumiblock periods with BCID granularity in internal FIFOs. These FIFOs are read via VME interface by the TDAQ software at the end of each integration period (Fig. 2.11). A pair of FIFOs is used for each set of integrated data: one FIFO is incremented while the other is read, ensuring no data loss occurs during FIFO switches.

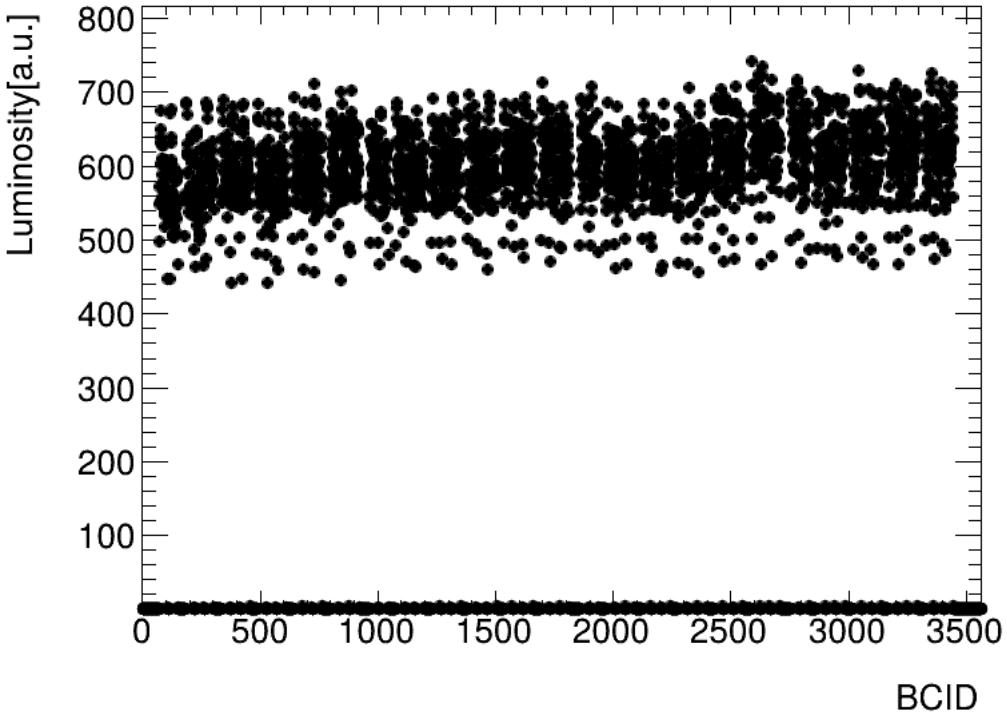

Figure 2.11: Example of bunch luminosity measured by LUMAT.

2.4.3 LUCID-2 Calibration

A crucial aspect of producing accurate luminosity measurements is the new calibration system, which is essential for monitoring the stability of the PMTs' gain of a year's running. Three independent calibration systems were designed and built, each utilizing a different principle and applied to a specific set of PMTs. Initially, 16 PMTs were fed with both LED and LASER light carried by quartz optical fibers, while an additional 4

PMTs were equipped with ^{207}Bi radioactive sources. The ^{207}Bi calibration demonstrated the best performance, as shown in Fig. 2.12; consequently, since 2017 onward, all LUCID PMTs are calibrated using this technique. Therefore, the discussion will focus solely on the ^{207}Bi calibration method.

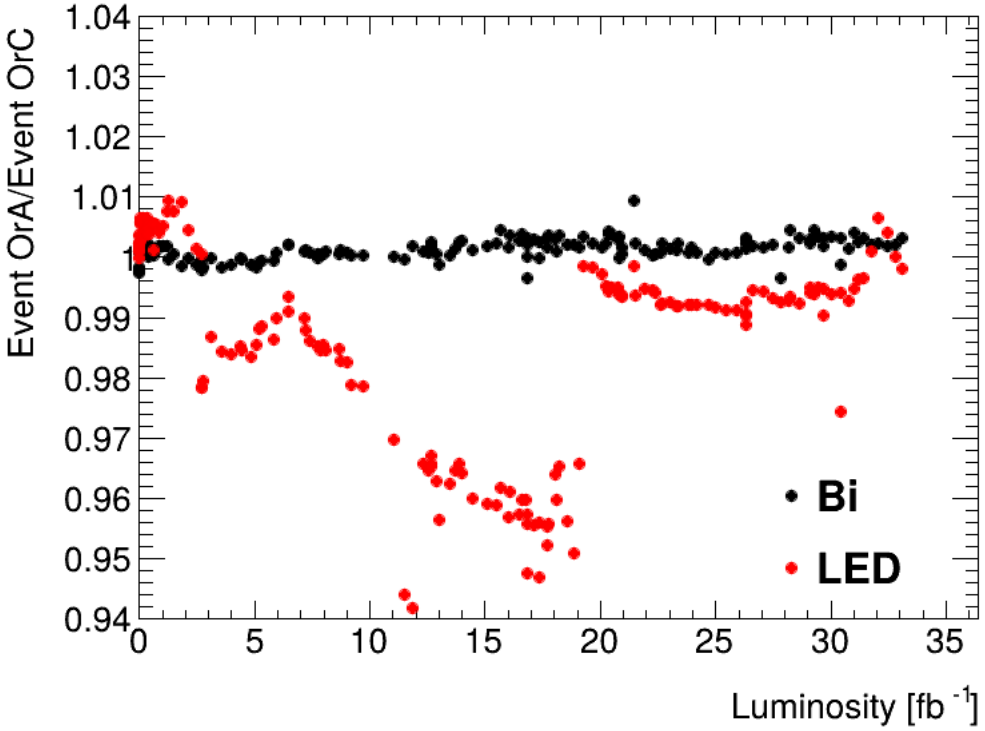

Figure 2.12: Ratio of Event OrA to Event OrC considering Bismuth-calibrated (black dots) and LED-calibrated (red dots) PMTs in 2016 (see Chapter 1.5).

^{207}Bi is a valuable source for PMT calibration because, in 11.5% of all disintegrations, it emits internal conversion electrons with energies of 482, 554, 566, 976, 1048, or 1060 keV, all of which exceed the Cherenkov threshold in quartz. Moreover, its half-life of 33 years ensures that the source's activity will remain stable throughout the detector's lifetime. This calibration method is intrinsically free from potential instabilities associated with LED or LASER input light and from possible degradation of the optical fibers transporting this light due to radiation damage. Furthermore, PMTs are calibrated using the same light spectra utilized during physics runs, allowing us to ignore any changes in PMT quantum efficiency due to radiation exposure.

A critical parameter to consider with this method is the activity of the deposited source: it must be sufficiently large to provide adequate statistics in a reasonable time while not so large as to interfere with luminosity measurements during data-taking. The

background produced by bismuth is indeed present at all times. While this does not pose an issue during normal high-luminosity operations, complications can arise during runs conducted under special conditions, such as the aforementioned van der Meer scans performed at very low luminosity, which are necessary for absolute luminosity calibration. Calibration data from 2015 indicated that an activity level between 30 and 45 kBq satisfies both efficiency and background requirements.

To monitor the gain stability of the photomultipliers, the mean charge and mean amplitude of self-triggered signals during calibration runs were measured for each PMT. These measurements are used to estimate the PMT gain. If a deviation from a chosen reference value is detected, an automatic procedure adjusts the PMT high voltage to compensate for it (Fig. 2.13).

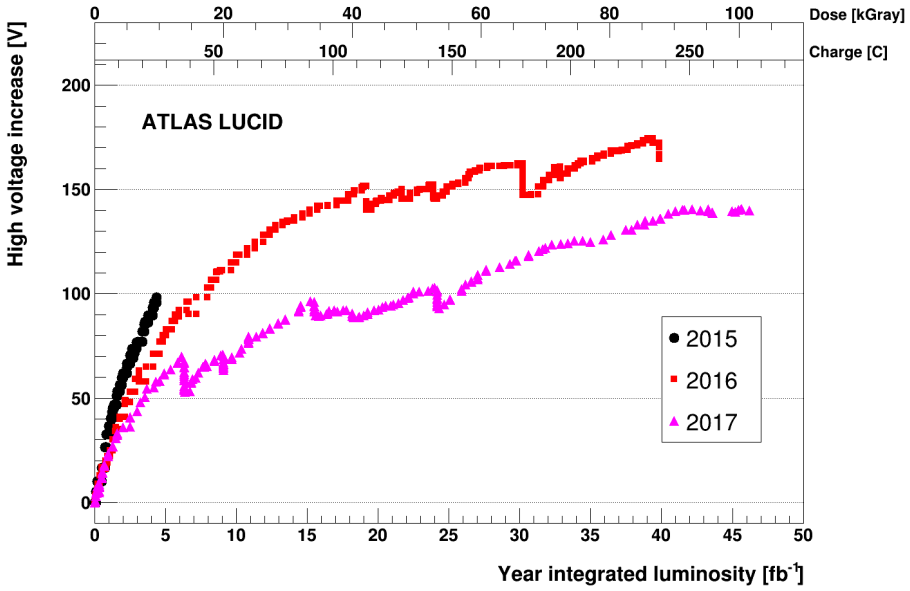

Figure 2.13: The increase in high voltage applied to a typical PMT is shown as a function of integrated luminosity delivered from 2015 to 2017, with data presented separately for each year. During long period without beams, PMTs recover therefore the HV is reduced to keep the gain constant

2.4.4 LUCID-2 Algorithms

The LUCID-2 electronics enables the implementation of various luminosity algorithms discussed in Chapter 1.5. The simplest algorithm utilizes a single PMT and counts an 'event' if the PMT records a signal above a specified threshold (a 'hit'), corresponding to one or more inelastic *pp* interactions detected in a given bunch crossing. Assuming

that the number of inelastic pp interactions in a bunch crossing follows a Poisson distribution, the probability for such an event P_{EVT} is given in terms of the single-PMT visible interaction rate $\mu_{vis} = \epsilon\mu$ by

$$P_{evt} = \frac{N_{EVT}}{N_{BC}} = 1 - e^{-\mu_{vis}}, \tag{2.1}$$

where N_{EVT} is the number of bunches where a signal is observed ("Event") and N_{BC} is the number of bunch crossings. Multiple PMTs can be combined in an "EventOR" (abbreviated as EvtOR) algorithm, which counts an event if any PMT in a group registers a hit in a given bunch crossing. This algorithm offers higher efficiency and σ_{vis} than a single-PMT approach, resulting in smaller statistical uncertainties at low bunch luminosity. However, at moderate single-bunch luminosity ($\mu > 20 - 30$), it suffers from "zero starvation," where two colliding bunches generate a hit every time they collide. Consequently, there are no bunch crossings left without an event, making it impossible to determine μ_{vis}.

The 'HitOR' algorithm provides an alternative method for combining PMTs at higher luminosity. The average probability P_{hit} of having a hit in any given PMT during N_{BC} bunch crossings can be evaluated from the total number of hits summed over all PMTs N_{hit} by:

$$P_{hit} = \frac{N_{hit}}{N_{BC}N_{PMT}} = 1 - e^{-\mu_{vis}}. \tag{2.2}$$

Here, N_{PMT} represents the number of PMTs. Various types of HitOR algorithms can be employed. The HitOrBi and HitOrBi2 algorithms combine four bismuth-calibrated PMTs on the A-side of LUCID with four additional PMTs on the C-side using the HitOr method.

The LUCID electronics also implements charge-based luminosity algorithms, which utilize signal charge instead of signal amplitude. The main advantages of this approach are:

- Charge is directly proportional to luminosity.
- It does not suffer from 'zero starvation'.

However, these algorithms are highly dependent on a stable baseline, on a stable gain during the run and a specific calibration procedure. For this reason, they were not used to provide luminosity during Run-2.

2.5 Additional Luminosity Detectors in ATLAS

The ATLAS luminosity measurements rely on multiple redundant luminosity detectors and algorithms. As previously discussed, the main luminosity detector during Run-2

is LUCID. This system is complemented by bunch-by-bunch measurements from the ATLAS Beam Conditions Monitor (BCM) diamond detectors, as well as offline measurements of the multiplicity of reconstructed charged particles in randomly selected colliding-bunch crossings (track counting).

The ATLAS calorimeters also contribute by providing bunch-integrated measurements (i.e., summed over all bunches) based on quantities that are proportional to instantaneous luminosity. Specifically, liquid argon (LAr) gap currents are utilized in the case of the ElectroMagnetic Endcap Calorimeter (EMEC) and the Forward Calorimeter (FCal), while photomultiplier currents are measured from the Scintillator-Tile Hadronic Calorimeter (TileCal). All these measurements are discussed in more detail below.

2.5.1 Beam Condition Monitor

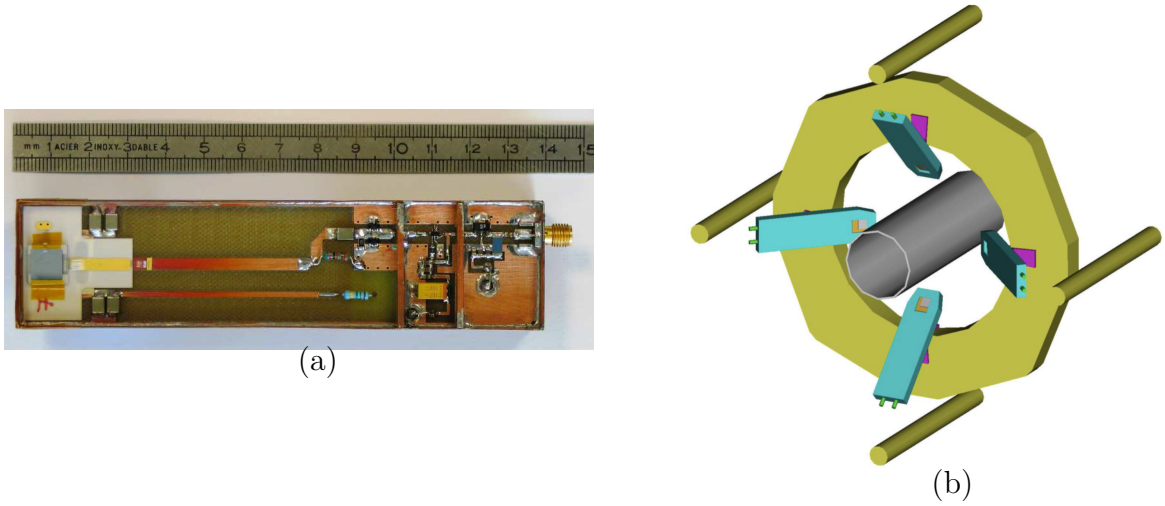

(a) (b)

Figure 2.14: On the left top view of the BCM module box showing the diamond sensors and their support ceramic. On the right placement of 4 BCM modules around the beampipe

The Beam Condition Monitor detector (Fig. 2.14) consists of four $8 \times 8\,\mathrm{mm}^2$ diamond sensors arranged around the beam pipe in a cross pattern at $z = \pm 1.84\,\mathrm{m}$ on each side of the ATLAS detector. The main goal of the BCM is to provide beam condition information and trigger the abort of the LHC beam under dangerous particle showers to protect the Inner Detector. It is also capable of providing a bunch-by-bunch luminosity signal with sub-nanosecond timing resolution.

Similar to LUCID, the BCM can combine hits from individual sensors in different ways (EvtOR, EvtAND). During most of Run 1, the BCM provided the primary ATLAS luminosity measurement; however, its performance was significantly impacted

during the physics data-taking conditions of Run 2, which featured 25 ns bunch spacing and higher pileup. This decline was attributed to a combination of radiation damage, charge-pumping effects, and bunch–position-dependent biases along bunch trains. Consequently, its use in Run 2 analysis was limited to consistency checks during certain van der Meer scan periods with isolated bunches and low instantaneous luminosity, as well as measurements during heavy-ion collisions.

An upgrade of the BCM, called BCM Prime or BCM', is foreseen for HL-LHC. Its μ dynamic range is expanded by segmenting each 645 sensor into a few smaller pads of different sizes, ranging from approximately 1 mm^2 to 50 mm^2.

2.5.2 The Inner Tracker

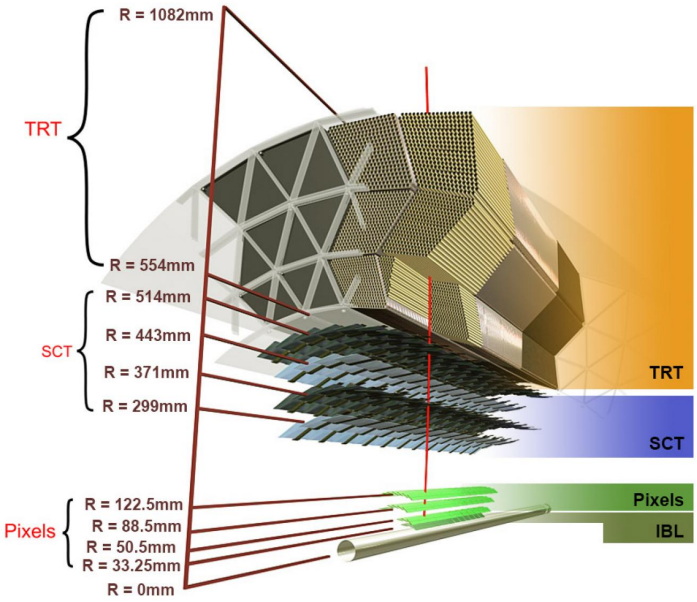

Figure 2.15: Scheme of ATLAS Inner Detector.

The Inner Detector (ID) system (Fig. 2.15) consists of a silicon pixel detector (PIX), a silicon microstrip detector (SCT), and the straw tubes of the Transition Radiation Tracker (TRT). It is designed to measure the trajectories and momentum of charged particles in the pseudorapidity region of $|\eta| < 2.5$. The ID surrounds the beam pipe and is located inside a solenoid magnet that provides a 2 T axial symmetric field. To improve track and vertex reconstruction performance at the high luminosities expected during Run 2 and to mitigate the impact of radiation damage to the innermost layer of the pixel detector, a fourth layer, the Insertable B-layer (IBL), was added to ATLAS.

The IBL was installed inside the previous innermost pixel layer of the ID and consists of 14 staves instrumented with planar and 3D silicon pixel sensor technology, extending 332 mm on each side from the center of the ATLAS detector.

The track-counting luminosity measurement determines the per-bunch visible interaction rate μ_{vis} from the mean number of reconstructed tracks per bunch crossing averaged over a luminosity block. The measurement is derived from randomly sampled colliding-bunch crossings, with data collected exclusively from the silicon tracking detectors (SCT, PIX, and IBL), typically at 200 Hz during normal physics runs and at much higher rates during van der Meer (vdM) scans and other special runs.

All reconstructed tracks used in the track-counting luminosity measurement were required to satisfy the TightPrimary requirements outlined in Ref. [12]. Additionally, tracks had to have a transverse momentum $p_T > 0.9$ GeV and a track impact parameter significance of $\mid d_0 \mid /\sigma_{d_0} < 7$, where d_0 is the impact parameter of the track with respect to the beamline in the transverse plane, and σ_{d_0} is the uncertainty in the measured d_0, accounting for the transverse spread of the luminous region. Several different track selection working points, applying additional criteria beyond these basic requirements, were employed, as summarized in Table 2.2.

The baseline selection A uses tracks only in the barrel region of the Inner Detector ($\mid \eta \mid < 1.0$), requires at least nine silicon hits N_{hits}^{Si} (counting both pixel and SCT hits), and allows at most one pixel 'hole' (N_{holes}^{PIX}), which is a missing pixel hit where one is expected, taking into account known dead modules. Selection B extends the acceptance into the endcap tracking region with tighter hit requirements for $\mid \eta \mid > 1.65$ and does not permit any pixel holes. Selection C is based on selection A, with a stricter requirement of at least ten silicon hits. Selection A serves as the baseline track-counting luminosity measurement, while the other selections are utilized to study systematic uncertainties.

Criterion	Selection A	Selection B	Selection C
$p_T[GeV]$	> 0.9	> 0.9	> 0.9
$\mid \eta \mid$	< 1.0	< 2.5	< 1.0
N_{hits}^{Si}	≥ 9	≥ 9 if $\mid \eta \mid < 1.65$ else ≥ 11	≥ 10
N_{holes}^{PIX}	≤ 1	$= 0$	≤ 1
$\mid d_0 \mid /\sigma_{d_0}$	< 7	< 7	< 7

Table 2.2: Track selection criteria for luminosity measurement

The statistical precision of the track-counting luminosity measurement is limited at low luminosity, making direct calibration using vdM scans impractical. Instead, the working points were calibrated to align with LUCID luminosity measurements in the same LHC fills as the vdM scans, using periods of stable, almost constant luminos-

ity when the beams were colliding head-on in ATLAS, typically while vdM scans were performed at the CMS interaction point. The average number of selected tracks per $\sqrt{s} = 13\,\text{TeV}$ inelastic pp collision was approximately 1.7 for selections A and C, and about 3.7 for selection B, which has a larger acceptance in $|\eta|$.

2.5.3 Calorimeters

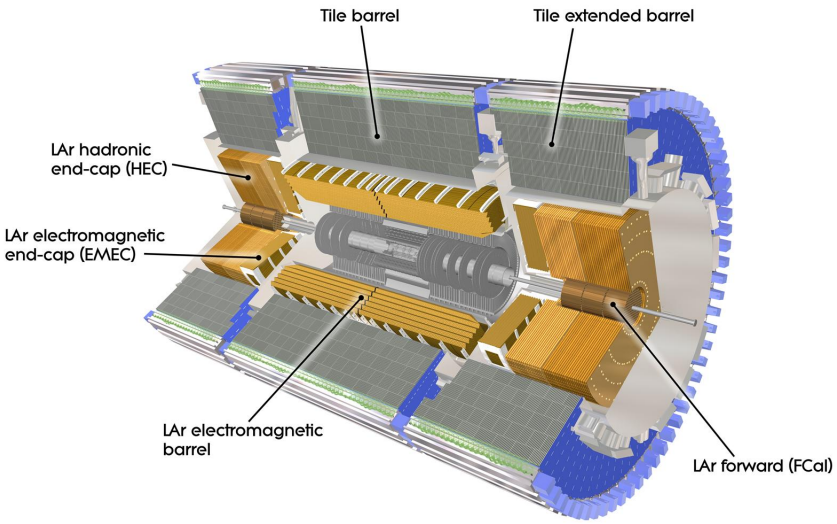

Figure 2.16: Scheme of ATLAS electromagnetic (LAr) and hadronic (TileCal) calorimeter.

The ElectroMagnetic Endcap Calorimeters (EMEC) (Fig. 2.16) are sampling calorimeters that utilize liquid argon as the active medium and lead/stainless-steel absorbers, covering the region $1.5 <|\eta|< 3.2$ on each side of the ATLAS detector. Ionization electrons produced by charged particles traversing the LAr-filled gaps between the absorbers generate a current through the high-voltage (HV) power supplies, which is proportional to the instantaneous luminosity after subtracting the electronics pedestal determined from the collision-free period at the start of each LHC fill. A subset of the EMEC HV lines is used to produce a luminosity measurement, independently from the A- and C-side EMEC detectors.

A similar measurement is available from the Forward Calorimeters (FCal), which cover the region $3.2 <|\eta|< 4.9$ and are longitudinally segmented into three modules. The first module employs copper absorbers optimized for detecting electromagnetic showers, and the HV currents from the 16 azimuthal sectors are combined to produce a luminosity measurement, separate from the A- and C-side calorimeters. Since both

EMEC and FCal luminosity measurements rely on 'slow' ionization currents, they cannot resolve individual bunches, providing instead bunch-integrated measurements that are read out every few seconds and averaged per luminosity block. These calorimeters have insufficient sensitivity at low luminosity for calibration during vdM scans, so they were cross-calibrated to track-counting measurements in high-luminosity physics fills.

The TileCal hadronic calorimeter (Fig. 2.16) employs steel absorber plates interleaved with plastic scintillators as the active medium, which are read out by wavelength-shifting fibers connected to photomultiplier tubes (PMTs). It is divided into a central barrel section covering $| \eta | < 1.0$ and extended barrels on each side of the detector (A and C) covering $0.8 < | \eta | < 1.7$. Both the barrel and extended barrels are segmented azimuthally into 64 sectors and longitudinally into three sections. The current drawn by each PMT (after pedestal correction) is proportional to the total number of particles traversing the corresponding TileCal cell, and thus to the instantaneous luminosity.

In principle, all TileCal cells can be used for luminosity measurement; however, the D-cells, located at the largest radius in the last longitudinal sampling, are least affected by variations in response over time due to radiation damage. The D6 cells, situated at the highest pseudorapidity in the extended barrels on the A- and C-sides, were employed for the primary TileCal luminosity measurements in this analysis, with other D-cells at lower pseudorapidity used for systematic comparisons. Changes in the gains of the PMTs were monitored between physics runs using a laser calibration system that injects pulses directly into the PMTs. The response of the scintillators was also assessed once or twice per year using ^{137}Cs radioactive sources circulating through the calorimeter cells during shutdown periods. The TileCal D-cells exhibit insufficient sensitivity for calibration during vdM scans, necessitating cross-calibration to track-counting measurements, similar to the EMEC and FCal measurements.

The TileCal system additionally includes the E1 to E4 scintillators (Fig. 2.17), which are installed in the gaps between the barrel and endcap calorimeter assemblies, primarily designed to measure energy loss in this region. These E-cells are much more exposed to particles from the interaction point than the rest of the TileCal scintillators (shielded by the electromagnetic calorimeters). Specifically, E3 and E4 (the latter being closest to the beamline) are sensitive enough to allow precise luminosity measurements during vdM fills. They play a crucial role in constraining calibration transfer uncertainties due to the significant differences in the μ range between the calibration runs (vdM scans) and the physics data taking (as discussed in 2.7). However, their response changes rapidly over time due to radiation damage, making them unsuitable for long-term stability studies. Furthermore, the high currents drawn by the E-cell PMTs can lead to slight increases in PMT gains at high luminosity, resulting in an overestimation of the actual luminosity.

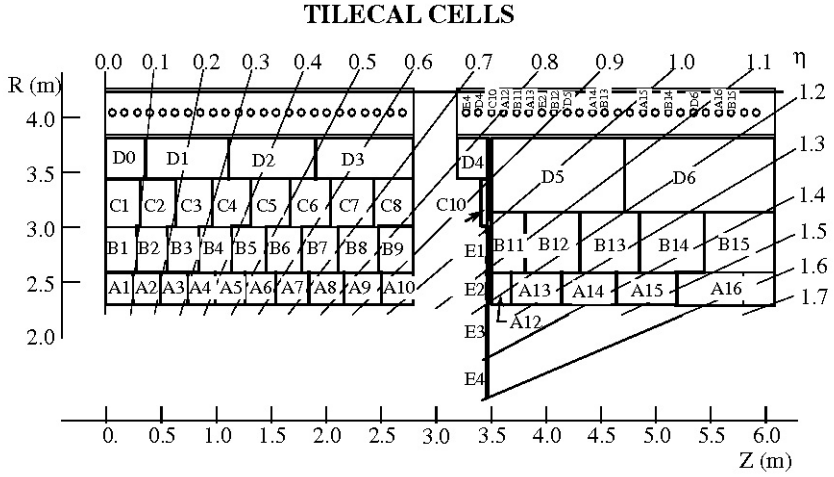

Figure 2.17: Placement of the TileCal cells.

2.6 Van der Meer scans in ATLAS

The absolute luminosity calibration of LUCID and BCM, corresponding to the determination of the visible cross-section σ_{vis} for each of their algorithms, was derived using dedicated van der Meer (vdM) scan sessions during special LHC fills in each data-taking year. Table 2.3 reports the breakdown of vdM systematic uncertainties for Run 2.

A brief description of all systematic effects reported in Table 2.3 is presented below. A complete description of all systematic effects can be found in Ref. [6].

- **Fit model:** The choice of function used to fit data recorded during vdM scans is crucial for an unbiased estimate of σ_{vis}. Therefore, different fit functions are used. The main fit function employed is a Gaussian convoluted with a fourth-order polynomial (GP4) summed with an additional Gaussian (GP4+G) to better fit the central region. A Gaussian function multiplied by a sixth-order polynomial (GP6) was found to give a similar goodness-of-fit to GP4+G, and the difference between the σ_{vis} obtained from these two functions was used to define the uncertainty.

- **Background subtraction:** The primary background for LUCID during vdM scans is dominated by the ^{207}Bi calibration source, which was estimated by subtracting the counting rate measured in the preceding bunch slot. This procedure also accounts for a smaller background due to 'afterglow' from photons produced in the decay of nuclei emitted in hadronic showers. A further minor background arises from the interaction of the protons in each beam with residual gas molecules in the beam pipe, which scales with the bunch population n_1 or n_2. This background was estimated using the counting rate in the bunch slots corresponding

Data Sample	2015	2016	2017	2018	Combined
Integrated Luminosity [fb^{-1}]	3.24	33.40	44.63	58.79	140.07
Total Uncertainty [fb^{-1}]	0.04	0.30	0.50	0.64	1.17
Uncertainty Contributions [%]:					
Statistical Uncertainty	0.07	0.02	0.02	0.03	0.01
Fit Model*	0.14	0.08	0.09	0.17	0.12
Background Subtraction*	0.06	0.11	0.19	0.11	0.13
FBCT Bunch-by-Bunch Fractions*	0.07	0.09	0.07	0.07	0.07
Ghost Charge and Satellite Bunches*	0.04	0.04	0.02	0.09	0.05
DCCT Calibration*	0.20	0.20	0.20	0.20	0.20
Orbit Drift Correction	0.05	0.02	0.02	0.01	0.01
Beam Position Jitter	0.20	0.22	0.20	0.23	0.13
Non-Factorisation Effects*	0.60	0.30	0.10	0.30	0.24
Beam-Beam Effects*	0.27	0.25	0.26	0.26	0.26
Emittance Growth Correction*	0.04	0.02	0.09	0.02	0.04
Length Scale Calibration	0.03	0.06	0.04	0.04	0.03
Inner Detector Length Scale*	0.12	0.12	0.12	0.12	0.12
Magnetic Non-Linearity	0.37	0.07	0.34	0.60	0.27
Bunch-by-Bunch σ_{vis} Consistency	0.44	0.28	0.19	0.00	0.09
Scan-to-Scan Reproducibility	0.09	0.18	0.71	0.30	0.26
Reference Specific Luminosity	0.13	0.29	0.30	0.31	0.18
Total vdM Calibration	0.96	0.70	0.99	0.93	0.65

Table 2.3: Breakdown of vdM calibration uncertainties for each year of the Run 2 *pp* data sample and the full combined sample. * indicates the uncertainties that are correlated between years.

to 'unpaired' bunches, where a bunch from one beam passes through the ATLAS interaction point without meeting a bunch traveling in the opposite direction.

- **Bunch population measurement:** The determination of bunch populations is based on LHC beam instrumentation. The LHC Direct-Current Transformers (DCCT) can measure the total intensity in each beam with a precision better than 0.1%. This measurement is used to normalize the measurements performed by the Fast Beam-Current Transformers (FBCT) and the ATLAS beam-pickup timing system (BPTX), which resolve the current in each of the 3564 nominal bunch slots in each beam. The FBCT bunch population measurements (corrected using the BPTX) were used for the baseline σ_{vis} results, with the alternative BPTX-only results used to define the 'FBCT bunch-by-bunch fractions' uncertainty. The DCCT measurement used to normalize the BPTX and FBCT results summed over all filled bunches is also sensitive to additional contributions to the total circulating beam currents from ghost charge and satellite bunches. Ghost charge refers to circulating protons present in nominally unfilled bunch slots, which are included in the DCCT reading but are typically below the FBCT or BPTX threshold. Their contribution was measured by comparing the rate of beam–gas vertices reconstructed by the LHCb experiment in nominally empty bunch slots with the rate in those bunch slots containing an unpaired bunch. A further uncertainty of 0.2% arises from the absolute calibration of the DCCT current measurements, derived from a precision current source.

- **Orbit-drift correction:** Gradual orbit drifts of up to $O(10\,\mu\text{m})$ in the positions of one or both beams have been observed during a single vdM scan. These drifts change the actual beam separation from the nominal one produced by the LHC steering corrector magnets and were monitored using two independent Beam Position Monitor (BPM) systems. The dominant effect on the vdM analysis arises from in-plane drifts, defined as horizontal (vertical) drifts during a horizontal (vertical) scan. These distort the beam-separation scale in Figure 1.6, changing the values of $\Sigma_{x,y}$ obtained from Eq. (1.69).

- **Beam position jitter:** Short-term movements of the beams during the 30 s duration of a single vdM scan step may lead to fluctuations in the luminosity, distorting the measured scan curve. The potential effect of this beam position jitter was characterized by studying the distribution of the individual arc BPM beam position extrapolations, which were sampled every 5-7 s, i.e., several times per scan step.

- **Non-factorisation effects:** The vdM formalism described in Chapter 1.6.2 assumes that the particle density distributions in each bunch can be factorized into independent horizontal and vertical components, such that the term $1/2\pi\Sigma_x\Sigma_y$

in Eq. (1.68) fully describes the overlap integral of the two beams. Evidence of non-factorisation was clearly seen during Run 1 [13].

- **Beam-beam effects:** The mutual electromagnetic interaction between colliding bunches produces two effects that may bias their overlap integral, depending on the beam separation. First, a transverse deflection induces a non-linear distortion of the intended separation; second, a defocusing of one beam by the other modulates the optical demagnification from the LHC arcs to the interaction point and modifies the shape of the transverse bunch profiles.

- **Emittance growth correction:** The determination of σ_{vis} from Eq. (1.70) implicitly assumes that the convolved beam sizes $\Sigma_{x,y}$ (and therefore the transverse emittances of the two beams) remain constant during a single x or y scan and between the peaks of the two scans. The result may be biased if the beam sizes (and hence also the peak interaction rates) change during or between x and y scans.

- **Length scale calibration:** The $\Sigma_{x,y}$ measurements require knowledge of the length scale, i.e., the actual beam displacements (and hence beam separation) produced by the settings of the LHC steering magnets intended to produce a given nominal displacement. This was determined using length scale calibration (LSC) scans, separately for each beam and plane (x and y). In each scan, the target beam being calibrated was moved successively to five equally spaced positions within $\pm 3\sigma^{b}_{nom}$, and its position measured using the luminous centroid (or beamspot) position fitted from primary collision vertices reconstructed in the ATLAS Inner Detector when the two beams were in head-on collision. The statistical uncertainty from the beamspot position measurements is shown as the 'Length scale calibration' uncertainty in Table 2.3, and is below 0.1%. A further uncertainty ('Inner detector length scale') of 0.12% arises from uncertainties in the absolute length scale of the Inner Detector, determined from simulation studies of various realistic misalignment scenarios.

- **Magnetic non-linearity:** This arises due to non-perfect linearity with respect to the nominal position of the actual beam movement at the level of $1\,\mu$m in $\pm 300\,\mu$m of displacement.

- **Consistency checks:** Since the value of σ_{vis} for a given luminosity algorithm is independent of beam parameters, the ability to determine it separately for each colliding bunch pair and x-y scan set allows for checks on the stability and reproducibility of the calibrations. Within one scan, the spread of σ_{vis} values over all bunch pairs is a measure of potential systematic bunch-to-bunch inconsistencies in the absolute luminosity scale. The largest such value for each year was taken as the 'Bunch-by-bunch σ_{vis} consistency' uncertainty. Differences in bunch-averaged

σ_{vis} (Fig. 2.18) between scans indicate the reproducibility of the calibration on a timescale of hours or longer, especially in 2015 and 2016 where scans were distributed over several LHC fills. The sampling-corrected standard deviation of these values was used to define the 'Scan-to-scan reproducibility' uncertainty. In each year, the vdM calibration procedure was utilized to determine σ_{vis} for all available LUCID and BCM algorithms. Since the acceptances of the algorithms differ, the σ_{vis} values vary; however, all algorithms should agree on the values of $\Sigma_{x,y}$ and hence on the specific luminosity $\mathscr{L}_{spec}$ for each colliding bunch pair, given by

$$\mathscr{L}_{spec} = \frac{f_{\mathrm{r}}}{2\pi\Sigma_x\Sigma_y}.$$

The consistency of the different algorithms was quantified by calculating the per-bunch-pair and per-scan relative deviation of $\mathscr{L}_{spec}$ for each algorithm compared to the average over all algorithms, and then averaging this deviation over all bunch pairs and scans in each year ('Reference specific luminosity').

2.7 Calibration Transfer to High-Luminosity Running

The procedures described above provide the absolute calibration of the LUCID and BCM luminosity measurements for low-μ data-taking, which involves a limited number of isolated bunches. In this regime, the instantaneous luminosities are at least three orders of magnitude smaller than those typical of normal physics running with bunch trains. The LUCID detector experiences significant non-linearity with respect to μ, necessitating a downward correction of $\mathcal{O}(10\%)$ in the physics data-taking regime. This correction was derived using track-counting luminosity measurements and validated with calorimeter measurements, particularly from the TileCal E-cell scintillators.

The natural luminosity decay during a long LHC physics fill - where the luminosity and, consequently, the bunch-averaged pileup $\langle\mu\rangle$ decrease by a factor of two or three - provides a means to study the relative responses of different luminosity measurements as a function of $\langle\mu\rangle$.

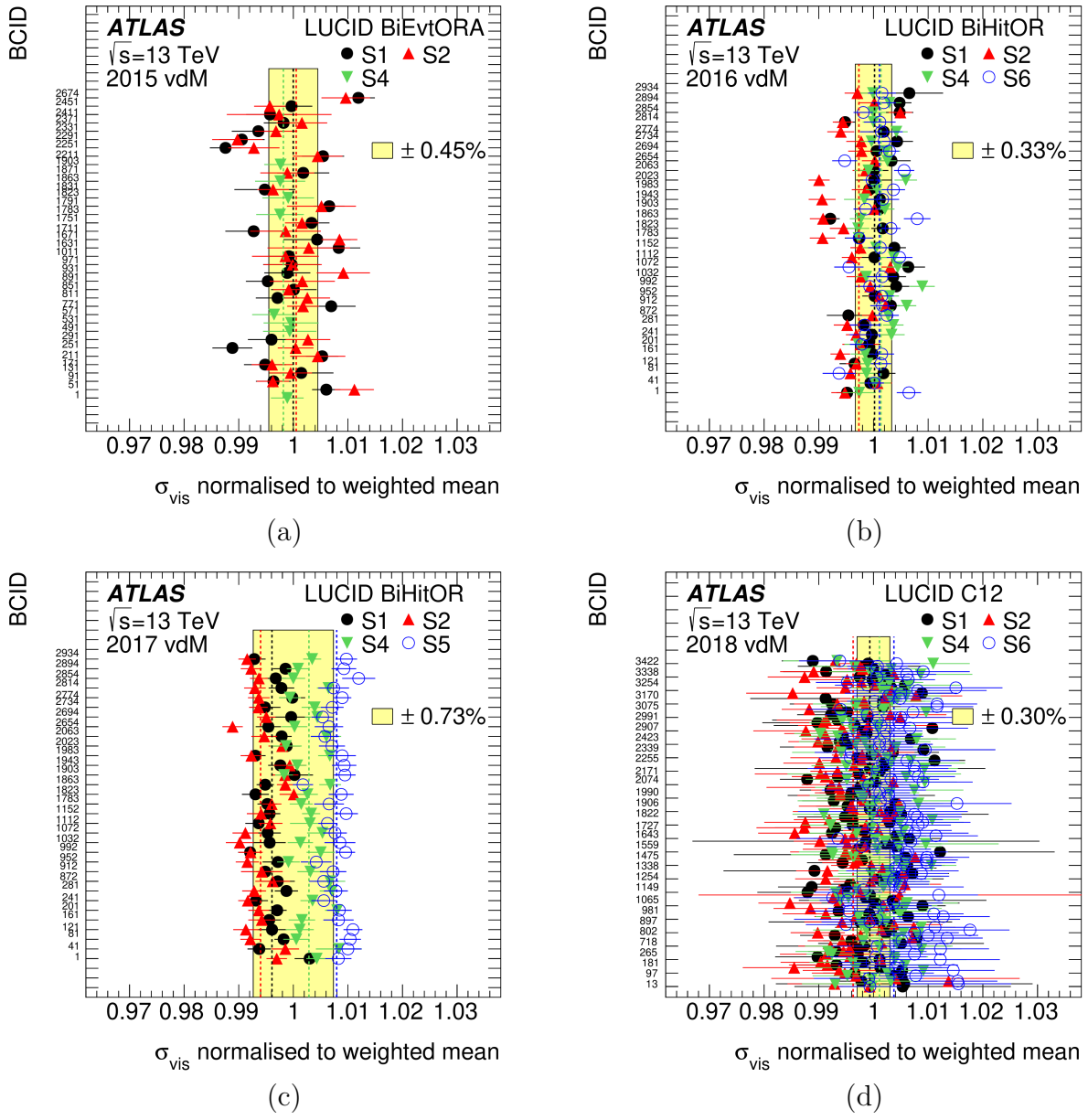

Figure 2.18: Ratio of bunch-by-bunch σ_{vis} to the weighted mean of σ_{vis} for all colliding bunch pairs across all on-axis scans from each year's data-taking, utilizing the reference LUCID algorithm in each case. The different scan periods are highlighted by different markers. The vertical dashed lines indicate the mean σ_{vis} for all bunches in each individual scan set. The uncertainties are statistical and are larger for 2018 due to the use of a single-PMT algorithm, referred to as C12, instead of the HitOr algorithm employed in 2015-2017. The yellow bands represent the combination of bunch-to-bunch and scan-to-scan consistency uncertainties for each year, with the numerical values indicated in the legends.

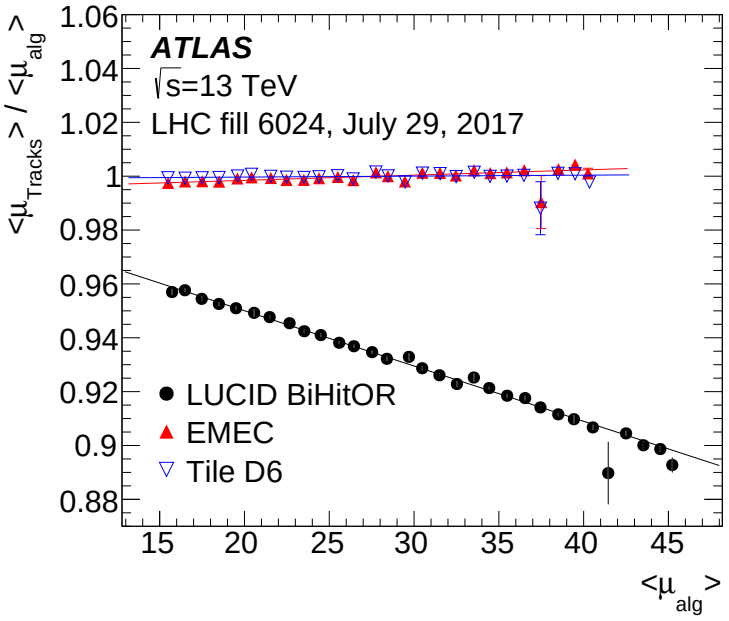

Figure 2.19: Ratios of $\langle\mu\rangle$ (equivalent to ratios of instantaneous luminosity) measured by track-counting to those measured by LUCID (black points), EMEC (red filled triangles), and TileCal D6 (blue open inverted triangles) as a function of the mean number of interactions per bunch crossing $\langle\mu\rangle$, measured by the latter algorithms.

Figure 2.19 shows the ratios of track-counting luminosity to several other measured luminosities during one long physics fill in 2017, plotted as a function of $\langle\mu\rangle$, which decreases steadily as the fill progress. The ratios of track-counting to TileCal D6-cell luminosities change by at most 0.3% as the instantaneous luminosity decreases by a factor of three. The EMEC measurements include a contribution from material activation, which builds up over the first few hours of the fill and eventually contributes about 0.5% of the luminosity signal. This leads to a somewhat larger decrease in the track-counting to EMEC ratio, which is approximately 0.7% over the course of this long fill. In contrast, the track-counting/LUCID ratios are $\mathcal{O}(10\%)$ smaller than unity at the start of physics fills and exhibit a strong dependence on $\langle\mu\rangle$, which is well-described by a linear function, with different slopes for each year of data-taking mainly due to statistical fluctuation.

The relative dependence of the LUCID and track-counting luminosity measurements was further studied by performing μ-scans, where the luminosity was varied between zero and the maximum achievable by partially separating the beams in the transverse plane at the ATLAS interaction point. Since both LUCID and track-counting measure μ for individual bunches, this setup allows investigation of performance as a function of the LHC bunch pattern and the position of individual bunches within a bunch train.

Exploiting the excellent stability of the track-counting luminosity measurement, the

non-linearity in LUCID was corrected as a function of $\langle\mu\rangle$ using one or more long high-luminosity reference fills in each year of data-taking. Each reference fill was utilized to derive a correction of the form

$$\langle\mu_{corr}\rangle = p_0\langle\mu_{uncorr}\rangle + p_1(\langle\mu_{uncorr}\rangle)^2 \ , \tag{2.3}$$

where $\langle\mu_{uncorr}\rangle$ is the uncorrected and $\langle\mu_{corr}\rangle$ is the corrected LUCID $\langle\mu\rangle$ value. The parameters p_0 and p_1 were obtained from a linear fit to the ratio of $\langle\mu\rangle$ values measured by track-counting and LUCID,

$$R = \langle\mu_{\text{Tracks}}\rangle/\langle\mu_{\text{LUCID}}\rangle,$$

as a function of $\langle\mu_{uncorr}\rangle$, as shown in Figure 2.19. The track-counting luminosity was first normalized to the absolute luminosity measured by LUCID in parts of the vdM fill with stable head-on collisions at ATLAS, ensuring that $R = 1$ at low pileup ($\mu \approx 0.5$) with isolated bunches. This correction also incorporates the $\mathcal{O}(1\%)$ change in the LUCID calibration caused by the non-zero LHC beam crossing angle used in physics runs, along with the $\mathcal{O}(0.2\%)$ afterglow contribution to the LUCID luminosity signal during bunch train running.

In principle, Eq. 2.3 could also be expressed in terms of the bunch-by-bunch μ, correcting the LUCID measurement as a function of the instantaneous luminosity in each individual bunch and potentially compensating for bunch-to-bunch variations. However, since ATLAS physics analyses utilize data from all LHC bunches, an average correction based on $\langle\mu_{uncorr}\rangle$ suffices, and a more complex bunch-position-dependent correction scheme was not employed.

The correction of Eq. 2.3 ensures that the LUCID luminosity aligns well with track-counting throughout the reference fill. If the LUCID response exhibits no time dependence, a single reference fill and correction would suffice for an entire year of data-taking. The regular PMT high-voltage adjustment, based on the LUCID ^{207}Bi calibration signals, helps maintain this approximation. However, comparisons with track-counting reveal some residual variations, particularly during the first few weeks of data-taking each year, when the number of colliding bunches and instantaneous luminosity increase during the LHC intensity ramp-up phase. This specific aspect will be discussed in Chapter 2.12 using 2023 and 2024 data.

2.8 Long-Term Stability

The LUCID correction strategy provides a calibrated LUCID luminosity measurement for every luminosity block in each physics run. However, drifts in the response of LUCID over time that are not fully corrected by the ^{207}Bi calibration system, or drifts in the track-counting measurement used to determine corrections to LUCID during reference

runs, could still introduce a time-dependent bias in the baseline luminosity measurement. To investigate these potential biases, we compared the run-integrated luminosity measurements from LUCID with independent measurements from the EMEC, FCal, and TileCal D6-cell calorimeter algorithms for every physics run. Since the calorimeter measurements cannot be calibrated at low luminosity during the vdM runs, they were normalized, or "anchored," to agree with the run-integrated track-counting measurements from up to ten physics runs near the vdM fill. Discrepancies between LUCID and calorimeter measurements in physics runs far from the vdM fill are indicative of long-term drifts in either of the two measurements.

A comparison of FCal luminosity with track-counting, EMEC, and TileCal D6 cells revealed a non-linearity in FCal that strongly depends on instantaneous luminosity. The FCal data were corrected as a function of instantaneous luminosity to ensure agreement with track-counting in a single reference fill.

After applying the correction to the FCal luminosity, the anchoring procedure involved setting the unweighted mean of the ratio $\mathscr{L}_{algo}/\mathscr{L}_{tracks}$ to unity across ten physics runs with a high number of colliding bunches close to the vdM fill. Figure 2.20 illustrates the run-to-run spread between luminosity measurements and their relative trends as a function of time. The root mean square (RMS) of this distribution is then used to define the long-term stability uncertainty.

2.9 Luminosity Results in Run-2

Since most physics analyses utilize the full Run-2 datasets, the final uncertainty must account for possible correlations between each year in Run-2. Table 2.4 presents the breakdown of each uncertainty for the Run-2 dataset.

The largest single uncertainty in the total luminosity is 0.5% due to calibration transfer. The total uncertainty from the absolute vdM calibration is 0.65%, with the largest contributions arising from non-factorisation corrections, beam-beam effects, magnetic non-linearity, and scan-to-scan reproducibility, all contributing at a comparable level.

2.10 Z Counting

Continuous monitoring of high-rate physics processes, such as the production of Z bosons, offers a valuable method for measuring luminosity. The leptonic decays $Z \to ee$ and $Z \to \mu\mu$ are particularly attractive due to their distinctive signatures, which are easy to trigger and reconstruct, along with having less than 1% background contamination (see Chapter 5.6). Moreover, the two lepton channels provide opportunities for internal consistency checks. With a rate of approximately 10 Hz of reconstructed events per lepton flavor at $\sqrt{s} = 13$ TeV and $\mathscr{L}_{inst} = 10^{34}\,\mathrm{cm}^{-2}\mathrm{s}^{-1}$, statistical precision well below 1% can

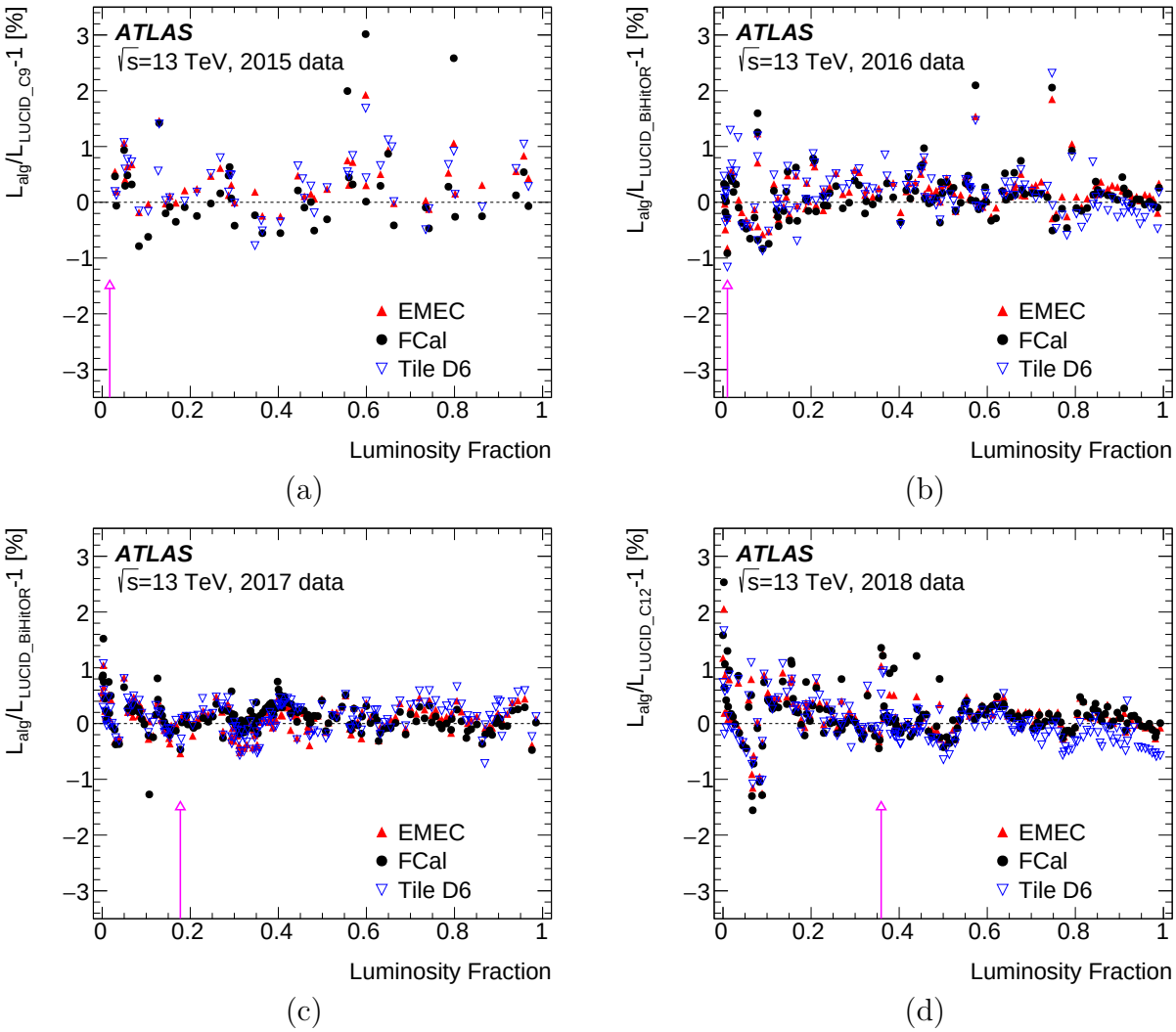

Figure 2.20: Fractional differences in run-integrated luminosity between EMEC, FCal, and TileCal D6 luminosity measurements and the baseline LUCID luminosity measurement, plotted as functions of the fractional cumulative integrated luminosity in each data-taking year. The positions of the vdM fills are indicated by the purple arrows.

Data Sample	2015	2016	2017	2018	Combined
Integrated Luminosity [fb^{-1}]	3.24	33.40	44.63	58.79	140.07
Total Uncertainty [fb^{-1}]	0.04	0.30	0.50	0.64	1.17
Uncertainty Contributions [%]:					
Statistical Uncertainty	0.07	0.02	0.02	0.03	0.01
Fit Model*	0.14	0.08	0.09	0.17	0.12
Background Subtraction*	0.06	0.11	0.19	0.11	0.13
FBCT Bunch-by-Bunch Fractions*	0.07	0.09	0.07	0.07	0.07
Ghost-Charge and Satellite Bunches*	0.04	0.04	0.02	0.09	0.05
DCCT Calibration*	0.20	0.20	0.20	0.20	0.20
Orbit-Drift Correction	0.05	0.02	0.02	0.01	0.01
Beam Position Jitter	0.20	0.22	0.20	0.23	0.13
Non-Factorisation Effects*	0.60	0.30	0.10	0.30	0.24
Beam-Beam Effects*	0.27	0.25	0.26	0.26	0.26
Emittance Growth Correction*	0.04	0.02	0.09	0.02	0.04
Length Scale Calibration	0.03	0.06	0.04	0.04	0.03
Inner Detector Length Scale*	0.12	0.12	0.12	0.12	0.12
Magnetic Non-Linearity	0.37	0.07	0.34	0.60	0.27
Bunch-by-Bunch σ_{vis} Consistency	0.44	0.28	0.19	0.00	0.09
Scan-to-Scan Reproducibility	0.09	0.18	0.71	0.30	0.26
Reference Specific Luminosity	0.13	0.29	0.30	0.31	0.18
Subtotal vdM Calibration	0.96	0.70	0.99	0.93	0.65
Calibration Transfer*	0.50	0.50	0.50	0.50	0.50
Calibration Anchoring	0.22	0.18	0.14	0.26	0.13
Long-Term Stability	0.23	0.12	0.16	0.12	0.08
Total Uncertainty [%]	1.13	0.89	1.13	1.10	0.83

Table 2.4: Summary of the integrated luminosities (after standard data-quality requirements) and uncertainties for the calibration of each individual year of the Run-2 *pp* data sample at $\sqrt{s} = 13$ TeV, as well as the full combined sample. The table provides the integrated luminosities, total uncertainties, and a breakdown of contributions to the absolute vdM calibration, including additional uncertainties for the physics data sample and the total relative uncertainty in percent. Contributions marked * are considered fully correlated between years, while the other uncertainties are considered uncorrelated.

be achieved during runs lasting several hours. However, since the Z production cross-section is only predicted with a precision of 3-4% due to uncertainties in proton parton distribution functions, this method is most effective as a relative luminosity measurement, normalized to an absolutely calibrated reference. Consequently, it can be utilized to study stability over time or in relation to other parameters, such as pileup $\langle\mu\rangle$.

To select events, the following criteria are applied:

- Only 2 opposite-sign leptons with p_t (the component of momentum transverse to the beam line) $> 27\,\text{GeV}$.
- $66\,\text{GeV} < m_{ll} < 116\,\text{GeV}$.
- $|\,\eta\,| < 2.4$.
- At least one lepton must match the corresponding trigger signature.

The resulting samples are approximately 99.5% pure in $Z \to \ell\ell$ events, with the small background estimated using simulations and subsequently subtracted. Trigger and reconstruction efficiencies were evaluated for each luminosity block from data, resulting in corrections of 1-2% for $Z \to \mu\mu$ and up to about 10% for $Z \to ee$. The measurements yield a statistical precision of 2-5% per 20-minute period and demonstrate excellent consistency between the electron and muon channels, both as a function of time and $\langle\mu\rangle$.

Figure 2.21 shows a comparison of the combined Z-counting measurements (from $Z \to ee$ and $Z \to \mu\mu$) with baseline luminosity measurements over the entire Run 2 data-taking period. The Z-counting measurement has been normalized to the baseline integrated luminosity of the full sample. This comparison is sensitive to differences in the baseline luminosity calibration between years and tests the consistency of the absolute vdM calibrations performed in each year. Year-averaged systematic differences of -0.5%, 0.2%, 0.4%, and -0.4% for 2015, 2016, 2017, and 2018, respectively, are observed between the Z-counting and baseline luminosity measurements.

2.11 Preliminary Results in 2022

As Run-3 data taking is still ongoing, this section discusses preliminary results based on the 2022 data.

Table 2.5 presents the systematic uncertainties for the 2022 luminosity measurement. As observed in the Run-2 dataset, the primary uncertainties arise from the vdM calibration and calibration transfer. The vdM uncertainty is predominantly influenced by horizontal-vertical correlations, known as non-factorisation, in the bunch density distributions during the vdM scan. Various effects related to beam characteristics, calibration methods, consistency, reproducibility, and stability contribute smaller amounts to the overall uncertainty.

Data Sample	2022
Uncertainty Contributions [%]:	
Statistical Uncertainty	0.01
Fit Model	0.24
Background Subtraction	0.06
FBCT Bunch-by-Bunch Fractions	0.01
Ghost-Charge and Satellite Bunches	0.17
DCCT Calibration	0.20
Orbit-Drift Correction	0.06
Beam Position Jitter	<0.01
Non-Factorisation Effects	1.07
Beam–Beam Effects	0.25
Emittance Growth Correction	0.21
Length Scale Calibration	0.03
Inner Detector Length Scale	0.24
Magnetic Non-Linearity	0.32
Bunch-by-Bunch σ_{vis} Consistency	0.50
Scan-to-Scan Reproducibility	0.27
Reference-Specific Luminosity	0.43
Subtotal vdM Calibration	1.45
Calibration Transfer	1.50
Calibration Anchoring	0.53
Long-Term Stability	0.41
Total Uncertainty [%]	2.19

Table 2.5: Systematic uncertainties associated with the preliminary luminosity calibration of the 2022 *pp* data sample at $\sqrt{s} = 13.6\,\text{TeV}$. The fractional systematic uncertainty is broken down into four main contributions: absolute vdM calibration (detailed per uncertainty source and subtotal), calibration transfer from the vdM to the physics regime, calibration anchoring of the calorimeters for physics runs, and long-term stability of the luminometer response.

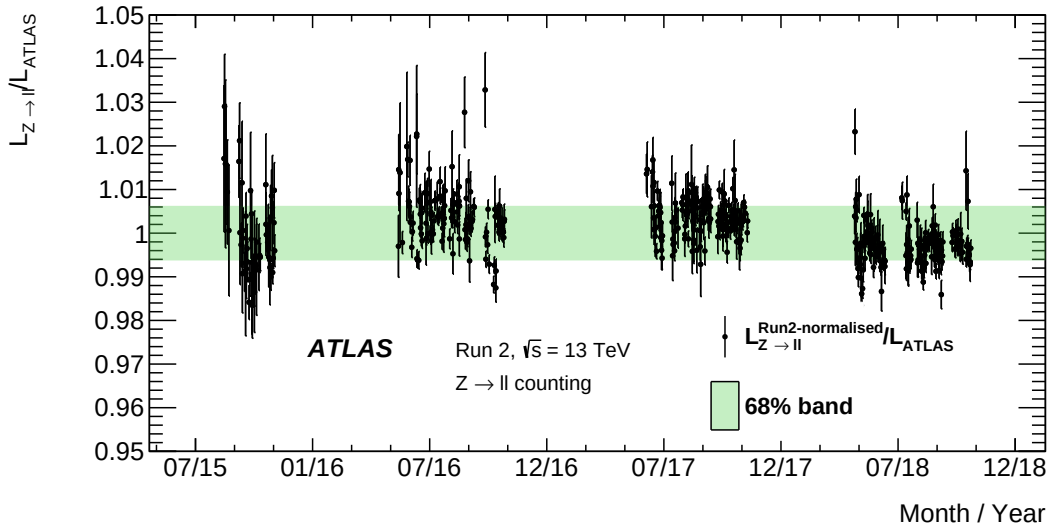

Figure 2.21: Ratios of the run-integrated Z-counting (combining $Z \to ee$ and $Z \to \mu\mu$) and baseline ATLAS luminosity measurements as a function of run date. The Z-counting measurements are normalized to the baseline luminosity measurement integrated over the entire Run 2 data-taking period. The error bars indicate statistical uncertainties, and the green bands encompass 68% of all runs centered around the mean.

2.12 LUCID-2 in 2023 and 2024

In preparation for the High-Luminosity Large Hadron Collider (HL-LHC) upgrade, portions of the LUCID-2 system, including fibers and BiM, have been changed or decommissioned (see Chapter 3.4). During Run-3, LUCID-2 consisted of 8 Bi PMTs, 8 Bi2 PMTs, and 8 spare PMTs. In 2023, one of the Bi-MOD PMTs was replaced with a Hamamatsu R1635 PMT (the model planned for the upgrade), and by 2024, all PMTs had been replaced with R1635s. This chapter focuses on the performance of the Bi and Bi2 PMTs, which will serve as references for evaluating the performance of the LUCID prototypes.

The first aspect to characterize is the μ dependence. For the 2023 datasets, ten runs were selected close to the van der Meer (vdM) scan, all consisting of 2340 colliding bunches arranged in trains of 36 bunches. For the 2024 dataset, a single run was chosen, also close to the vdM scan, featuring 2340 colliding bunches and 65 trains of 36 bunches. As the analysis of the 2024 vdM is still ongoing, the σ_{vis} calculated from the 2023 vdM was applied to the 2024 dataset. The year-to-year difference in σ_{vis} is approximately 2-3%. Figure 2.22 presents the LUCID μ dependence fit for HitOrBi and HitOrBi2. The intercept reflects the absolute calibration of the algorithm, while the slope quantifies the degree of non-linearity. In 2023, both algorithms exhibit an intercept compatible with 1

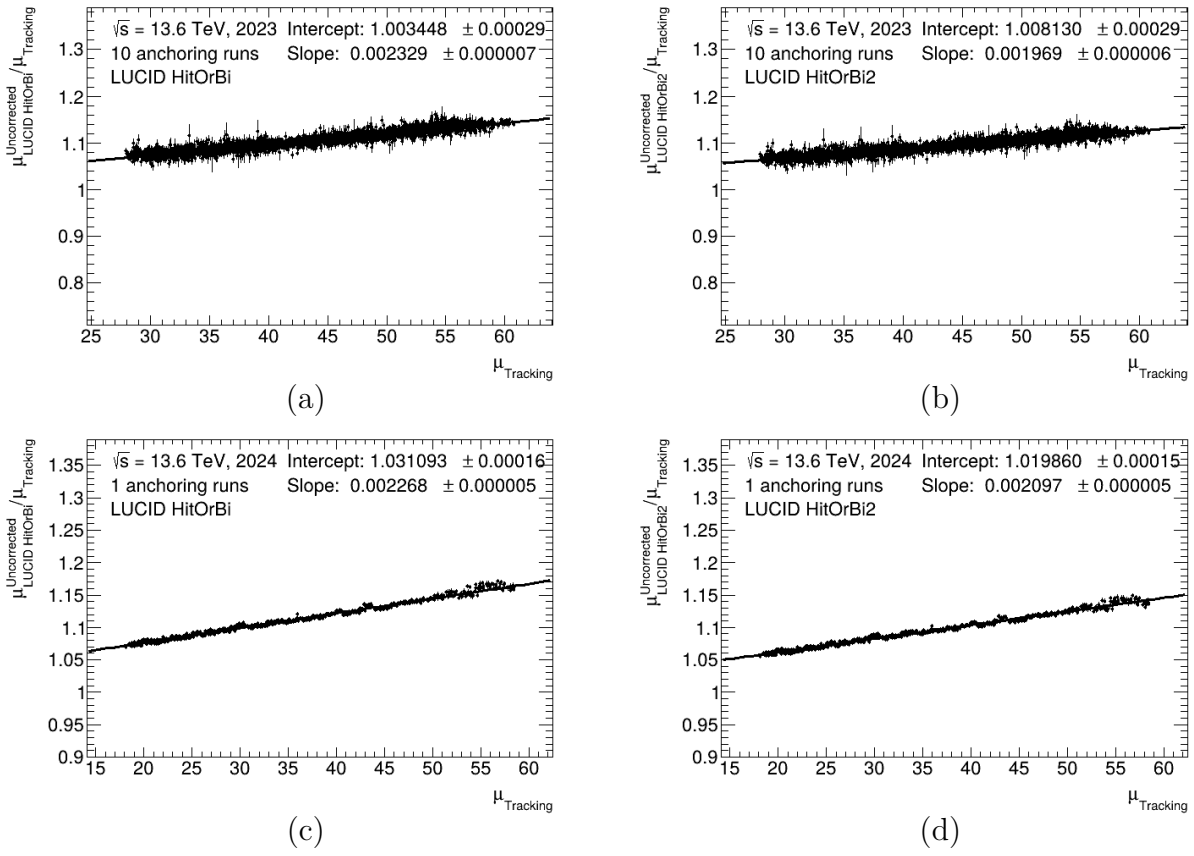

Figure 2.22: μ-dependence fit for HitOrBi (left) and HitOrBi2 (right) using data from 2023 (top) and 2024 (bottom).

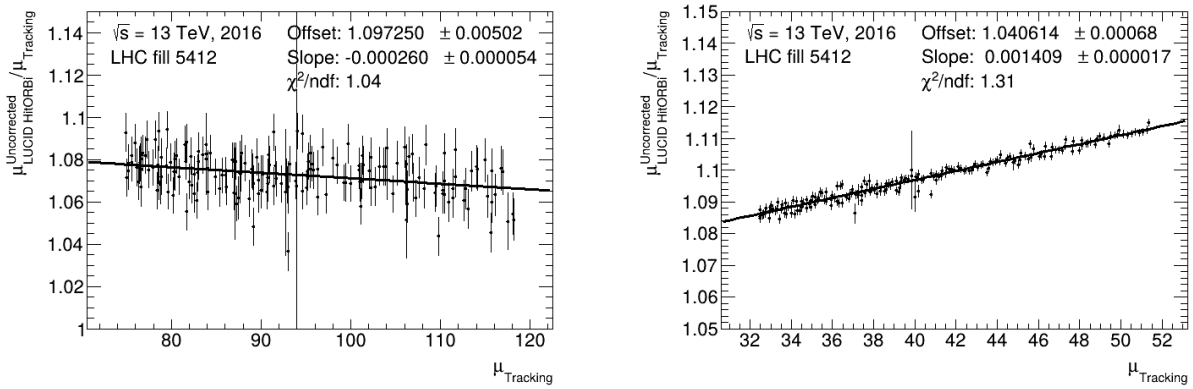

(a) (b)

Figure 2.23: μ-dependence fit performed on isolated bunches at very high μ (left) compared to the fit performed on trains (right) within the same fill.

and a similar slope. However, in 2024, the intercept deviates from 1 due to the use of the 2023 σ_{vis} instead of one obtained from the 2024 vdM scan, although the slopes remain similar.

Analyzing only the global μ dependence does not provide sufficient insight into the source of the observed effects, as it does not reveal how the intercept and slope vary within the trains. In 2016, a special run was conducted where isolated bunches had a very high μ (approximately 140) and trains were at nominal μ (approximately 40-60). It was observed that LUCID demonstrated perfect linearity with respect to tracks for isolated bunches, but exhibited non-linearity within trains, as shown in Fig. 2.23. To investigate whether LUCID's perfect linearity at high μ was due to isolated bunches, and to explore any differences in linearity as the LHC filling scheme changes, fills were selected based on the following criteria:

- Fills must have a sufficiently long luminosity decay period after luminosity leveling to ensure a wide range of μ values.
- High track rate acquisition is necessary to ensure a good track statistic for track counting.

The 2023 fills that meet both requirements are listed in Table 2.6. Fill 9029 is a special run, referred to as the calibration transfer run (CT run), used to study the calibration transfer from the vdM regime to the physics regime.

The fills from 2024 used in this analysis are listed in Table 2.7.

For each BCID inside a train, the mean luminosity (and hence the pileup μ) is measured using both LUCID (HitOrBi and HitOrBi2) and track counting in each luminosity block (LB). If a fill contains trains of different lengths, only the longest trains are consid-

Fill	# Colliding Bunches	Train Structure
8644	62	5 trains (12) + 2 isolated
8645	62	5 trains (12) + 2 isolated
8675	398	11 trains (36) + 2 isolated
8686	386	21 trains (8) + 6 trains (36) + 2 isolated
9029	2345	77 trains (8) + 48 trains (36) + 1 isolated

Table 2.6: List of 2023 LHC fills used to study the μ dependence inside the train.

Fill	# Colliding Bunches	Train Structure
9512	818	17 trains (48) + 2 isolated
9514	818	17 trains (48) + 2 isolated
9523	1199	3 trains (47) + 22 trains (48) + 2 isolated
9537	1772	6 trains (47) + 31 trains (48) + 2 isolated
9539	1778	37 trains (48) + 2 isolated
9543	1970	41 trains (48) + 2 isolated
9568	2198	61 trains (36) + 2 isolated
9573	2340	65 trains (36)
9603	2340	65 trains (36)
9687	2340	65 trains (36)
9691	2340	65 trains (36)

Table 2.7: List of 2024 LHC fills used to study the μ dependence inside the train.

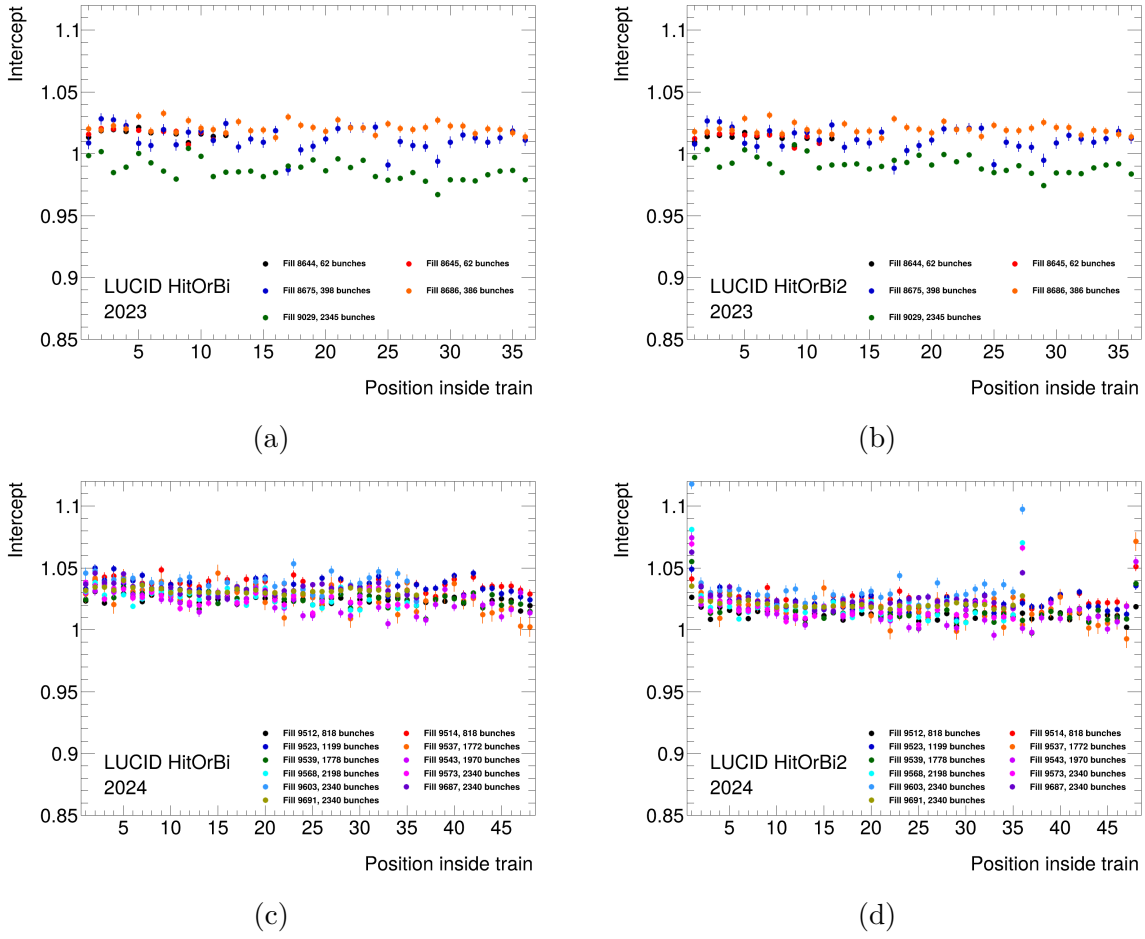

Figure 2.24: Intercept of the μ-dependence as a function of position inside the train for HitOrBi (on the left) and HitOrBi2 (on the right) using the 2023 (top) and 2024 (bottom) datasets.

ered for the mean calculation. The ratio μ_{LUCID}/μ_{Tracks} is plotted against μ_{Tracks} and fitted with a first-degree polynomial.

The intercepts (Fig. 2.24) and slopes (Fig. 2.25) are plotted as functions of the position inside the train. The intercepts are compatible with 1 for every position inside the train for both algorithms in 2023, but in 2024, deviations from 1 are observed. This could be due to the fact that the σ_{vis} values used in 2024 are the same as the 2023 values since the 2024 vdM analysis is still ongoing. A shift of a couple of percent in the intercept would be expected. In some 2024 fills, the HitOrBi2 intercept is not compatible with neighboring positions inside the train or with other runs' intercepts in the same position. This behavior is not observed in HitOrBi, and the cause is not yet clear.

The slope increases in the first 4-5 BCIDs inside the train and then stabilizes around

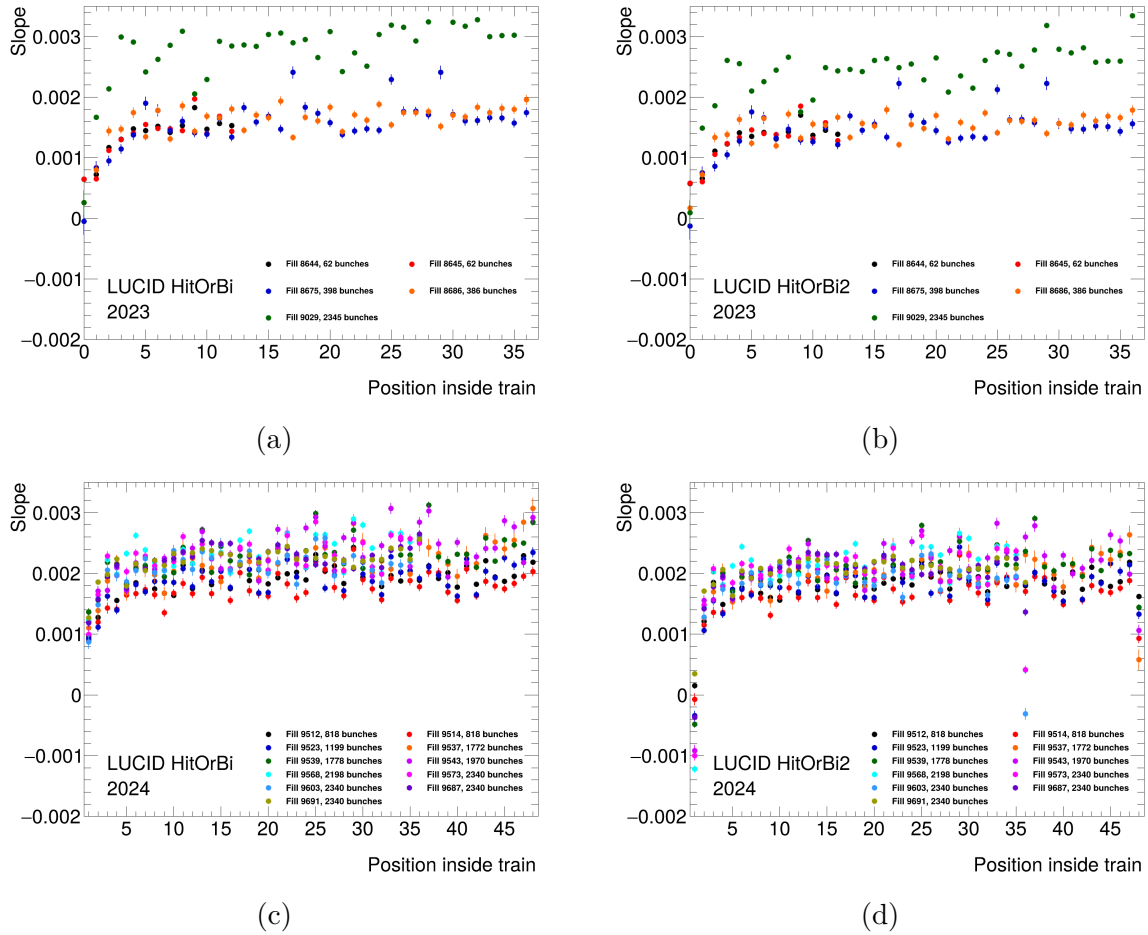

Figure 2.25: Slope of the μ-dependence as a function of position inside the train for HitOrBi (on the left) and HitOrBi2 (on the right) using the 2023 (top) and 2024 (bottom) datasets.

a certain value, approximately 0.0029 for fill 9029, while for all other fills, it is approximately 0.0018. This last value is also compatible with those observed in 2024 and obtained by the global μ-dependence fit. It seems that the 2023 CT run overestimates the real μ-dependence of LUCID, although the cause is not yet clear. As noted in the intercepts, some slopes for HitOrBi2 in 2024 are not compatible with others. The increase in the slope is likely caused by the activation of the material generated by the collision, which builds up for 4-5 BCIDs (100-125 ns) and then stabilizes.

Even after reaching a plateau, fluctuations in the slope can be observed (i.e., 9^{th} and 10^{th} BCID in fill 9029, 9^{th} BCID in fill 8645, and 17^{th}, 25^{th}, 29^{th} BCID in fill 8675). These BCIDs are also characterized by a higher μ compared to the other BCIDs in the same fill. To evaluate the possible correlation between the slope and μ, I calculated the mean μ for each BCID and plotted the slope as a function of the mean μ. To better isolate this possible correlation, I excluded the first 4 BCIDs, as there are other effects in these BCIDs that can spoil possible correlations. As shown in Fig. 2.26, there is a clear correlation between the slope and the mean μ; in particular, the slope tends to be lower when μ is higher. This observation is compatible with findings from the 2016 special run, which showed no μ dependence at very high μ. There are two possible explanations:

- Hit migration can be less significant when μ is higher because the number of bunch crossings with no hits, resulting in a fake hit generated by migration, is lower.
- Track counting may begin to exhibit non-linear behavior, thereby reducing the non-linearity of LUCID with respect to tracks.

Since the track acquisition rate for luminosity measurement is limited, the statistical error on track luminosity can be significant. This problem is mitigated when considering the mean over several bunches but cannot be alleviated when considering isolated bunches since there are at most two in almost every run. For example, fills 8675, 8686, 9029, and all 2024 fills have a poor rate of tracks for isolated bunches, as shown in Fig. 2.27, where the fit performed on isolated bunches in fill 8645 is reported on the left and in fill 8686 on the right. Only fills 8644 and 8645 will be considered when discussing the isolated bunches (see Fig. 2.28). The slope of the isolated bunches is almost the same as the slope measured in the 1^{st} BCID inside the train, but it is not 0. This observation is compatible with the activation hypothesis since, before an isolated bunch or the 1^{st} BCID of a train, there are no colliding BCIDs causing activation. Moreover, the fact that the slope is not 0 in isolated bunches means that the perfect linearity observed at very high μ in the 2016 special run was not only due to the isolated bunches.

Another crucial aspect to be characterized is the long-term stability, which has been evaluated with both the 2023 and 2024 datasets. For both datasets, short runs (less than 100 lumiblocks during physics data taking) are discarded. For 2023, only lumiblocks in which all detectors are in good condition are counted. For 2024, only the lumiblocks where the difference between EMEC and LUCID HitOrBi2 is less than 20% are retained.

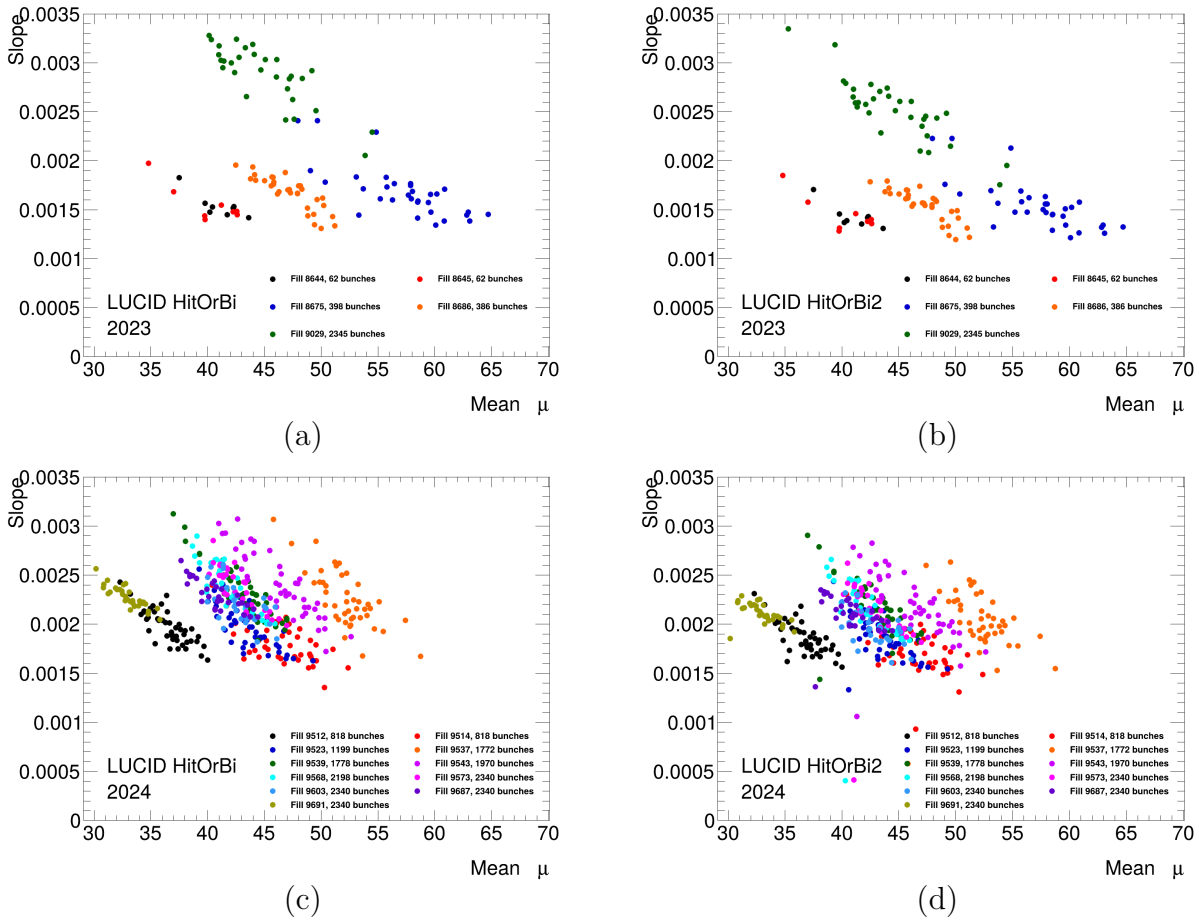

Figure 2.26: Slope of the μ-dependence extracted by the fits as a function of mean μ for HitOrBi (on the left) and HitOrBi2 (on the right) using the 2023 (on the top) and 2024 (on the bottom) datasets.

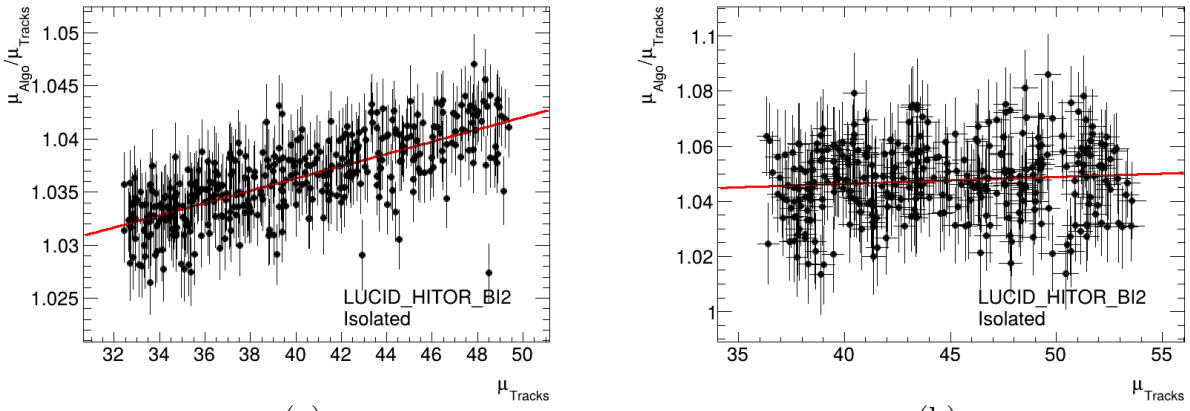

(a) (b)

Figure 2.27: μ dependence fit performed only on isolated bunches in fill 8645 on the left and in fill 8686 on the right.

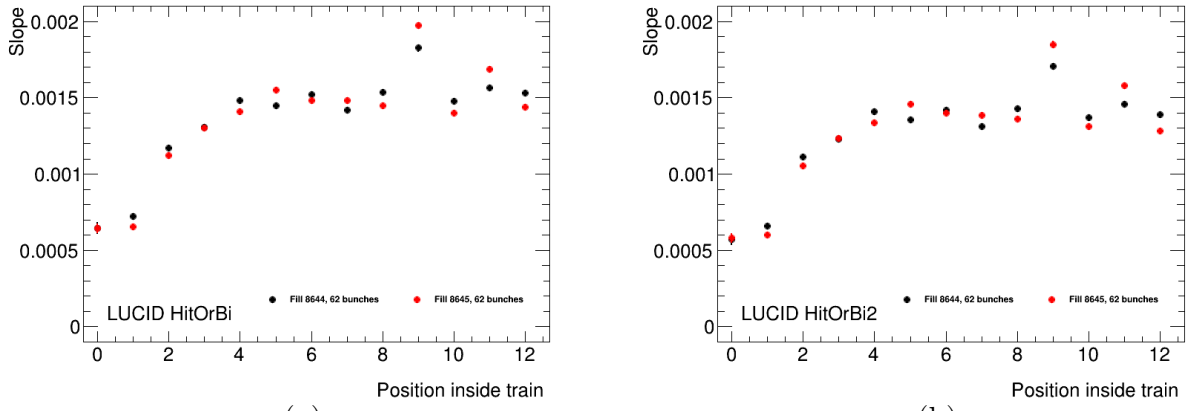

(a) (b)

Figure 2.28: Slope of the μ-dependence as a function of position inside the train and for isolated bunches for HitOrBi (on the left) and HitOrBi2 (on the right).

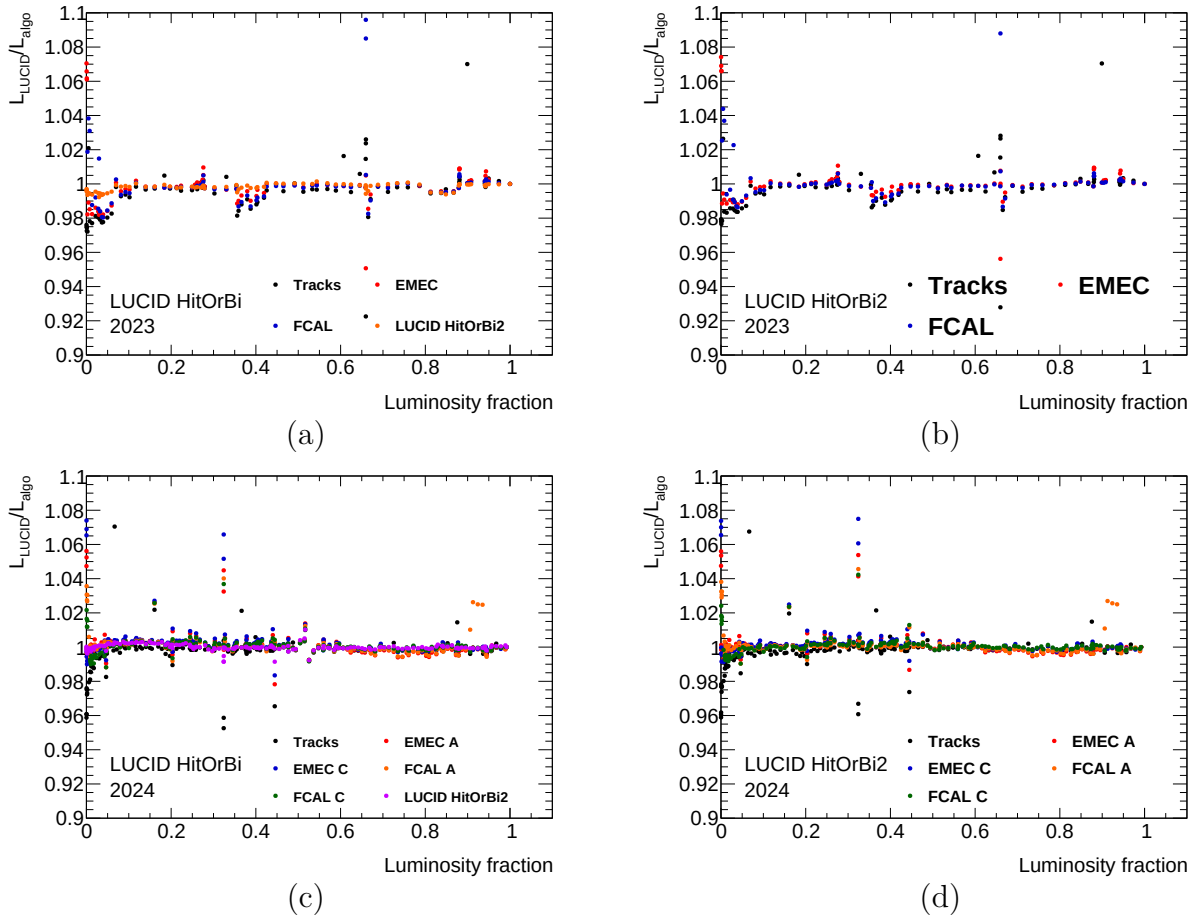

Figure 2.29: Long-term stability for HitOrBi (on the left) and HitOrBi2 (on the right) in 2023 (on the top) and in 2024 (on the bottom).

Additionally, for the 2023 dataset, offline corrections to EMEC and FCAL are available, so the combination of luminosity measurement from A and C side is performed. TileCal is not included in this study since it requires offline corrections that are not yet available for the 2023 and 2024 datasets. In Fig. 2.29, the run-by-run ratio of the luminosity measured by LUCID HitOrBi and HitOrBi2 with tracks, EMEC, and FCAL is reported with respect to each other as a function of the luminosity fraction. As expected, for both datasets and both algorithms, there is an instability at the beginning of data taking. This is due to the ramp-up of the number of colliding bunches that induce instability in the luminosity measured with calorimeters. For LUCID HitOrBi in 2024, a step occurred around 0.5 luminosity fraction caused by a faulty PMT that was replaced with a spare, and it took a couple of runs to stabilize. There are no other signs of instabilities in either algorithm.

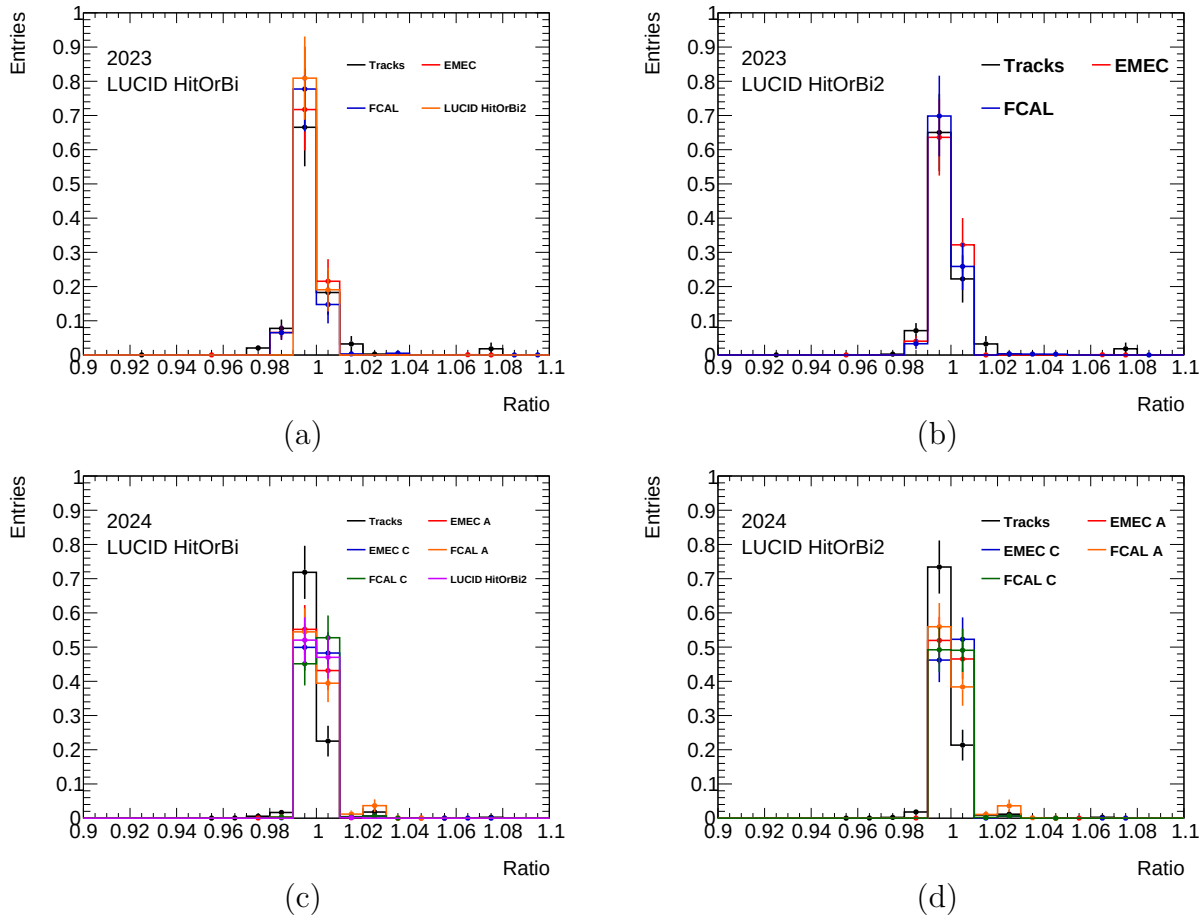

Figure 2.30: Distribution of the ratio of luminosity measured with HitOrBi (on the left) and HitOrBi2 (on the right) over luminosity measured with other algorithms using 2023 (on the top) and 2024 (on the bottom) datasets.

To properly evaluate the stability, the RMS of the distribution must be assessed. The distribution of the ratio for each LUCID algorithm and for each reference algorithm is calculated by weighing each run by its own luminosity. These distributions are reported in Fig. 2.30. The RMS values are reported in Tab. 2.8 and Tab. 2.9 for the 2023 and 2024 datasets, respectively. The RMS when comparing with tracks in 2023 is significantly worse compared to that obtained with tracks in 2024. This is due to problems with track counting already encountered when studying the μ-dependence inside the train. There is no substantial difference between 2023 and 2024 in the comparison with the other detectors. These results are similar to those obtained in 2022 (see Tab. 2.5) and are compatible with the Run-2 results.

The final aspect to fully characterize the performance of LUCID-2 (and LUCID-3

	HitOrBi	HitOrBi2
Tracks	0.012	0.011
EMEC	0.0046	0.0037
FCAL	0.0051	0.0045
HitOrBi2	0.0018	-

Table 2.8: RMS of the distributions of the ratio of HitOrBi and HitOrBi2 over other luminosity algorithms using the 2023 dataset.

	HitOrBi	HitOrBi2
Tracks	0.0059	0.0056
EMEC A	0.0037	0.0030
EMEC C	0.0037	0.0031
FCAL A	0.0056	0.0054
FCAL C	0.0032	0.0054
HitOrBi2	0.0016	-

Table 2.9: RMS of the distributions of the ratio of HitOrBi and HitOrBi2 over other luminosity algorithms using the 2024 dataset.

prototypes) is the calibration transfer. To properly evaluate it, reliable data from other detectors (ID, LAr, and Tile) are necessary. For both 2023 and 2024 datasets, TileCal data are not yet available, and offline corrections for LAr are still in a preliminary phase, so the calibration transfer will not be discussed in this thesis.

Chapter 3

LUCID at High Luminosity LHC

3.1 Introduction

To achieve its target integrated luminosity during its physics programme, HL-LHC will have to run at conditions way beyond the design of LUCID-2. The luminosity measurement thus requires a new detector design: LUCID 3. After analyzing all the reasons why LUCID-2 won't be compatible with the ATLAS physics program for HL-LHC, the possible designs for LUCID-3 will be analyzed and, at the end, a description of the prototypes of LUCID-3 that are currently under testing will be presented.

3.2 HL-LHC Running Conditions

	Baseline	Ultimate
Number of colliding bunches in ATLAS	2748	2748
Peak luminosity [$cm^{-2}s^{-1}$]	5×10^{34}	7.5×10^{34}
Peak pile-up [collisions/event]	131	197
Luminosity leveling time [hours]	7.4	3.6
End-of-fill luminosity [$cm^{-2}s^{-1}$]	3×10^{34}	4.5×10^{34}
Peak pile-up line-density [events/mm]	1.3	1.95
Average pile-up line-density [events/mm]	0.8	1.2
RMS time spread of the luminous region [ps]	178	178
Integrated luminosity [fb^{-1}/year]	262	326

Table 3.1: Two scenarios for the beam conditions expected for Run-4 and beyond.

The expected LHC conditions in Run-4 are summarized in Table 3.1 and include a 'baseline' and 'ultimate' scenario, with a peak luminosity of $5 \times 10^{34} cm^{-2} s^{-1}$ (peak

μ of about 130) and $7.5 \times 10^{34} cm^{-2} s^{-1}$ (peak μ of about 200), respectively. In both cases, LHC will operate in luminosity-leveling (see Chapter 2.4) mode in order to ensure a safe operation of the detectors and ensure an efficient use of the beam allowing the achievement of 3000 fb^{-1} and 4000 fb^{-1} of integrated luminosity, respectively. The ultimate scenario will probably be reached after Run-4 although the experiments require LHC to ramp up to this condition as fast as possible. Therefore, all the detectors must be redesigned in order to cope with these requirements.

3.2.1 Requirements for Offline Luminosity

Precision measurements foreseen by the ATLAS physics program in Run-4, including the Higgs sector, call for a precision of about 1% in the offline measurement of the integrated luminosity, to be compared to the 0.8% achieved in Run-2 on the full data sample, but in an harsher condition. This limits to the sub-percent level the various contribution to the uncertainty, the main ones being van der Meer absolute calibration, the calibration transfer for the low- to the high-luminosity regimes and the long term stability.

The stringent requirement on precision calls for a multiplicity of luminosity detectors including at least 2, preferably 3, detectors vdM-calibratable and capable of measuring at high luminosity. LUCID-3 is expected to be one of these detectors. Additional detectors with a high level of linearity must be cross-calibrated in the vdM luminosity regime and will be used to correct the non-linearities of the main luminometers, while other complementary devices will be used for long-term stability assessment and/or for non-linearity corrections of the main luminometers and must be cross-calibrated at least at high luminosity.

The same strategy was applied in Run-2, although the needed redundancy could not be achieved since LUCID was the only detector able to provide per-bunch measurement in all luminosity regimes. The limitations of the LUCID measurement in Run-2 and their implication for Run-4 will be discussed later (see section 3.2.3).

3.2.2 Requirements for Online Luminosity

Online luminosity measurement does not have such stringent requirements as the offline in terms of absolute precision but additional features must be guaranteed to ensure a proper beam operation by LHC, in particular for the luminosity leveling operation and for an efficient use of the beam by ATLAS. The main requirements on the online luminosity measurement are:

- capability to measure luminosity on a bunch-by-bunch basis with a precision of $2 - 3\%$;
- compatibility to provide the delivered luminosity without dead-time and independently of the ATLAS acquisition system at a rate of about 1 Hz;

- operation in all beam modes, in particular outside standard physics runs;
- redundancy and flexibility to immediately switch among different algorithm or detector in case of detector malfunctioning to avoid glitches in providing the luminosity to LHC;
- linearity and long-term stability (same requirements as for the offline measurement).

All these features are available now and will be ensured by LUCID also in Run-4, although concerns about the ability to measure in time-intervals as short as one second must be solved without saturating computing resources of LUCID acquisition.

3.2.3 Limitations of LUCID-2 at HL-LHC

One of the main concerns about using Event-counting and Hit-counting algorithms to measure luminosity is the saturation effect, namely the fact that the detector observes an event (or a hit) in each bunch crossing during a luminosity block. In this case, the logarithmic formula used to linearize the measurement fails and the luminosity cannot be determined (see Chapter 1.5.2). Even when getting close to this point, the detector enters into the so-called 'zero-starvation': the statistical uncertainty of the measurement depends from the number of not saturated events, leading to large statistical uncertainties and fluctuations.

In Run-2 Event counting algorithms saturated at $\mu \approx 20-30$ (depending on the type of algorithm), while Hit counting algorithms did not saturate in the probed μ-range, and are not expected to saturate until $\mu \approx 110 - 120$. This μ-value is too low for Run-4 operation. One possibility to avoid saturation is to lower the geometrical acceptance of the detector, either by reducing the active area of the sensors or by moving them into a region with lower particle fluxes or both at the same time. The first option was tested during Run-2 by installing Bi-MOD (see Chapter 2.4). As shown in Chapter 2.4, the μ-dependence is much higher compared to usual Bi and Bi2 PMTs. There are also indications that the function needed to correct for μ-dependence might be more complex than the simple quadratic formula applied to the standard PMTs in the μ-range probed in Run-2. Even if it is not possible to predict the non-linearity at the higher μ-values of Run-4, the larger effect of the Bi-MODs suggests that a detector based on that PMTs might run into problems.

The saturation effect does not affect the charge-integrating algorithms, where the observed charge is proportional to the luminosity, provided that the dynamic range of the electronic chain and the working conditions are correctly dimensioned. This was the case for Run-2 by working with a PMT gain of the order of 10^5 which allowed to have sensitivity in both the low and high luminosity range.

3.3 The LUCID-3 detector

The present LUCID-2 detector is using, as discussed previously, two main methods for measuring luminosity with more than 100 different algorithms: Hit counting (i.e. pulses above a certain threshold), and Charge counting (i.e. the integral of pulses).

One of the main problems with Hit-counting is the so called μ-dependence calling for an appropriate correction. This correction increases with μ and, since the average μ is expected to increase by a factor of 2.5-3.8, the correction will be larger during Run-4. Another, and even more serious problem, is the saturation: an hit occurs in every bunch crossing during a lumiblock. If this happens, LUCID is no more able to measure luminosity using this algorithm.

The drawback with charge-counting is the higher sensitivity of the PMT to gain variations. The charge is basically proportional to the gain while one percent reduction of the PMT gain typically gives only a $0.3-0.4\%$ underestimation of the luminosity with hit-counting.

The most obvious design of a new LUCID-3 [14] detector would be a copy of the present LUCID-2 detector. In this case the detector would again be attached to the beampipe and sit inside a new support cone in a similar position as LUCID-2. A serious complication will be the new vacuum equipment (the VAX) that will be installed close to the present LUCID-2 location in LHC Run-4 (Fig 3.1). VAX will therefore introduce some constrain in the placement of PMTs and it will get activated during the data taking causing problems in the maintenance of the detector. Due to these complications and hit saturation, this possible design for a new LUCID has been discarded.

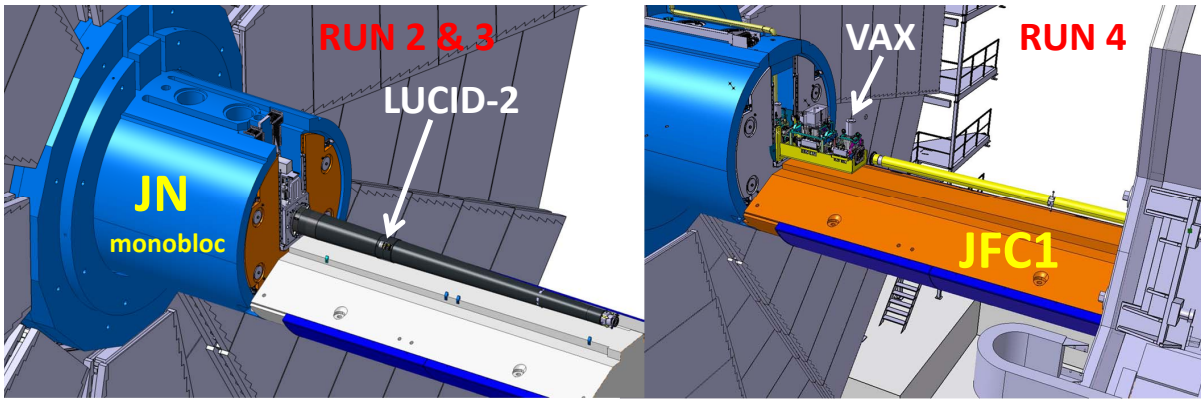

Figure 3.1: Left: location of the present LUCID-2 detector in the beampipe support cone. In this drawing only the bottom part of the forward shielding (JFC1) is installed. Right: new vacuum equipment (VAX) that will be installed in Run-4.

Another possibility would be to attach the new detector to one of the forward shielding. The shielding that is under consideration is JFC3 (see Fig. 3.2). This shielding is,

like all forward shieldings, removed during each end-of-year-shutdown (EOYS). The new detector would thus be available for maintenance in the buffer zone of a surface building every winter. The yearly maintenance will consist mostly of replacing photomultipliers and this would be more difficult if the detector is attached to the beampipe.

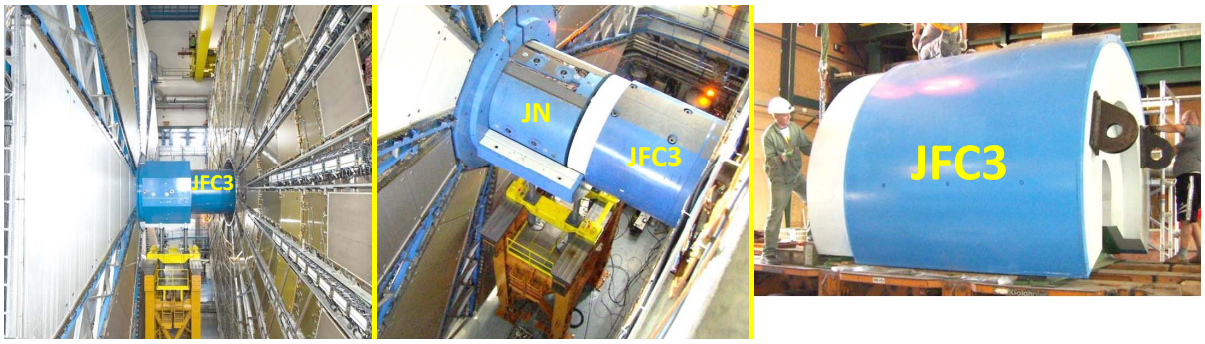

Figure 3.2: Photos of the forward shielding piece JFC3 during different stages of an ATLAS opening. The situation with whole shielding installed is visible on the left. The top octagonal shielding piece has been removed in the middle photo. The JFC3 shielding piece after removal from ATLAS is shown in the photo on the right.

The main advantages of having the new detector attached to the shielding instead to the beampipe would be:

- the detector and services will be more accessible during shutdowns;
- no interference with the VAX or the beampipe design;
- less radiation and saturation problem thanks to larger distance from beampipe
- no need for water cooling during beampipe bakeout (if JFC3 is not installed).

The main disadvantages would be:

- the detector has to be disconnected and connected every shutdown;
- the location of JFC3 and LUCID might change slightly every year;
- some additional machining to the shielding might be needed.

In addition of having two main methods to measure luminosity (Hit and Charge counting), two possible detector technologies were developed. The main detector during LHC Run-2 was a PMT detector. However, also 4 bundles of 37 quartz fibers coupled with PMTs have been installed on each side. Since any deterioration of the light transmission of the fibers in latter detector could not be monitored and the PMT gain could only be monitored by LED signals, the fiber detector has not been able to produce a stable

luminosity measurement during LHC Run-2. With improved methods of gain monitoring it could, however, be a competitor for LHC Run-4 where the increase in luminosity results in a potential increase of radiation damage to a PMT detector.

There are therefore two different LUCID-3 detectors under consideration:

- a PMT detector attached to the shielding;
- a fiber detector attached to the shielding.

Taking into account the above discussed advantages and disadvantages of different methods, locations and detector technologies, it has been decided that the baseline LUCID-3 detector will be a PMT detector attached to the JFC3 shielding (Fig 3.3). A fiber detector attached to the JFC3 shielding is regarded as the main back-up possibility. The final choice of detector will be determined based on the performance of prototype detectors that are already installed and under testing in LHC Run-3. The first study of the performances of the prototypes will be presented in this thesis.

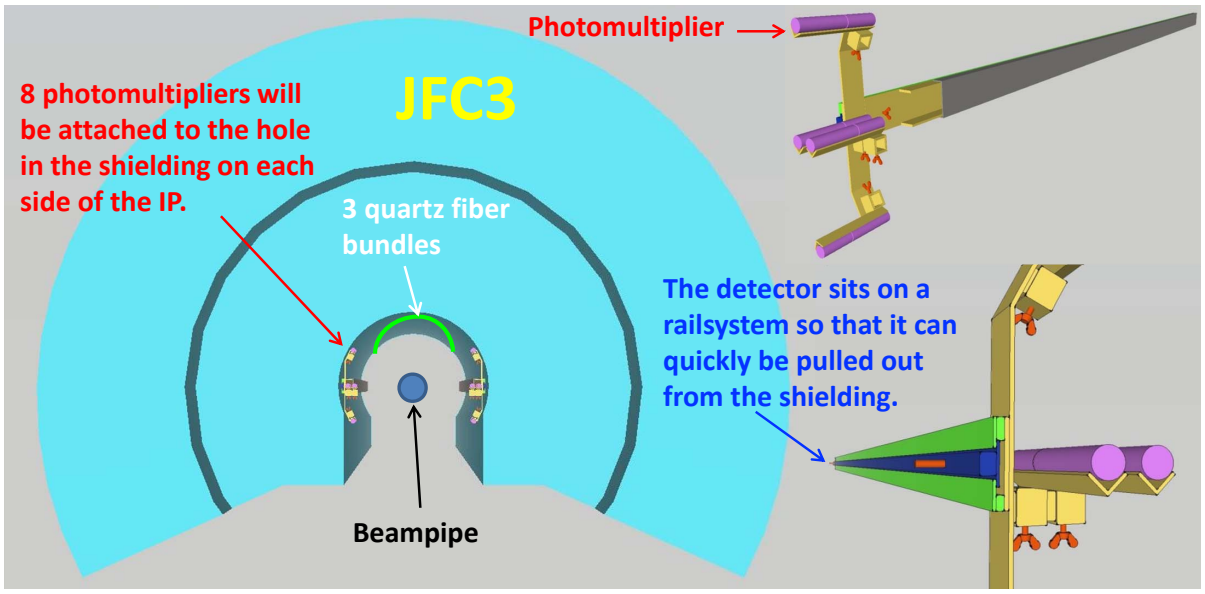

Figure 3.3: A front-view of the JFC3 forward shielding piece with the location of the PMT and fiber detectors.

3.3.1 The PMT Detector

The proposed PMT detector would sit on a rail system (Fig. 3.4) such that the detector could be slid forwards or backwards out of the shielding beampipe hole. The inside of the beampipe hole becomes very activated, so the idea is to be able to get quickly some

distance between people doing maintenance on the photomultipliers and the shielding hole.

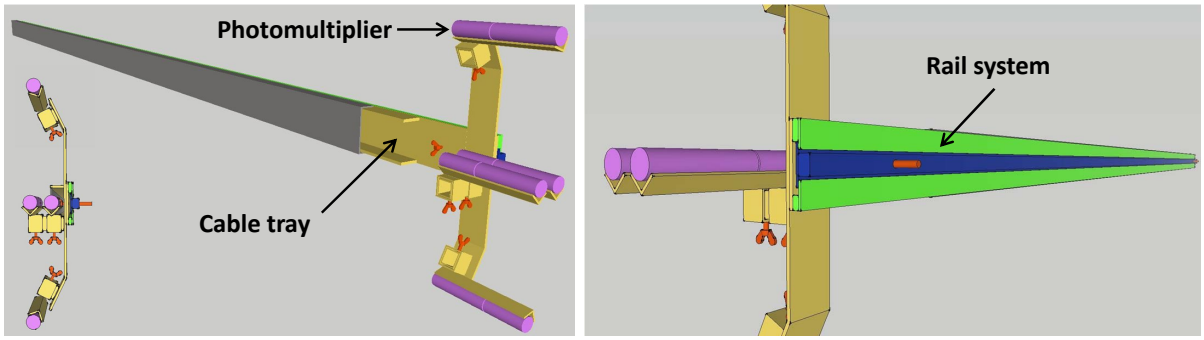

Figure 3.4: The PMT detector is attached to the forward shielding with a rail system so that it can easily be removed from the shielding during maintenance work in an end-of-year shutdown.

The services to the detector would run in a cable tray to the back of the shielding and then up to the top. A major advancement of this design is due to the option of replacing parts during YETS in case of radiation damage. For LUCID-2 instead, only the photomultipliers and the bases could be replaced.

Another big advantage is that the installation of the JFC3 with the detector can wait until a beampipe bake-out has been made. The proposed detector therefore does not need a cooling system nor temperature probes to monitor LUCID temperatures during the bake-out (note that during normal operation LUCID-3, as well as the present LUCID-2, does not need any cooling and operates at room temperature). This is a considerable simplification over the present detector.

LUCID-2 has 16 PMTs on each side of the interaction point. The proposed new detector would have only 8 in order to minimize the number of connectors that have to be disconnected before the JFC3 shielding can be removed.

The photomultipliers will be placed 350 mm away from the beamline (125.5 mm for LUCID-2) in the new detector and the particle density is expected to be lower in the new locations by 30%. In the best case scenario, the standard PMTs can therefore be used also at the higher luminosity during LHC Run-4. The simulations are not accurate enough to determine if this will indeed be the case and a measurement with a prototype detector is therefore taking place during LHC Run 3. An option to further reduce the acceptance using smaller PMTs is also being investigated.

3.3.2 The Fiber Detector

An upgrade of the Run-2 fiber detector is also under study. It consists in 3 bundles of radiation hard quartz fiber (UVNSS 600/624/660) [1] coupled with Hamamatsu R7459 PMT for the readout attached to the upper part of JFC3 shielding (Fig 3.5). The novelty of this design is the double calibration system. The gain of these photomultipliers would be monitored with radioactive ^{207}Bi sources applied to the edge of window in the same was as LUCID-2 PMTs. Any deterioration of the fibers due to radiation damage would be monitored by a set of LEDs connected to the other end of the fiber bundles. The LEDs would also be connected directly to the PMTs so that the stability of the LEDs could be monitored. A prototype of this monitoring system is being tested in Run-3.

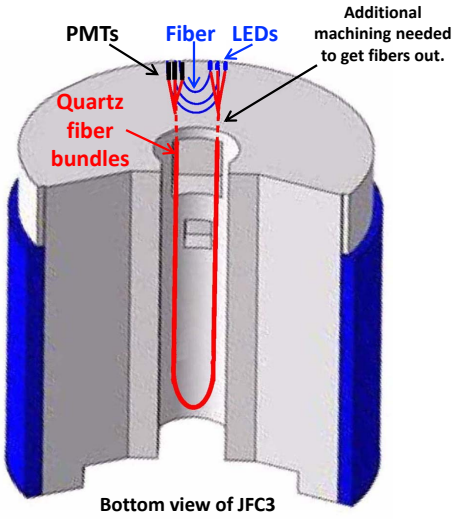

Figure 3.5: A bottom-view of the JFC3 forward shielding piece with the location of the fiber detector.

3.3.3 The radiation dose to the detector

Another aspect to be taken into account in the design of the detector is the amount of radiation. At the location of the quartz windows of the LUCID-2 PMTs the simulation gives 3.0 kGray/fb^{-1}. A PMT attached to the shielding would then receive about 400-520 kGray during a year according to the simulation under an assumption that a year in run 4 would give 200-260 fb^{-1}. The PMT of the fiber detector, being hidden inside the JFC3 shielding, is expected to receive only 12 kGray during 4 years of running corresponding to an integrated luminosity of 60+200+200+200 fb^{-1} during Run 4. However, the radiation

[1] https://www.ceramoptec.com/products/fibers/optran-uv-nss.html

to the fibers could be 2.6 MGray so already in Run 4 with the baseline HL-LHC scenario, the radiation to the fibers is large, and if the ultimate scenario in Run 6 gives 2000 fb^{-1} then the dose to the fibers could be 4 MGray.

3.4 LUCID-3 Prototypes in Run-3

The various options for a LUCID-3 detector have been discussed in the previous section. GEANT 4 simulations have been made to give predictions of the efficiency of PMTs at different locations but without the required accuracy to determine if hit-saturation will occur. A prototype of a PMT detector attached to the JFC3 shielding during LHC Run-3 measures what the efficiency will be in the new location. The effect of the VAX equipment cannot be unfortunately predicted. However, the VAX will be more than one meter behind the PMTs and the effect of back-splash from interactions in the VAX will probably be small.

An additional PMT detector has also been installed. It consists of 2 PMTs placed behind the forward shielding. Simulations have shown that it can get enough hits to provide a low-rate measurement.

A prototype of the fiber detector has been installed in a different position to the one expected for Run 4: attached to the VJ cone.

3.4.1 The PMT detector

Figure 3.6: Photo of the PMT prototype detector attached to the JFC3 forward shielding.

The prototype PMT detector that is attached to the JFC3 shielding, called LUCID-JF, is shown in Fig. 3.6. The prototype placed on C side has been equipped with one set of two standard R760 PMTs while another set of two new smaller R1635 PMTs has been attached to the A-side. The detector has only 2+2 PMTs since no empty read-out channels are available and only the four channels used for the old fiber detector can be used. The rail system is identical to what proposed for the final detector and it has already been tested. This prototype is expected to have similar linearity and stability compared to LUCID-2, as discussed in next sections.

3.4.2 The LUCID-JF Prototype in 2023 and 2024

The characterization of this prototype will follow the same steps described in Chapter 2.12. Since the prototypes on side A and side C are equipped with different type of

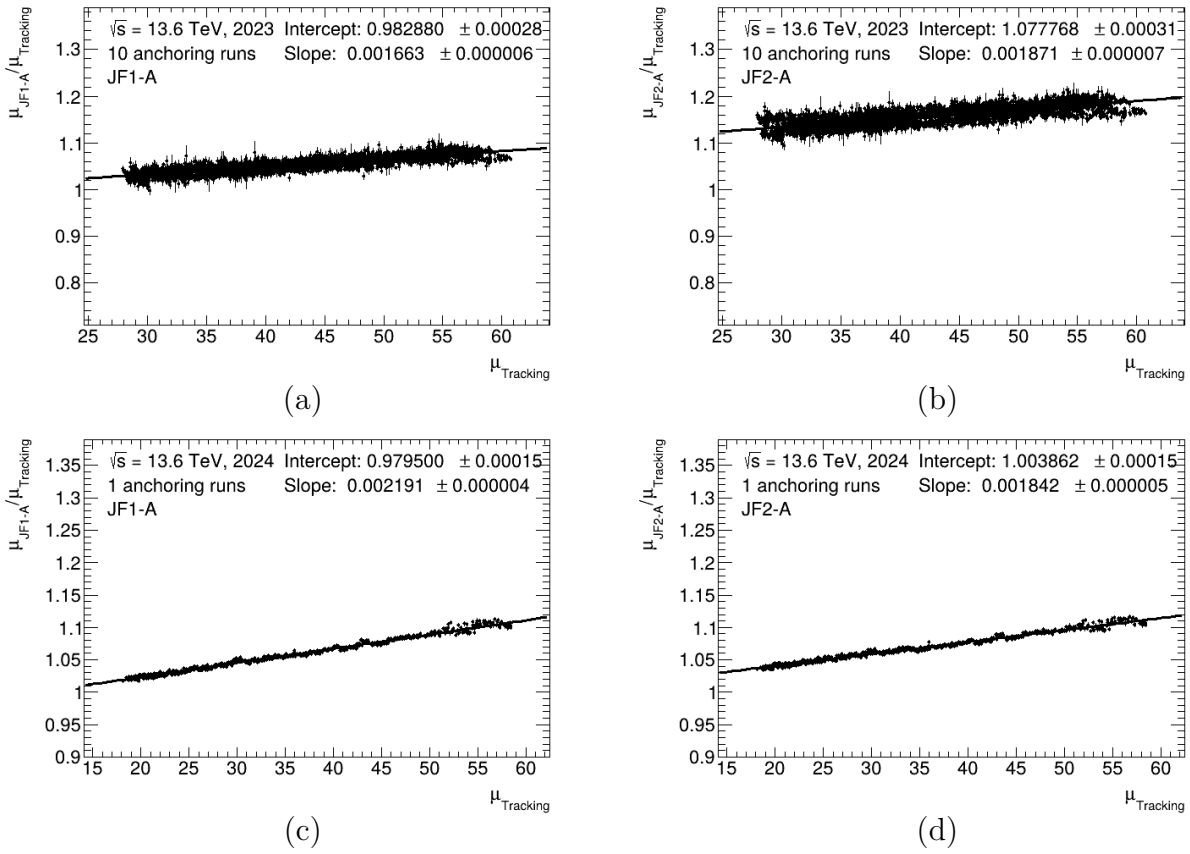

Figure 3.7: μ-dependence fit for JF1-A (on the left) and JF2-A (on the right) using 2023 (on the top) and 2024 dataset (on the bottom).

PMTs, the two prototypes will be discussed separately and then a comparison of the performances will be made.

LUCID JF-A (Hamamatsu R1635)

In both 2023 and 2024, the two central PMTs were turned on and were not changed after 2023. These will be henceforth called JF1-A for the one closer to the shielding and JF2-A for the furthest.

The μ-dependence fits, as defined in Chapter 2.12 are reported in Fig. 3.7 for both PMTs and for both datasets. The two PMTs are characterized by a similar slope and they are also similar to LUCID-2. In Fig 3.8 the intercept as function of position inside the train for both 2023 and 2024 datasets for both PMTs is reported. The intercept remains reasonably constant inside the train. The σ_{vis} of these PMTs is slightly off since the intercept is not always compatible with 1. Morevoer, the PMTs settings were

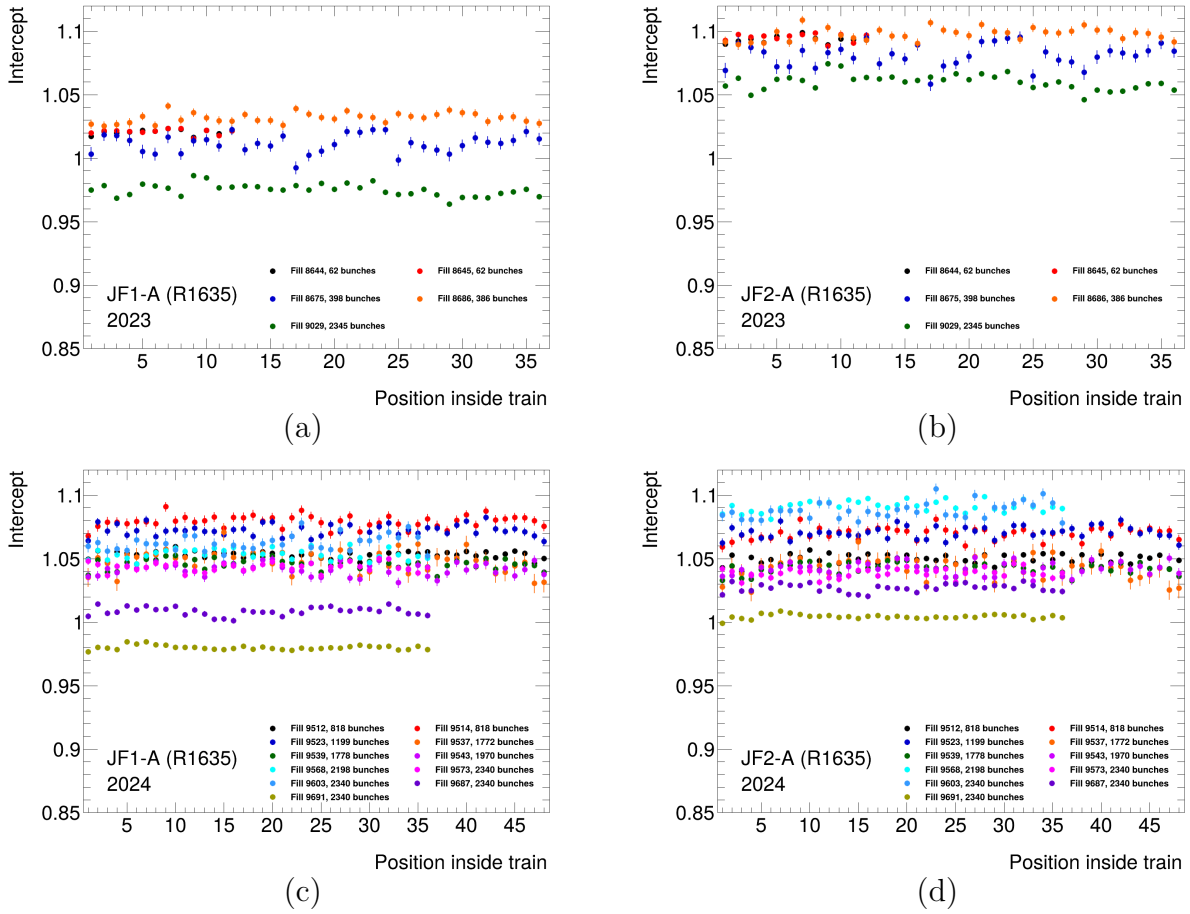

Figure 3.8: Intercept of the μ-dependence as function of position inside train for JF1-A (on the left) and JF2-A (on the right) when using the 2023 (on the top) and 2024 (on the bottom) datasets.

changed during the year, and this reflects in a smaller intercept in fills 9687 and 9691 compared to all other fills (especially for JF1-A). This change will have an effect also on the long term stability that will be discussed later. In Fig. 3.9 the slope as function of the position inside the train is reported. As for LUCID-2, the slope increases in the first 4 BCIDs inside the trains and then remains stable at a value that is compatible with the one obtained by the global μ-dependence fit. The change in setting of the PMTs did not have a sizeable impact on the slope. Fig 3.10 shows the slope as function of mean μ calculated in every position inside trains. There is a strong anti-correlation between the slope and the mean-μ like in LUCID-2.

In Fig. 3.11, the ratio of the luminosity measured with both LUCID-JF on side A PMTs to other luminosity algorithm as function of the luminosity fraction is shown

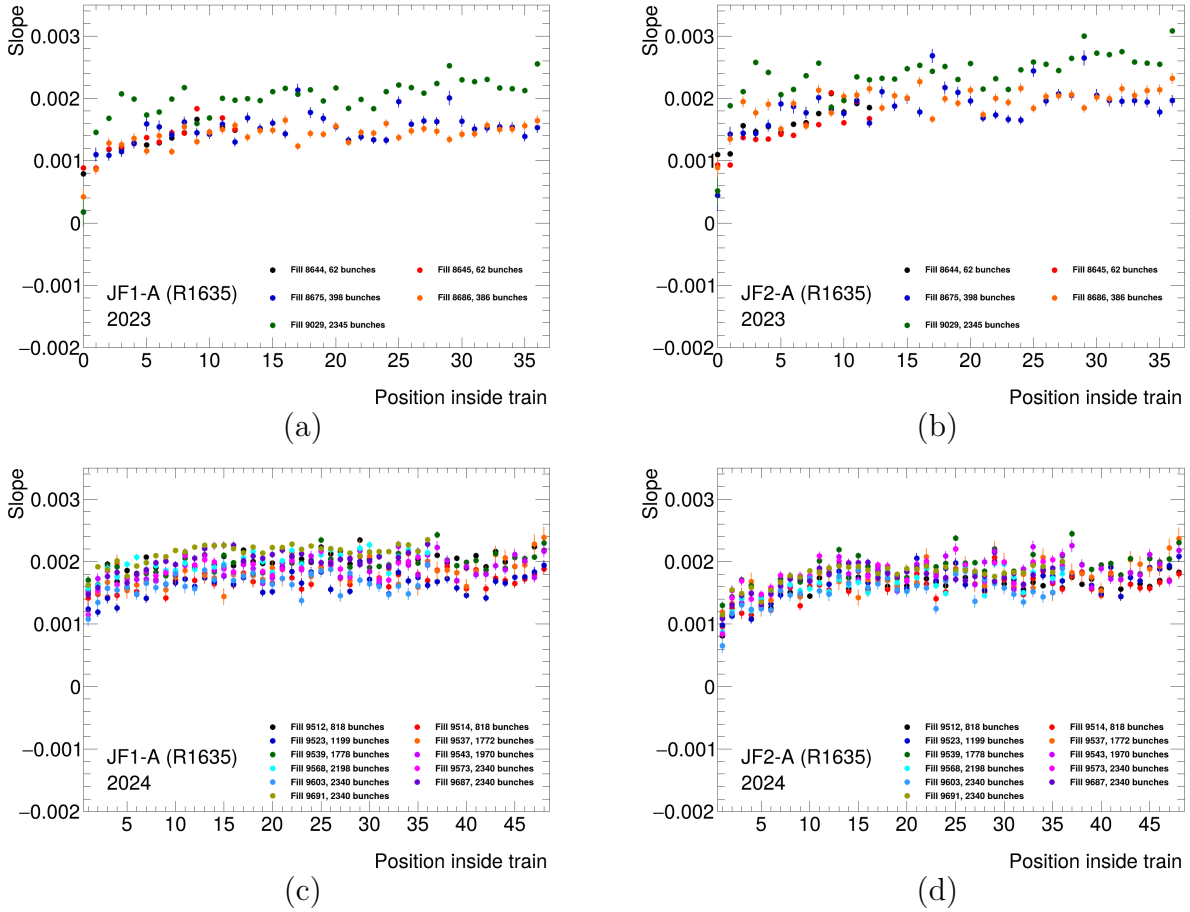

Figure 3.9: Slope of the μ-dependence as function of position inside train for JF1-A (on the left) and JF2-A (on the right) when using the 2023 (on the top) and 2024 (on the bottom) datasets.

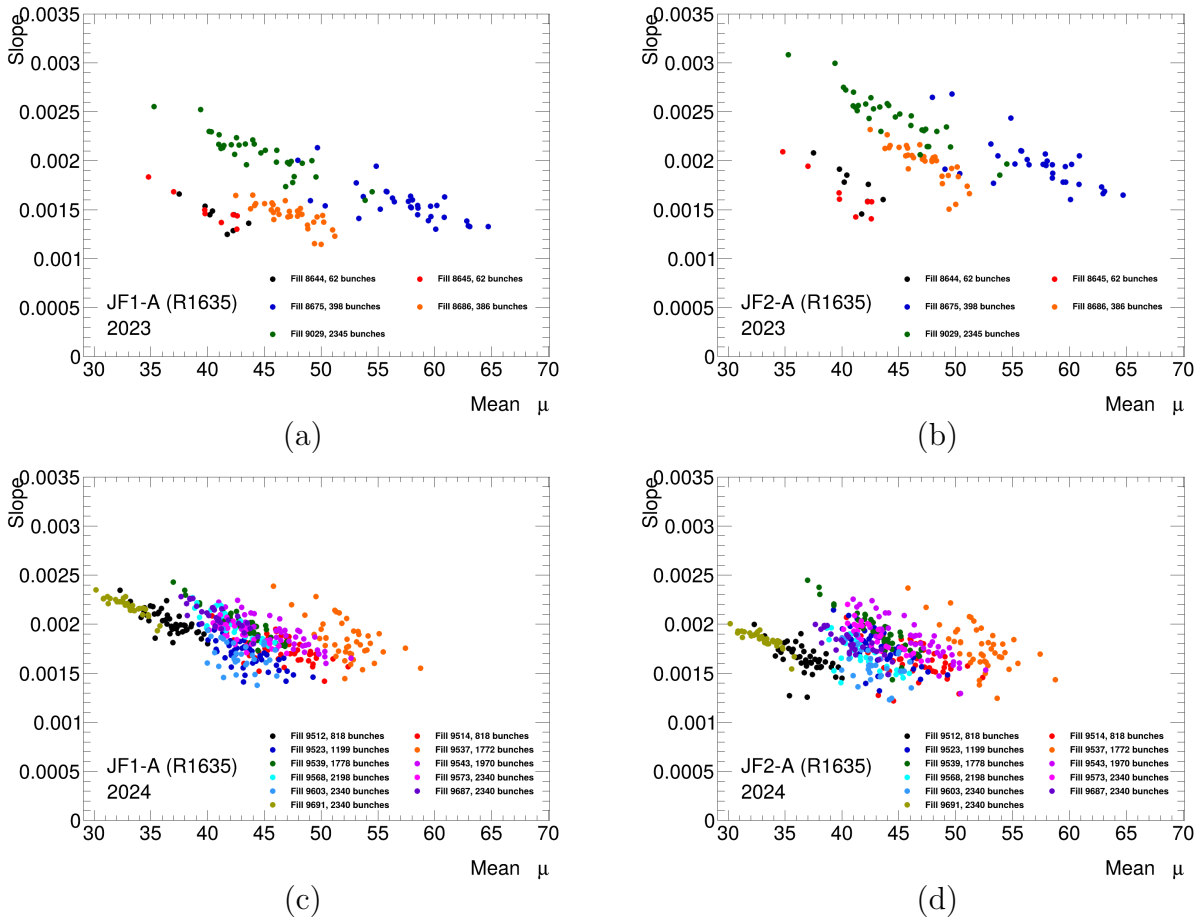

Figure 3.10: Slope of the μ-dependence extracted by the fits as function of mean μ for JF1-A (on the left) and JF2-A (on the right) when using the 2023 (on the top) and 2024 (on the bottom) datasets.

for both 2023 and 2024 datasets. JF1-A seems to be slightly more stable compared to JF2-A in 2023. PMTs settings have been changed during the 2024 data taking. Each setting is highlighted with a different marker. In order to properly evaluate the stability of the detector, the last run before the setting change has been rescaled to 1 and all the other runs with the same settings are rescaled by the same amount. In 2024, one of the main concern regarding this type of PMTs is the anodic current. In fact, the maximum anodic current recommended by Hamamatsu is 30 μA while for R760 maximum is 100 μA. Even though this limit is not a problem during Run-3, it may become a problem during HL-LHC since the μ will be 2 to 3 times higher. To try to reduce the anodic current, the gain of these PMTs was lowered in 2024. In the first period (filled circled in c and d), both PMTs had a very poor stability so the gain was brought back to the same setting as 2023 (empty squares in c and d). After a period of testing, the stability remained quite poor.

It was observed, during bismuth calibrations performed just after the end of the physics fill, a high hit rate due to activation induced by the materials surrounding the PMTs (see appendix A). To compensate for this effect, the threshold used to define a hit was increased without changing the gain (filled triangles in c and d) to cut out this noise. JF1-A prototype demonstrated to be quite stable so these settings were kept for the rest of the data taking. Instead, JF2-A could not get enough bismuth signal during calibration so its threshold was decreased (empty triangles in d).

It is clear that this type of PMT is much more sensitive to material activation compared to R760s. Since activation will be much more important in HL-LHC due to the higher μ, several strategies to mitigate the effects of activation are under study. One of the main ideas to solve this issue is to produce custom R1635 with a thicker window (currently, R1635 PMT window thickness is 0.8 mm compared to the 1.2 mm of the R760 who seem to be immune from this effect). A thicker window should allow electrons coming from bismuth (or more in general, particles coming from the front of the PMT) to produce more Cherenkov photons without affecting the numbers of photons produced by particles coming from the side of the PMT. Another idea is the use of R760s with a window of 1.2 mm; this will be discussed in the next section when discussing the LUCID JF on side C.

Fig. 3.12 reports the distribution of the ratio of luminosity measured with both PMTs over other luminosity algorithms while in Tables 3.2, 3.3 and 3.4 the RMS of each distribution is reported. The lower gain at the beginning of the 2024 data taking induced a worse stability in both PMTs. By bringing back the PMTs to the settings of 2023 data taking, the RMS went back to a value similar to the 2023 one. Increasing the threshold improved even further the stability for both prototypes. Nevertheless, the stability of JF2-A has not reached yet the requirement and further tests to optimize this detector are needed.

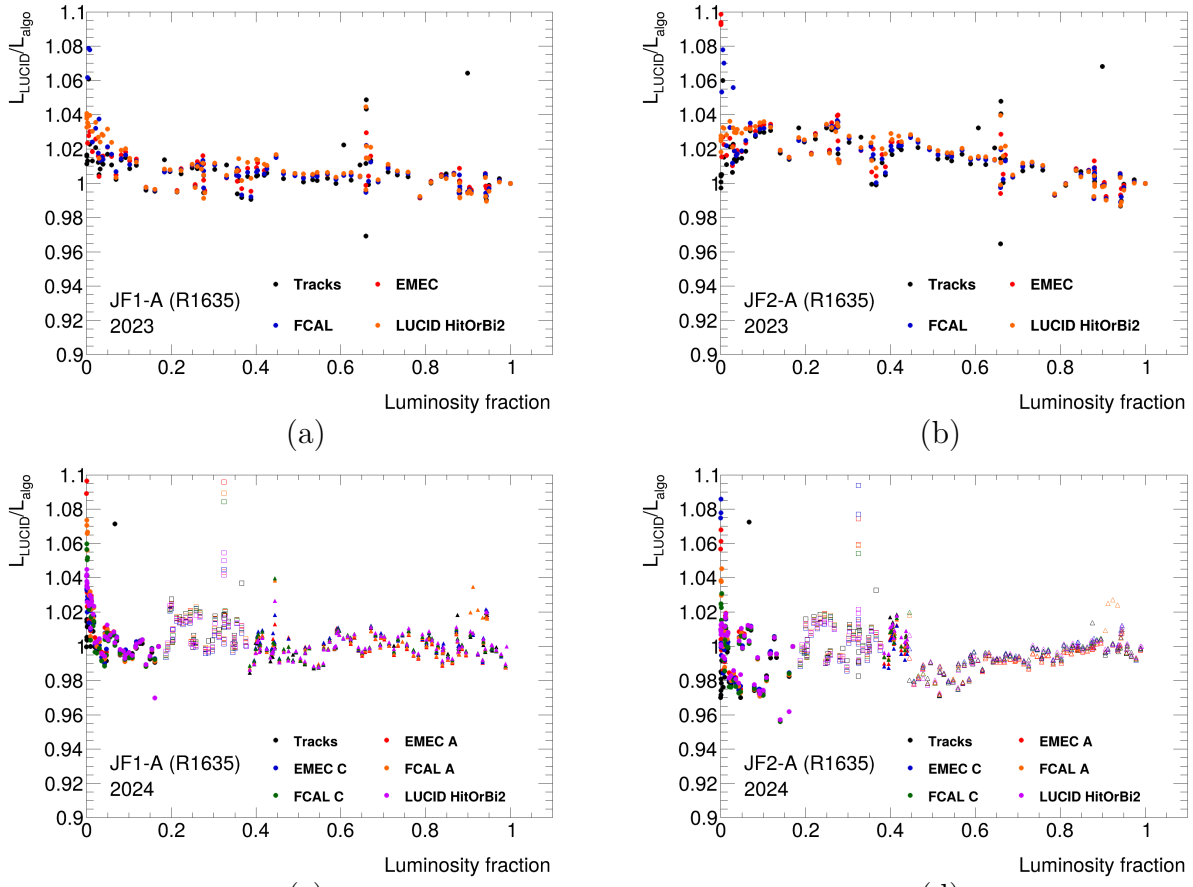

Figure 3.11: Long term stability for JF1-A (on the left) and JF2-A (on the right) in 2023 (on the top) and in 2024 (on the bottom).

	JF1-A	JF2-A
Tracks	0.011	0.013
EMEC	0.0067	0.011
FCAL	0.0088	0.012
HitOrBi2	0.0085	0.012

Table 3.2: RMS of the distributions of the ratio of JF1-A and JF2-A over other luminosity algorithms using 2023 dataset.

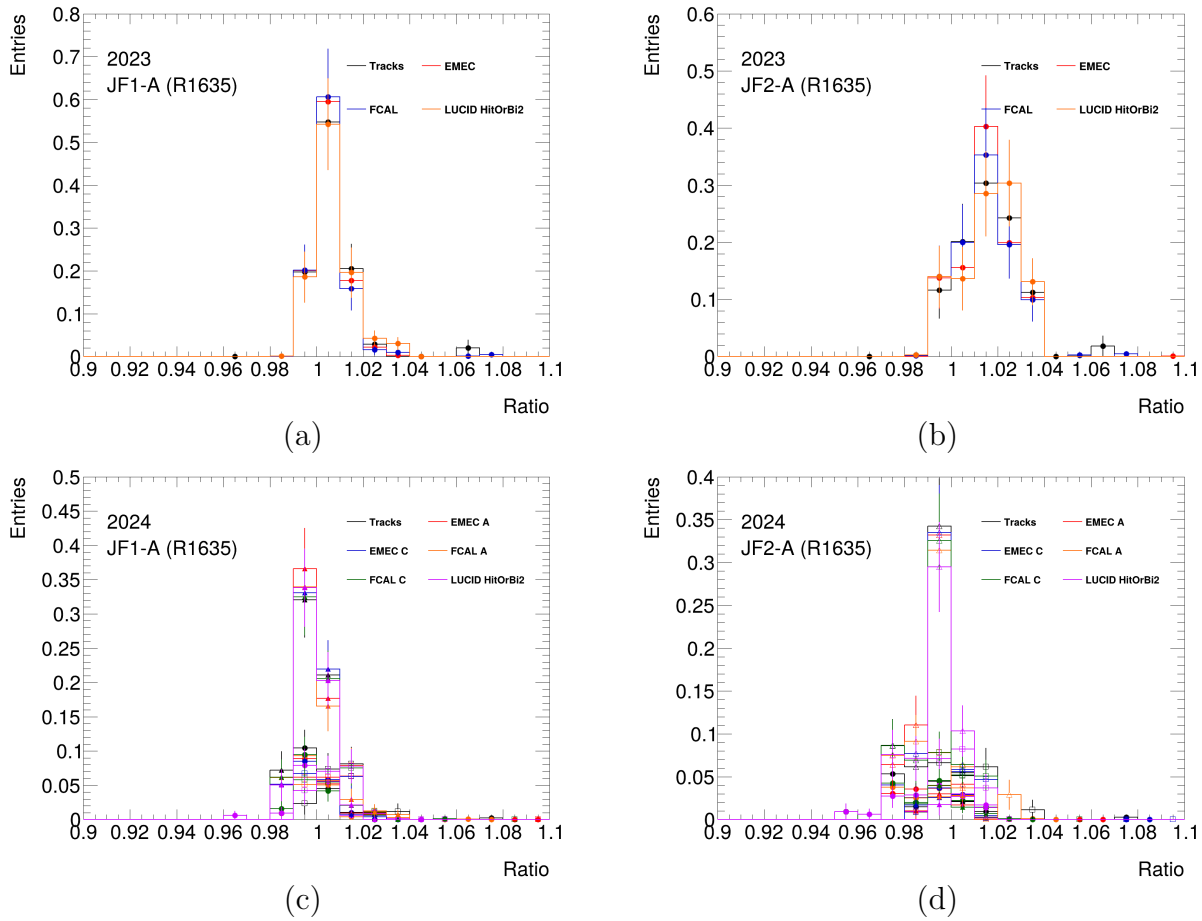

Figure 3.12: Distribution of the ratio of luminosity measured with JF1-A (on the left) and JF2-A (on the right) over other luminosity measured with other algorithms using 2023 (on the top) and 2024 (on the bottom) datasets.

	JF1-A(1)	JF1-A(2)	JF1-A(3)
Tracks	0.011	0.010	0.0062
EMEC A	0.0091	0.0085	0.0059
EMEC C	0.0079	0.0083	0.0063
FCAL A	0.011	0.0083	0.0084
FCAL C	0.0095	0.0083	0.0063
HitOrBi2	0.011	0.0078	0.0064

Table 3.3: RMS of the distributions of the ratio of JF1-A over other luminosity algorithms using 2024 dataset. Different columns indicate different PMT setting.

	JF2-A(1)	JF2-A(2)	JF2-A(3)	JF2-A(4)
Tracks	0.018	0.011	0.0078	0.0082
EMEC A	0.015	0.0087	0.0070	0.0073
EMEC C	0.015	0.0088	0.0075	0.0080
FCAL A	0.016	0.0087	0.0068	0.011
FCAL C	0.016	0.0087	0.0072	0.0082
HitOrBi2	0.016	0.0081	0.0067	0.0083

Table 3.4: RMS of the distributions of the ratio of JF2-A over other luminosity algorithms using 2024 dataset. Different columns indicate different PMT setting.

LUCID JF-C (Hamamatsu R760)

As already said, the PMTs installed in the JF-C prototype are R760 (the same as LUCID-2). In 2023, the two PMTs in the middle were turned on and they are named JF1-C, the closer one to the wall of the JFC-3 shielding, and JF2-C, one farther one. At the beginning of 2024, the JF2-C had noise issues so it was replaced with a spare PMT (called JF3-C). Since the number of runs in which JF2-C was on in 2024 is very limited, its performance in 2024 will not be considered while the JF3-C performance will be.

The μ-dependence fits are shown in fig. 3.13. The slopes are similar to the ones obtained by JF-A prototype and LUCID-2. Fig. 3.14 reports the intercept as function of the position inside the trains. There is no sign of dependence of the intercept on the position inside the train. A good run-to-run stability independent of the bunch configuration is observed in particular in 2024. Fig 3.15 instead reports the slope as function of the position inside the trains. As already seen with LUCID-2 and JF-A, also this prototype slope increases in the first 4-5 bunches inside the train and then stabilize at a value similar to the one obtained with the standard μ-dependence fit. Fig 3.16 shows the slope as function of mean μ calculated in every position inside trains. The strong correlation already seen in LUCID-2 and JF-A can also bee seen in all JF-C PMTs.

In Fig 3.17 the ratio of the luminosity measured with LUCID-JF prototype on side C to other luminosity algorithms as function of the luminosity fraction is reported. In 2023, both PMTs were stable. In the first period of 2024 data taking JFC1-C was quite stable while JFC3-C had a drift at the beginning of the data taking and at the end of this first period. The cause of this drift is not yet understood. After the discovery of the lack of stability of LUCID-JF on side A, the idea of using R760 PMTs in LUCID-3 was reconsidered. The problem is that the acceptance of this detector is too large and will lead to saturation at $\mu = 200$. For this reason the threshold for the two PMTs was increased in order to reduce the acceptance. The low threshold period is the one marked full circles in plot c and d. As already done for JF-A, the last run of every period is set to 1 and the other run are rescaled by the same quantity. After the threshold increase (empty squares in c and d) both PMTs were quite stable for the rest of data taking.

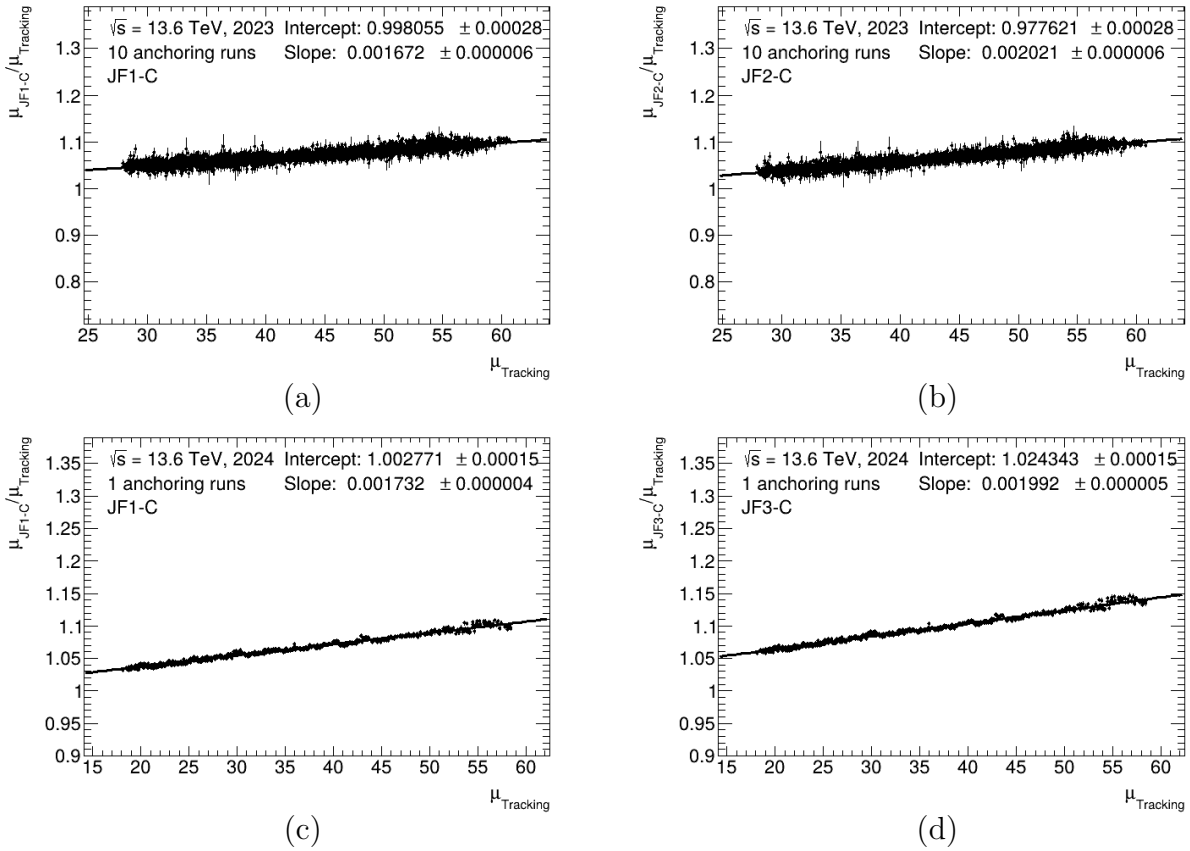

Figure 3.13: μ-dependence fit for JF1-C (on the top left) and JF2-C (on the top right) using 2023 dataset and of JF1-C (on the bottom left) and JF3-C (on the bottom right) using 2024 dataset.

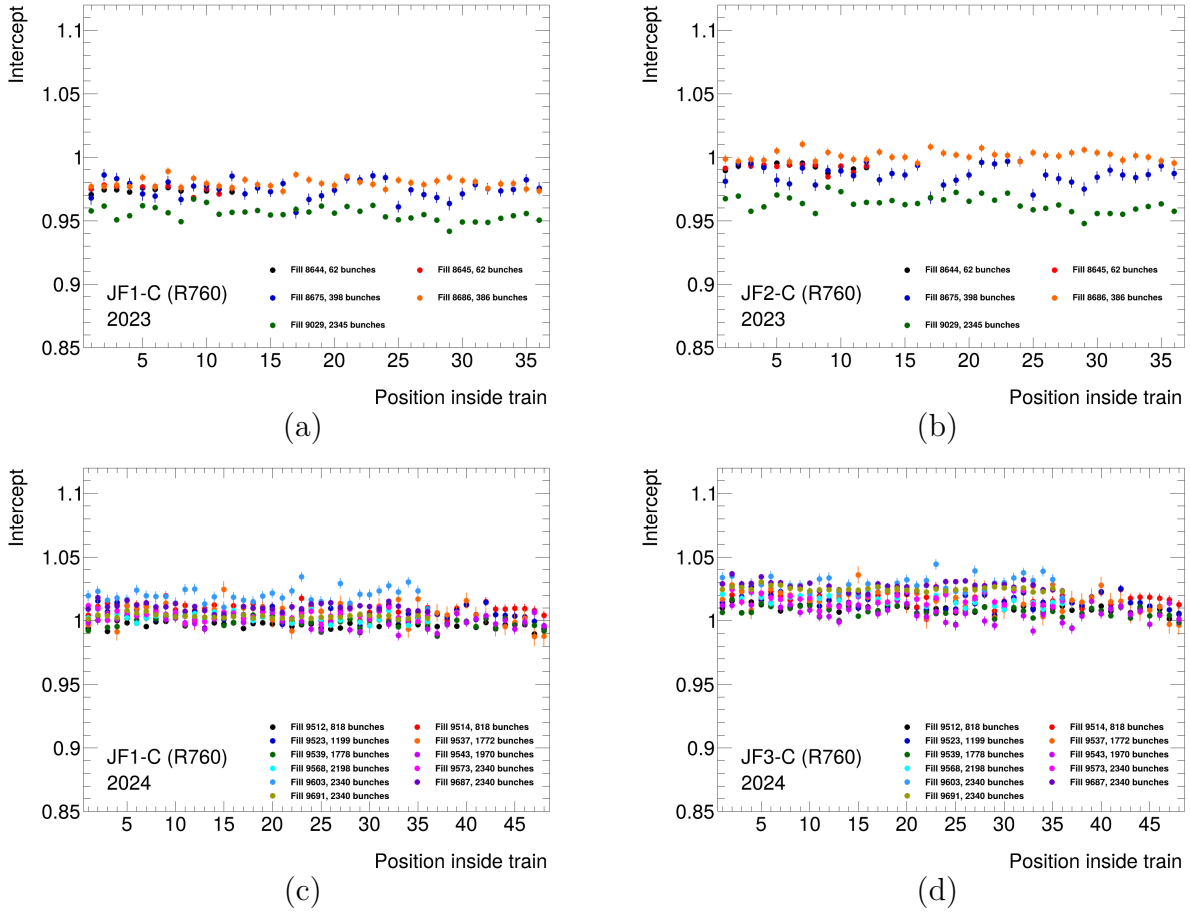

Figure 3.14: Intercept extracted by the fits as function of mean μ in all the fills for JF1-C (on the top left) and JF2-C (on the top right) using 2023 dataset and of JF1-C (on the bottom left) and JF3-C (on the bottom right) using 2024 dataset.

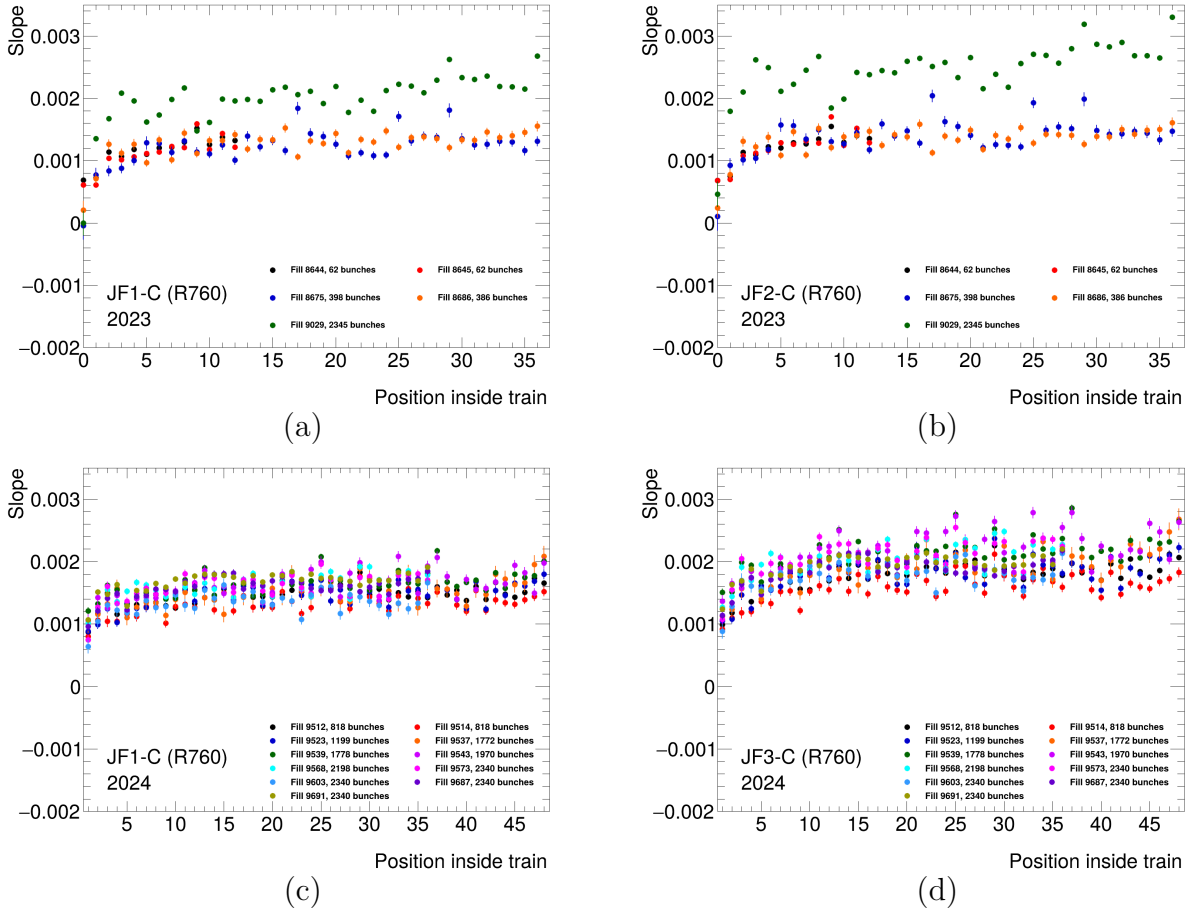

Figure 3.15: Slope extracted by the fits as function of mean μ in all the fills for JF1-C (on the top left) and JF2-C (on the top right) using 2023 dataset and of JF1-C (on the bottom left) and JF3-C (on the bottom right) using 2024 dataset.

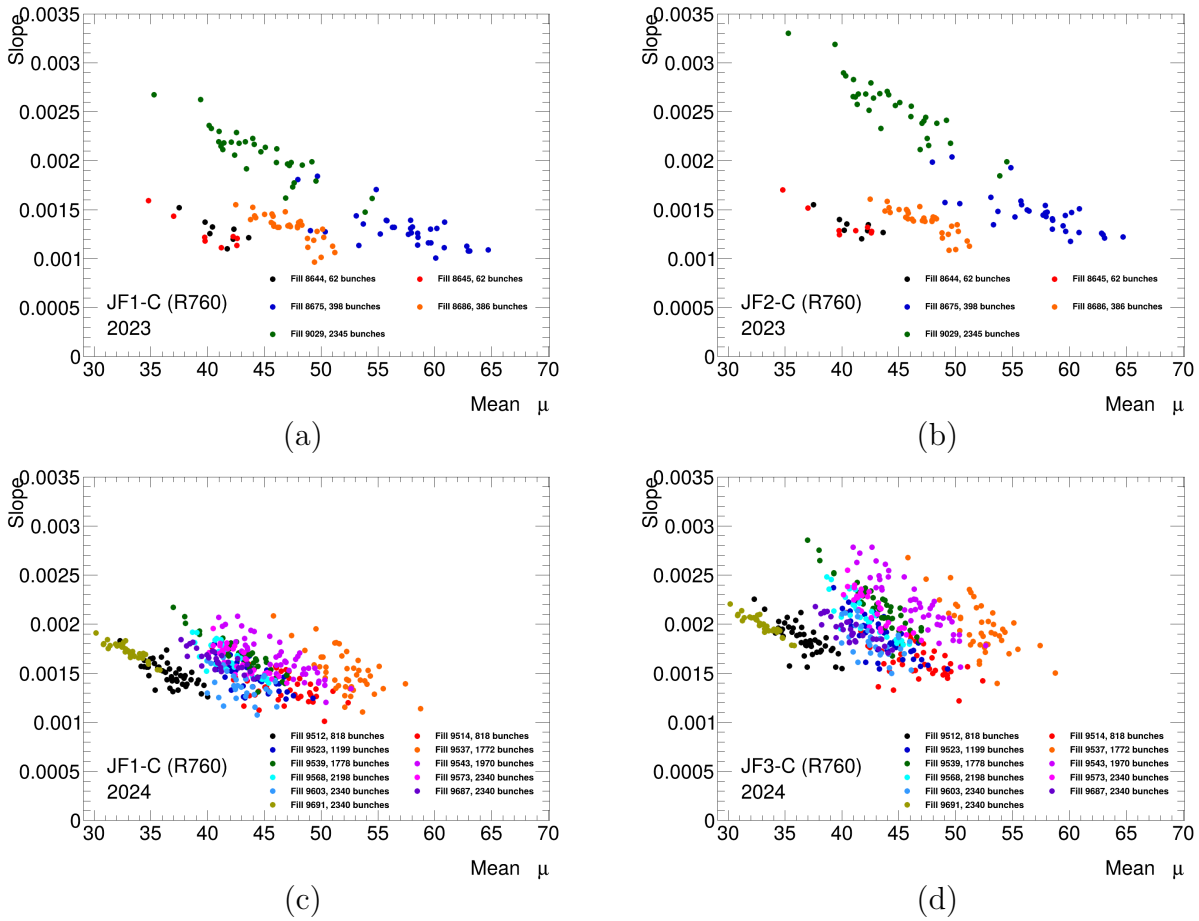

Figure 3.16: Slope extracted by the fits as function of mean μ in all the fills for JF1-C (on the top left) and JF2-C (on the top right) using 2023 dataset and of JF1-C (on the bottom left) and JF3-C (on the bottom right) using 2024 dataset.

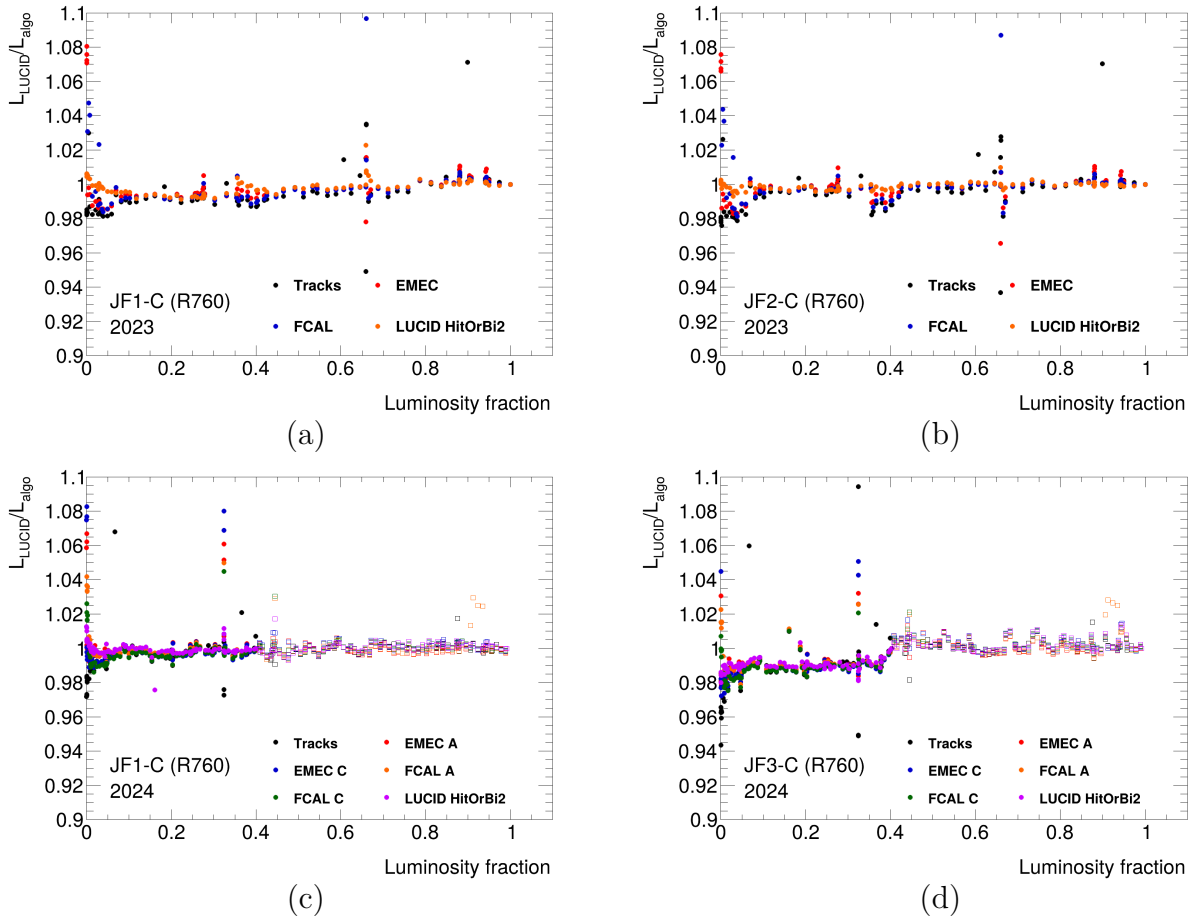

Figure 3.17: Long term stability for JF1-C (on the top left) and JF2-C (on the top right) in 2023 and for JF1-C (on the bottmom left) and JF3-C (on the bottom right) in 2024.

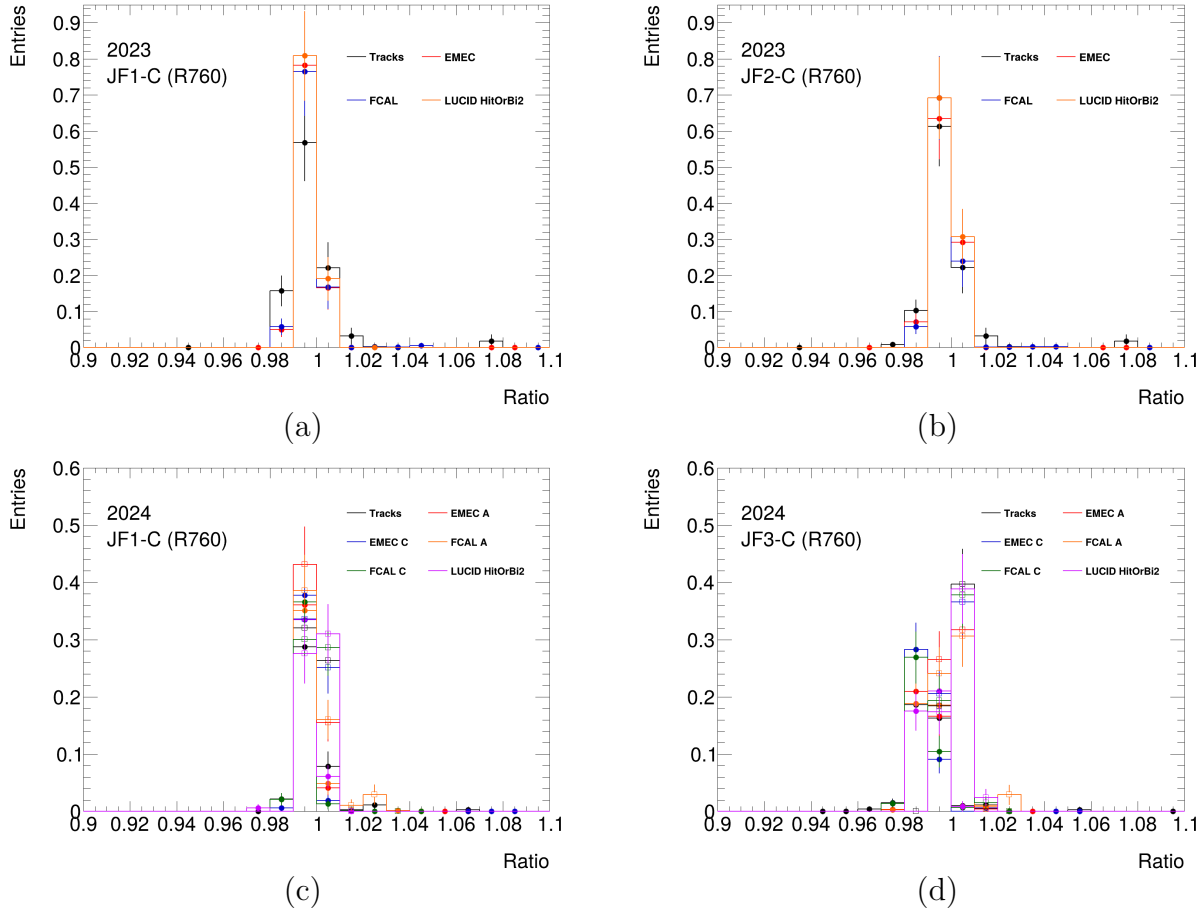

Figure 3.18: Distribution of the ratio of JF1-C (on the top left) and JF2-C (on the top right) over other luminosity algorithms using 2023 dataset and of JF1-C (on the bottom left) and JF3-C (on the bottom right) using 2024 dataset.

	JF1-C	JF2-C
Tracks	0.012	0.012
EMEC	0.0048	0.0045
FCAL	0.0058	0.0051
HitOrBi2	0.0032	0.0017

Table 3.5: RMS of the distributions of the ratio of JF1-C and JF2-C over other luminosity algorithms using 2023 dataset.

	JF1-C(1)	JF1-C(2)	JF3-C(1)	JF3-C(2)
Tracks	0.0079	0.0027	0.0093	0.0035
EMEC A	0.0027	0.0021	0.0044	0.0035
EMEC C	0.0035	0.0023	0.0050	0.0036
FCAL A	0.0033	0.0065	0.0043	0.0066
FCAL C	0.0031	0.0024	0.0049	0.0033
HitOrBi2	0.0032	0.0025	0.0031	0.0036

Table 3.6: RMS of the distributions of the ratio of JF1-C and JF3-C over other luminosity algorithms using 2024 dataset. Different columns indicate different PMT setting.

Fig. 3.18 reports the distribution of the ratio of luminosity measured with LUCID-JF PMTs on side C over other luminosity algorithms. In Tables 3.5 and 3.6 the RMS of each distribution is reported. In 2023, both PMTs performed at the same level of LUCID-2. JF1-C PMT had the same stability also in the first part of 2024. After the threshold increase, the RMS for this PMT decreased. JF3-C had instead a very poor RMS in the first period, probably due to the drift mentioned above. In the second period the RMS decreased and became similar to JF1-C and LUCID-2.

The change of threshold reduced the acceptance of both PMTs by ≈10%. Further tests will be carried out in 2025 to understand if the acceptance could be reduced even further by acting on the threshold without affecting negatively the stability. If this proves to be the case, the R760 operated with a high threshold could be considered a valid alternative to the smaller R1635 for operation in the HL-LHC without hit saturation.

LUCID JF comparison

From the above results it appears that both R760 and R1635 are characterized by a similar non-linearity with respect to μ. Also, the increase of the non-linearity inside trains is similar. The major difference between these two PMTs is the long term stability. In fact the prototype with R760 is characterized by a much better long term stability with respect to the prototype with R1635 and this is most likely due to the smaller sensitivity of the R760 to the activation of the surroundng materials. The main problem

with a LUCID JF made up with R760 is the saturation of the luminosity algorithm. Two possible solutions are under study:

- acceptance reduction by reducing the number of hits read by the PMTs. Two possible strategies are being studied: increase of the threshold to define the hit, as already tested in 2024, and the placement of material in front of the PMT window to block particles. For this last method to be effective, the flux of particle, and in particular which type of particle and its energy, must be done to poperly choose the material and the thickness
- increase the number of PMTs: a possible idea is to use 8 R760 for each side and combine them using 2 HitOr algorithm as it is done now with LUCID-2. Increasing the number of PMT not only increase the value of μ at which the luminosity algorithm saturates but also grants redundancy of LUCID luminosity measurement.

3.4.3 Low Rate PMT Prototype

It is not clear if the reduction of the particle flux when moving the detector position from the beampipe to the wall of the JFC3 will be enough to allow for the use of standard R760 PMTs. For this reason, additional PMTs were located behind the forward shielding. In this way the hit-rate in the PMTs could be possibly reduced to any desired level. GEANT4 simulations have shown that PMTs installed outside of the forward shielding would have a far too low hit-rate. An intermediate solution was devised: two PMTs were installed between the JFC3 shielding, the JN shielding and the Target Absorber for Secondary particles (TAS) as shown in Fig. 3.19. This prototype is called LUCID-JN.

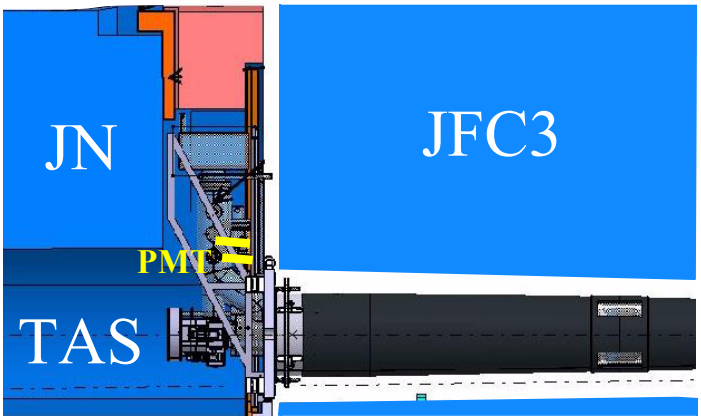

Figure 3.19: The drawing shows a sideview of low-rate PMT prototype detector that is located in the shadow of the forward shielding.

According to the GEANT4 simulations, the rate at the back of the JFC3 shielding will be reduced quickly as a function of distance from the beamline. It is therefore important to locate the new photomultipliers in a proper location to reduce substantially, but not to zero, the particle flux. A location 1-2 cm above the beampipe hole would see only 15-30% of the Hit-rate observed in LUCID-2. At a distance larger than 3 cm the rate would be less than 10% of the rate in LUCID-2. A reduction of 15-30% should be enough not to saturate luminosity algorithms.

Finding the right location so that the hit-rate will not be too small or too large is the main difficulty. Therefore two of the new ^{207}Bi calibrated PMTs were put on top of each other on side A as shown in Fig. 3.20 and Fig. 3.21.

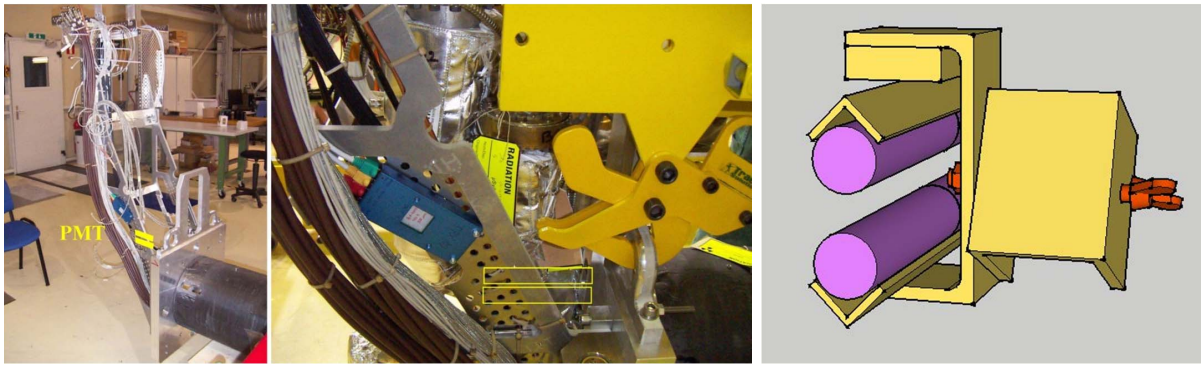

Figure 3.20: These photos indicate where the photomultipliers were attached (yellow rectangles) in the low-rate PMT prototype detector in order for the photomultipliers to be behind the forward shielding. The drawing to the right shows the support mechanism.

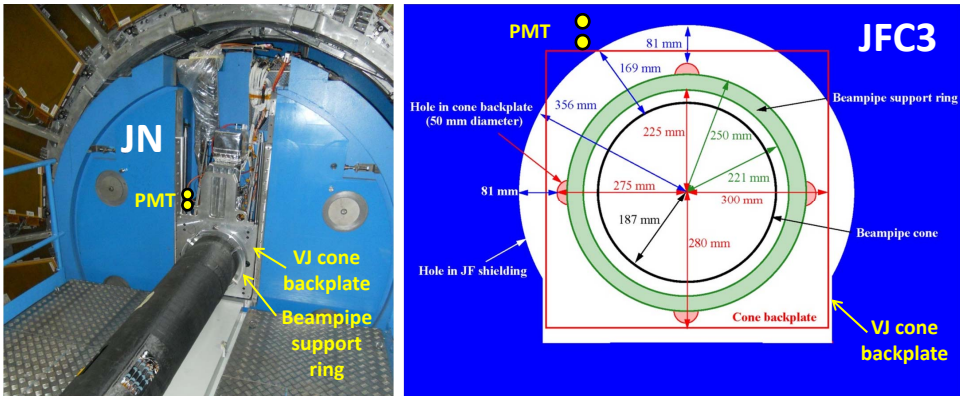

Figure 3.21: The photo on the left shows where the photomultipliers would be located. The drawing on the right shows where the photomultipliers are located in relation to the forward shielding after the top piece of the latter has been installed.

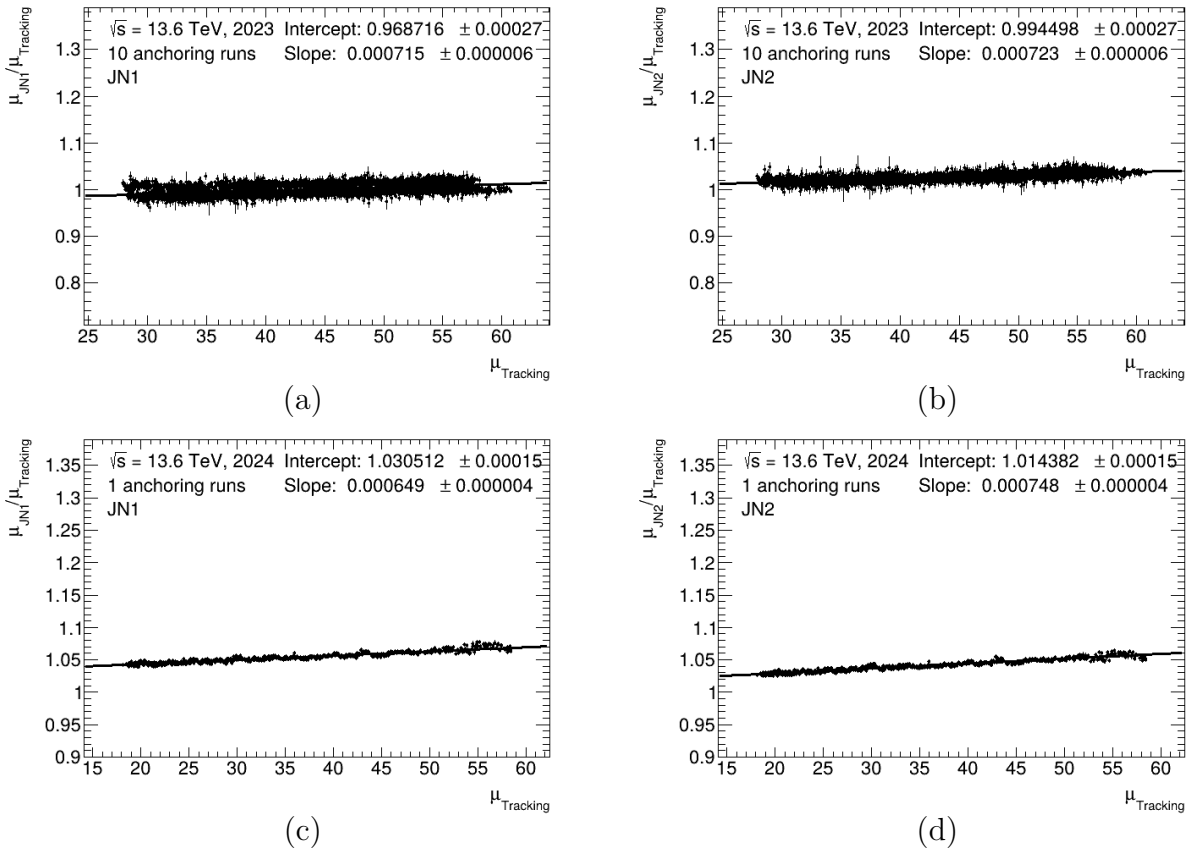

Figure 3.22: μ-dependence fit for JN1 (on the left) and JN2 (on the right) using 2023 (on the top) and 2024 (on the bottom) dataset.

The basic idea behind the proposal of this prototype is to have a highly linear reference detector to be used to correct the main JF detector for non linearity with respect to μ. It is therefore necessary to prove the linearity using Run-3 data (see next section).

3.4.4 LUCID-JN prototype in 2023 and 2024

As already mentioned, the LUCID-JN prototype is made of 2 PMTs, the top one will be called JN1 while the bottom one JN2. The first step in the characterization is the global μ-dependence. Fig. 3.22 reports the μ-dependence fit for both PMTs for 2023 and 2024 datasets. The slope is ≈4 times smaller than the one obtained with LUCID-2. Fig. 3.23 shows the intercept as function of the position inside the train for both 2023 and 2024 datasets. In 2023, the intercept was constant at about 0.95 for JN1 and 0.97 for JN2 for every position inside train and are well in agreement independent of the bunch configuration. In 2024 instead, both intercept were constant at 1.02-1.03 with

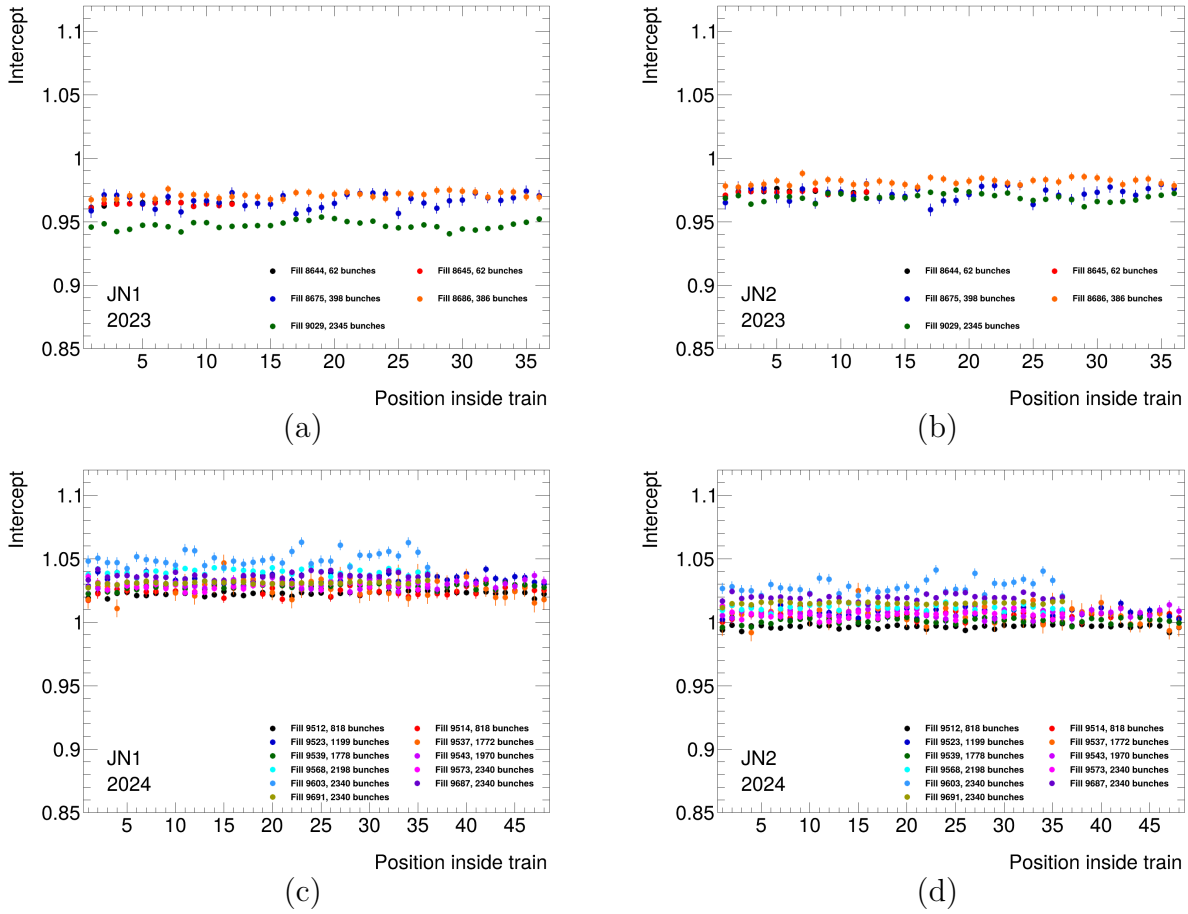

Figure 3.23: Intercept extracted by the μ-dependence fits as function of the position inside the trains for JN1 (on the left) and JN2 (on the right) using 2023 (on the left) and 2024 (on the right) dataset.

an even better stability with respect to the bunch configuration for every position with acceptable run to run fluctuation. Fig. 3.24 shows the slope as function of the position inside the train for both 2023 and 2024 datasets. The slope is much smaller compared to the LUCID-2 one, as already seen with the global μ-dependence fit and also the increase of the slope in the first bunches of the train is much smaller than in the LUCID2 or JF detectors. This is an important observation as it indicates that the non-linearity with μ is mostly related to the occupancy of the PMTs: the smaller is the occupancy, the smaller is the μ-dependence, and so it is for the train-dependence i.e. the dependence of the non-linearity on the bunch structure of the beam. Fig. 3.25 shows the slope as function of mean μ calculated in every position inside trains. There is an anti-correlation between the slope and the mean-μ like in LUCID-2 and LUCID-JF prototype.

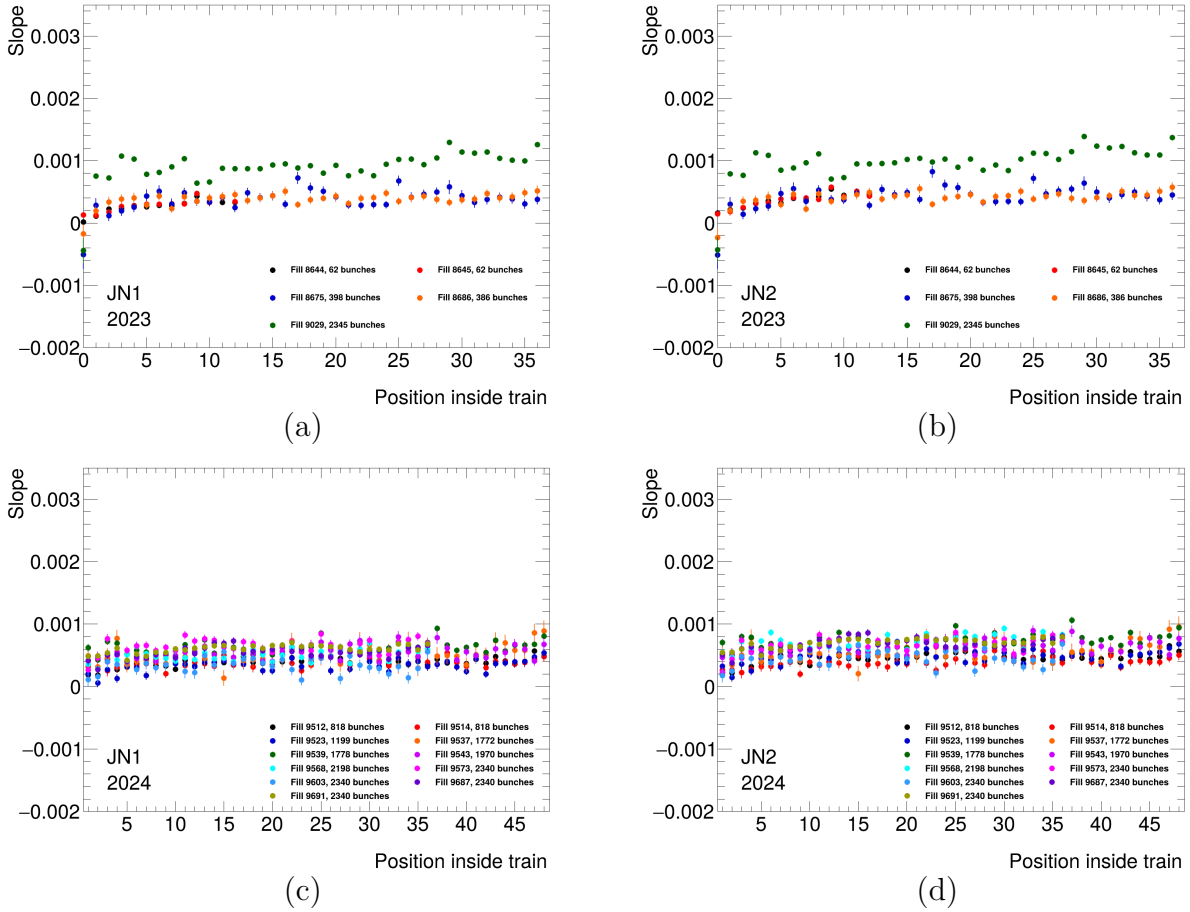

Figure 3.24: Slope extracted by the μ-dependence fits as function of the position inside the trains JN1 (on the left) and JN2 (on the right) using 2023 (on the top) and 2024 (on the bottom) dataset.

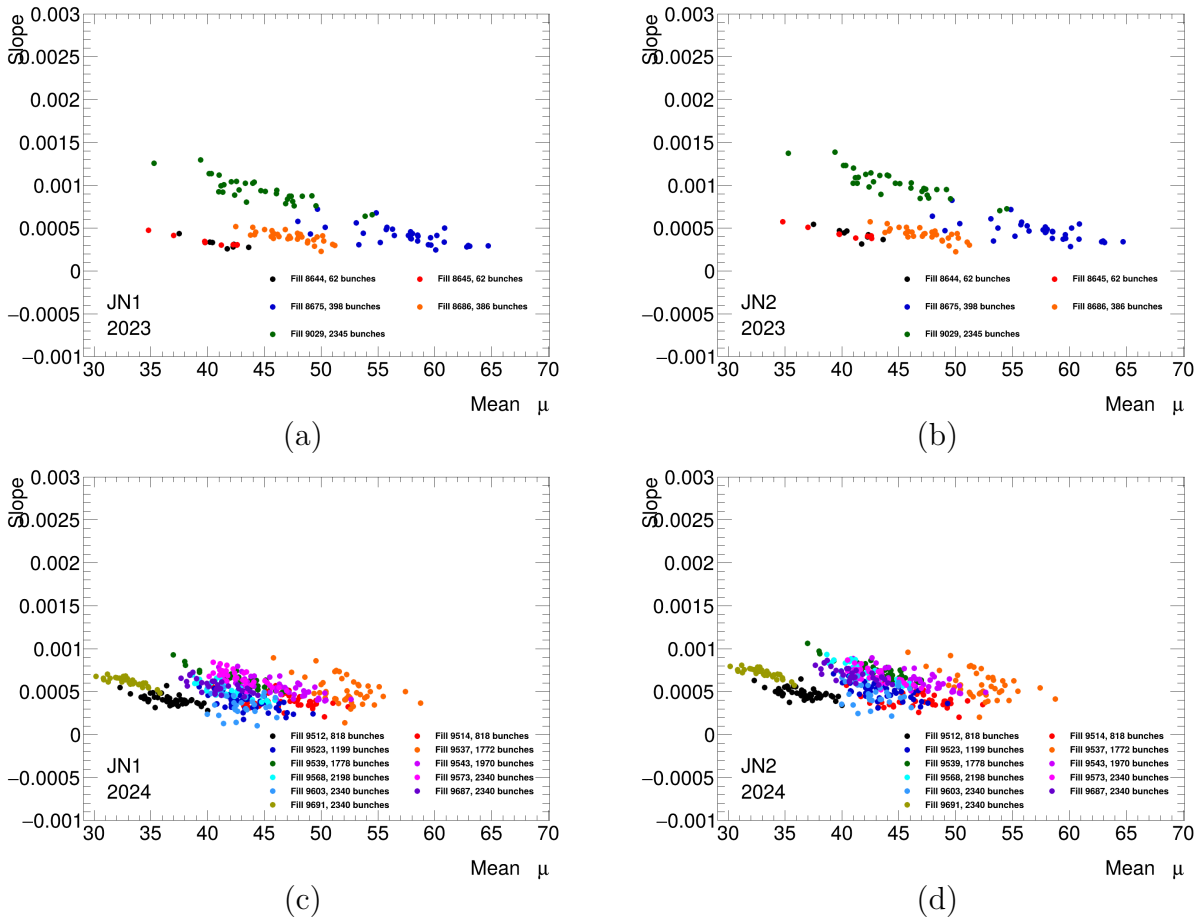

Figure 3.25: Slope extracted by the μ-dependence fits as function of mean μ for JN1 (on the left) and JN2 (on the right) using 2023 (on the top) and 2024 (on the bottom) dataset.

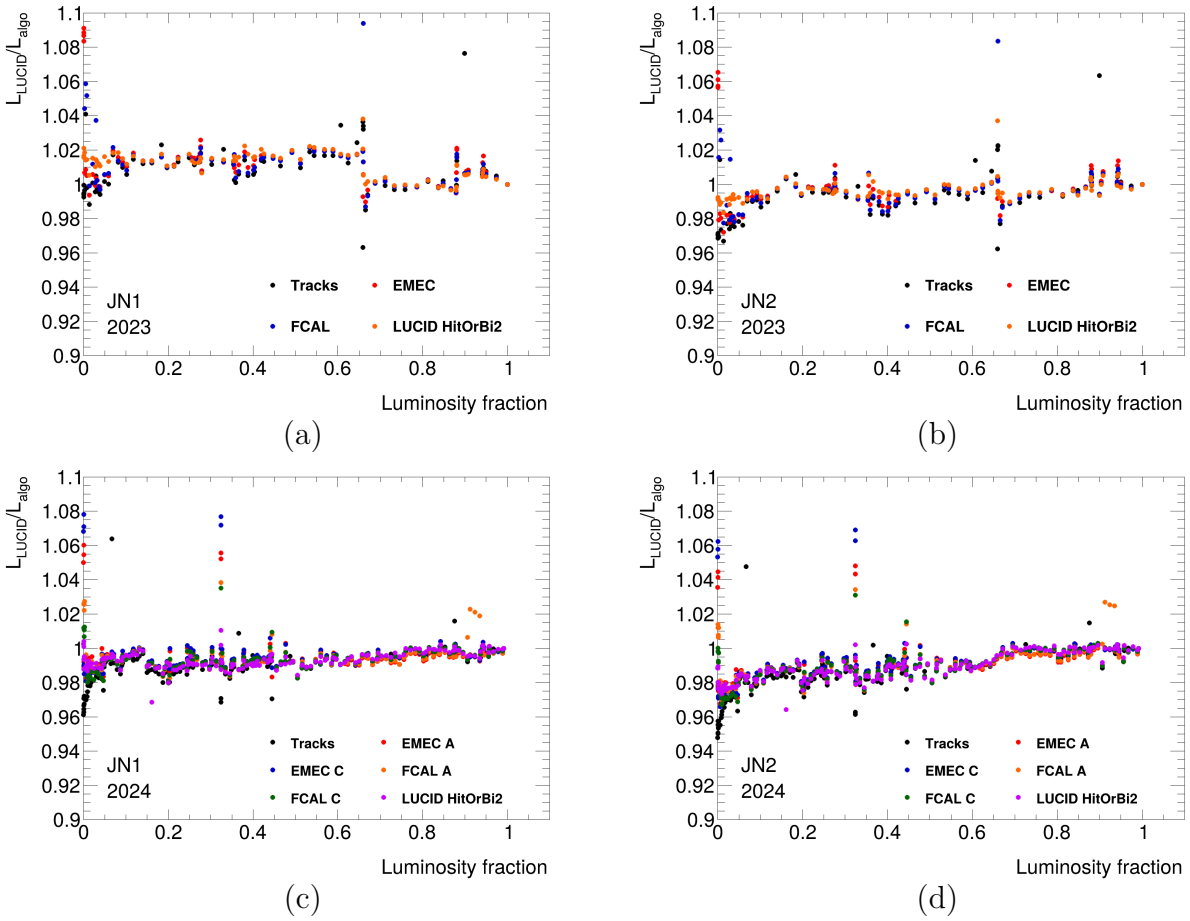

Figure 3.26: Long term stability for JN1 (on the left) and JN2 (on the right) using 2023 (on the left) and 2024 (on the right) dataset.

In Fig. 3.26, the ratio of the luminosity measured with both LUCID-JN over other luminosity algorithms as function of the luminosity fraction is shown for both 2023 and 2024 datasets. JN1 is stable during the whole data taking, although a step is present in 2023 which cause is not understood. JN2 is stable in 2023, while in 2024 a drift of its luminosity measurement by about 2% is observed.

Fig. 3.27 reports the distribution of the ratio of the luminosity measured with LUCID-JN PMTs over other luminosity algorithms while in Tables 3.7 and 3.8 the RMS of each distribution are reported. As expected, JN1 RMS is much lower in 2024 than in 2023 as no step is observed in this year. For both JN PMTs RMS is slightly worse than the LUCID-2 one due to the lower statistical precision of the JN PMTs compared to LUCID2 and JF prototypes due to the reduced acceptance. This reduced acceptance on the other hand ensure that the JN PMTs will not saturate even at the highest μ foreseen

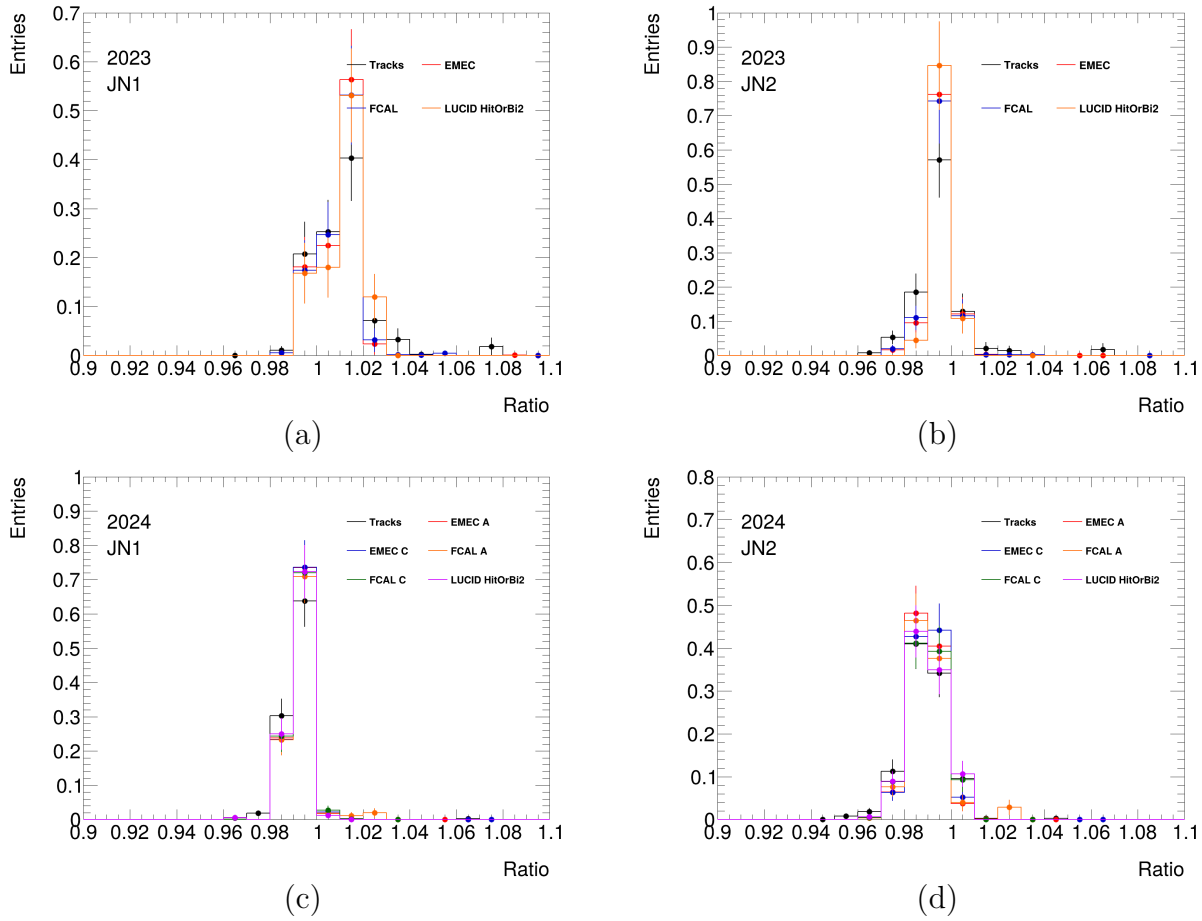

Figure 3.27: Distribution of the ratio of luminosity measured with JN1 (on the left) and JN2 (on the right) over other luminosity algorithms using 2023 (on the left) and 2024 (on the right) datasets.

in the ultimate HL-LHC scenario.

3.4.5 Fiber detector

As already mentioned, the fiber detector is meant to be a complementary technology to the PMTs, featuring positive aspects that must be validated. For this reason, a two-channel prototype of such a detector on side C was installed for LHC Run-3 as visible in Fig 3.28.

	JN1	JN2
Tracks	0.0130785	0.0123638
EMEC	0.00801138	0.00591723
FCAL	0.00840654	0.00602514
HitOrBi2	0.00773893	0.00365332

Table 3.7: RMS of the distributions of the ratio of JN1 and JN2 over other luminosity algorithms using 2023 dataset.

	JN1	JN2
Tracks	0.0069	0.0096
EMEC A	0.0039	0.0067
EMEC C	0.0044	0.0073
FCAL A	0.0064	0.0091
FCAL C	0.0045	0.0078
HitOrBi2	0.0046	0.0077

Table 3.8: RMS of the distributions of the ratio of JN1 and JN2 over other luminosity algorithms using 2024 dataset.

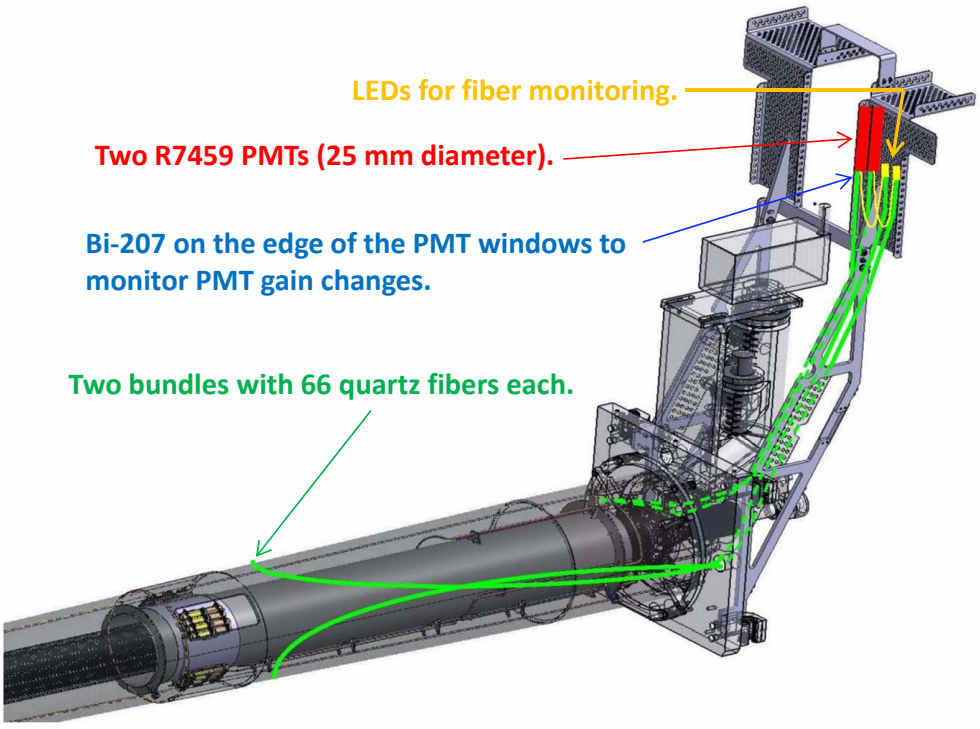

Figure 3.28: The LUCID fiber prototype detector that is installed in Run-3.

The PMTs and fiber ends are located in the same 65 mm gap between the JN plug and the JN monobloc where the old LUCID-2 four fiber PMTs were located. The bundles go through two holes that already exist in the VJ cone backplate as depicted in Fig 3.29. One bundle goes over the top while the other one over the bottom of the VJ cone and they have been placed in copper tubes in order to be mechanically protected. The clearance of these fiber bundles from the forward shielding is not a problem as can be seen in the drawing in Fig. 3.30. The fibers then loop back to the top and connect to the LED system for aging monitoring.

The two new photomultipliers are of the type Hamamatsu R7459 with 28 mm diameter while the quartz fibers are of the type UVNSS 600/624/660. These fibers have a silica glass core with a diameter of 0.6 mm and a polyimide jacket that results in an outer diameter of 0.66 mm. While the old LUCID-2 fiber bundles had 37 fibers, the new one have 66 fibers so that the total core diameter in the bundles is approximately the same. The most important difference between the old and new fibers is the cladding. The old fibers used a silicon cladding while the new fibers have a more radiation hard fluorine-doped silica cladding. This results in a smaller numerical aperture of 0.28 compared to the 0.40 of the old fibers. The change of aperture can result in less light being collected by the new fibers and this aspect of the new detector must be studied. On the other hand the new fibers should be more radiation tolerant.

Photomultiplier gain stability is one of the major problems when PMTs are used to measure luminosity. While the old fiber detector used LEDs monitored by PIN diodes to monitor and control the gain, the new detector is using radioactive ^{207}Bi sources, applied to the edges of the PMT windows as for all other PMTs, and an LED system to monitor fiber degradation. The radiation dose PMTs and LEDs are exposed in LHC Run-3 is estimated to be about 700 Gray based on previous measurements in LHC Run-2 and an assumption of a total integrated luminosity of 400 fb^{-1}.

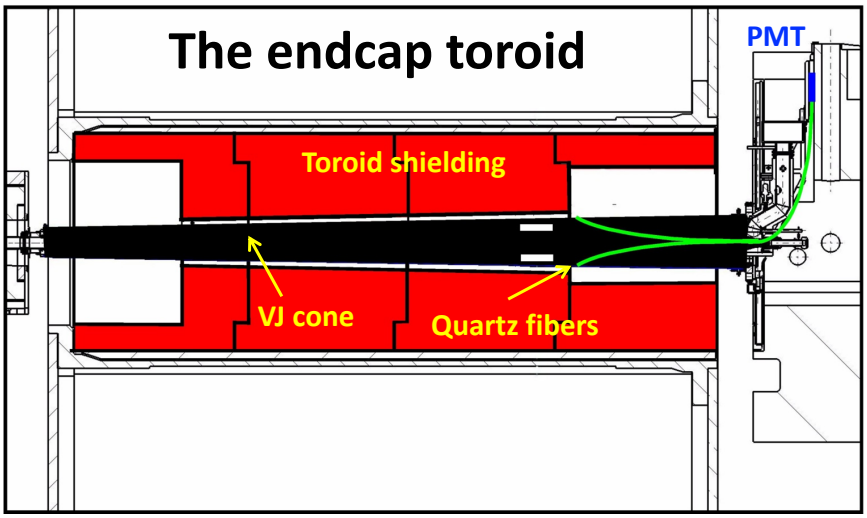

Figure 3.29: The drawing shows the location of the endcap toroid shielding in relation to the beampipe cone and the fiber detector during a standard ATLAS opening when the toroid is moved back over the beampipe until it is almost in contact with the JN shielding.

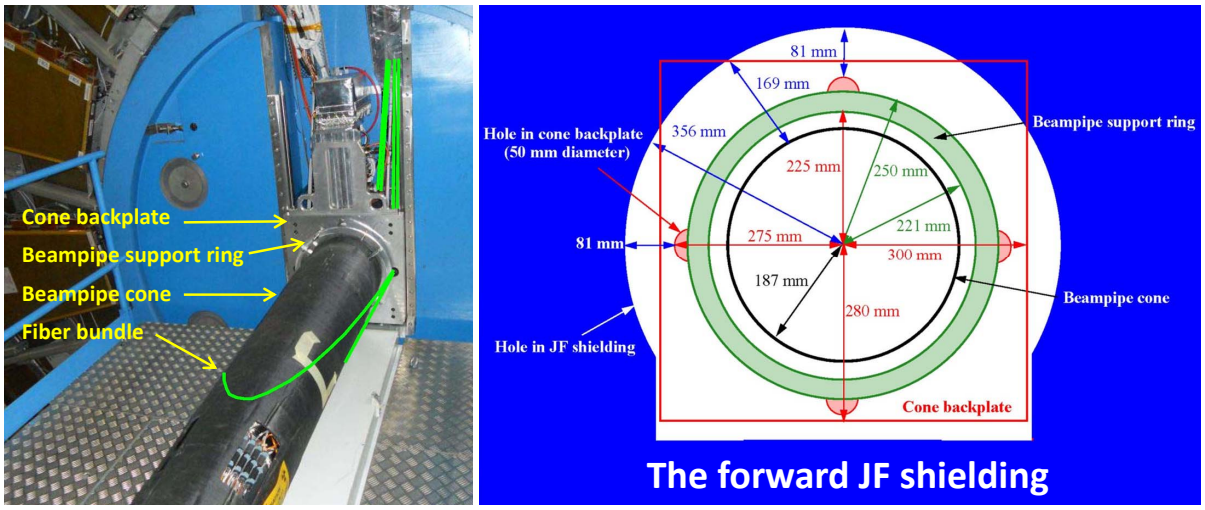

Figure 3.30: Left: The VJ cone, with its backplate and support ring. The new fiber bundles goes through holes in the backplate as indicated in the photo. Right: Dimensions of the backplate with its holes in relation to the forward shielding.

A γ irradiation session was performed to measure radiation damage on the fiber (see Chapter 3.5.1). These measurements demonstrated the tendency of the fiber to lose UV

light transmittance very fast. Therefore a UV filter (Cleartran, 10% transmission limits 0.37 μm – 14 μm)[2] was inserted in one of the two channels to improve long term stability.

3.4.6 Fiber Detector Stability Monitoring

The old fiber detector did not have any monitoring of degradation of the optical fibers due to radiation while the new detector has a set of LEDs to monitor its degradation. LED light is splitted in two parts by a fiber distribution circuit: one goes directly to the PMT (prompt signal) and the other one goes through the fiber and is then measured by the same PMT (delayed signal). The delay between the 2 signals was adjusted by properly choosing the lenght of an LED additional fiber in order to be larger than 50 ns so to be able to distinguish the 2 signals in the readout electronics. In Fig. 3.31 a typical prompt and delayed signal are reported. In the event of significant degradation of fiber transmissivity due to radiation, the delayed signal would be reduced, while the prompt signal would remain unaffected as it does not travel along the fiber. This implies that any reduction in the delayed-to-prompt signal amplitude/charge can be correlated with the degradation of the optical properties of the fiber, allowing an offline correction to be evaluated and applied to the luminosity measured by the fiber. Several LEDs with different wavelengths make it possible to monitor the degradation as a function of the wavelength of the light.

[2]https://lightmachinery.com/media/1543/cleartran.pdf

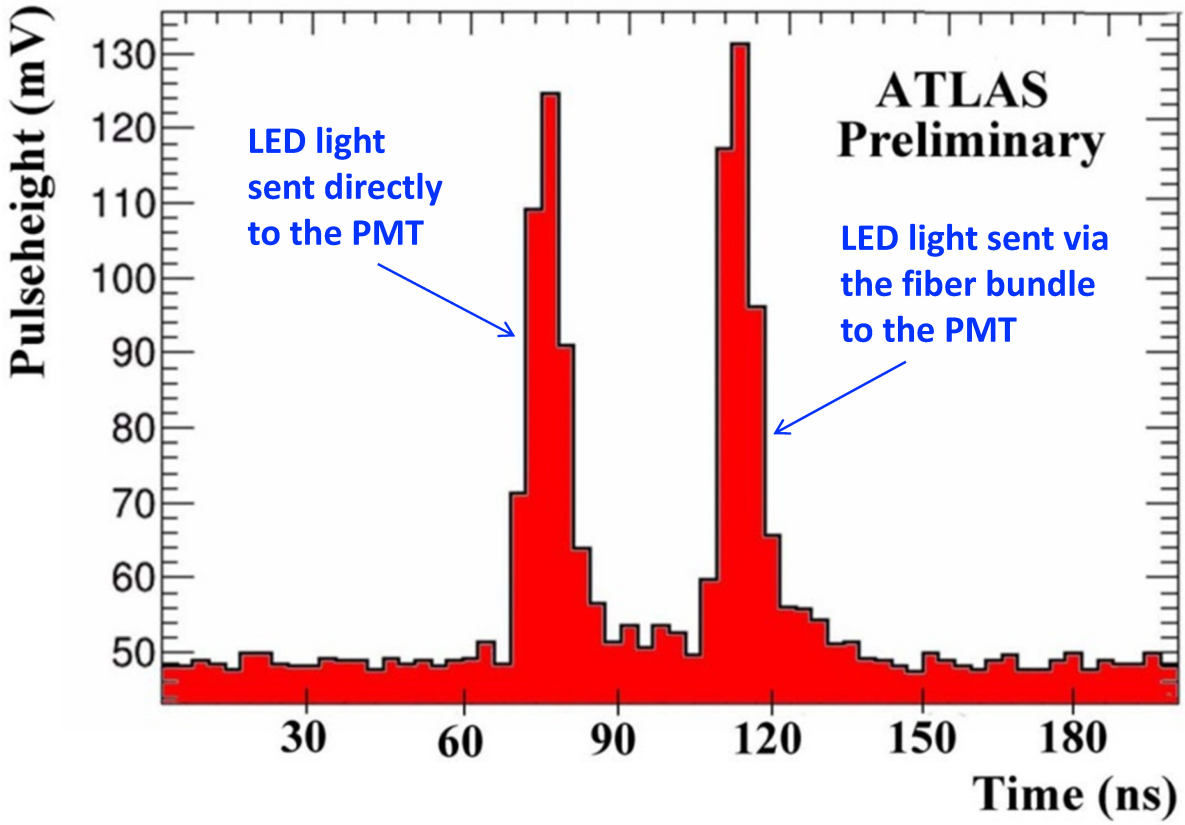

Figure 3.31: Example of LED calibration signal. First peak is generated by light going directly into the PMT, the second one is generated by light going through the fiber.

A detailed study of how to use the information provided by the delayed-to-prompt signal ratio to correct the luminosity measurement is not trivial. Various factors must be considered:

- the opacification is not the same for all wavelengths, with a distribution that varies with time and fiber material used;
- the LED light experiences losses over the whole length of the fiber, while the collision light experiences a smaller loss that depends on the distribution of the light produced and of the opacification.

To face these two complications several measurements and simulations are needed:

- the opacification dependence on wavelength and irradiation was measured in a dedicated gamma irradiation test using 6 different wavelengths in the range between 280 and 630 nm;

- during the calibration runs in ATLAS, 6 different wavelength LEDs are used; the variation in time of the ratio between these two signals provides a measurement of the integrated opacification at a specific wavelength;
- the spatial and wavelength distribution of the light produced in the fiber during collisions was measured in the beam test and simulated. It will be used as an essential input for the calibration algorithm;
- the spatial distribution of the dose absorbed by the fiber needs be simulated as the final input to the calibration program.

The calibration LED light can thus be used to scale the wavelength-dependent opacification distribution measured in lab and irradiation tests. The simulation of the wavelength distribution is then convoluted with the normalized quantum efficiency of the PMT to obtain the input light without opacification. For each fiber segment, the spatial distribution comes into play, determining how much light is absorbed from the production point to the PMT, using the opacification in that specific segment.

3.5 Characterization of the Fiber Prototype

The fiber detector, being the most complex LUCID prototype, requires many ingredients for its characterization:

- Fiber radiation hardness: it's crucial to determine if the fiber will be able to survive to the radiation damage in HL-LHC and it is one of the ingredient required for the offline correction of the luminosity measurement;
- Cherenkov light production inside the fiber: it is a crucial information for the development of the offline correction of luminosity measurement;
- Linearity with respect to μ: the fiber prototype is expected to be perfectly linear with respect to μ;
- Long term stability: the detector should guarantee a stable luminosity measurement during the data taking.

3.5.1 Fiber Radiation Hardness

To study the radiation hardness of the fibers, I performed a γ irradiation session at the Calliope facility at Enea, Rome. The main goal of the irradiation was to measure the fiber degradation during the irradiation session itself. Since the fiber transmittance

degradation is wavelength dependent, 4 different LEDs (MTE280F13-UV [3] λ=280 nm, MTE340H21[4] λ=340 ns, VCC VAOL-5GUV8T4 [5] λ=385 nm, LEDRGBE[6] λ=627.5, 525, 467.5 nm) were turned on alternately (after each cycle all LEDs are turned off to monitor background). Light is injected into a light distribution circuit (Fig. 3.32) that splits the light into two parts: one goes to a Pin-diode (called LED Pin-diode) that should monitor the incoming light and the other part goes into the 2 fibers under testing. The light goes into the fibers, is attenuated by the fibers themself and is sent into a second light distribution circuit that merge the light coming from the 2 fibers. A second Pin-diode (called Fiber Pin-diode) finally collect the outcoming light. The evolution of the ratio

$$\frac{I_{fiber} - I_{fiber}^{BKG}}{I_{LED} - I_{LED}^{BKG}}, \tag{3.1}$$

is a measure of the overall fiber degradation due to radiation damages. $I_{fiber/LED}$ are the currents generated by the Fiber/LED Pin-diode when an LED is on and $I_{fiber/LED}^{BKG}$ are the currents generated by the Fiber/LED Pin-diode when all LEDs are off.

The fibers under testing were 3 quartz fiber model UVNSS600/624/660, 2 of them with a numeric aperture of 0.28 (used in the detector) and the last one with a numeric aperture of 0.22 (old batch) but, due to the lack of readout channels, only the fibers with numeric aperture of 0.28 were monitored. From now on, the 0.28 numeric aperture fiber will be called fiber 0.28 while the other one fiber 0.22. During the irradiation session, fibers absorbed 704.06 kGy in the hottest point. Integrating the dose over the full fiber length, the absorbed dose (2.4 MGy·m) is equivalent to the one absorbed in the first 3 years of HL-LHC data taking (≈2.5 MGy·m). In Fig. 3.33 the ratio of Eq. 3.1 is reported as function of the integrated absorbed dose. Ratio is normalized in order to have the mean of the first 5 points equal to 1 for each wavelength. The missing points at the beginning of the irradiation were caused by a failure of the PC that controlled the acquisition. As expected, a larger transmittance loss was observed in the UV region compared to the visible region. As an immediate consequence of this observation, a UV filter was inserted in one of the fiber prototypes. The effect of the UV on the stability will be discussed in section 3.5.4.

In preparation for a beam test to measure the production of Cherenkov light inside the fiber performed 2 year after the irradiation session, additional measurement of the fiber transmittance loss were performed. The first measurement was done using pulsed LED light. The experimental setup is similar to the one used to monitor fiber degradation inside ATLAS: light emitted by LEDs is divided in two parts by a first light distribution circuit, part of the light goes into the fiber while the other part goes into another light

[3] https://www.alldatasheet.com/datasheet-pdf/pdf/622244/MARKTECH/MTE280F13-UV.html
[4] https://eu.mouser.com/datasheet/2/1094/MTE_H21_Series_27-2941758.pdf
[5] https://eu.mouser.com/datasheet/2/423/VAOL-5GUV8T4-1064834.pdf
[6] https://www.farnell.com/datasheets/3497864.pdf

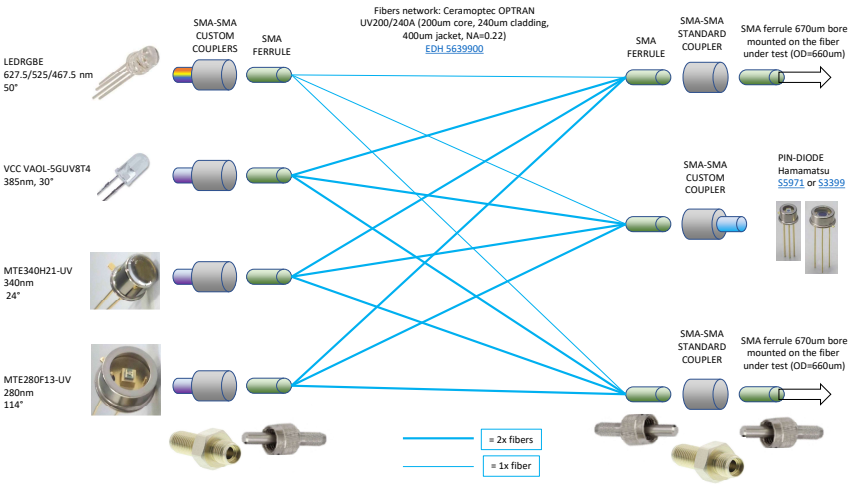

(a) Scheme of the fiber distribution network used to split LED light.

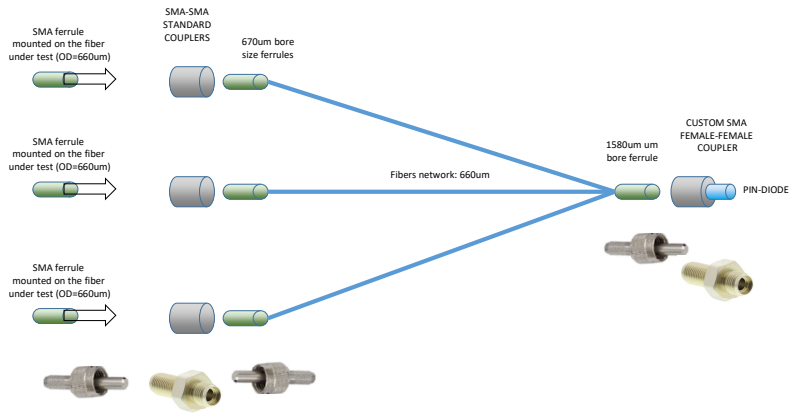

(b) Scheme of the fiber distribution network used to merge LED light.

Figure 3.32: Scheme of the two fiber distribution networks.

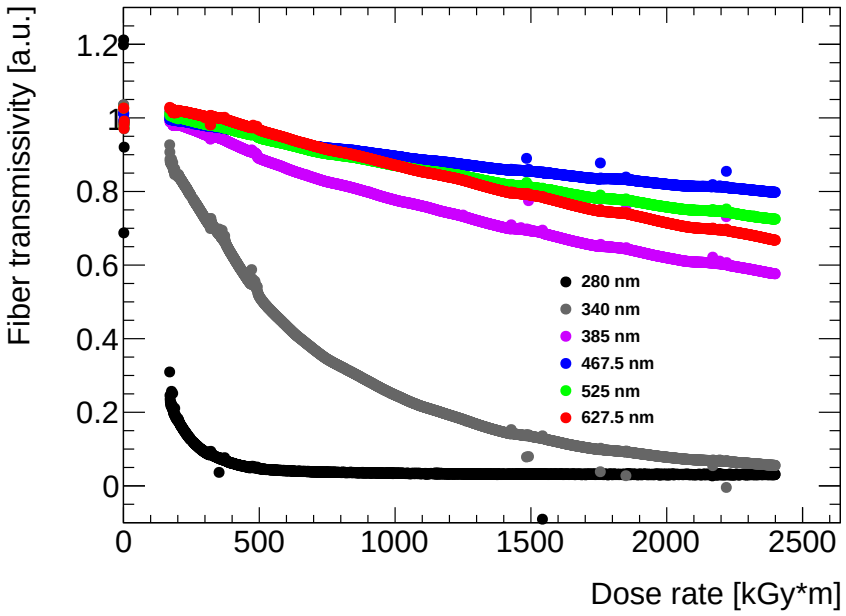

Figure 3.33: fiber transmittance loss as function of absorbed dose for different wavelengths.

distribution circuit. This circuit merges the light coming from the fiber with the one coming from the first light distribution circuit and send it to a PMT for the readout. Using this setup, the PMT reads 2 signals: the prompt and the delayed one. The ratio of the integral of the two signal is a measurement of the fiber transmittance. In order to cancel all of the inefficiencies in light collection of this setup, the ratio obtained for each fiber is compared with the one obtained with a non irradiated UVNSS600/624/660 fiber with numeric aperture of 0.28 (from now on called simply non irradiated fiber). This measurement was repeated twice. To study the transmittance with continuous light, the setup used during the irradiation session was replicated using one fiber at a time. To cancel out the inefficiency in the light collection of this setup, the ratio obtained for each fiber is compared with the one obtained with the non irradiated fiber.

Tab 3.9 reports the measurements obtained with the fiber 0.28 while Tab 3.10 reports the measurement obtained with the fiber 0.22. For both fibers, there are differences between the first and second measurement with continuous light. These are due to small differences in the LED-fiber, fiber-fiber and fiber-Pin-diode couplings. The variation can be considered an estimate of the reproducibility of the experiment. The transmittance measured at the end of the irradiation session and after 2 two years in preparation for the beam test are compatible for the fiber 0.28. This means that the recovery of the radiation damage is negligible. The fiber 0.22 transmittance is comparable with the

non irradiated fiber transmittance. The reason of this behavior is not clear and will be investigated in a second irradiation session.

λ [nm]	Pulsed light	Continuous light 1	Continuous light 2	γ irradiation
280	-96.3%	-96.6%	-97.6%	-97%
340	-86.5%	-92.2%	-92.0%	-95%
385	-19.7%	-21.6%	-18.9%	-43%
467.5	-5.1%	-32.5%	-6.7%	-20%
525	-7.0%	-44.4%	-22.7%	-27%
627.5	-24.9%	-52.7%	-34.8%	-34%

Table 3.9: transmittance loss of the fiber 0.28 compared to the non-irradiated one.

λ [nm]	Pulsed light	Continuous light 1	Continuous light 2
280	-20.0%	+1.4%	-14.0%
340	-0.6%	+5.9%	-4.5%
385	-5.0%	+14.9%	+28.4%
467.5	+5.0%	-6.6%	+19.9%
525	-21.6%	-12.5%	+12.3%
627.5	+1.7 %	-6.7%	+21.7%

Table 3.10: transmittance loss of the fiber 0.22 compared to the non-irradiated one.

3.5.2 Cherenkov Light Produced inside the Fiber

Another crucial ingredient for the offline correction algorithm is the distribution of the light produced in the fiber as function of the incident particle direction. To study this aspect, a beam test with 200 MeV electrons (10 pC) was performed at the Clear Facility at CERN. To study the dependence on the incident beam angle, a support for the fibers specifically designed for this beam test was made. For the readout, 3 PMTs were used. An LED system was used to monitor the fiber degradation during the beam test. LED light was monitored using a 4^{th} PMT. No significant degradation was observed.

Fig. 3.34 is a photo of the setup. On the bottom a rotative engine can perform rotation of 1° and can be remotely controlled via a MATLAB script. The upper part instead is the fiber holder: it is made of a portal made of aluminium bars, 2 holders for the fibers (one on the bottom and one on the top) and 2 holders for PMTs (on the top left and the top right of the portal). The fibers are wrapped and attached to the fiber holder that keeps them fixed in position during the data taking. The bottom holder (Fig.

Figure 3.34: Photo of the experimental setup used during the beam test.

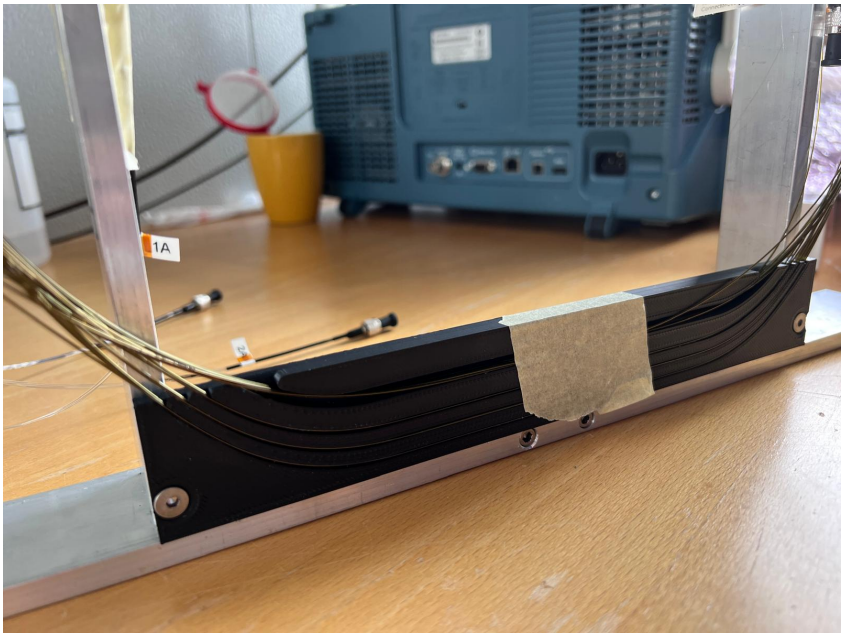

Figure 3.35: Photo of the bottom holder.

3.35) is a piece of 3D-printed plastic with 4 groves. Its goal is to hold and separate the various spires in which the fibers were wrapped in order for the beam to hit just some chosen segment of the fibers. The 4 grooves (from bottom to top) were used:

- 1^{st} groove (named also bot): contains the part of the fiber closer to the PMT;
- 2^{nd} groove (named also mid): contains the middle part of the fiber;
- 3^{rd} groove (named also top): contains the part of the fiber further from the PMT;
- 4^{th} groove: contains all the remaining spires, not hit by the beam.

The fiber is inserted inside the grooves in order to maximise the distance between the part of the fibers hit by the beam. The top holder is a piece of 3D-printed plastic with 2 grooves. The 2 grooves are used to hold the fibers and keep the fiber bending ratio of ≈15 cm. The two PMT holders goal is to keep in position two R760, a R1635 and a R7459.

Since the electron beam may induce radiation damage to fibers, a monitor system is also implemented. 3 LEDs (MTE340H21 λ=340 nm, VAOL-5GUV8T4 λ=385 nm and LEDRGBE λ=467.5 nm) are attached to the light distribution circuit reported in Fig. 3.32a that splits the light. Part of the light is injected into the fiber under test while part of it is sent to a PMT that monitors the stability of the LED. The light injected into the fibers is then measured by the same PMTs that are used to measure the Cherenkov

light produced inside the fiber by the beams. The fiber-PMT coupling has been changed during the beam test so it will be described for every data taking session. The PMTs are read out by digitizers that receives a trigger synchronized with the beam and acquire 400 samples at a frequency of 1 GHz (400 ns). For each angular position of the fiber support, 60 different acquisitions are done. To reduce electronics noise, the sample by sample mean of these 60 shapes is considered.

1^{st} data taking

The first data taking consist in a rotation of the support from -85° to +85° (0° is when the beam and the plane containing the spires are perpendicular) at steps of 1°. The PMT-fiber coupling is as follow:

- R7459 with fiber 0.22;
- R760 with the non irradiated fiber;
- R760 with fiber 0.28;
- R1635: LED monitoring (turned ON even if LEDs are off).

During this data taking, the beam was pointing the mid groove. Fig 3.36 reports the signal amplitude read by the four PMTs as function of time and angle.

The fiber 0.22 shows only 3 signals:

- 70 ns, -40°: signal generated by Cherenkov light when it is pointing towards the PMT (Fig 3.37a), this signal will be called main signal;
- 100 ns, 40°: signal generated by Cherenkov light when it is pointing the opposite direction with respect to the PMT. In this case, Cherenkov light gets reflected by the LED windows and comes back into the fiber, as depicted in fig. 3.37b, and generates a signal delayed with respect to the main signal by ≈40 ns. The time required by the light to go from the point in which is generated to the LED windows and back (8.9 m) in a medium with a refractive index of 1.4 is 41 ns. This confirm the hypothesis of reflection into the LED window.
- ±85°: beam is hitting the fiber support generating scattering.

Fiber 0.28 shows more signals compare to the fiber 0.22:

- 60 ns, 40°: main signal, in this case the angle is positive because the PMT sits on the opposite side of the fiber support with respect to the R7459 PMT.
- 100 ns, -40°: reflected signal, in this case it is not just a dot but it is an arc shape signal. The arc shapes is caused by the internal reflection of light inside the fiber that delays the signal arrival time.

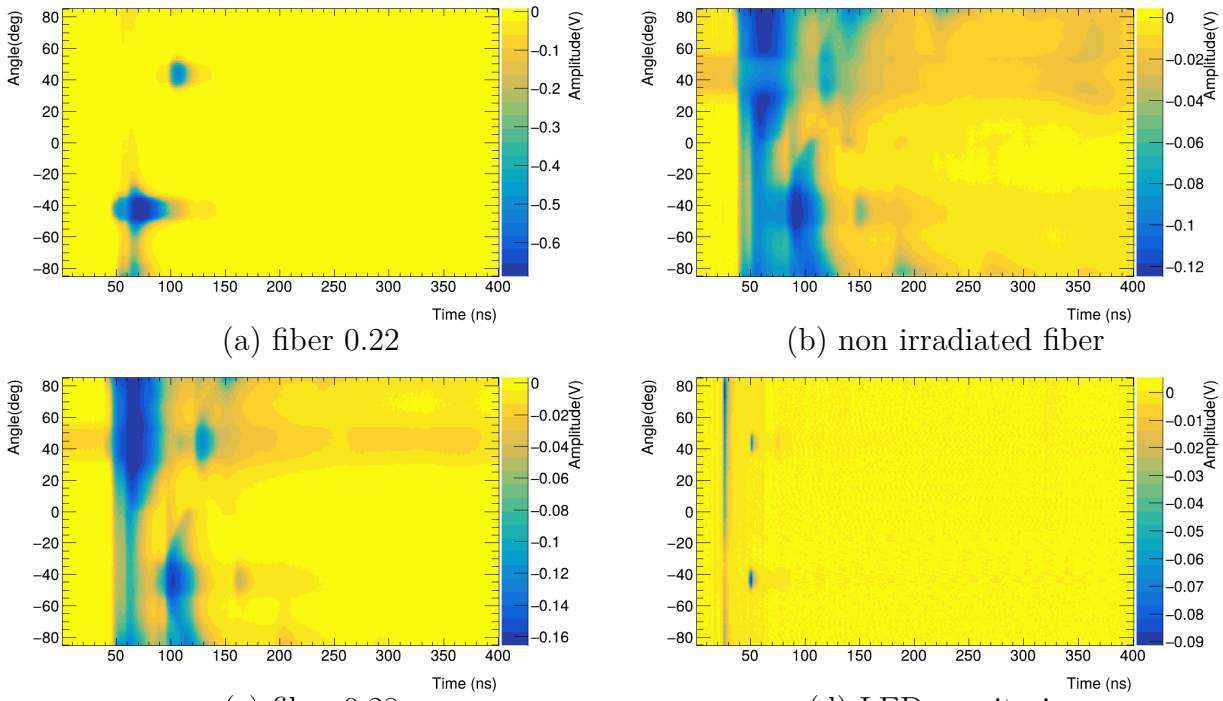

(a) fiber 0.22 (b) non irradiated fiber

(c) fiber 0.28 (d) LED monitoring

Figure 3.36: Signal amplitude as function of time and angle recorded by the four PMTs during the first data taking when the beam hits the mid groove.

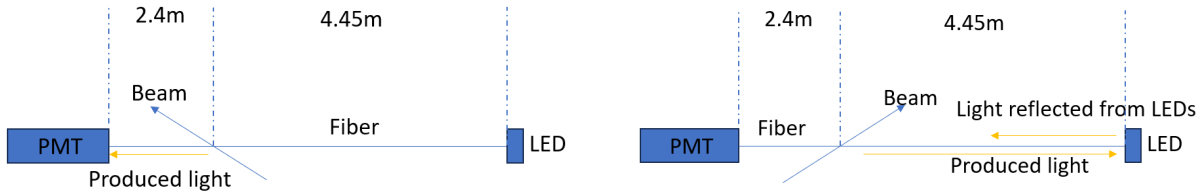

(a) (b)

Figure 3.37: Scheme of the light propagation inside the fiber when the Cherenkov light is pointing towards the PMT (left) and when is pointing to the opposite direction (right).

- 125 ns, 40°: main signal light gets reflected back into the fiber by the PMT window, gets reflected again by the LED window and then is read by the PMT.
- 60 ns band: constant signal for every angle, probably generated by scattered particle hitting the fiber.
- 40°-60°: very long constant signal started before the trigger and lasting for ≈300 ns. This signal will be discussed later.
- ±85°: beam is hitting the fiber support generating scattering.

The signal generated inside the non irradiated is similar to the 0.28 one with just a couple of differences:

- generally more sensitive to backgrounds
- at 60 ns; 40°: in this region with fiber 0.28 the signal amplitude reaches its maximum while with the non irradiated fiber there is a valley

The PMT used to monitor LEDs sees three different signals:

- 30 ns band: this signal is probably generated by particles hitting directly the PMT window or the fiber that is used to split the light produced by the LEDs
- 50 ns, ±40 °: when the light is produced in the opposite direction with respect to the PMT get reflected by the LEDs window and a small amount of it is read by the LED monitoring PMT.

These measurement were repeated using the exact same setup but pointing the beam into the bot groove (Fig. 3.38). The general structure of the signal is almost the same as the previous one with some changes in the timing due to different position in which the beam hits the fiber. The main difference between these 2 runs is that there is a valley in at 50 ns +40 °like the non irradiated fiber. The cause of this valley is the long signal that is registered in the same region both with the irradiated and non-irradiated fiber. Long signal like this may induce a temporary gain loss that reduce the signal amplitude causing the valley.

In order to understand better the source of this long signal, the beam was deviated and dumped before hitting the fiber. As reported in Fig 3.39, all 3 PMTs connected to the fibers see a signal. The amplitude of this signal is much smaller in fiber 0.22 compared to the other two. This explain why fiber 0.22 is not affected by this problem. The cause of this signal is the so called beam dark current [15], i.e. a cloud of electrons that stems from surface electrons emitted in RF cavities and accelerated in their electric field. In order to try to mitigate the effects of beam dark current the PMT-fiber coupling was changed.

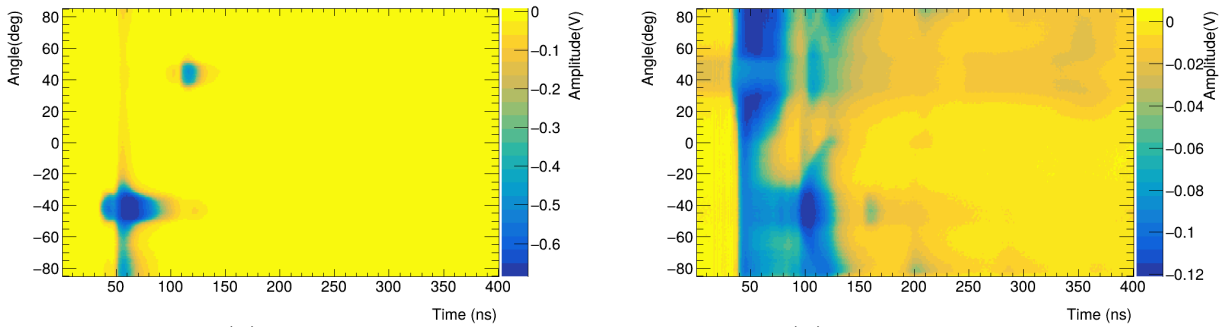

(a) fiber 0.22

(b) non irradiated fiber

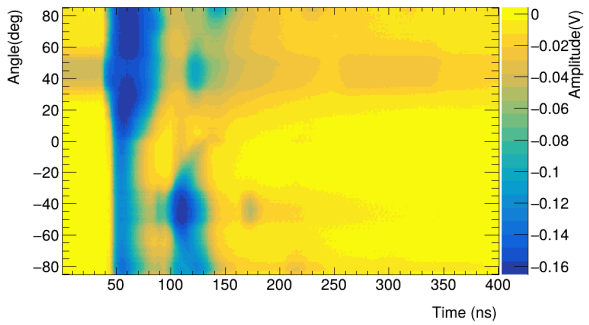

(c) fiber 0.28

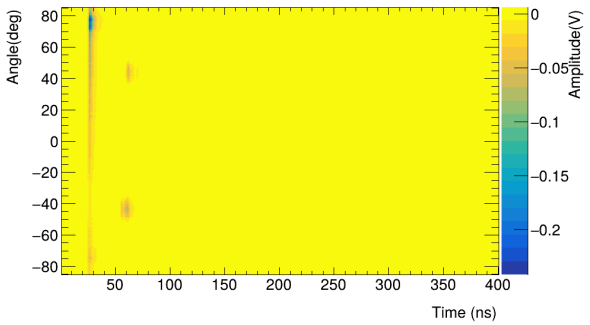

(d) LED monitoring

Figure 3.38: Signal amplitude as function of time and angle recorded by the four PMTs during the first data taking when the beam hits the bot groove.

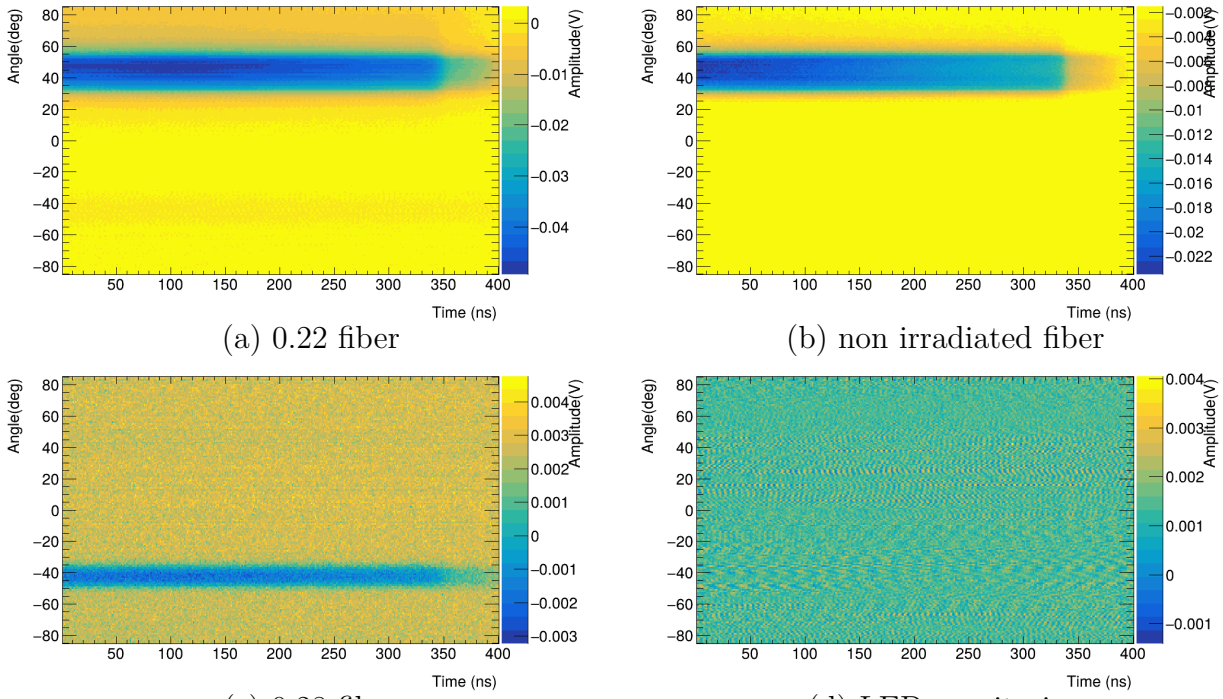

(a) 0.22 fiber

(b) non irradiated fiber

(c) 0.28 fiber

(d) LED monitoring

Figure 3.39: Signal amplitude as function of time and angle recorded by the four PMTs during the first data taking when the beam is deviated before hitting the fiber.

2^{nd} data taking

In this second session of data taking, the PMT-fiber coupling is:

- R7459 with fiber 0.22;
- R760 LED monitoring (turned ON even if LEDs are off);
- R760 with fiber 0.28;
- R1635 with the non irradiated fiber.

Figs. 3.40, 3.41 and 3.42 report the signals read by the PMT with this second setup when the beam hits the top, mid and bot groove respectively. There is no relevant difference between these three runs. Instead, the non irradiated fiber looks much similar to fiber 0.22 rather than fiber 0.28 as it was with the previous setup. Due to how the PMT holders were made, the distance between the PMTs and the end of the fiber may vary from ≈1 mm when using R760 to 3-4 mm when using R1635 and R7459. This difference may cause the loss of the light that is not collinear to the fiber. This hypothesis was later tested and confirmed in laboratory. It also suggest that the signal seen in fiber 0.22 is biased by this effect. To test this hypothesis, the PMT-fiber coupling was changed again.

3^{rd} data taking

In this third session of data taking, the PMT-fiber coupling is:

- R7459 with fiber 0.28;
- R760 non irradiated fiber;
- R760 with fiber 0.22;
- R1635 LED monitoring but OFF.

Fig. 3.43 report the signals read by the PMT with this third setup when the beam hits mid groove. Due to infrastructure problems, the beam quality was not the same as before. By reducing the distance between the fiber and PMT window, the same structure seen in the other fibers appeared also in the 0.28 numerical aperture fiber.

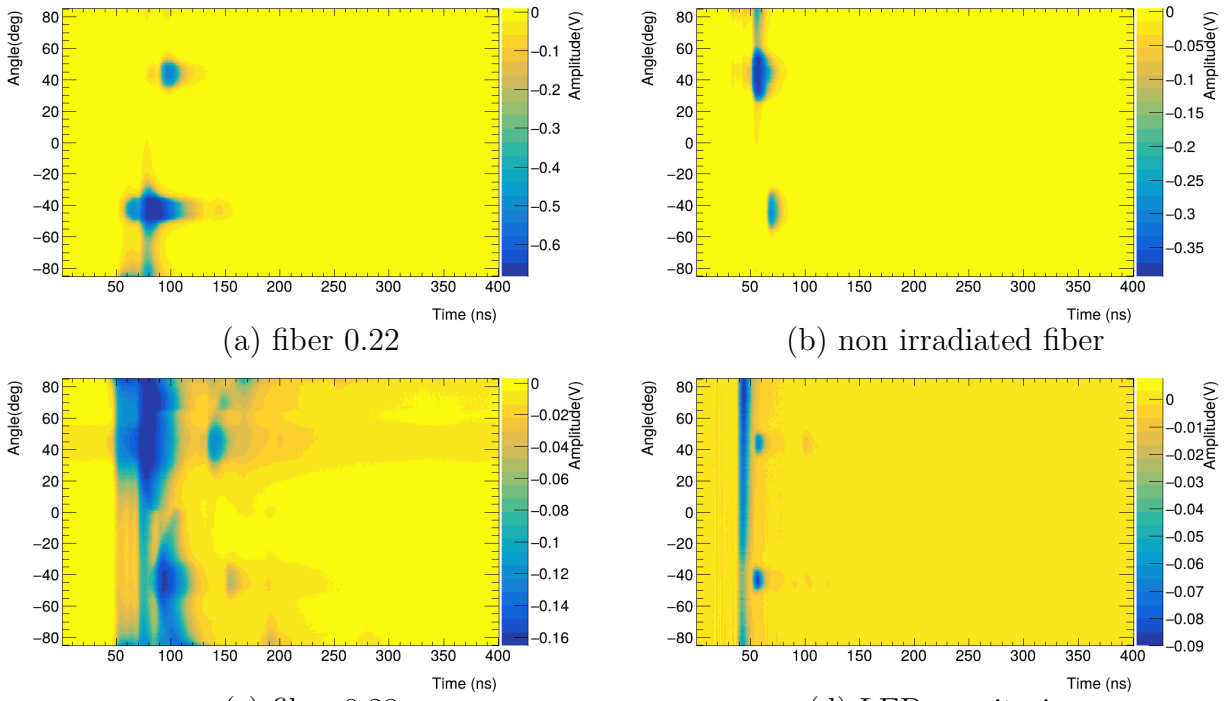

(a) fiber 0.22

(b) non irradiated fiber

(c) fiber 0.28

(d) LED monitoring

Figure 3.40: Signal amplitude as function of time and angle recorded by the four PMTs during the second data taking when the beam is hitting the top groove.

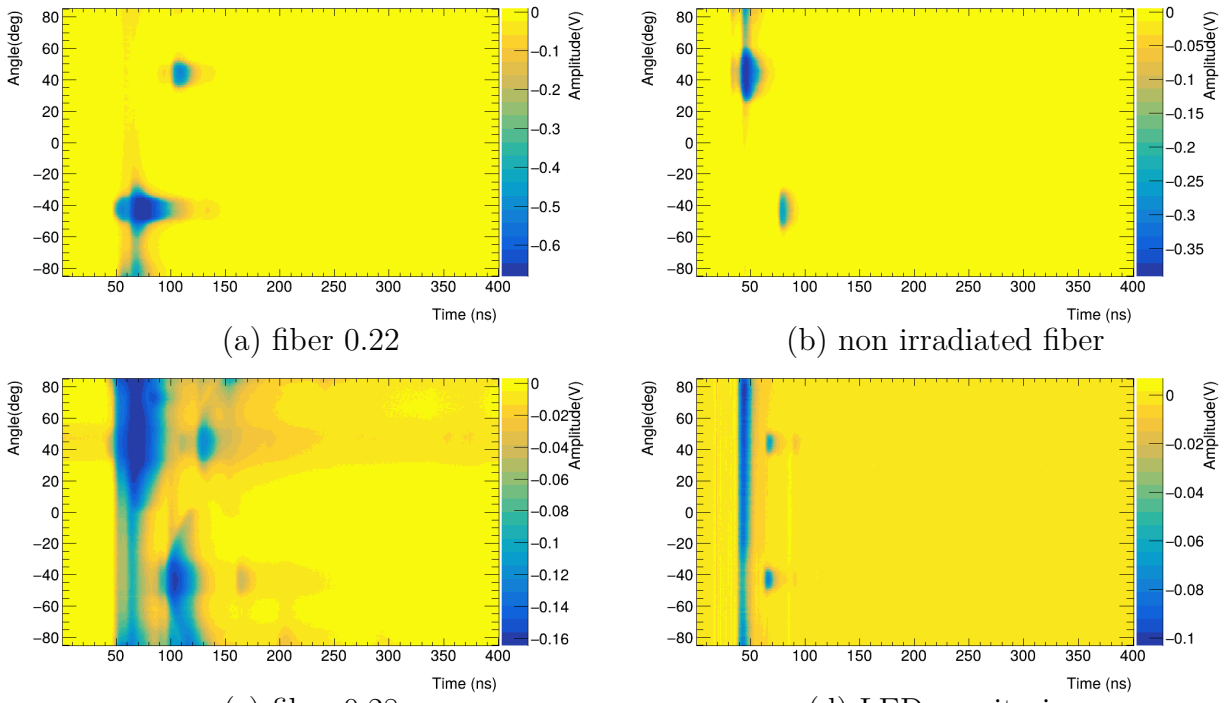

(a) fiber 0.22

(b) non irradiated fiber

(c) fiber 0.28

(d) LED monitoring

Figure 3.41: Signal amplitude as function of time and angle recorded by the four PMTs during the second data taking when the beam is hitting the mid groove.

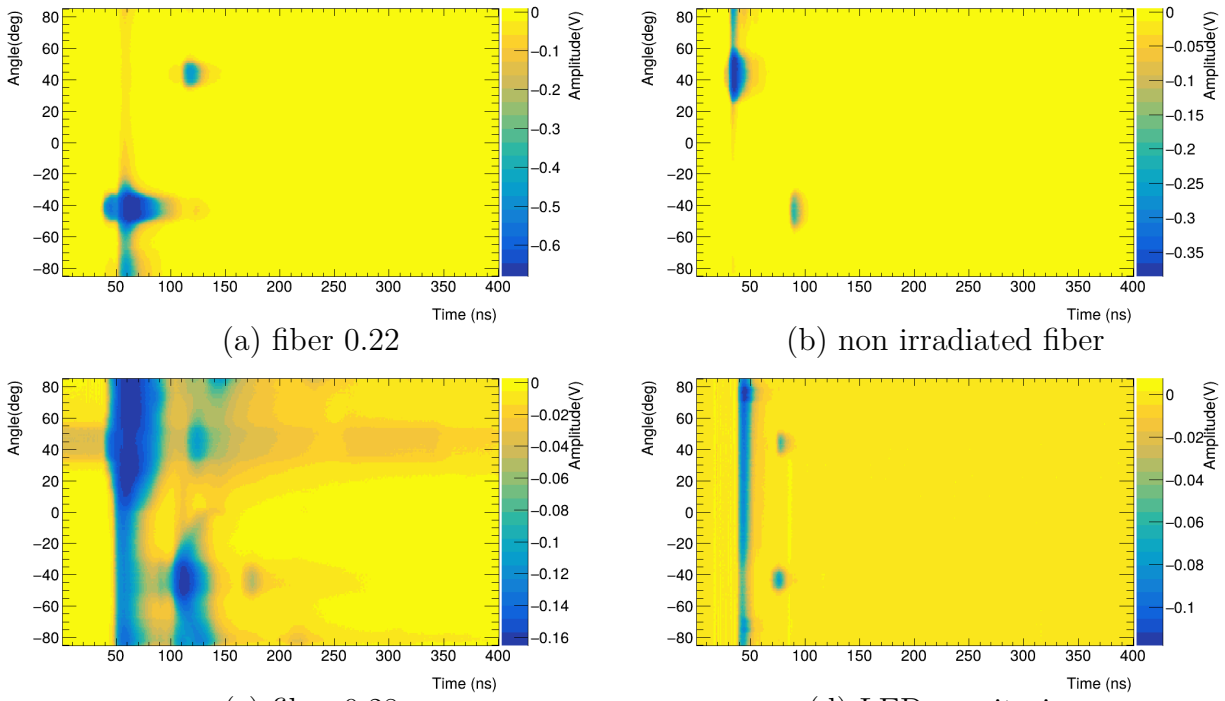

(a) fiber 0.22

(b) non irradiated fiber

(c) fiber 0.28

(d) LED monitoring

Figure 3.42: Signal amplitude as function of time and angle recorded by the four PMTs during the second data taking when the beam is hitting the bot groove.

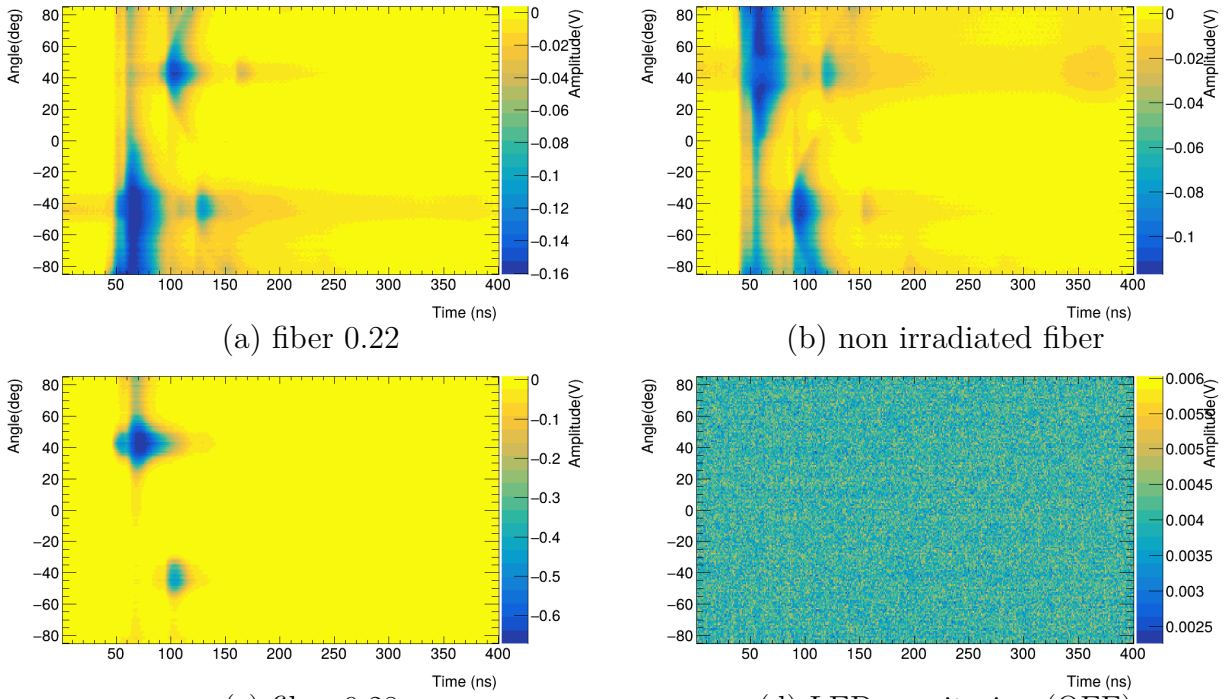

(a) fiber 0.22

(b) non irradiated fiber

(c) fiber 0.28

(d) LED monitoring (OFF)

Figure 3.43: Signal amplitude as function of time and angle recorded by the four PMTs during the third data taking when the beam is hitting the mid groove.

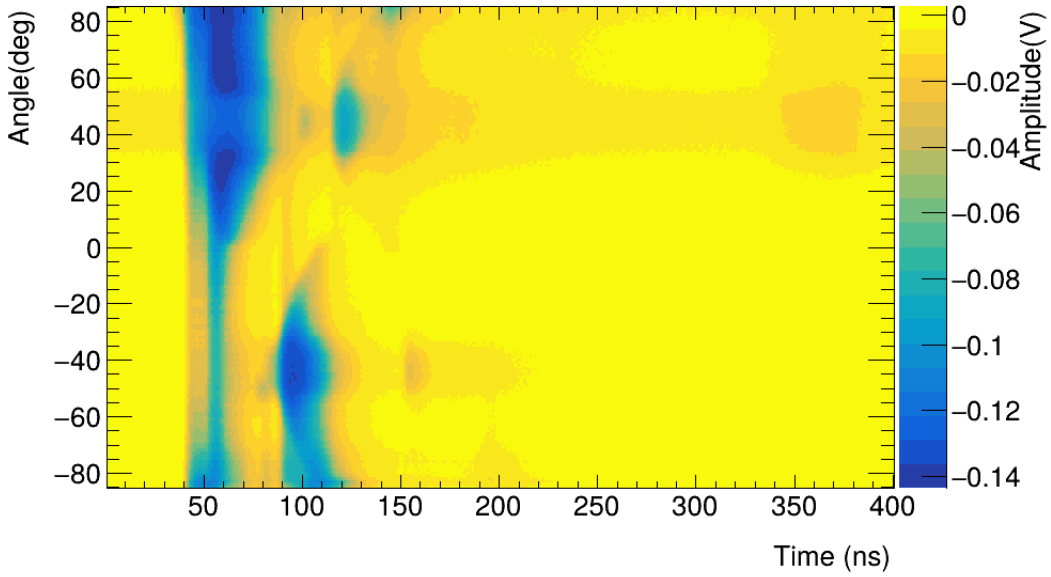

Figure 3.44: Signal amplitude as function of time and angle recorded by a R760 PMTs during the fourth data taking when the beam is hitting the mid groove.

4^{th} data taking

In this last data taking, only one R760 was turned on and it was coupled with the non irradiated fiber. All others PMT were off because their power lines were used to power the boosters of this PMT to check if the valley seen when the signal should have a maximum is corrected or at least, attenuated. As reported in Fig. 3.44, boosters did not had any impact.

Due to the many unexpected problems encountered in this beam test (beam dark current effect, PMT-fiber coupling), a new experimental setup is currently under prepration to repeat the beam test without these issues.

Conclusions

In the beam test, the production and propagation of light within the fiber was studied. As expected, the highest signal is generated when the angle between the fiber and the incident particle is 45°. By combining this information with the particle flow in ATLAS it is possible to optimize the positioning of the fibers themselves. Internal reflections can create reflected and delayed signal, which could become an issue in ATLAS if signals are not recorded in the correct BCID. However, this behavior has not yet been observed in ATLAS. A strong dependence of the signal distribution on the PMT-fiber coupling was observed. With thorough study and characterization, this dependence could be used to

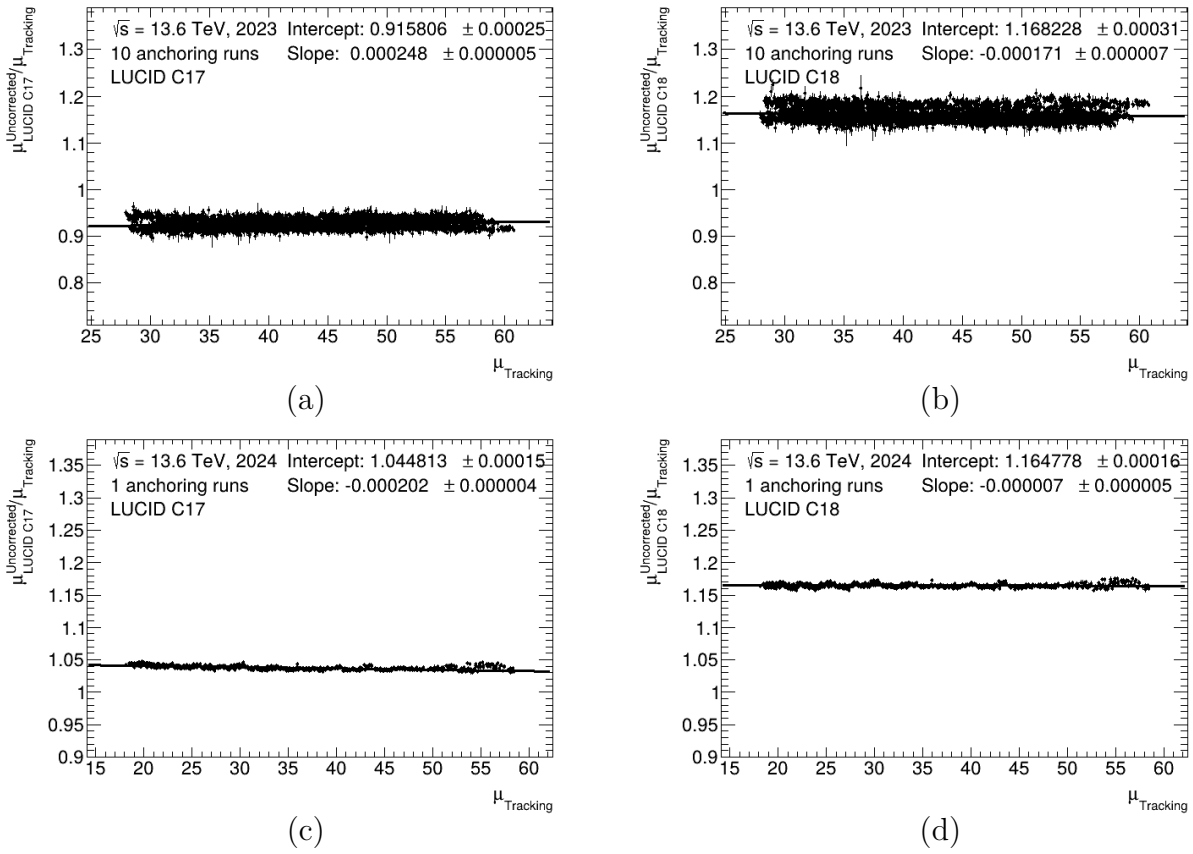

Figure 3.45: μ-dependence fit for Fiber prototype without UV filter (on the left) and with UV filter (on the right) with 2023 (on the top) and 2024 (on the bottom) datasets.

reduce the spread of signal arrival times, thereby preventing BCID contamination. Long signals may induce a temporary gain loss in R760 PMTs; however, such an effect has not been observed in LUCID, as only pulsed signals are measured. Another beam test with an improved setup is planned. An algorithm to correct offline luminosity measurements using these data is currently under development.

3.5.3 Linearity with respect to μ

As already described in Chapter 2.12, the first step in a detector characterization is to study the linearity.

Fig. 3.45 reports the μ-dependence fit. Both prototype in both years are characterized by a slope that is compatible with 0 as expected, since fiber can only use charge algorithm (i.e. particle counting which is by definition proportional to the luminosity). This means that the fiber detector exploiting charge counting algorithm provides a perfectly linear

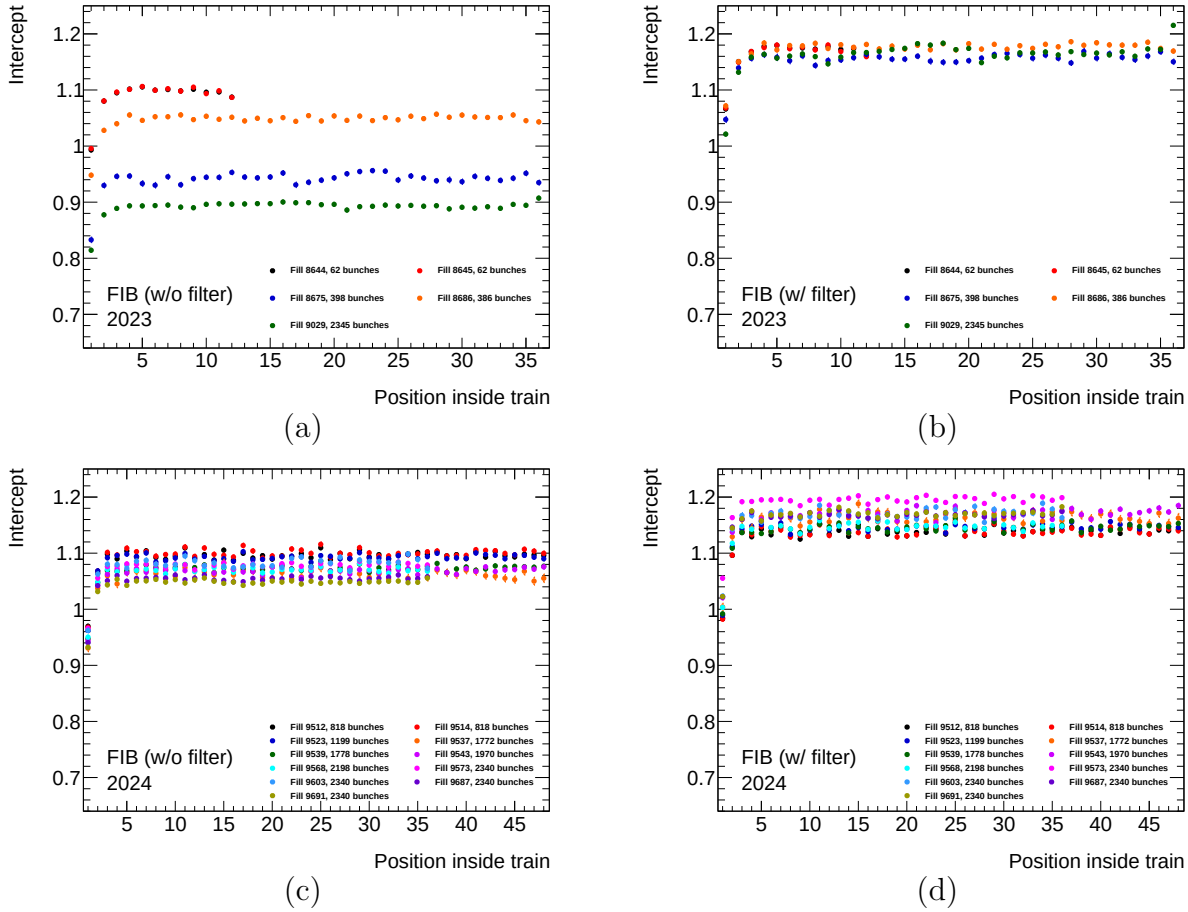

Figure 3.46: Intercept of the μ-dependence as function of position inside train for Fiber prototype without UV filter (on the left) and with UV filter (on the right) with 2023 (on the top) and 2024 (on the bottom) datasets.

measurement of the luminosity, which is not the case for the LUCID-2 and JF prototypes, and is even better than the JN prototypes in this respect. None of these prototype intercepts is compatible with 1. The reason of this incompatibility will be discussed better below when looking at the μ-dependence fit inside the trains.

The intercept as function of the position inside train are reported in fig 3.46. In both prototypes, there is a jump in the value of the intercept between the first and the second BCID in the trains. The reason is the leak of the signal into the BCID following the colliding BCID as shown in Fig. 3.47. Most of the charge is produced in the BCID in which the collision happens (in this case 865) but a non-negligible charge is measured also in the next BCID in which no collision happened. Even though it is not a problem when considering isolated bunches, it will be when considering trains since, from the 2^{nd}

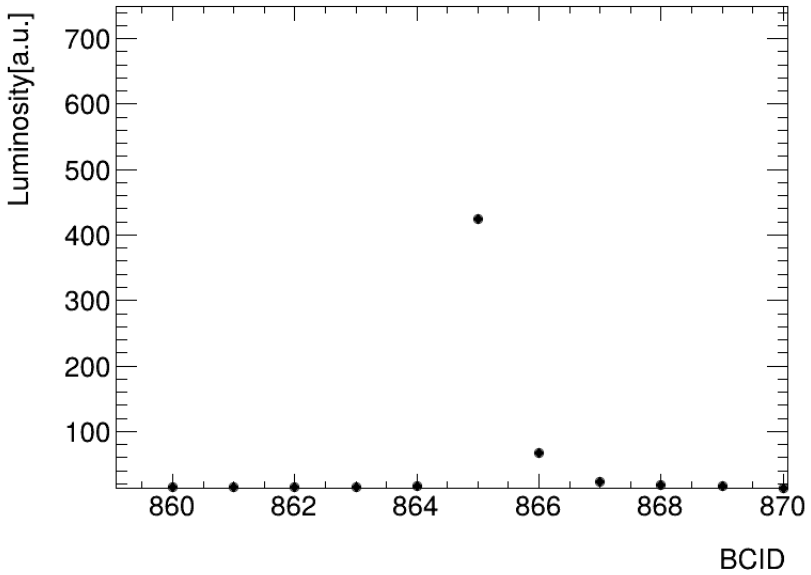

Figure 3.47: Example of a charge measurement by the fiber detector with the UV filter as function of BCID close to an isolated colliding bunch (865).

BCID, the luminosity is overestimated due to the additional charge from the previous BCID. Looking at the 2024 data collected by the prototypes, it seems that the difference between the intercept measured in the first bunch in a train and the one measured in the second is reasonably constant. This suggests that the charge leakage is constant, making it possible to characterize the charge leakage in runs with isolated bunches and transporting it in runs without isolated bunches. A correction for the charge leakage will be discussed later. The prototype with the UV filter is characterized by smaller fill-to-fill variations compared to the one with in 2023 while in 2024 they are almost equivalent.

In Fig 3.48 the slope as function of the position inside the trains is reported. In 2023 (top plots), the prototype without the UV filter is characterized by a wider spread both within a run and between runs compared to the prototype with UV filter. In 2024 (bottom plots), instead, both prototypes are characterized by an almost perfect linearity with respect to μ, with negligible run to run fluctuations. The reason of the improvement in the performance of the prototype without filter is not yet clear. The linearity of the two fiber detector is only due to the use of charge algorithm and the filter does not have any role as expected.

All of the fills used in this study, except the ones with 2340 colliding bunches, have at least 1 isolated colliding bunch, therefore a simple correction for charge leakage can be applied. For each lumiblock, the fraction f of charge leaked in the following BCID

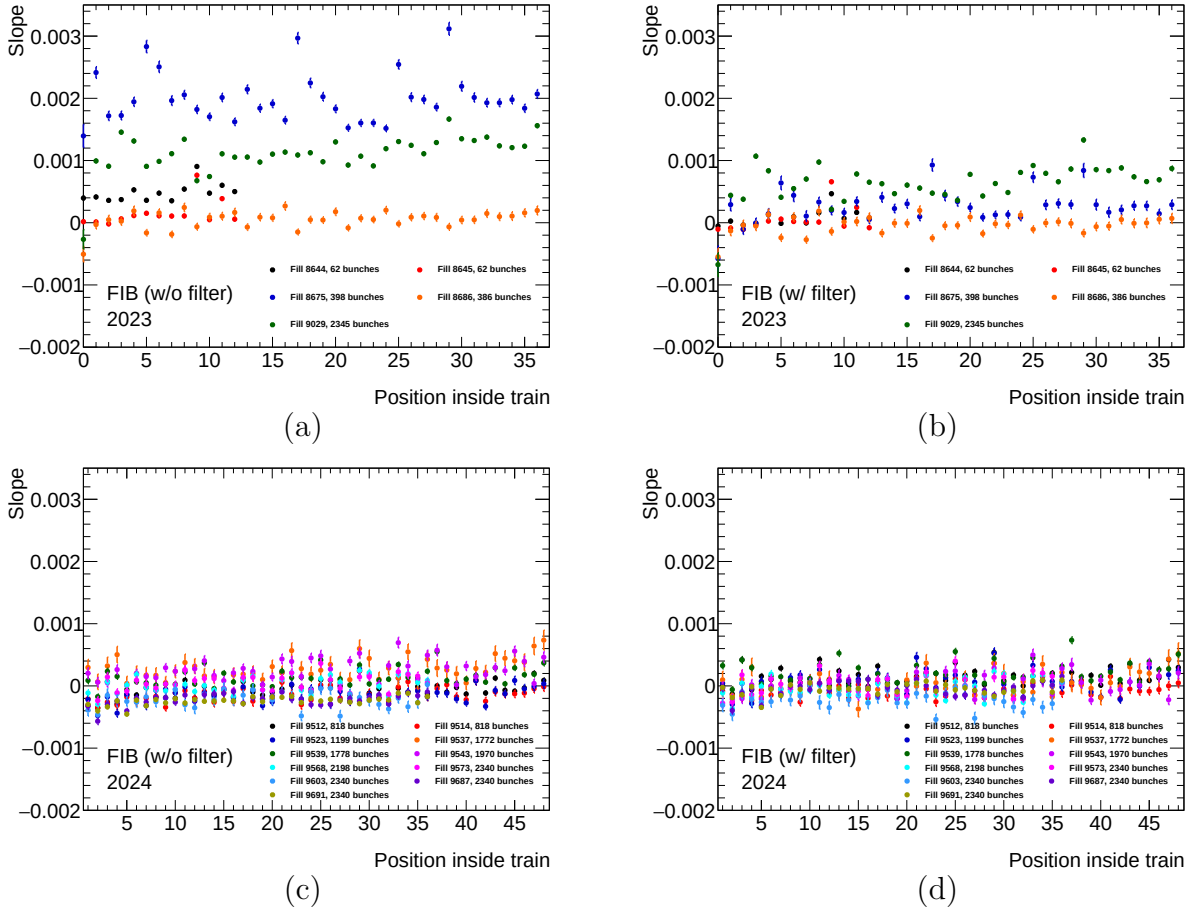

Figure 3.48: Slope of the μ-dependence as function of position inside train for Fiber prototype without UV filter (on the left) and with UV filter (on the right) with 2023 (on the top) and 2024 (on the bottom) datasets.

can be estimated as:

$$f = \frac{Q_{BCID+1}}{Q_{BCID}} \tag{3.2}$$

where Q_{BCID} is the charge measured in the isolated BCID and Q_{BCID+1} is the charge measured in the BCID after the isolated one. To correct for the charge leakage inside trains, the following algorithm is used:

- 1^{st} bunch: no correction is needed;
- 2^{nd} bunch: $Q_2^{corr} = Q_2^{uncorr} - f \cdot Q_1$, where Q_2^{corr} is the corrected charge measured in the second BCID of a train, Q_2^{uncorr} is the uncorrected one and Q_1 is the charge in the first one;
- 3^{rd} bunch: $Q_3^{corr} = Q_3^{uncorr} - f \cdot Q_2^{corr}$ and so on till the last BCID inside the train.

The intercept and slope as a function of position inside the train corrected for the charge leakage are reported in Fig 3.49 and 3.50 (fills with 2340 bunches are not reported since they don't have any isolated bunch). The intercept after the correction does not show anymore the step between the 1^{st} and 2^{nd} BCID inside the train but the same fill to fill deviations are observed. This correction has also a small impact on the slope slightly reducing their fluctuation. In 2024 an exceptional stability of both intercept and slope is observed for both prototypes, which is an indication that the fiber prototype (in particular the one with the UV filter) is perfectly linear and independent of the bunch structure of the fill, although it is necessary to apply the offline correction for the charge leak.

Applying this correction to runs without isolated colliding bunches is more complicated because there is no direct way of calculating the amount of charge leakage. To apply this correction, the evolution within a fill and between different fills of the fraction f must be characterized. A detail analysis in this respect is still ongoing.

3.5.4 Long Term Stability

The last topic in the fiber prototype is the long term stability. Fig. 3.51 reports the ratio of the luminosity measured with both fiber prototypes over other luminosity algorithm as function of the luminosity fraction for both 2023 and 2024 datasets. In both years, the prototype without the filter is characterized by a drift that leads to the underestimation the luminosity. The cause is the fiber degradation due to radiation that leads to transmissivity loss. An offline correction using both the γ irradiation session and the data collected during the beam test is still under development. The fiber with the UV filter does not exhibits any drift. Instead, in 2023, it was characterized by a sawtooth shape (see Fig. 3.51b), caused by an insufficient precision in the PMT HV adjustment during calibration. The calibration procedure was revised before the start of the 2024 taking

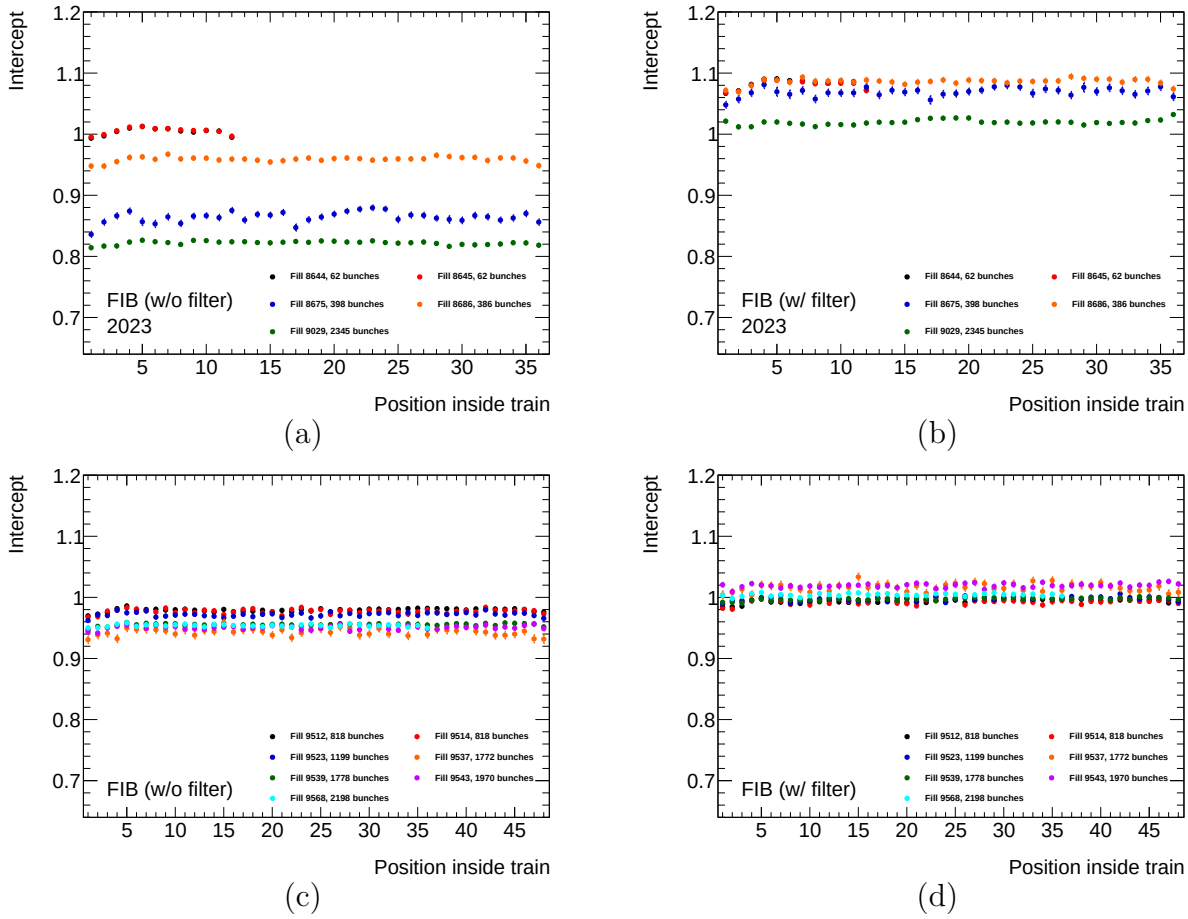

Figure 3.49: Intercept as function of position inside train for Fiber prototype without UV filter (on the left) and with UV filter (on the right) after applying the correction for charge leakage with 2023 (on the top) and 2024 (on the bottom) datasets.

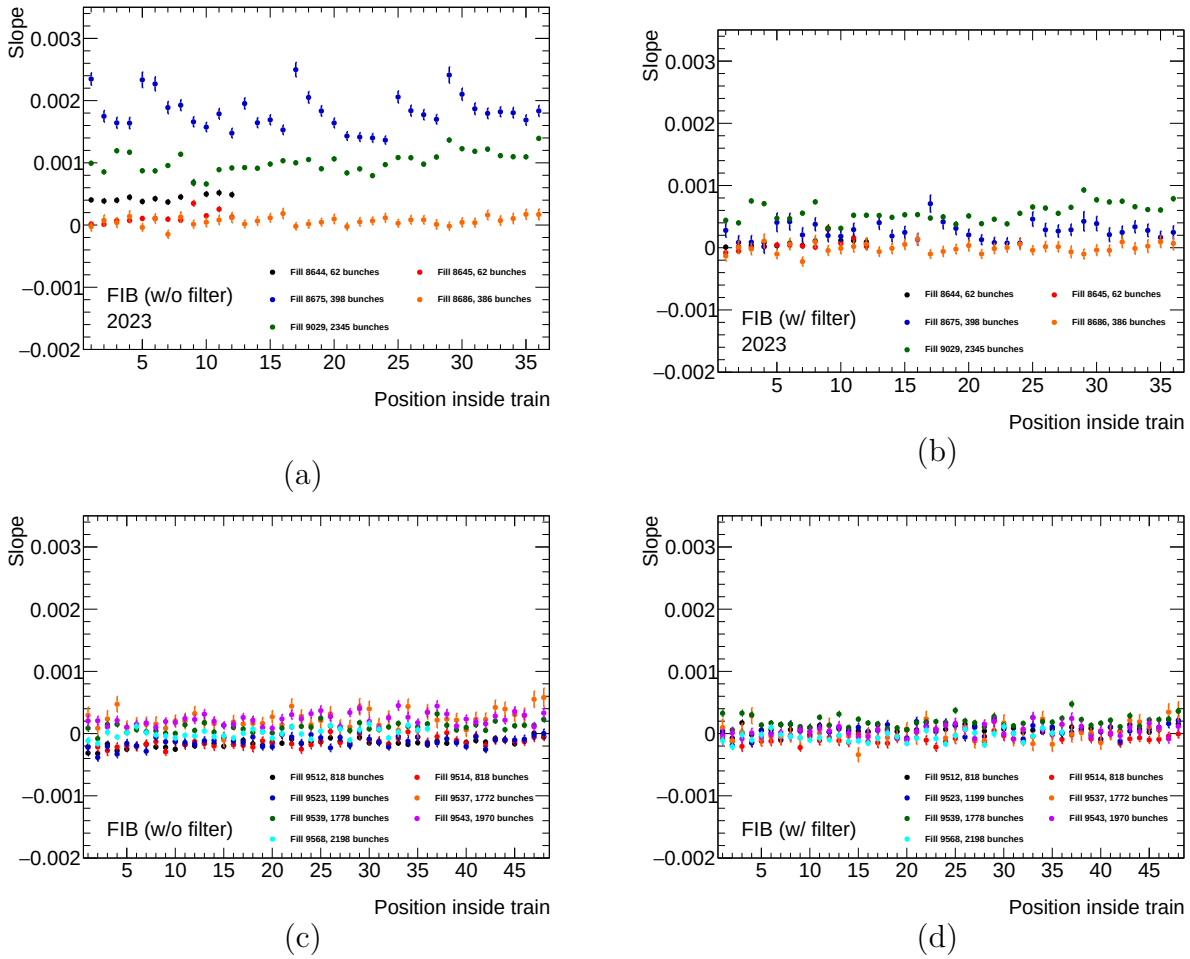

Figure 3.50: slope as function of position inside train for Fiber prototype without UV filter (on the left) and with UV filter (on the right) after applying the correction for charge leakage with 2023 (on the top) and 2024 (on the bottom) datasets.

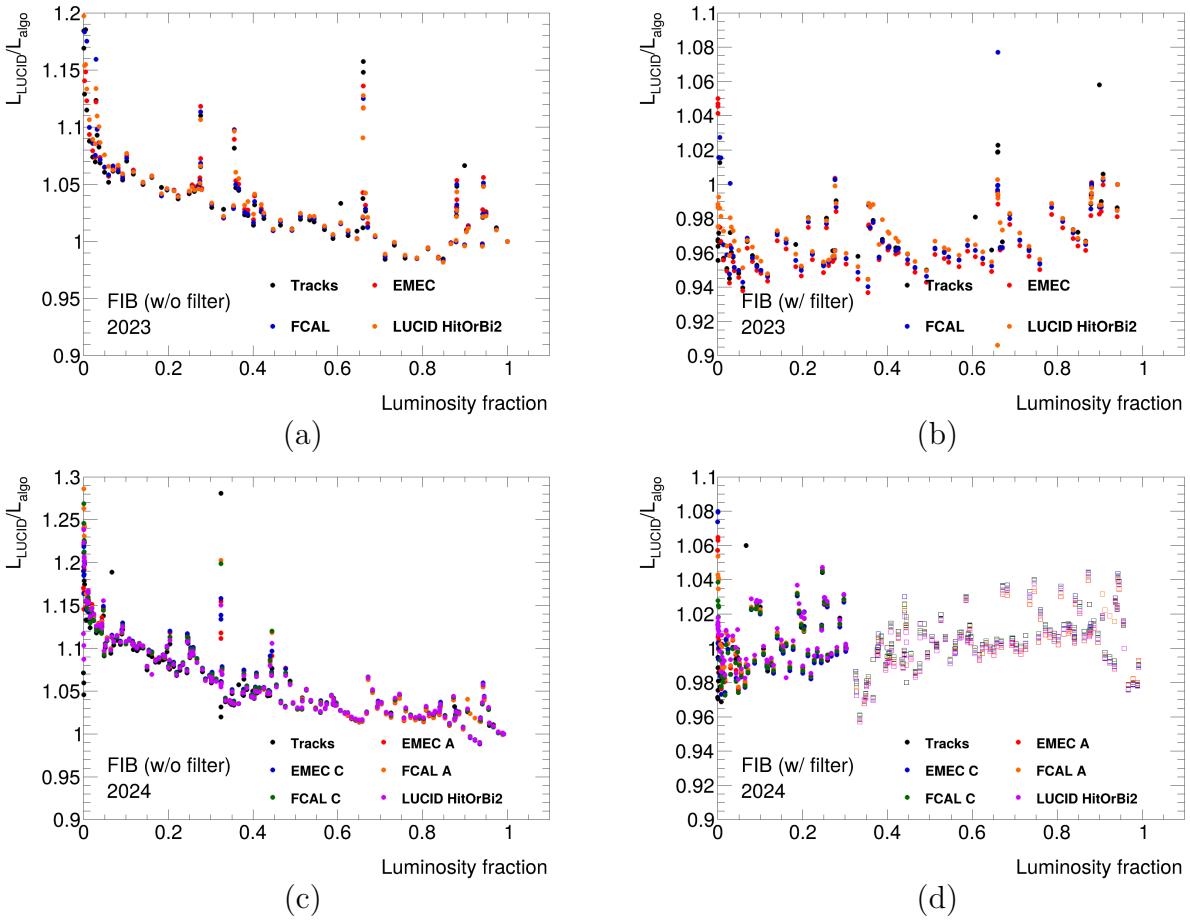

Figure 3.51: Long-term stability for fiber without the UV filter (on the left) and with the UV filter (on the right) in 2023 (on the top) and in 2024 (on the bottom).

and it mitigated the sawtooth shape and reduced a little bit the run to run fluctuations (see Fig. 3.52 and Tables 3.11 and 3.12). It is foreseen to install a high precision Power Supply before the 2025 data taking to overcome this limitation. Meanwhile, in order to try to reduce the run-to-run fluctuations, an attempt was done aimed at increasing the PMT gain (empty squares in Fig. 3.51d). Although these operations managed to reduce the sawtooth shape, the run-to-run fluctuations were not reduced. 2025 data with the new Power Supply will be the final test-bench on the stability of the fiber detector for the long-term stability, but the linearity with μ is already a strong point as it would allow to linearize the PMT detector without the use of the track-counting algorithms.

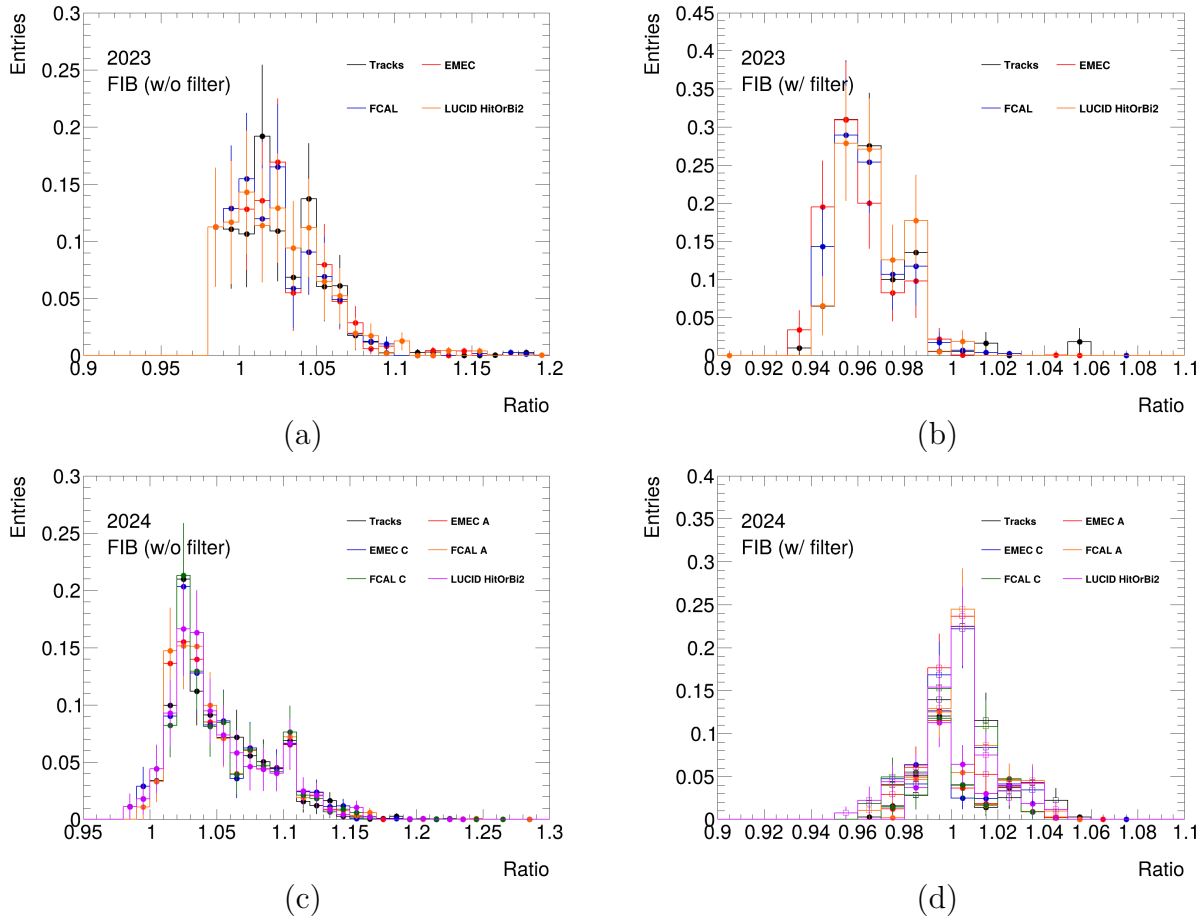

Figure 3.52: Distribution of the ratio of Fiber prototype without the UV filter (on the left) and with the UV filter (on the right) over other luminosity algorithms using 2023 (on the left) and 2024 (on the right) datasets.

	w/o filter	w/ filter
Tracks	0.026	0.024
EMEC	0.026	0.018
FCAL	0.028	0.018
HitOrBi2	0.028	0.017

Table 3.11: RMS of the distributions of the ratio of Fiber prototype with and without the UV filter other luminosity algorithms using 2023 dataset.

	w/o filter	w/ filter(1)	w/ filter(2)
Tracks	0.034	0.0074	0.015
EMEC A	0.036	0.0066	0.014
EMEC C	0.036	0.0068	0.015
FCAL A	0.035	0.015	0.015
FCAL C	0.035	0.013	0.015
HitOrBi2	0.035	0.0067	0.015

Table 3.12: RMS of the distributions of the ratio of Fiber prototype with and without the UV filter over other luminosity algorithms using 2024 dataset. The two periods are reported inside the parenthesis.

3.6 Summary

Due to the harsher conditions expected for Run-4, LUCID-2 requires an upgrade. Three prototypes for the new LUCID detector, utilizing different technologies (PMT and fiber), have been installed and are currently under testing.

The first PMT prototype consists of four PMTs attached to the JFC-3 shielding and is equipped with both Hamamatsu R760 (LUCID-2) and new, smaller Hamamatsu R1635 PMTs. This prototype exhibits linearity similar to LUCID-2, with no significant differences between the PMT types. However, the Hamamatsu R760 has shown much better long-term stability than the R1635. Simulations indicate that a detector using R760 PMTs cannot reach the nominal pile-up of 200 without saturation. Two strategies are under investigation to improve performance:

- Increasing the R1635 window thickness to 1.2 mm to match the R760, aiming to enhance long-term stability.
- Increasing the R760 threshold used to define a hit, thereby reducing the detector's acceptance.

The second PMT prototype comprises two R760 PMTs positioned behind the JFC-3, with very low acceptance. It has 4-5 times better linearity than LUCID-2 but exhibits larger run-to-run fluctuations, likely due to the low acceptance. Moreover it will not be possible to calibrate it directly in the vdM scans but only perform a cross calibration to the JF PMTs.

The fiber detector consists of two independent quartz fiber bundles, read out by two Hamamatsu R7459 PMTs. PMT gain is monitored using ^{207}Bi, as with all LUCID PMTs, and fiber degradation is tracked by an LED system. Tests revealed that fiber transmissivity decreases more rapidly in the UV than in visible wavelengths, leading to the insertion of a Cleartran UV filter in one prototype for enhanced radiation resistance and stability. A beam test was conducted to investigate Cherenkov light production

and propagation in the fibers; these results will contribute to an algorithm for offline corrections to account for radiation damage in luminosity measurements. The fiber prototype demonstrates perfect linearity both with and without the UV filter. The prototype without the filter showed drift in long-term stability due to fiber degradation, while the prototype with the UV filter exhibited no drift, though it showed larger run-to-run fluctuations than LUCID-2.

The optimal future LUCID design combines the advantages of all prototypes: the JF detector, with either R760 or R1635 PMTs based on performance (see the main characteristcs of the PMTs in Appendix B), will serve as the primary detector and be directly calibrated during vdM scans. A potential issue for the JF detector, particularly with the R760 at lower thresholds, is saturation in the 1-second online luminosity algorithm. The JN detector, with its very low acceptance, will mitigate saturation issues and assist with online luminosity monitoring. Lastly, the fiber detector, as the most linear option, can perform μ-corrections for the main detector independently of other detectors, such as the inner tracker.

Chapter 4

The Z boson physics

The current understanding of elementary particle interactions is based on the Standard Model (SM) of particle physics. Developed in the early 1970s, it describes the electromagnetic, weak, and strong fundamental forces. The Standard Model has been rigorously tested and validated over several decades through numerous experiments. However, at the beginning of the 21^{st} century, many questions remain unanswered:

- The fermion mass hierarchy and quark flavor mixing in the SM have a distinctive structure that may originate from unknown physics at yet unexplored very high energy scales.
- The observed neutrino flavor oscillation cannot be explained within the SM, as it implies lepton-number violation.
- The nature of Dark Matter (approximately 27% of the Universe) and Dark Energy (approximately 68% of the Universe) remains unknown.
- The theory of gravity cannot be integrated into the SM, as no renormalizable quantum field theory of gravity exists.

In the late 20^{th} century, the LHC was constructed to address these unresolved questions. The ATLAS and CMS experiments were designed as general-purpose detectors to explore a wide range of experimental signatures. The high detection efficiencies of ATLAS and CMS enabled the observation of a new particle with a mass of 125 GeV (in unit $c = 1$), consistent with the SM Higgs boson.

4.1 The Standard Model of particle physics

The Standard Model of particle physics is a gauge theory that describes the fundamental particles in nature and their interactions. It is based on the existence of local gauge

symmetries, which explain particle interactions through force-mediating fields. The SM Lagrangian reflects the symmetries under the transformation of $SU(3)_C \times SU(2)_L \times U(1)_Y$ gauge group [16]. Each component of the SM Lagrangian corresponds to one of the fundamental forces in nature, expressed in terms of quantum fields: the electromagnetic force through invariance under the $U(1)_Y$ transformation, the weak force through $SU(2)_L$, and the strong force through $SU(3)_C$.

4.1.1 The fundamentals particles

The basic constituents of matter are represented by fermionic fields of spin-1/2 particles, which follow Fermi-Dirac statistics and comply with the Pauli exclusion principle. The symmetry principles postulated in the Standard Model imply the existence of conserved quantities (Noether's theorem), described by quantum numbers [16]. The quantum numbers associated with the $SU(2)_L$ and $U(1)_Y$ gauge groups are called isospin I and hypercharge Y, respectively. The relationship with electric charge is given by $Q = I_3 + \frac{Y}{2}$ where I_3 is the third component of the weak isospin. The chiral symmetry of the $SU(2)_L$ group leads to the associated gauge boson to couple only to left-handed fermion fields. Fermion fields are organized into left-handed doublets, with weak isospin $I = \frac{1}{2}$, and right-handed singlets with $I = 0$.

Fermions are divided into leptons and quarks. Leptons experience weak and electromagnetic forces, but not the strong interaction, and are grouped into three families (isospin doublets):

$$\begin{pmatrix} e \\ \nu_e \end{pmatrix} \quad \begin{pmatrix} \mu \\ \nu_\mu \end{pmatrix} \quad \begin{pmatrix} \tau \\ \nu_\tau \end{pmatrix}$$

Each family contains massive particles (e, μ, and τ) with charge -1, interacting through both electromagnetic and weak forces, and their corresponding neutrinos, which interact only weakly. In the Standard Model, neutrinos are neutral, massless leptons, contrary to experimental evidence of their oscillation, which implies a non-zero mass. The third component of weak isospin takes the values $+\frac{1}{2}$ for charged leptons and $-\frac{1}{2}$ for neutrinos. Leptons are described by the leptonic quantum number L, conserved by all interactions, and each weak doublet has a specific leptonic number: L_e, L_μ and L_τ [17].

Quarks experience electromagnetic, weak, and strong forces and come in six different flavors labeled u, d, c, s, t and b. Flavor is conserved by all forces except the weak interaction. Due to the similarity between u and d quark masses, these two quarks are grouped into a strong isospin doublet ($I = \frac{1}{2}$ and $I_3 = \pm\frac{1}{2}$). Similarly, all quarks are organized into three weak isospin doublets:

$$\begin{pmatrix} u \\ d \end{pmatrix} \quad \begin{pmatrix} c \\ s \end{pmatrix} \quad \begin{pmatrix} t \\ b \end{pmatrix}$$

where the u-like quarks carry a $+\frac{2}{3}$ charge and the d-like quarks a $-\frac{1}{3}$ charge. All quarks are described by the baryonic quantum number B ($+\frac{1}{3}$ for quarks and $-\frac{1}{3}$ for antiquarks),

conserved by all interactions. The quantum number associated with the $SU(3)_C$ group is called color, representing the 'charge' of the strong interaction, and can take three possible values, conventionally called red, blue and green. Due to confinement, quarks do not exist as free particles but are bound in baryons (mesons with $B = 0$, or hadrons with $B = 1$), which are color-neutral particles.

4.1.2 The fundamental forces

In the Standard Model, particles interact by coupling to specific fields, whose quanta are spin-1 particles called bosons. Bosons arise from the requirement of local gauge invariance under certain transformations (symmetries) of the fermionic fields. Using this formalism, the structure of the different interaction contributions can be described starting from the free Dirac Lagrangian:

$$\mathcal{L}_{\text{free}} = \bar{\psi}(i\gamma^\mu \partial_\mu - m)\psi \tag{4.1}$$

where ψ represents the fermion field with mass m. The global invariance of the Lagrangian in Eq. 4.1 under specific transformations implies the conservation of the electromagnetic, weak and strong charges, as guaranteed by Noether's theorem. Local gauge invariance allows particles to interact by introducing bosons as necessary components in the covariant derivative. The strength of these interactions is described by coupling constants, which are part of the matrix element of each process.

The electromagnetic interaction

The Quantum Electrodynamics (QED) is the theory that describes the electromagnetic interaction, which is symmetric with respect to gauge rotations of the $U(1)_Y$ group. The electric charge causes the coupling of charged particles with the field. The QED coupling constant is a dimensionless quantity defined in terms of the electric charge e: $\alpha_e = \frac{e^2}{4\pi\epsilon_0\hbar c} \approx \frac{1}{137}$. The running behavior of α_e as a function of the energy involved in the process is explained by the vacuum polarization effect. This phenomenon states that more energy is needed to probe the true value of a particle's charge when it is surrounded by the vacuum medium.

The QED Lagrangian is derived by requiring the invariance of the Lagrangian in Eq. 4.1 under local $U(1)_Y$ transformations. Therefore, the partial derivative is replaced by the covariant derivative:

$$\partial_\mu \rightarrow \mathcal{D}_\mu = \partial_\mu + ieA_\mu(x) \tag{4.2}$$

where the quantum of the vector field A_μ is the photon. The resulting QED Lagrangian is:

$$\mathcal{L}_{\text{QED}} = \mathcal{L}_{\text{free}} - J^\mu A_\mu - \frac{1}{4}F^{\mu\nu}F_{\mu\nu} \tag{4.3}$$

where J^μ is the electromagnetic current and the last term represents the propagation of free photons, with Maxwell's electromagnetic tensor $F^{\mu\nu}$. A term in the form $\mathcal{L} = \frac{1}{2}m^2 A^\mu A_\mu$ representing the photon mass is not present in Eq. 4.3 as it is forbidden by the gauge invariance: this implies the massless nature of the photon.

The strong interaction

The Quantum Chromodynamics (QCD) is the quantum field theory describing strong interactions, symmetric with respect to gauge rotations of the $SU(3)_C$ group. The QCD coupling constant α_s varies with energy. In vacuum, the color charge of a bare quark is surrounded by quark-antiquark pairs and colored gluons, leading to an enhancement of the strong charge with increasing distance (the 'antiscreening' effect). The divergence of the strong coupling at low energy indicates confinement, explaining why free quarks and gluons have never been observed. Conversely, when the transferred momentum is large and quarks are close together, the strong interaction is weak, a property known as asymptotic freedom.

To determine the QCD Lagrangian, it must be noted that each quark field q_a in Eq. 4.1 can occur in three colors ($q_a = (q_{a,r}, q_{a,g}, q_{a,b})$). The covariant derivative introduced to ensure invariance under $SU(3)_C$ rotations is:

$$\mathcal{D}_\mu = \partial_\mu + igt_A\mathcal{A}^A_\mu(x) \tag{4.4}$$

where $\mathcal{A}^A_\mu$ is the gauge field of the strong interaction (the gluon), and the t_A matrix is a fundamental representation of $SU(3)$. The field strength tensor $G^A_{\mu\nu}$ is expressed as:

$$G^A_{\mu\nu} = \partial_\mu\mathcal{A}^A_\nu - \partial_\nu\mathcal{A}^A_\mu - gf_{ABC}\mathcal{A}^B_\mu\mathcal{A}^C_\nu \tag{4.5}$$

where indices A, B, and C run over the eight color degrees of freedom of the gluon field. The third term in Eq. 4.5 is a characteristic feature of a non-Abelian theory and generates triple and quartic gluon self-interactions. The QCD Lagrangian is:

$$\mathcal{L}_{QCD} = \sum_{\text{flavours}} \bar{q_a}(i\gamma_\mu\mathcal{D}^\mu - m)_{ab}q_b - \frac{1}{4}G^A_{\mu\nu}G^{\mu\nu}_A \tag{4.6}$$

Similar to $\mathcal{L}_{QED}$, it does not contain quadratic-field terms representing the quanta mass; hence, gluons are massless bosons in the Standard Model.

The weak interaction

The weak interaction involves all fundamental particles of the Standard Model. Initially observed in β decays, it was originally described by Fermi as an effective point-like theory. Although valid at low transferred momentum, this approximation fails to account for key features of this interaction, such as massive mediators and parity violation. A

quantum field theory based on a V-A (vector-axial) structure and described by the $SU(2)_L$ symmetry group was introduced, where the label L indicates coupling only to left-handed fermions. Fermion fields are represented by left-handed doublets L and right-handed singlets R. For the first family of fermions, this becomes:

$$L = \begin{pmatrix} e \\ \nu_e \end{pmatrix}_L \qquad R = e_R$$

$$L = \begin{pmatrix} u \\ d \end{pmatrix}_L \qquad R = u_R,\, d_R$$

The mediators of the weak interaction are three massive bosons: W^+ and W^- (carrying electric charge ± 1) and Z (which is neutral). These particles were initially predicted to be massless, which conflicted with experimental evidence of $M_{Z/W} \gg 0$. The large mass of these bosons explains the short range of the weak force.

Weak interactions among quarks from different isospin doublets are disfavored but not forbidden. The quark mixing is explained by considering the weak eigenstates as a rotation of the mass eigenstates through the Cabibbo-Kobayashi-Maskawa (CKM) matrix.

The electroweak theory

In the late 1960s, Weinberg, Salam and Glashow unified the electromagnetic and weak interactions into the electroweak theory, described by the $SU(2)_L \times U(1)_Y$ symmetry group [18] [19] [20]. Following a procedure similar to that used for QED and QCD, the Lagrangian of the left-handed (L) and right-handed (R) fermion fields must be invariant under global and local transformations of the gauge group. To ensure local invariance, the ∂_μ derivative is replaced by the covariant form:

$$\mathcal{D}_\mu = \partial_\mu + ig\frac{\tau_a}{2}W_\mu^a + i\frac{g'Y}{2}B_\mu \tag{4.7}$$

where W_μ^a and B_μ are the gauge bosons of the $SU(2)_L$ and $U(1)_Y$ groups, respectively. The Pauli matrices τ_a (a = 1, 2, 3) and the hypercharge Y represent the generators of these groups. The electroweak Lagrangian can be expressed as:

$$\begin{aligned} \mathcal{L}_{EW} = & -\frac{1}{4}\mathbf{W}_{\mu\nu}\mathbf{W}^{\mu\nu} - \frac{1}{4}B_{\mu\nu}B^{\mu\nu} \\ & + \bar{L}\gamma^\mu\left(i\partial_\mu - g\frac{1}{2}\tau\cdot\mathbf{W}_\mu - g'\frac{Y}{2}B_\mu\right)L + \bar{R}\gamma^\mu\left(i\partial_\mu - g'\frac{Y}{2}B_\mu\right)R. \end{aligned} \tag{4.8}$$

The first line contains the kinetic energy and self-coupling of the $\mathbf{W}_\mu$ fields and the kinetic energy of the B_μ field. The second line describes the fermion kinetic energy ($i\partial_\mu$)

and their interactions with the $W_\mu^{1,2,3}$ ($g\frac{1}{2}\tau\cdot\mathbf{W}_\mu$) and B_μ ($g'\frac{Y}{2}B_\mu$) fields. The Lagrangian in Eq. 4.8 describes interactions among massless fermions and massless gauge fields, which contradicts experimental observations.

The mass terms are introduced by adding a $SU(2)_L$ doublet of complex scalar fields ϕ, described by the Lagrangian:

$$\mathcal{L}_{Higgs} = (\partial_\mu\phi)^\dagger(\partial^\mu\phi) - V(\phi) = (\partial_\mu\phi)^\dagger(\partial^\mu\phi) - \frac{1}{2}\mu^2\phi^\dagger\phi - \frac{1}{4}\lambda(\phi^\dagger\phi)^2 \tag{4.9}$$

where μ is the mass of the scalar field ϕ, and λ is a positive dimensionless constant. If $\mu^2 > 0$, the potential has a ground state at the origin ($\phi_{min} = 0$). If $\mu^2 < 0$, the ground state is at $\phi_{min} = \pm\sqrt{\frac{-\mu^2}{\lambda}} = \pm v$, called the vacuum expectation value. Without loss of generality, we can choose $\phi_{min} = v = \sqrt{\frac{-\mu^2}{\lambda}}$, and by performing a perturbation expansion around one of the minima of the potential, a real mass term $-\lambda v^2$ appears in the Lagrangian of Eq. 4.9. The perturbation expansion must be performed around one of the minima, leading to spontaneous symmetry breaking. The $SU(2)_L \times U(1)_Y$ gauge-invariant expression of Eq. 4.9 using the covariant derivative is:

$$\mathcal{L}_{Higgs} = \left|(i\partial_\mu - g\frac{1}{2}\tau\cdot\mathbf{W}_\mu - g'\frac{Y}{2}B_\mu)\phi\right|^2 - V(\phi) \tag{4.10}$$

Choosing the minimum $\phi_{min} = \frac{1}{\sqrt{2}}\begin{pmatrix}0\\v\end{pmatrix}$, the gauge fields in the previous expression acquire mass and can be expressed as linear combinations of the $SU(2)_L \times U(1)_Y$ fields:

$$\begin{aligned} W_\mu^\pm &= \frac{1}{\sqrt{2}}(W_\mu^1 \mp iW_\mu^2) \\ Z_\mu &= \cos\theta_W W_\mu^3 - \sin\theta_W B_\mu \\ A_\mu &= \sin\theta_W W_\mu^3 + \cos\theta_W B_\mu \end{aligned} \tag{4.11}$$

where θ_W is the Weinberg mixing angle. The $W_\mu^\pm$, Z_μ, and A_μ fields can be identified with the $W^\pm$ bosons of mass $m_W = \frac{1}{2}vg$, the Z boson of mass $m_Z = m_W/\cos\theta_W$, and the massless photon field. The potential $V(\phi)$ introduces additional terms in the Lagrangian of Eq. 4.10, which are shown here for a parametrization of the field ϕ around the ground state:

$$\begin{aligned} \mathcal{L} = &\frac{1}{2}(\partial h)^2 + [m_W^2 W_\mu^+ W^{-\mu} + m_Z^2 Z_\mu Z^\mu]\left(1 + \frac{h}{v}\right)^2 \\ &- \lambda v^2 h^2 - \lambda v h^3 - \frac{1}{4}\lambda h^4 \end{aligned} \tag{4.12}$$

using $\phi = \frac{1}{\sqrt{2}}\begin{pmatrix}0\\v+h(x)\end{pmatrix}$. The Lagrangian contains a mass term for the $h(x)$ field (with $m_h = \sqrt{2\lambda v^2}$) which describes a scalar field particle referred to as the Higgs boson. The

interaction of the gauge bosons $W^{\pm}$ and Z with the Higgs field explains the generation of their masses.

Another $SU(2)_L \times U(1)_Y$ gauge-invariant term is introduced to describe the mass of the fermion fields, generated by coupling with the Higgs field:

$$\mathcal{L} = -(G_1 \bar{L}\phi R + G_2 \bar{L}\phi^* R + \text{hermitian conjugate}) \tag{4.13}$$

where $G_{1,2}$ are matrices of Yukawa couplings.

4.2 Proton-proton interactions at LHC

The calculation of the cross section of physics processes is challenging at hadron colliders such as the LHC, due to the complex interplay between perturbative theoretical computations, phenomenological models, and experimental data. At the LHC, the interacting protons must be considered as composites of quarks and gluons (partons). Consequently, the cross section for a process generated by the interaction of two partons with momenta p_1 and p_2 can be expressed as [21]:

$$\sigma(p_1, p_2) = \sum_{i,j=q,\bar{q},g} \int_0^1 dx_1 dx_2 f_i(x_1, \mu_F^2) f_j(x_2, \mu_F^2) \hat{\sigma}_{ij} \left(x_1 p_1, x_2 p_2, \alpha_S(\mu_R^2), \frac{Q^2}{\mu_R^2}, \frac{Q^2}{\mu_F^2} \right) \tag{4.14}$$

where x_1 and x_2 are the proton momentum fractions carried by partons 1 and 2, respectively. $f_i(x_1, \mu_F^2)$ and $f_j(x_2, \mu_F^2)$ are called Parton Distribution Functions (PDFs) and represent the probability for parton i (j) to carry a fraction x of proton 1 (2) momentum. PDFs are specific to the type of interacting partons and depend on the QCD factorization scale μ_F. $\hat{\sigma}_{ij}$ is the interaction cross section between the two partons involved in the interaction: it depends on the strong coupling constant (α_S), whose value is specified for a particular energy scale (the renormalization scale μ_R), and on the transferred momentum Q^2. The sum runs over all contributing parton configurations: i and j represent all possible combinations of quarks, antiquarks, and gluons.

Experimentally, the production cross section determines the number of observed events $N(X)$ for a given process $pp \to X$ with a specific detection efficiency ϵ and an integrated luminosity $\int \mathscr{L} dt$ (see Chapter 1.3):

$$N(X) = \epsilon \cdot \sigma(X) \int \mathscr{L} dt \tag{4.15}$$

4.2.1 The running coupling constant

In a perturbative field theory, the evaluation of cross sections is performed using the coupling constant, visualized through Feynman diagrams. These diagrams may contain

particle loops, leading to divergences in calculations. QCD and QED are renormalizable quantum field theories, allowing divergences to be absorbed into renormalized coupling constants and particle masses.

This renormalization introduces an arbitrary scale called the renormalization scale (μ_R), causing the coupling constant (α) to vary with μ_R, which characterizes its running behavior. The running of the coupling constant (α) is described by the equation [22]:

$$\alpha(Q^2) = \frac{\alpha(\mu^2)}{1 + \alpha(\mu^2) b_0 \ln\left(\frac{Q^2}{\mu^2}\right)} \tag{4.16}$$

where b_0 is a constant. In QED, $b_0 = -\frac{1}{3\pi}$, and in QCD, $b_0 = \frac{33-2n_f}{12\pi}$, with n_f representing the number of quark flavors. The sign of b_0 determines whether α increases or decreases with the energy involved in the process (μ^2) and the transferred momentum (Q^2). Q^2 is determined by the sum of the four-momenta of the interacting partons. For leading-order (LO) resonant scattering $q\bar{q} \to Z$, the energy scale is given by $Q^2 = sx_1x_2 = M_Z^2$, where s is the center of mass energy of the collision.

The running behavior of the strong coupling constant as a function of energy is depicted in Fig. 4.1, showing measurements from various experiments.

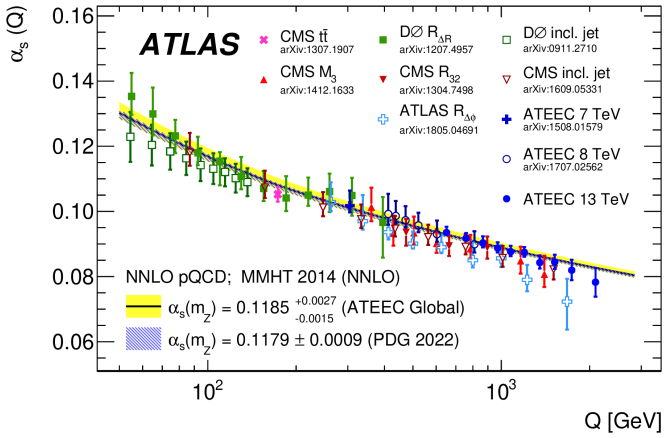

Figure 4.1: Summary of measurements of the strong coupling constant α_s as a function of the energy scale Q.[23]

4.2.2 Perturbative QCD

Feynman diagrams are useful tools in visualizing the calculation of cross sections for physics processes, as each vertex contributes with a term proportional to the coupling constant of the involved force. In the context of strong interactions among partons, each

vertex amplitude is proportional to α_s. The total partonic cross section can be expressed as [21]:

$$\hat{\sigma} = \alpha_s^k \sum_{m=0}^{\infty} c(m) \alpha_s^m \tag{4.17}$$

where $c(m)$ denotes the m-th order contribution to the cross section, and k represents the number of strong interaction vertices in the Feynman diagram. This equation defines a perturbative calculation that converges if $\alpha_s \ll 1$. Even if the precision of the calculation improves with higher-order terms, the series must be truncated at a given order m.

The cross section $\hat{\sigma}_{ij\to X}$ is expressed as a perturbative expansion:

$$\hat{\sigma}_{ij\to X} = \hat{\sigma}_{ij\to X}^{LO} + \alpha_s \hat{\sigma}_{ij\to X}^{NLO} + \alpha_s^2 \hat{\sigma}_{ij\to X}^{NNLO} + \alpha_s^3 \hat{\sigma}_{ij\to X}^{N^3LO} + O(\alpha_s^4) \tag{4.18}$$

where LO stands for leading-order (the lowest order in the calculation), NLO for next-to-leading order, NNLO for next-to-next-to-leading order, and so on, up to a certain perturbative order.

Divergences in the calculation necessitate the introduction of the renormalization scale μ_R. Physical observables, such as the cross section, should be independent of the choice of this scale. However, truncating the perturbative expansion introduces a residual dependence on μ_R, related to the higher-order terms that are not included.

4.2.3 Parton Distribution Functions

From Eq. 4.14, another crucial element in evaluating the total cross section of a process is the Parton Distribution Functions (PDFs) $f_i(x_1, \mu_F^2)$ and $f_j(x_2, \mu_F^2)$, which represent the probability that a parton (i or j) carries a fraction x (Bjorken variable) of the total proton momentum. The functions $xf_i(x_1, \mu_F^2)$ and $xf_j(x_2, \mu_F^2)$ are known as Parton Density Functions, indicating the probability of finding a parton with a momentum fraction between x and $x + dx$. PDFs depend on the factorization scale (μ_F), an arbitrarily chosen scale that determines whether a parton emission is included in the PDF or in the partonic cross section $\hat{\sigma}$ of Eq. 4.14. A parton emitted with low transverse momentum ($< \mu_F$) is absorbed into the PDF definition and considered part of the proton structure, while a parton emitted with high transverse momentum ($> \mu_F$) is accounted for in the partonic cross section. Similarly to μ_R, the total cross section should be independent of the factorization scale if the perturbative calculation is performed to all orders.

PDFs are non-perturbative quantities that cannot be computed directly and are obtained from global fits to experimental data [24]. Typically, a physically motivated ansatz is chosen to parameterize the PDFs as a function of x at a given starting scale. The DGLAP equations allow PDFs to evolve to arbitrary scales, incorporating parton splitting and emission [25]. The resulting PDFs are used to fit experimental data, constraining the initial parameters. Global fits are conducted by groups such as MSTW,

CTEQ, and NNPDF using data from fixed-target deep inelastic scattering (HERA) and hadron collider (Tevatron and LHC) experiments. Different experimental datasets are sensitive to different parton density functions and probe complementary ranges of the Bjorken variable x and the partonic center-of-mass energy Q^2.

The dominant source of uncertainty in the PDF determination comes from the statistical treatment of the experimental data, followed by the fitting strategy, the arbitrary choice of the parameterization function at the initial scale, and the value of α_s used in the process calculation.

4.2.4 Monte Carlo Generators

The calculation of Eq. 4.14 provides a prediction for the production cross section of a specific process. However, performing the full calculation is complex and typically this is handled by Monte Carlo (MC) generators. In proton-proton (p-p) collisions, interactions occur between partons from different protons. These interactions can produce resonances that decay, transferring spin correlations to the decay products. As particles are accelerated, they can emit gluons or photons through bremsstrahlung: emissions associated with incoming partons are termed Initial State Radiation (ISR), while those associated with outgoing partons are referred to as Final State Radiation (FSR). Since protons are composed of multiple partons, several parton pairs may collide within a single p-p collision, leading to Multiple Interactions (MI). The colliding partons carry a fraction of the energy of the incoming hadrons, but the majority of the initial energy remains with the beam remnants, which continue in their original directions. Quark confinement in QCD forces quarks to combine into color-neutral particles in a process known as hadronization. Hadrons are unstable and decay over various timescales; some of them, like B-hadrons, are sufficiently long-lived to be observed in a detector.

Monte Carlo generators simulate these steps sequentially, with each step governed by a set of rules applied iteratively to build more complex states. Figure 4.2 illustrates the different stages of the simulation.

The first element in the simulation of the entire process is the direct collision of the incoming partons, often referred to as 'hard scattering'. This hard scattering is described by Matrix Element (ME) calculations at a fixed order in α_s, starting from the parton momenta as described by PDFs. ME calculations expand the perturbative series in powers of α_s to include higher-order corrections and final states with multiple partons. Due to the divergence of the α_s coupling at low energies, perturbative QCD calculations become impractical, and ME calculations cannot explore the internal structure of a jet or be easily matched to hadronization models, which address soft partons.

To simulate soft and collinear emissions, the Parton Shower (PS) method is used. This method generates a random number of gluon or $q\bar{q}$ pair emissions through kinematic, interference, and helicity simplifications. It factors a complex $2 \to n$ process, where n represents many partons in the final state, into a simpler $2 \to 2$ process with added

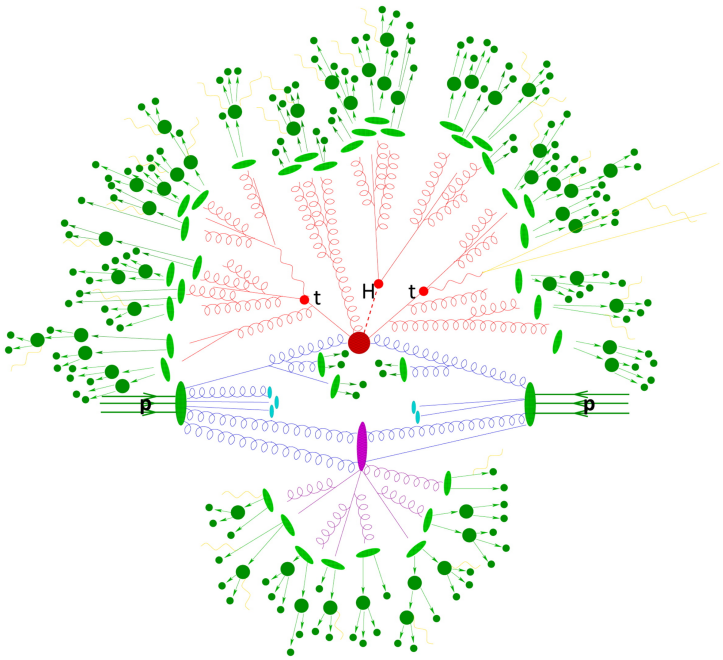

Figure 4.2: Sketch of p-p collision simulation. The hard part of the scattering (red) is simulated by the Matrix Element generators. Parton Showers produce bremsstrahlung (blue), and multiple interaction models simulate secondary interactions (purple). Fragmentation models describe the hadronization of partons (green), whose decays are simulated by specific tools (dark green).

showers. PS is based on a sequential stochastic branching process that models the splitting and emission of partons until the parton energy scale reaches approximately 1 GeV, which is typically associated with hadron formation.

At around 1 GeV, hadronization, the process of confining colored partons into hadrons, is described by non-perturbative models. The combination of PS and hadronization enables Monte Carlo generators to simulate the collimated showers of hadrons, or 'jets', observed in detectors.

The underlying event (UE) involves additional activity from multiple interactions and proton remnants and is handled with non-perturbative models that are tuned to experimental data. Multiple simultaneous interactions are modeled by overlaying inelastic p-p events ('minimum bias') on top of the hard scattering. The number of such collisions is stochastic and modeled to match the pileup level observed in data.

4.3 The Z boson

The Z boson was discovered in 1983 by the UA1 collaboration of the $Sp\bar{p}S$ collider at CERN, whose primary goal was the search of the massive intermediate bosons of the electroweak interaction. After the discovery of the W bosons in events with single isolated electrons and missing energy, the UA2 detector observed eight events interpreted in terms of the reaction

$$p\bar{p} \rightarrow Z + anything \quad \text{with} \quad Z \rightarrow e^+e^-$$

in a data sample corresponding to a total integrated luminosity of 131 nb^{-1}. Fig.4.3 [26] shows the distribution of 24 events passing loose requirements based on the energy in the clusters of the electromagnetic calorimeter. Requiring at least one isolated charged track with $p_T > 7$ GeV pointing to the electromagnetic cluster, the number of events was reduced to eight and their distributions as a function of the invariant mass of the dilepton pair is shown in Fig. 4.3a. As can be seen from the plot, the eight events are distributed around a mass value of ≈ 90 GeV. Requiring the track of isolated electron to point to both energy deposits in the electromagnetic calorimeter, only three events survived (shaded band in Fig.4.3b). From these events, the UA2 collaboration measured the mass of the Z boson to be:

$$M_Z = (91.8 \pm 1.3 \pm 1.4) GeV$$

where the first error accounts for the analysis strategy and the second error for the uncertainty on the energy scale. Assuming the Breit-Wigner distribution of the events, an upper limit on the full width was placed to $\Gamma < 11$ GeV, corresponding to ≈ 50 different neutrino types in the universe. In analogy with the studies performed in the electron channel, in the same year measurements of the Z boson were carried out in the muon decay mode $Z \rightarrow \mu^+\mu^-$. Three events survived to the full selection chain and were used to measure the Z mass with a value $M_Z = 85.8^{+7.0}_{-5.4}$ GeV, consistent with the value measured in the electron decay channel.

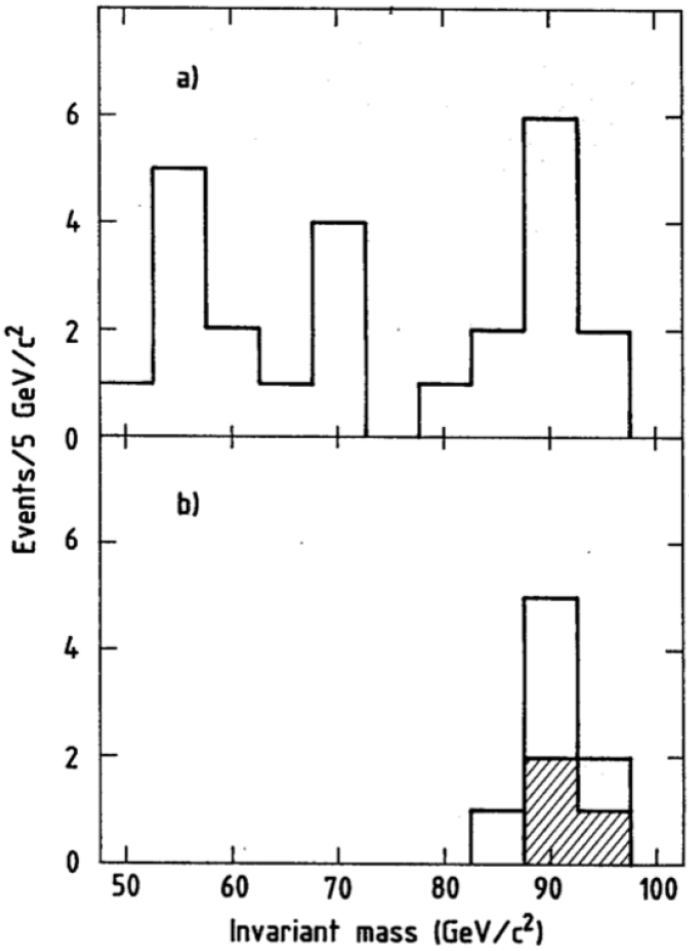

Figure 4.3: Invariant mass distribution of electron pairs in first observed Z candidate events at the UA2 experiment of the S$p\bar{p}$S collider. Fig.a) shows the distribution of 24 events passing requirements on the energy deposits in the electromagnetic clusters. Introducing identification criteria the number of events was further reduced to eight, whose invariant mass distribution peaks around a 90 GeV, as presented in Fig.b). The shaded band in Fig.b) represents the three events surviving the requirement of an isolated track matched with both electromagnetic clusters.

4.3.1 Z boson properties

Precision measurements of the Z-boson resonance were performed by LEP, an electron-positron collider built at CERN in 90's. During a first phase (LEP1) the centre of mass energy was kept in an interval of ± 3 GeV around the m_Z; this allowed experiments to collect $\approx 2 \cdot 10^4$ Z decays during 1989-1995 and to perform high precision measurements,

which still dominates the world average.

The Z boson lineshape parameters, like the mass (m_Z), the total width (Γ_Z) and the partial widths ($\Gamma_{f\bar{f}}$), have been determined from an analysis of the production cross sections of fermionic final states starting from e^+e^- collisions. The shape of the cross section variation around the Z peak can be parametrised by a Breit-Wigner function, with an energy dependent total width. The determination of these parameters was done via an analytic expression of this cross section in term of the parameters themselves

$$\sigma(s) = \sigma^0_{f\bar{f}} \frac{s\Gamma_Z^2}{(s - m_Z^2)^2 + \frac{s^2}{m_Z^2}\Gamma_Z^2} \tag{4.19}$$

and fitting the calculated cross section to the measured one, by varying these parameters. In Eq. 4.19 $\sigma^0_{f\bar{f}}$ represents the cross section for the process $e^+e^- \to f\bar{f}$ at $\sqrt{s} = m_Z$. If the final state involves the fermionic e^+e^- couple, the above cross section must be integrated to take into account small (O(1%)) contributions from photons exchange and $\gamma - Z$ interference. The world average value of the Z boson mass and total width are:

$$m_Z = (91.1876 \pm 0.0021) GeV$$
$$\Gamma_Z = (2.4952 \pm 0.0023) GeV$$

The pole cross section can be expressed as a function of the partial widths of the Z decay modes $\Gamma_{f\bar{f}}$

$$\sigma^0_{f\bar{f}} = \frac{12\pi}{m_Z^2} \frac{\Gamma_{ee}\Gamma_{f\bar{f}}}{\Gamma_Z^2} \tag{4.20}$$

According to the Standard Model, which predicts the Z boson to decay with comparable probability into all species of fermions kinematically allowed, the total width can be expressed as $\Gamma_Z = N_\nu \Gamma_\nu + 3\Gamma_{ee} + \Gamma_{hadrons}$ where N_ν is the number of neutrino families. Measuring the Z decay probabilities in leptons and in hadrons, LEP obtained $N_\nu = 3.27 \pm 0.30$, discarding the hypothesis of a fourth generation of fermions at 98% CL.

4.4 The inclusive production cross section

The dominating contribution to the Z boson production at LHC is the Drell-Yan process, based on the proton-proton scattering at high energy. At the parton level, the annihilation of a couple of quark-antiquark of the same flavour produces a Z boson (or a virtual photon) decaying in a couple of fermions with high transverse momentum. The leading order Feynman diagram of the Drell-Yan production is shown in Fig 4.4

Considering the hadronic structure of the proton, made of two u- and one d-quarks, the Drell-Yan process can be originated by one valence quark and one antiquark coming from the virtual-sea. Because of the different nature of the initial state quark and

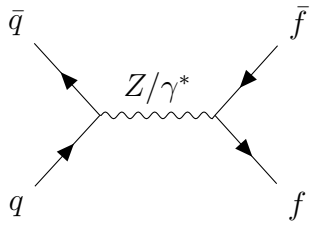

Figure 4.4: Feynman diagram for the Drell-Yan process.

antiquark, the valence quark propagates with a larger fraction x of transverse momentum of the proton. At the leading order, the invariant mass of the fermions in the final state is $M_Z^2 \approx x_1 x_2 s$; as a consequence, at the centre of mass energy of $\sqrt{s} = 13$ TeV, the Z boson is produced if $x_1 x_2 > 10^{-6}$ The partonic cross section for the Z inclusive production is described in Eq. 4.19; next-to-leading-order corrections increment the cross section value by about $\approx 20 - 30\%$.

The production of the Z vector boson at hadron colliders through the Drell-Yan mechanism is extremely important for physics studies. The process has large production rate and offers a clear signature, given the presence of two high-p_T leptons in the final state. Since the discovery at CERN S$p\bar{p}$S, several measurements of the Z boson production cross section at hadron colliders have been performed in $p - \bar{p}$ collisions at Tevatron by the CDF and D0 experiments at centre of mass energy $\sqrt{s} = 1.8$ TeV and $\sqrt{s} = 1.96$ TeV and at LHC by ATLAS and CMS in p-p collisions. These high precision measurements concurred to the determination of the properties of the Z boson. Since the Z boson is considered a Standard Model candle useful for detector calibration and alignment, it is one of the first measurements to be performed after any change in experimental conditions (i.e. centre of mass energy or detector layout).

For the above reasons, accurate theoretical predictions for the vector boson cross sections and the associated kinematic distributions are essential. Cross section calculations are performed at LO as an hard-scatter reaction at the energy scale of the Z mass; significant QCD corrections are then considered at higher order of calculation which increase the value of the cross section itself. Nowadays predictions of the Z boson are generally available up to NNLO in perturbation theory.

At LHC, high precision measurements are performed in kinematic domains never explored before and the comparison with accurate theoretical predictions allows to perform challenging tests of perturbative QCD and helps in the determination of the initial condition of PDF evolution. The knowledge of PDFs of the proton mainly comes from deep inelastic scattering (DIS), which cover a broad range of transferred momentum Q^2 and momentum fraction x. In the region $x \leq 0.01$, PDFs are constrained by the precise measurements performed at HERA, which determine a specific combination of light quark and antiquark distributions. However the flavour composition of the total light sea

$x\Sigma = 2x(\bar{u} + \bar{d} + \bar{s})$ has not been established at $x \leq$0.01 values. In order to achieve this measurement, two fundamental components contribute to complement the information from deep inelastic scattering: the rapidity distribution of the Z boson and the ratio of the W and Z cross sections. The rapidity (y) dependence of Z production in the Drell-Yan process provides constraints on the PDFs of the proton, since it is strongly correlated with the proton momentum fraction x_1, x_1 carried by the partons participating in the hard scattering process:

$$y = \frac{1}{2} = \ln \frac{x_1}{x_2} \tag{4.21}$$

The ratio of (W^++W^-) and Z cross sections in a leading-order calculation can be expressed as

$$\frac{W^+ + W^-}{Z} \approx \frac{u_v + d_v + 2s}{(V_u^2 \cdot A_u^2)(u_v + s) + (V_d^2 \cdot A_d^2)(d_v + s)} \tag{4.22}$$

where $u_v(d_v)$ is the up (down) valence quark distribution functions and $V_{u,d}$ and $A_{u,d}$ are the vector and axial-vector weak neutral current couplings of the light quarks. As the numerical values for the Z coupling to the up and down-quarks $V_{u,d}^2 \cdot A_{u,d}^2$ are of similar size, the $W^{\pm}/Z$ ratio measures a PDF insensitive quantity, providing the flavour composition of the light sea.

Another important measurement which benefits from the high precision reachable in the Z analysis is the ratio of the top pair production cross section to the Z cross section. Since top-pairs are mainly produced through the gluon-gluon fusion, the $t\bar{t}$ process is sensitive to the gluon distribution within the proton. Given that at a fixed centre of mass energy the luminosity uncertainty cancels, the ratio $t\bar{t}/Z$ has a significant sensitivity to the gluon-to-quark PDF ratio. Considering that the gluon fraction has a stronger dependence on the centre of mass energy than the quark-antiquark one, the measurements of the $t\bar{t}/Z$ ratio has already been performed at $\sqrt{s}$=7, 8 and 13 TeV in order to study the gluon PDFs in different x-Bjorken regions. In this thesis, the ratio will be measured at $\sqrt{s}$= 13.6 TeV.

Chapter 5

Z cross section

5.1 Introduction

The production of the electroweak vector boson Z at hadron colliders provides a benchmark for the understanding of strong (QCD) and electroweak (EW) processes. The relatively large production cross section at the LHC energy and the decay in two high-p_T leptons result in a clear experimental signature of the Z boson and, therefore, in a quite easy identification. These features provide the possibility to perform high precision measurements, sensitive to the sea-quark distributions inside the colliding protons. Given that the production cross section depends on the Parton Distribution Functions (PDFs) and on the underlying strongly interacting particles, a precise measurement offers also the possibility to test models of parton dynamics. Moreover, the measurement of the Z production cross section is one of the first analyses performed at the beginning of any new data taking period, because it offers the possibility to check detector calibration and alignment, to perform luminosity check through the Z-counting technique and, in this case, to test theoretical prediction at a center-of-mass energy of 13.6 TeV. For this reason, the data used in this analysis have been collected during 2022 (the first year of Run-3 data taking) for a total integrated luminosity of 29.9 ± 0.6 fb^{-1}. Basic data quality criteria were applied in order to select data with fully operational detectors.

In this Chapter the measurement of the Z production cross section is presented. In Section 5.2, the general analysis strategy is discussed. Then the object reconstruction and the Monte Carlo samples are illustrated in Section 5.3 and 5.4. In Section 5.5 and 5.6 the event selection and background evaluation are summarised, respectively. In Section 5.7 the list of calibration and scale corrections applied to physics objects is presented. The results are presented in Section 5.9 and 5.10 for the Z channel only and for the combination with W and $t\bar{t}$. In the end, a preliminary Z-counting luminosity measurement is performed in Section 5.11.

5.2 Analysis strategy

The first step in the analysis is the object reconstruction. After applying cut on both data and MC to reduce backgrounds, correction were applied to MC in order to take into account the various detector inefficiencies. To measure the cross sections, two different techniques were used in this analysis: the event counting and the profile likelihood fit.

5.2.1 Event counting

The total cross section of the Z boson production is defined as:

$$\sigma_Z^{tot} \times BR(Z \to ll) = \frac{N_{ll}^{data} - N_{BKG}}{A_Z^{ll} \cdot C_Z^{ll} \cdot \mathscr{L}} \tag{5.1}$$

where the branching ratio (BR) is the probability for the Z boson to decay in a specific lepton channel (in this thesis l=μ or e). N_{ll}^{data} is the number of observed events that have been reconstructed by the ATLAS detector and that have passed the selection described in section 5.5 (detector level), N_{BKG} represents the number of background events, estimated with Monte Carlo generators, that have passed the same selection. $\mathscr{L}$ is the total integrated luminosity (Chapter 1.3) referred to the analysed dataset. A_Z^{ll} is the acceptance factor, which takes into account the geometrical and kinematic acceptance of the detector. A_Z^{ll} is evaluated from the Monte Carlo truth (born level) and it is defined as:

$$A_Z^{ll} = \Big(\frac{N(\text{fiducial region})}{N(66\ GeV < m_{ll} < 116\ GeV)} \Big)_{\text{Born}} \tag{5.2}$$

where $N(\text{fiducial region})$ is the number of events that pass the selection criteria described in section 5.5 but applied at born level while $N(66\ GeV < m_{ll} < 116\ GeV)$ are the number of events in which the Z boson has an invariant mass between 66 and 116 GeV (born level). This is needed to compare different MC generator that have different mass spectrum.

C_Z^{ll} represents the probability of reconstructing an event, if all the relevant physics objects characterising the event are in the detector acceptance and have passed the selection requirements. It can be expressed as:

$$C_Z^{ll} = \epsilon_{trig} \cdot \epsilon_{reco} \cdot \epsilon_{iso} \tag{5.3}$$

where ϵ_{trig}, ϵ_{reco} and ϵ_{iso} are, respectively, the lepton trigger, reconstruction and isolation efficiencies. C_Z^{ll} is evaluated as the ratio of the number of events passing the reconstruction level selection ($N(\text{fiducial region})_{\text{Reco}}$) to the number of events inside the fiducial volume at born level ($N(\text{fiducial region})_{\text{Born}}$):

$$C_Z^{ll} = \frac{N(\text{fiducial region})_{\text{Reco}}}{N(\text{fiducial region})_{\text{Born}}}. \tag{5.4}$$

Since C_Z^{ll} represents a correction from detector to truth level, it allows to perform measurements at particle level, namely corrected for detector resolutions and efficiencies. The total production cross section measurement is performed in the full phase-space, including regions outside the detector acceptance. Therefore, it heavily relies on the extrapolation in an unmeasured region, described only by the Monte Carlo modelling, which is sensitive to purely theoretical uncertainties (i.e. the PDF). For this reason, experimentally the cross section is first measured in the fiducial volume described above, and then corrected to the full phase-space by means of the acceptance factor A_Z^{ll}. The fiducial cross section is therefore defined as:

$$\sigma_Z^{fid} \times BR(Z \to ll) = \frac{N_{ll}^{data} - N_{BKG}}{C_Z^{ll} \cdot \mathscr{L}} \tag{5.5}$$

5.2.2 Profile likelihood fit

The profile-likelihood approach builds a likelihood function that includes the statistical model as well as all the sources of the systematic uncertainties directly in the likelihood. Maximising the likelihood provides the most probable values (and their uncertainties) for the parameters of interest (POIs) as well as the nuisance parameters (NPs). The likelihood, L, that is maximised (or the negative logarithm of the likelihood is minimised) can be schematically written as follows:

$$L\left(\vec{n}|\mu,\vec{\theta},\vec{k}\right) = \prod_{r\in\text{region}}\prod_{i\in\text{bin}} \text{Pois}\left(n_{i,r}|\mu S_{i,r}(\vec{\theta}) + B_{i,r}(\vec{\theta},\vec{k})\right) \times \prod_{j\in\text{NP}} G\left(\theta_j\right), \tag{5.6}$$

where $\vec{n}$ represents the data vector, with $n_{i,r}$ representing data yields in the bin i and region r. $\vec{\theta}$ denotes the NPs, that affect the number of signal events $S_{i,r}$ as well as the number of background events $B_{i,r}$ in the bin i and region r. $\vec{k}$ represents free floating normalisation parameters that also affect the number of background events. Finally, μ is the signal strength, which is the parameter of interest in the likelihood and it represents the ratio of the measured over predicted signal cross-section. The terms, Pois and G, represent the Poisson and Gaussian distributions, respectively. It is clear from Eq. 5.6 that the NPs are constrained by the Gaussian term[1] while the normalisation parameters, $\vec{k}$ are unconstrained. The full form of the likelihood can be found in the *HistFactory* reference [27].

Internally, the provided systematically varied histograms are compared to the nominal histograms and the difference is split into pure shape (total yield of the variation is forced to match the nominal prediction) and pure normalisation (only the total yield difference is considered) components. For each bin, the shape variation is interpolated and

[1]For the *gamma* terms, representing the MC statistical uncertainty, the constraint term is Poisson — in Bayesian statistics this would result in Gamma function posterior distribution, hence the name.

extrapolated using linear interpolation, while for the normalisation component an exponential times polynomial of 6-th order is used[2], however both components are controlled by the same parameter θ. This results in a Gaussian constraint for the shape component and approximate log-normal constraint for the normalisation component, that prevents unphysical negative normalisation.

The likelihood from Eq. 5.6 is maximised to obtain the best fitted valued for all the parameters as well as their uncertainty. The profile-likelihood fit is implemented in the *TRExFitter* framework.

5.3 Object reconstruction

5.3.1 Tracks and primary vertex

Particle tracking is performed in ATLAS by the Inner Detector (ID) (see also Chapter 2.5.2), the detector closest to the interaction point. Since the ID is immersed in a 2 T magnetic field generated by a central solenoid, the measurements of the charge and momentum can be achieved from particle bending. By extrapolating tracks to their origin point in the beam pipe, interaction vertices are reconstructed: in particular, the primary vertex corresponds to the vertex where p-p collisions take place, while secondary vertices correspond to the position of heavy particle decays. Tracks are reconstructed with a resolution in the transverse momentum measurement $\sigma_{p_T}/p_T = 0.05\% \times p_T/GeV \oplus 1\%$. The reconstruction algorithm fits five parameters: d_0, z_0, ϕ, θ, p/q, where d_0 and z_0 are the impact parameters to the beam line in the transverse and the longitudinal planes, respectively, q is the track charge, p is the track momentum and θ and ϕ are the azimuthal and polar angles.

In general, primary vertices are reconstructed by extrapolating tracks to the beam pipe and looking for intersection of multiple tracks. First of all, tracks must satisfy certain quality criteria, such as $p_T > 400$ MeV, $\geq$9 silicon pixel hits with no pixel holes (when a particle passes through inert material or dead modules) and $\mid d_0 \mid < 4$ mm. The constrain on d_0 prevents the reconstruction of vertices outside the beam pipe. Then, vertex finding is seeded using the z coordinate of each extrapolated track with the beamline. Tracks within 7σ of the seed are candidates for the vertex reconstruction. The overall vertex reconstruction efficiency is 50% for crossing with more than 40 interactions.

5.3.2 Electrons

In ATLAS electrons are reconstructed using a combination of the Inner Detector tracks and Electromagnetic Calorimeter clusters. The information from the ID define the di-

[2]The polynomial is needed to have a smooth transition for the function and its first and second derivative between the up and down variations.

rection at the interaction point, while the EM clusters are used to measure the energy of the electron. The reconstruction algorithm begins finding the seed-clusters as longitudinal towers in the $\eta \times \phi$ plane of the EM middle layer, with total cluster energy above 2.5 GeV. Then the reconstruction methodology involves track reconstruction from the ID, taking into account energy loss due to bremsstrahlung, the number of precision hits in the ID and the track-cluster EM matching.

The Particle IDentification (PID) determines whether the reconstructed electron candidates are signal-like objects or background-like objects, such as hadronic jets or converted photons. The PID algorithms use quantities related to the electron cluster and track measurements, including calorimeter shower shapes, information from the Transition Radiation Tracker (TRT), track-cluster matching related quantities, track properties and variables measuring bremsstrahlung effects. The baseline PID algorithm used in Run 2 and Run 3 analyses is the Likelihood based (LH) method. It is a Multivariate (MVA) technique that simultaneously determines several properties of the candidate when a selection decision is made. The LH procedure uses the signal and background Probability Density Function of the discriminating variables. Based on these functions, an overall probability is calculated for the object to be signal or background. Three working points are typically provided for the electron PID: ordered by background rejection power, they are referred to as Loose, Medium and Tight. Each working point includes the tighter one. The PID operating points are optimised in several bins of η and E_T, since the distributions of electron showers depend on the amount of material the electron crosses and on its energy.

In addition to the ID criteria described above, this analysis requires electrons to fulfil isolation requirements. Isolation quantifies the energy of the particles produced around the electron candidate and allows to distinguish prompt electrons coming from heavy resonance decays (i.e. $W \to e\nu$ and $Z \to ee$) from non-isolated candidates, such as electrons coming from converted photons produced in (heavy) hadron decays and light hadrons misidentified as electrons. The variables designed for this purpose are:

- the calorimetric isolation energy $E_T^{cone0.2}$, defined as the sum of the transverse energy of topological calibrated clusters in EM calorimeter, within a cone of ΔR[3] = 0.2 around the candidate electron cluster;
- the track isolation $p_t^{varcone0.2}$, defined as the sum of the transverse momentum of all tracks, satisfying quality requirements, within a cone of ΔR = min(0.2, 10 GeV/E_T) around the candidate electron track and originated from the reconstructed primary vertex of the hard collision.

The energy of the electrons is measured by the Liquid Argon (LAr) electromagnetic calorimeter. The LAr calorimeter allows to achieve an energy resolution, independent on η, for electrons of 100 GeV better than 1.5% ($\frac{\sigma_E}{E} = \frac{10\%}{\sqrt{E}} \oplus 0.2\%$).

[3] $\Delta R = \sqrt{(\Delta\eta)^2 + (\Delta\phi)^2}$

5.3.3 Muons

The muon spectrometer is designed to reconstruct muons, which travel in the detector much more than the other charged particles generated in the collisions, since they hardly interact with materials, they radiate bremsstrahlung far less than the electrons and are long-lived particles. The features mentioned above explain the reason why the muon systems is located in the outermost part of ATLAS, within the toroidal magnetic field and covers the pseudorapidity region $\mid \eta \mid < 2.7$. The direction of the magnetic field causes muons to bend in the R-z plane, orthogonal to the solenoid field in the ID. The muon spectrometer is composed of several sub-detectors, grouped according to two main features:

- chambers providing precision measurement of the momentum;
- chambers with fast response for on-line triggering and coarser granularity.

The first type of sub-detectors are the Monitored Drift Tube (MDT) chambers. The MDTs form the bulk of the muon spectrometer, with several layers of drift tubes, operated with Ar/CO_2 gas at 3 bar pressure. The MDT layout is projective, increasing the layer dimensions and chamber sizes as a function of the distance from the interaction point. The second type of sub-detectors provide a ϕ coordinate measurement, completing the MDT precision. Benefiting from a very fast response, they provide the on-line event selection (trigger), identifying the bunch crossing that originated an event with 99% accuracy. In the barrel region ($\mid \eta \mid < 1.05$) they consist of Resistive Plate Chambers (RPC) and in the end-caps ($1.05 < \mid \eta \mid < 2.4$) of Thin Gap Chambers (TGC). The RPC sub-system has planes arranged in three cylindrical layers around the z-axis; each layer is composed of two chambers and each one is able to measure both η and ϕ coordinates. The TGC sub-detector complements the MDTs, measuring the azimuthal coordinate. TGCs are segmented radially into one end-cap and forward region. The TGC wire groups measure the bending plane coordinate and the radial strips provide the ϕ measurements. In order to benefit from the expected high luminosity performance that will be provided by the Phase-I upgraded LHC, the first station of the ATLAS muon end-cap system (Small Wheel, SW) was replaced. The New Small Wheel (NSW) operates in a high background radiation region (up to 15 kHz/cm^2) while reconstructing muon tracks with high precision as well as furnishing information for the trigger. The NSW has two chamber technologies, one primarily devoted to the trigger function (small-strip Thin Gap Chambers, sTGC) and one dedicated to precision tracking (Micromegas detectors, MM). The sTGC are primarily deployed for triggering given their single bunch crossing identification capability. The MM detectors have exceptional precision tracking capabilities due to their small gap (5 mm) and strip pitch (approximately 0.5 mm). Being in a development phase, the NSW trigger was not used in 2022 and 2023. The precision of the momentum measurement for a high-p_T muon track depends on the resolution of

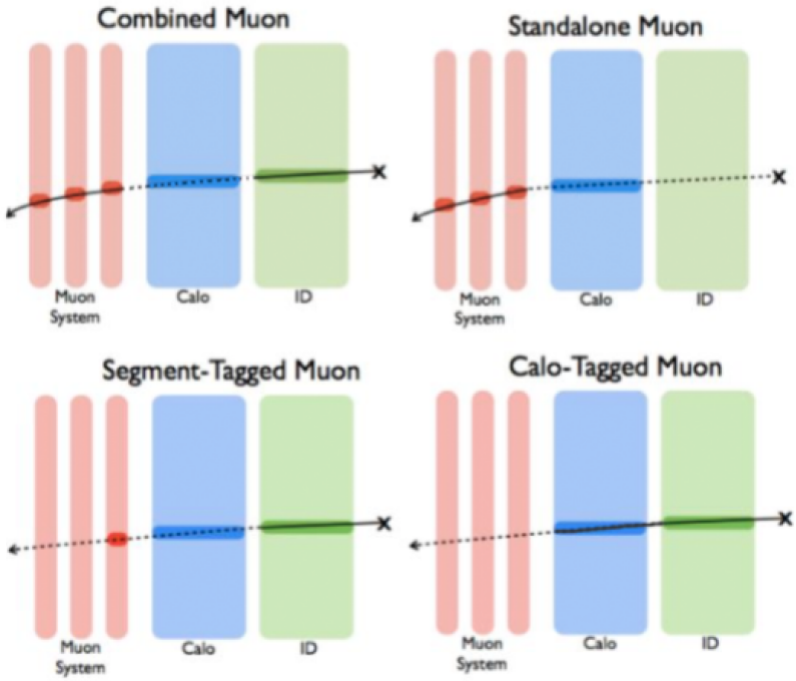

Figure 5.1: Schematic view of the four reconstruction types of candidate muons, defined according to the detection in different subdetectors.

the sagitta, namely the deviation in the R-z plane with respect to a straight line. For a high-momentum track ($p_T \approx 1$ TeV), the typical sagitta is around 500 μm. The MDTs provide a momentum measurement with $\sigma_{p_t}/p_t \approx 10\%$ resolution for 1 TeV muons, and 2-3% for lower momenta. In case of low-momentum muons, the measurement of the MS must be complemented with information from the Inner Detector.

Muon reconstruction is performed independently in the ID and MS, then the information from individual sub-detectors is combined to form the muon tracks used in the physics analyses. The first step in the muon reconstruction is the seach for hit patterns inside each muon chamber to form segments. In each MDT chamber and nearby trigger chamber, the Hough transform pattern recognition algorithm [28] is used to search for hits aligned to a trajectory in the bending plane of the detector. Then, the MDT segments are reconstructed by performing a straight-line fit to the hits found in each layer. Muon tracks are then built by fitting together hits from segments in different layers.

The ID-MS muon reconstruction is performed according to various algorithms based on the information from the ID, MS and calorimeters. Four muon types are defined according to which sub-systems are used in the reconstruction (see Fig.5.1):

- Combined (CB) muon: track reconstruction is performed independently in the ID and MS and a combined track is formed with a global fit that uses the hits from

both sub-systems;

- Segment-Tagged (ST) muon: a track in the ID is classified as a muon if, once extrapolated to the MS, it is associated with at least one local track segment in the MDT;
- Calorimeter-Tagged (CT) muon: a track in the ID is identified as a muon if it can be matched to an energy deposit in the calorimeter compatible with a minimum-ionizing particle;
- Extrapolated or Standalone (ME) muons: the muon trajectory is reconstructed based only on the MS track and a loose requirement on compatibility with origin from the IP.

Muon identification is performed by applying quality requirements that suppress background, mainly from pion and kaon decays, and select prompt muons with high efficiency and robust momentum measurement. Four muon identification operating points are provided to address the specific needs of different physics analyses:

- the Loose identification criteria are designed to maximise the reconstruction efficiency and provide good-quality muon tracks;
- the Medium identification operating point provides the default selection for muons in ATLAS. This selection minimises the systematic uncertainties associated with muon reconstruction and calibration;
- tight muons are selected to maximise the purity of muons at the cost of loosing efficiency;
- the High-p_T selection aims at maximising the momentum resolution for tracks with transverse momentum above 100 GeV.

Muons originated from the decay of heavy particles, such as W, Z or Higgs bosons, are produced isolated from other particles. The measurement of the muon isolation is therefore a powerful tool for background rejection in many physics analyses. As for electron, track-based and calorimeter-based isolation variables are defined. Track-based isolation variable $p_t^{varcone0.2}$ is defined as the scalar sum of the transverse momenta of the tracks with p_T>1 GeV in a cone of size $\Delta\mathrm{R} = \min(0.2, 10\ \mathrm{GeV}/p_t^{\mu})$ around the muon. The cone size is p_t dependent in order to improve the performance for muons produced in the decay of particles with a large transverse momentum. The calorimeter-based isolation variable $E_T^{topcone20}$ is defined as the sum of the transverse energy of topological clusters in a cone of size $\Delta\mathrm{R} = 0.2$ around the muon, after subtracting contributions from pile-up and underlying events. The isolation selection criteria are determined using the relative isolation variable, defined as the ratio of the track- or calorimeter-based isolation variables to the transverse momentum of the muon [28].

5.3.4 Jets

Hadronic collisions in ATLAS produce a variety of particles, including large numbers of quarks and gluons. These particles immediately hadronise, producing a collimated shower of particles with a net momentum equal to the initiating quark or gluon one. This shower of particles is called "jet" and is extremely common in LHC collisions. Within the terminology of event reconstruction in a detector, "jet" takes an additional meaning. Track jets are the ensemble of ID tracks by charged particles, composing the jet. However, more often, "jet" refers to the calorimeter object. The calorimeter purpose is to measure the energy of particles, and, in this case, of jets. Instead of tracks, cone-shaped groups of energy deposits are reconstructed. A jet may have tracks in the ID corresponding to the passage of the particles belonging to the jet, as well as tracks in the MS if a muon is produced as part of the jet or the hadronic calorimeter fails to absorb all the energy of the jet.

The jet reconstruction begins with the formation of calorimetric clusters, performed by a topological clustering algorithm, from a high energy seed cell [29]. Seed cells are required to have an energy significance at least 4σ above the noise level, defined as the quadratic sum of electronic and pile-up signals. Neighbour cells with energy significance higher than 2σ with respect to the noise are iteratively added to build topo-clusters. The topo-clusters group neighbour cells in the $\eta - \phi$ plane with significant energy deposit, in order to reconstruct jets. After the topo-cluster reconstruction, a splitting algorithm divides clusters in energy categories using a local energy maxima criterion.

A correct energy measurement is crucial in jet reconstruction. This is not-trivial due to the lower response of the hadronic calorimeter with respect to the electromagnetic one, the energy deposited outside the calorimeter and outside the jet, pile-up effects and noise thresholds. Jet calibration combines several complementary corrections and calibrations:

- a correction to the jet origin, which changes only the jet direction to point to the primary vertex and does not affect the energy of the jet;
- a pile-up correction, obtained by in-situ measurements depending on the number of reconstructed primary vertices, the jet pseudorapidity and the bunch spacing;
- energy and η calibration, which involves corrections for energy loss in inert material or deposited outside the jet cone;
- a residual in-situ calibration is applied only to jets in collision data and it is determined from collisions events by comparing the energy of the reconstructed jet to a reference object such as a photon, a Z or another jet.

In order to distinguish jets from pile-up, ATLAS main approach for track-based tagging is the Jet Vertex Tagger (JVT). It is derived from variables based on the sum of transverse

momentum of jet ID tracks and the number of primary vertices. The reconstruction algorithm is a multivariate (MVA) technique called k-Nearest Neighbourhood, which evaluates the probability for a jet to arise from a hard-scatter vertex. The relative probability for a jet to be of "signal-type" is computed as the ratio of the number of hard-scatter jets to the number of hard-scatter plus pile-up jets found in a local neighbourhood of the jet. According to the JVT efficiency and fake reduction, several operating points are defined: Loose, Medium and Tight.

5.3.5 Missing energy

The ATLAS geometry and coverage allows to reconstruct most of the particles produced in the collisions. The conservation of the momentum in the plane transverse to the beam axis (x - y) implies that the vector sum of transverse momenta of the collision products should be zero. To measure the momentum balance in the event, the missing transverse energy (E_T^{miss}) quantity is used. E_T^{miss} is defined as the negative vectorial sum of energy in the transverse plane of all objects reconstructed in the event. Since neutrinos do not interact with the ATLAS detector, in a Standard Model event a large E_T^{miss} is a signature of events with one or more high-p_T neutrinos. However E_T^{miss} can result from other sources, such as beam halo muons, cosmic muons and possible physics beyond SM.

The E_T^{miss} is computed as:

$$\begin{cases} E_x^{miss} = -\sum_{i=1}^{N_{cell}} E_i \sin\theta_i \cos\phi_i \\ E_y^{miss} = -\sum_{i=1}^{N_{cell}} E_i \sin\theta_i \sin\phi_i \end{cases} \tag{5.7}$$

$$E_T^{miss} = \sqrt{(E_x^{miss})^2 + (E_y^{miss})^2} \tag{5.8}$$

where E_i, θ_i and ϕ_i are the calorimeter cell energy, the polar angle and the azimuthal angle respectively. The sum excludes cells flagged as noisy by the ATLAS database and only includes cells belonging to topo-clusters in order to suppress noise.

5.4 Monte Carlo samples

Monte Carlo (MC) simulations are used to evaluate the detector efficiency and background events and, therefore, are crucial ingredients for the cross section determination.

The production of Z and W bosons was simulated with the Sherpa 2.2.12 [30] generator using next-to-leading order (NLO) matrix element (ME) for up to two partons, and leading order (LO) ME for up to five partons calculated with Comix [30] and OpenLoops [31, 32, 33] libraries. They were matched with the Sherpa parton shower [34] using the MEPS@NLO prescription [35] and the set of tuned parameters developed by the Sherpa authors. The NNPDF3.0NNLO PDF set [36] was used and the samples were normalised to a NNLO prediction [37].

An alternate sample of Z bosons was simulated with the POWHEG BOX v2 generator [38, 39, 40] at NLO accuracy of the hard-scattering processes of boson production and the decay into the electron, muon, and τ-lepton channels. The ME simulation is interfaced to PYTHIA 8.307 [41] for the modelling of the parton shower, hadronisation, and underlying event, with parameters set according to the AZNLO tune [42]. The CT10NLO PDF set [43] was used for the hard-scattering processes, whereas the CTEQ6L1 PDF set [44] was used for the parton shower. The effect of QED final-state radiation was simulated with PHOTOS++ 3.64 [45, 46]. Likewise, an alternate sample of W bosons was simulated with the POWHEG BOX v2 configuration described above for the Z bosons sample. Both samples have been used for systematic studies.

Samples of diboson final states were simulated with SHERPA 2.2.12, including off-shell effects and Higgs boson contributions where appropriate. Fully leptonic final states and semileptonic final states, where one boson decays leptonically and the other hadronically, were generated using MEs at NLO accuracy in QCD for up to one additional parton and at LO accuracy for up to three additional parton emissions. Since no dedicated calculation for the cross section is available currently, the same k-factors as used in Run 2 analyses, evaluated to be 0.91, are used for the 13.6 TeV normalisation.

The production of a top-quark pair $t\bar{t}$ and the associated production of a single top-quark and a W boson Wt were modelled using the POWHEG BOX v2 generator interfaced to PYTHIA 8.307 with the parton shower tune A14 [47]. The MEs are calculated at NLO precision in QCD using the NNPDF3.0NLO PDF set. The $t\bar{t}$ sample was normalised to the cross-section prediction at NNLO in perturbative QCD including the resummation of next-to-next-to-leading logarithmic (NNLL) soft-gluon terms calculated using Top++ 2.0 [48, 49, 50, 51, 52, 53, 54].

5.5 Event selection

This analysis uses single-lepton (electron or muon) triggers: triggers requiring at least one low transverse momentum electron or muon in the final state. The single-lepton triggers differ in their requirements on the object identification, isolation and p_{T}. The triggers with lower p_{T} requirements impose tighter identification and isolation criteria, while the triggers with higher p_{T} threshold require looser (or no) identification and isolation criteria. A logical OR is applied between the triggers. To operate in the plateau regime of the triggers, events are required to have leptons with $p_{\mathrm{T}} > 27\,\mathrm{GeV}$. Additionally, the leptons that fired the trigger are required to have the offline and online object be matched in space.

In the Z-boson analysis, events in the dilepton channels are required to have exactly two same flavour leptons (electrons or muons) with opposite electric charge. The invariant mass of the dilepton pairs is required to be in the mass range $66 < m_{\ell\ell} < 116\,\mathrm{GeV}$.

In the W-boson analysis, events are required to have exactly one identified and iso-

lated lepton, $E_{\mathrm{T}}^{\mathrm{miss}} > 25$ GeV, and a transverse mass $m_{\mathrm{T}}^{W}=\sqrt{2p_{\mathrm{T}}^{\nu}p_{\mathrm{T}}^{\ell}(1-\cos\Delta\phi^{\nu})}$ greater than 50 GeV.

All the event selections are summarised in Table 5.1.

Electron selections	
Trigger	Single electron trigger
p_{T}	$p_{\mathrm{T}} >27$ GeV
η	$\lvert\eta\rvert < 2.47$ and veto $1.37 < \lvert\eta\rvert < 1.52$ (crack region)
ID	Tight LH
Isolation	Tight_Varcone
Muon selections	
Trigger	Single muon trigger
p_{T}	$p_{\mathrm{T}} >27$ GeV
η	$\lvert\eta\rvert < 2.5$
ID	Medium
Isolation	Tight_Varcone
W boson selections	
N leptons	exactly 1
$E_{\mathrm{T}}^{\mathrm{miss}}$	$E_{\mathrm{T}}^{\mathrm{miss}} > 25$ GeV
m_{T}	$m_{\mathrm{T}} > 50$ GeV
Z boson selections	
N leptons	exactly 2 same flavour opposite charged leptons
$m_{\ell\ell}$	$66 < m_{\ell\ell} < 116$ GeV

Table 5.1: Overview of the event selections.

The event selection for the $t\bar{t}$ analysis is described in detail in Ref. [55].

5.6 Background evaluation

Background contributions to the W and Z final states correspond to two main categories: electroweak (EW) and top processes, estimated using MC, and the multijet (MJ) background, which is data driven.

5.6.1 Electroweak and top backgrounds

The EW backgrounds include single boson productions, $W^{\pm} \to \tau^{\pm}\nu$ and $Z \to \tau\tau$ for both channels and $W^{\pm} \to e^{\pm}\nu$ and $W^{\pm} \to \mu^{\pm}\nu$ for the Z channels. Diboson production (WW, WZ and ZZ) can have similar signatures to single Z events if one of the bosons decays hadronically or invisibly or if leptonic decay products fail the object selection.

Likewise, $t\bar{t}$ pair and associated Wt production can result in similar signatures to Z events, if one or two W decay leptonically. For inclusive Z selections, all EW backgrounds are at sub-percentage level. The event yields of these background processes together with signals are shown in Table 5.2.

	$Z \to e^+e^-$	$Z \to \mu^+\mu^-$
$Z \to ee$	$7,690,000 \pm 240,000$	–
$Z \to \mu\mu$	–	$1.4200 \times 10^7 \pm 550,000$
$Z \to \tau\tau$	$2,740 \pm 88$	$4,050 \pm 170$
$W \to l\nu$	139 ± 9.7	40.0 ± 6.8
Top	$24,900 \pm 2,600$	$37,000 \pm 4,100$
VV	$15,000 \pm 1,100$	$24,100 \pm 1,900$
Multijet	–	–
Total	$7,730,000 \pm 250,000$	$1.4270 \times 10^7 \pm 550,000$
Data	$7,803,884$	$14,242,875$

Table 5.2: Event yields of data and predictions after the selections.

5.6.2 Multijet background

The multijet (MJ) background has major contributions from leptons produced in semi-leptonic decays of heavy quarks, in-flight pion decays, photon conversions, etc. Although this type of background processes is efficiently rejected by the isolation selection and in the W case by the $E_{\mathrm{T}}^{\mathrm{miss}}$ and m_{T}^{W} requirements, due to the large production cross section and large $E_{\mathrm{T}}^{\mathrm{miss}}$ generated through jet energy mis-measurements in the event, MJ processes still dominate the background in W-boson measurements at high-pile-up, contributing to up to around 4% of data events. Because of the difficulties in the precise simulation of these processes, data-driven techniques are used for the estimation of the MJ background based on a sophisticated ABCD method similar to the one described in [56]. Due to the significant restriction to lepton quality, like the TightLH identification of electrons, and the tight isolation working point for both electrons and muons, the fraction of the MJ background is expected to be smaller than Run 2 measurements.

While MJ constitutes a major background in the W channels, in the Z channels, the requirement of one more isolated lepton directly gets rid of almost all MJ contributions. A rough estimate based on a same-sign selection results in a MJ contribution lower than 0.1% in the Z samples, and is usually affected by charge-misidentification.

In this thesis, only the estimation of the MJ background for Z boson is discussed.

Multijet background for $Z \to \ell\ell$ events

The multijet contribution to the Z channels is studied in data by inverting the requirement on the charge of the leptons. All the remaining requirements are kept the same.

In the Z→ ee channel, 46986 events survive the Z→ ee signal requirements (N_{SS}^{66-116})[4]. The distribution of these events for both data (left) and MC (right) can be found in Figure 5.2. This distribution peaks around the Z mass value, due to events in which one of the electrons emits a photon via bremsstrahlung which further undergoes photon pair conversion. In these cases one of the electrons in the final state is charge mis-identified. The charge misidentification can happen for either of the electrons in the final state. The rate of same sign events should thus be $r = 2 \times (1 - \epsilon) \times \epsilon$, in which ϵ stands for the charge misidentification rate. This approximates to 2ϵ, due to ϵ being small, so by consequence $N_{SS}^{66-116}/N_{OS}^{66-116} = 2\epsilon$. Given that the number of opposite sign events in the signal region is 7 964 189, this means the electron charge misidentification rate (for this p_t range) is $<(46986/7964189)/2 = 0.3\%$. This number is not used in the MJ calculation but serves only as an estimate of the charge mis-identification rate.

Despite the significant contribution from charge mis-identified electrons, setting a conservative upper limit on the multijet contribution using the number of same sign events in the 'sidebands' ($66 < m_{ee} < 76$ GeV and $106 < m_{ee} < 116$ GeV) is still possible. The 1980 SS data events in the sidebands are expected to contain a major fraction of charge-flip Z→ ee events (as can be shown by multiplying the number of OS Z→ ee events in the sidebands in Figure 5.2 with the data-driven charge-flip rate of 0.6% or by taking the number directly from Z→ ee MC). Nevertheless, a very conservative upper limit on the MJ can be set by assuming that all 1980 data events counted in the sidebands are MJ events. Assuming in addition a flat multijet background over the 50 GeV mass range, the extrapolation from the sidebands to the full mass considered is possible. Using $N_{SS}^{66-116} = 50/20 \times N_{SS}^{66-76||106-116}$, a conservative estimate of $N_{SS}^{66-116} < 5/2 * 1980 = 4\,950$ is calculated. This estimate represents 0.06% of the data, between 66 GeV and 116 GeV. Therefore the MJ fraction in Z→ ee events is smaller than 0.06% and hence negligible.

Additional studies of the SS fraction in data and MC were conducted to better understand the charge-missidentification in Z→ ee events. The same selection used in data was repeated using the Z→ ee MC sample. The distribution of same and opposite sign events in signal MC can be seen in Figure 5.2 (b). The ratio between the number of same sign events (N_{SS}^{66-116}) and opposite sign events (N_{OS}^{66-116}) for the Z→ ee channel in data and MC can be found in Table 5.3. This ratio was computed inclusively, but also considering different η regions of the detector (B denotes barrel and E denotes endcap). Events were divided in 3 categories: one in which both electrons were reconstructed in the detector barrel (BB); another in which both were reconstructed the endcaps (EE); and a finally, another in which one electron was reconstructed in the barrel and the other one in the

[4]The superscript indicates the mass range taken into account.

endcap (BE). The differences in the ratios show that the rate of charge misidentification increases for electrons in more forward regions of the detector. In conclusion, the MC models the rate of electron charge miss-id within 20%.

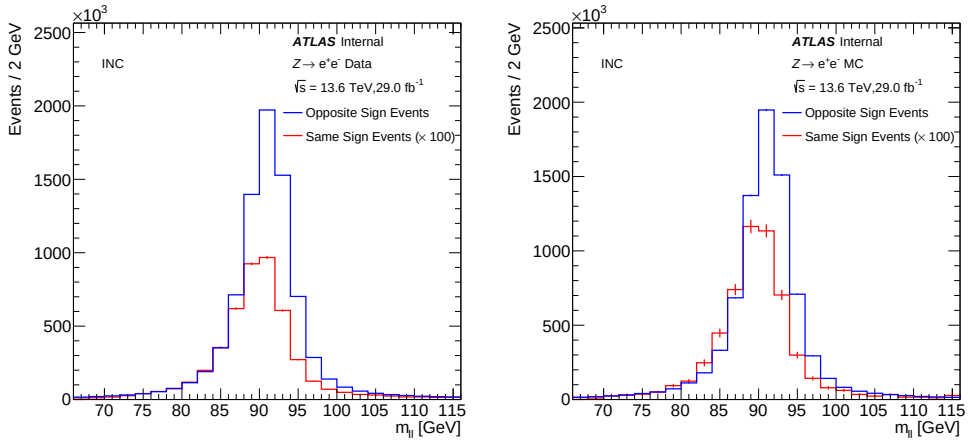

(a) (b)

Figure 5.2: Comparison between the distributions of same sign and opposite sign events reconstructed in the $Z \to ee$ channel, for (a) data and for (b) signal MC.

Region	Data	MC
Inclusive	0.00590 ± 0.00003	0.0071 ± 0.0001
BB	0.00417 ± 0.00003	0.0050 ± 0.0001
BE	0.00814 ± 0.00008	0.0099 ± 0.0004
EE	0.02183 ± 0.00021	0.0261 ± 0.0010

Table 5.3: Ratio between number of same sign events and opposite sign events for the $Z \to ee$ channel in data and MC, between 66 and 116 GeV. Results are reported for electrons reconstructed inclusively in different η regions of the detector named B for the lepton reconstructed in barrel region or E for lepton reconstructed in the endcap one.

The MJ background has also been estimated for the $Z \to \mu\mu$ channel. Figure 5.3 (a) shows the distribution of same sign events for the $Z \to \mu\mu$ channel in data, and the comparison with the distribution of opposite sign events. 528 events survive the signal region requirements (compared to 14 559 908 opposite sign events). This indicates that as expected, the multijet contribution to the $Z \to \mu\mu$ channel is smaller than $528/14\,559\,908 = 3.6 \times 10^{-5}$. Unlike in the Z→ ee case, the distribution is flat and no peak is observed originating from muon charge mis-id. Figure 5.3 (b) shows the distribution of same sign events for the $Z \to \mu\mu$ channel in MC. As expected, the ratio

of the number of same sign over opposite sign events for signal is practically 0 (1.5×10^{-7}). In conclusion, the MJ fraction in both channel is smaller than 0.1% and hence negligible, therefore they are going to be ignored in the rest of the analysis.

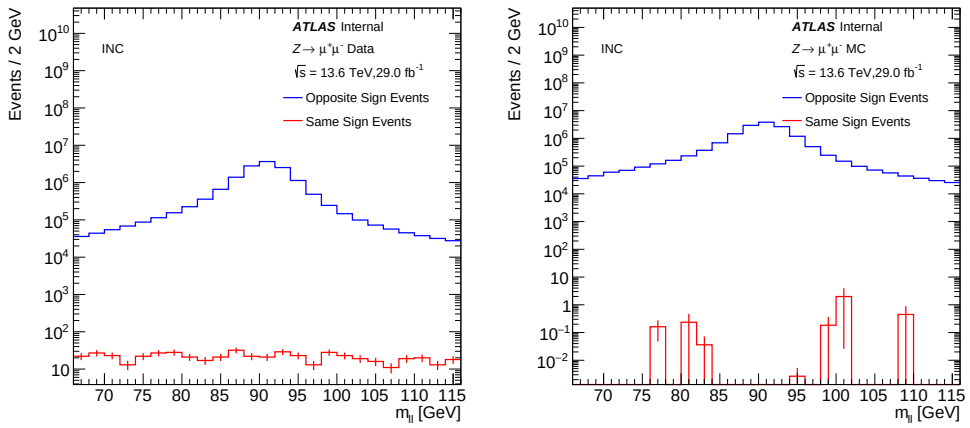

(a) (b)

Figure 5.3: Comparison between the distributions of same sign and opposite sign events reconstructed in the $Z \to \mu\mu$ channel, left for data and right for signal MC sample.

5.7 Corrections and scale variations

In general, the sum of signal and background Monte Carlo samples is expected to describe data. Moreover, a proper estimation of C_Z^{ll} requires reliable efficiencies for triggering, reconstruction and isolation. For these reasons, several event-by-event corrections are applied to simulated samples to match the data. Corrections to physics objects are given by the so-called "Scale-Factors" (SFs), defined as the ratio of efficiency in data ϵ_{data} with respect to efficiency in Monte Carlos ϵ_{MC}: SF $= \epsilon_{data}/\epsilon_{MC}$.

Other corrections applied at this stage take into account lepton calibration and number of pileup vertices in the event. The pileup re-weighting makes the distribution of MC events as a function of the number of reconstructed primary vertices similar to the distribution observed in data. Scale Factors, calibrations and Pileup reweighting are provided by specific tools within the ATLAS Framework, with associated statistical and systematic uncertainties. The uncertainty on the signal and background events is evaluated by varying within $\pm1\sigma$ the nominal value of corrections and scale factors.

In the following, a list of all the ATLAS tools employed in the analysis and the corresponding corrections and uncertainties is presented:

- Muon SFs: correct for muon reconstruction, identification, trigger and calibration differences between data and Monte Carlo;
- Electrons SFs: correct for different electron energy scale/resolution calibration, identification, trigger and isolation between data and Monte Carlo;
- JET: correct for jet energy scale (JES), resolution (JER) and JVT difference between data and Monte Carlo;
- Pileup: adjust MC pileup to data.

None of the MC used for this analysis was able to reproduce well the p_t distribution of the Z boson. To model it better during this analysis, I calculated an additional SF. The Z p_t distribution was calculated at N3LO+N3LL using as PDF PDF4LHC21 and setting $\mu_r = \mu_F = \sqrt{m_{ll}^2 + p_t^2}$. Since the prediction at are compunationally heavy, a variable bin width was used. I calculated the same distribution at truth level with MC samples. The bin-by-bin ratio of these two distributions give the value of the SF that needs to be applied (Fig 5.4). By applying this additional SF, the MC prediction agrees better at high p_t (see Fig. 5.5). The disagreement at low p_t is due to missing higher order corrections. The distribution of other observable are reported in Appendix C

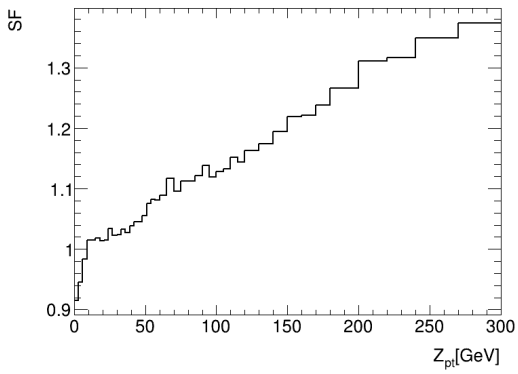

(a) $Z \to ee$ *with Powheg+Pythia*

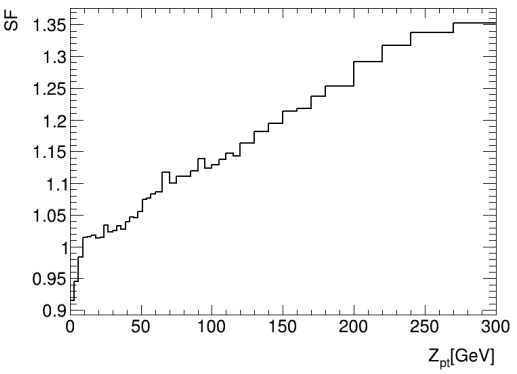

(b) $Z \to \mu\mu$ *with Powheg+Pythia*

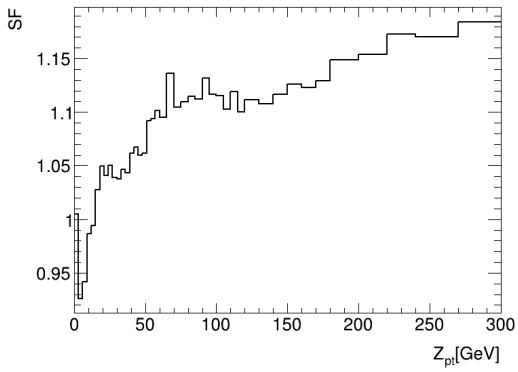

(c) $Z \to ee$ *with Sherpa*

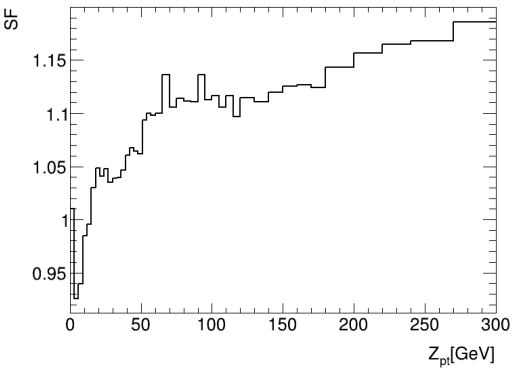

(d) $Z \to \mu\mu$ *with Sherpa*

Figure 5.4: SF used to correct p_t^Z distributions as function of p_t^Z for different channel and different MC samples.

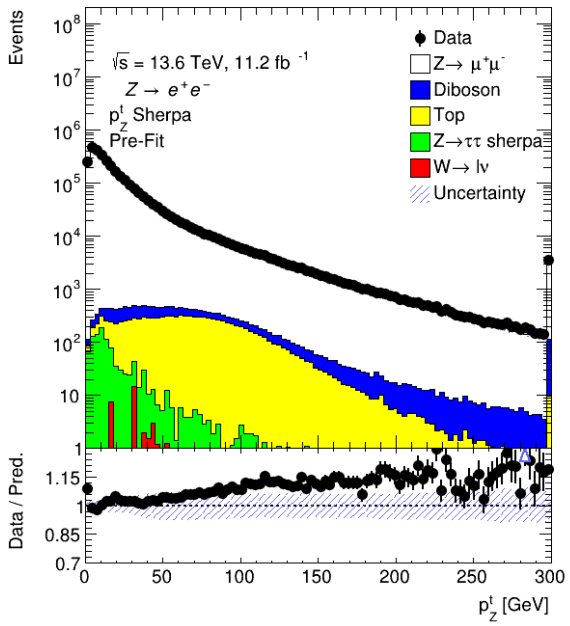

(a) $Z \to ee$ *uncorrected*

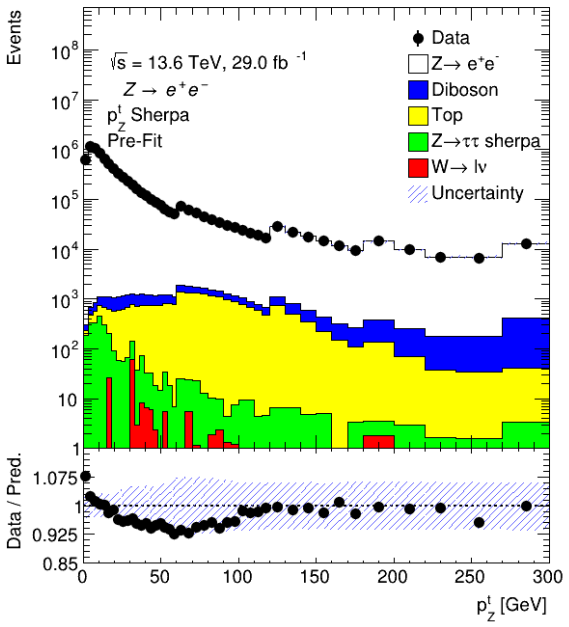

(b) $Z \to ee$ *corrected*

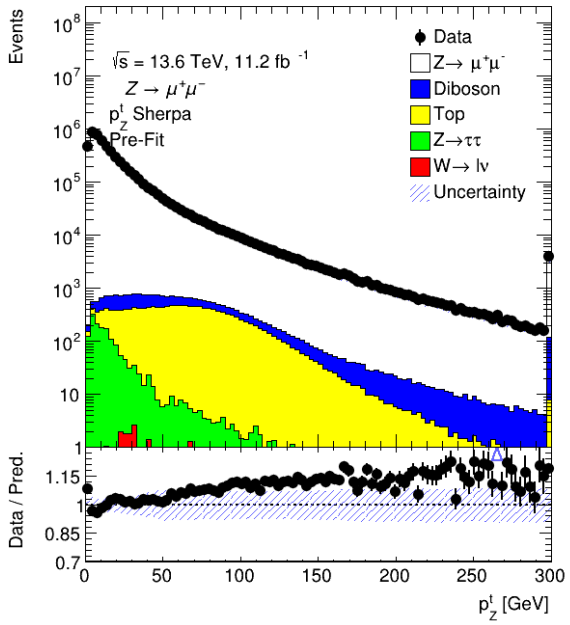

(c) $Z \to \mu\mu$ *uncorrected*

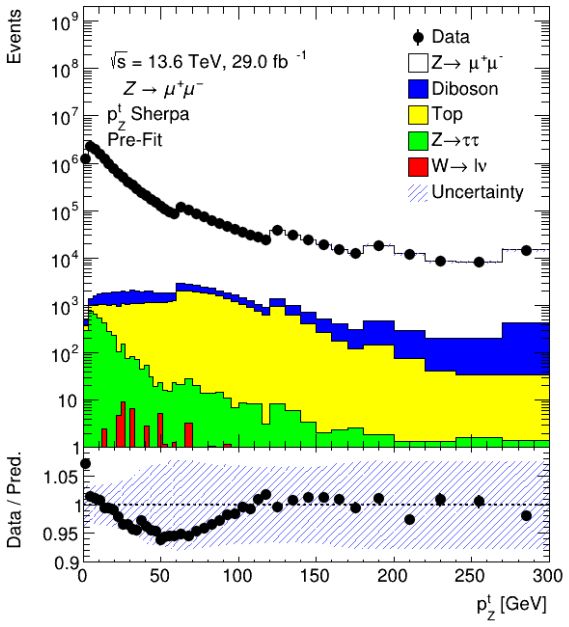

(d) $Z \to \mu\mu$ *corrected*

Figure 5.5: Comparison of the distribution of p_t^Z without using the additional SF (on the left) and with the correction (on the right).

5.8 C_Z and A_Z evaluation

5.8.1 C_Z evaluation

The systematic uncertainties on C_Z are due to the corrections applied to physics objects, to the order of approximation of the Monte Carlo generator and to the PDF choice. To evaluate the impact of the MC gnenerator and PDF, two different MC are used: Poweg+Pythia and Sherpa. For the event counting, the most used MC is Poweg+Pythia. The contributions to the systematic uncertainties in the determination of the correction factor C_Z are summarised in Table 5.4 for the electron channel and in Table 5.5 for the muon channel. A pruning of all systematics below 0.1% is performed.

Parameter	Nominal	Up	Down	Up(%)	Down(%)
Nominal	0.369				
Stat				0.057	-0.06
Pileup		0.358	0.366	-1.15	1.08
Reco		0.365	0.360	0.63	-0.63
ID		0.375	0.350	3.47	-3.41
Isol		0.367	0.358	1.18	-1.17
Trigger		0.363	0.362	0.18	-0.19
SIMPLIFIED ID		0.362	0.363	-0.14	0.14
SIMPLIFIED ID		0.362	0.363	-0.12	0.11
SIMPLIFIED ID		0.361	0.364	-0.44	0.44
SIMPLIFIED ID		0.363	0.362	0.10	-0.10
SIMPLIFIED ID		0.363	0.362	0.19	-0.19
JVT		0.367	0.358	1.34	-1.32

Table 5.4: Systematic uncertainties on C_Z for the channel Z→ee using Poweg+Pythia.

In the electron channel, the main contribution on uncertainties arises from the electron identification. In this analysis, the contribution of the ID SF was studied by separating each contribution (SIMPLIFIED ID) or by combining all together (ID). Moreover, for this analysis, the reconstruction and isolation SF were not yet fully available therefore they were set to 1 with conservative uncertainty to cover all possible deviations. For the muon channel, instead, the biggest uncertainties come from JVT, since the SF was in a preliminary phase, and the choice of the mass window for muon calibration [28] and the different isolation in Poweg and Sherpa.

Parameter	Nominal	Up	Down	Up(%)	Down(%)
Nominal	0.652				
Stat				0.0002	-0.0002
Pileup		0.650	0.653	-0.25	0.22
Trigger STAT		0.653	0.651	0.13	-0.062
Trigger SYST		0.654	0.649	0.36	-0.43
ID MATCHING		0.653	0.651	0.13	-0.13
ID TRUTH		0.654	0.649	0.35	-0.35
Isol MLLWINDOW		0.665	0.639	1.99	-1.97
Isol SHERPA POWHEG		0.663	0.641	1.66	-1.65
JVT		0.688	0.671	5.52	2.93
MUON SCALE CB		0.651	0.653	-0.057	0.12

Table 5.5: Systematic uncertainties on C_Z for the channel Z$\rightarrow \mu\mu$ using Poweg+Pythia.

5.8.2 A_Z evaluation

The geometrical acceptance A_Z is used to extrapolate the cross section measurement from the fiducial to the full phase-space in the specified invariant mass window. The main systematic is due to the different MC modelling and different PDF sets. To evaluate this contribution, a comparison between Poweg+Pythia and Sherpa has been done. The value of A_Z in each channel is:

$$A_Z^{ee} = 0.3691 \oplus 0.005(syst) \oplus 0.0002(stat) = 0.3691 \pm 0.005$$

$$A_Z^{\mu\mu} = 0.3695 \oplus 0.004(syst) \oplus 0.0001(stat) = 0.3695 \pm 0.004$$

5.9 Results and comparison with theoretical calculation

5.9.1 Theoretical predictions

The cross sections have been computed up to NNLO+NNLL QCD and NLO EW accuracy using the `DYTurbo-1.3.1` [57, 58, 59, 60] and `ReneSANCe-1.3.3` [61, 62], and combining them by means of an additive prescription, as used in the W/Z cross section measurement in 7 TeV ATLAS data [63]. Calculations are performed using different PDF sets: PDF4LHC21 [64], CT18 [65], MSHT20 [66, 67, 68], NNPDF4.0 [69], ABMP16 [70], ATLASpdf21 [71].

QCD scale uncertainties are evaluated using the standard 7-points variations for the renormalisation scale μ_R and factorisation scale μ_F, which corresponds to varying

μ_R and μ_F independently by factors of 1/2 and 2 to the combinations of $(\mu_R, \mu_F) = (\mu_R/2, \mu_F/2), (2\mu_R, 2\mu_F), (\mu_R, 2\mu_F), (2\mu_R, \mu_F), (\mu_R, \mu_F/2)$ and $(\mu_R/2, \mu_F)$ and taking the envelope of the predictions as error estimate.

In Table 5.6, fiducial NNLO+NNLL QCD + NLO EW W and Z cross sections are reported. Results are presented for each PDF set and are supplemented with PDF and scale variations error. Total cross sections have been computed as well and they are reported in Table 5.7.

Table 5.8 reports the predictions for ratios of W^+ to W^- and $W^\pm$ to Z-boson production. The ratio of W^+ to W^--boson cross sections is mostly sensitive to the difference of u_v and d_v valence-quark distributions at low Bjorken-x [72], while the ratio of $W^\pm$ to Z constrains the strange-quark distribution.

The cross sections have also been computed with NNLO QCD + NLO EW accuracy using the `MATRIX` [73] code. The cross sections agree with the `MATRIX` results at the per-mille level, thus further validating the calculations.

PDF set	$pp \to \ell^+\ell^-$ [pb]	$pp \to \ell^-\bar{\nu}_\ell$ [pb]	$pp \to \ell^+\nu_\ell$ [pb]
CT18	$733.16^{+0.1\%,+0.5\%,+5.9\%}_{-0.1\%,-0.5\%,-6.2\%}$	$3372.54^{+0.1\%,+1.0\%,+1.7\%}_{-0.1\%,-0.9\%,-3.1\%}$	$4385.38^{+0.1\%,+0.9\%,+1.8\%}_{-0.1\%,-0.8\%,-3.0\%}$
CT18A	$750.52^{+0.1\%,+0.5\%,+3.7\%}_{-0.1\%,-0.5\%,-4.3\%}$	$3398.85^{+0.1\%,+0.9\%,+2.4\%}_{-0.1\%,-0.9\%,-2.5\%}$	$4364.99^{+0.1\%,+0.9\%,+2.3\%}_{-0.1\%,-0.8\%,-2.4\%}$
MSHT20	$747.52^{+0.1\%,+0.5\%,+2.2\%}_{-0.1\%,-0.7\%,-2.7\%}$	$3360.94^{+0.1\%,+0.9\%,+1.3\%}_{-0.1\%,-1.0\%,-1.6\%}$	$4317.57^{+0.1\%,+0.8\%,+1.4\%}_{-0.1\%,-0.8\%,-1.6\%}$
NNPDF4.0	$767.39^{+0.1\%,+0.3\%,+0.9\%}_{-0.1\%,-0.5\%,-0.9\%}$	$3463.40^{+0.1\%,+0.9\%,+0.6\%}_{-0.1\%,-0.8\%,-0.6\%}$	$4455.24^{+0.1\%,+0.8\%,+0.5\%}_{-0.1\%,-0.9\%,-0.5\%}$
PDF4LHC21	$746.14^{+0.1\%,+0.4\%,+2.8\%}_{-0.1\%,-0.6\%,-2.8\%}$	$3387.04^{+0.1\%,+1.0\%,+1.5\%}_{-0.1\%,-1.1\%,-1.5\%}$	$4345.91^{+0.1\%,+0.9\%,+1.5\%}_{-0.1\%,-1.0\%,-1.5\%}$
ATLASpdf21	$787.24^{+0.1\%,+0.4\%,+3.2\%}_{-0.1\%,-0.6\%,-4.1\%}$	$3545.58^{+0.1\%,+1.1\%,+2.5\%}_{-0.1\%,-1.0\%,-2.9\%}$	$4579.11^{+0.1\%,+1.0\%,+2.6\%}_{-0.1\%,-1.0\%,-3.0\%}$
ABMP16	$746.11^{+0.1\%,+0.6\%,+1.5\%}_{-0.1\%,-0.6\%,-1.5\%}$	$3383.72^{+0.1\%,+1.0\%,+0.9\%}_{-0.1\%,-0.9\%,-1.0\%}$	$4332.77^{+0.1\%,+0.9\%,+0.6\%}_{-0.1\%,-0.9\%,-0.6\%}$

Table 5.6: Single boson production fiducial cross-section results for a series of different PDF sets. The first error which is quoted corresponds to statistical uncertainty, the second to scale error, while the third to PDF error.

5.9.2 Event counting

Using ingredients described in the previous section, the fiducial cross sections is measured to be

$$\sigma^{fid}_{Z\to ee} = \frac{N^{data}_{ee} - N_{BKG}}{C^{ee}_Z \cdot \mathcal{L}} = \frac{N_{ee}}{C^{ee}_Z \cdot \mathcal{L}} = 724 \pm 34\,\text{pb} \tag{5.9}$$

$$\sigma^{fid}_{Z\to \mu\mu} = \frac{N^{data}_{\mu\mu} - N_{BKG}}{C^{\mu\mu}_Z \cdot L} = \frac{N_{\mu\mu}}{C^{\mu\mu}_Z \cdot \mathcal{L}} = 749 \pm 41\,\text{pb} \tag{5.10}$$

where N^{data}_{ll} is the number of selected data in channel l ($l = e, \mu$), N_{BKG} is the number of background events evaluated using MC and $\mathcal{L}$ is the luminosity. The total cross sections

PDF set	$pp \to \ell^+\ell^-$ [nb]	$pp \to \ell^-\bar{\nu}_\ell$ [nb]	$pp \to \ell^+\nu_\ell$ [nb]
CT18	$1.984^{+0.04\%,+0.5\%,+5.9\%}_{-0.04\%,-0.5\%,-6.2\%}$	$8.922^{+0.05\%,+1.0\%,+1.7\%}_{-0.05\%,-0.9\%,-3.1\%}$	$12.055^{+0.05\%,+0.9\%,+1.8\%}_{-0.05\%,-0.8\%,-3.0\%}$
CT18A	$2.010^{+0.04\%,+0.5\%,+3.7\%}_{-0.04\%,-0.5\%,-4.3\%}$	$8.962^{+0.05\%,+0.9\%,+2.4\%}_{-0.05\%,-0.9\%,-2.5\%}$	$12.087^{+0.05\%,+0.9\%,+2.3\%}_{-0.05\%,-0.8\%,-2.4\%}$
MSHT20	$1.999^{+0.04\%,+0.5\%,+2.2\%}_{-0.04\%,-0.7\%,-2.7\%}$	$8.866^{+0.05\%,+0.9\%,+1.3\%}_{-0.05\%,-1.0\%,-1.6\%}$	$11.948^{+0.05\%,+0.8\%,+1.4\%}_{-0.05\%,-0.8\%,-1.6\%}$
NNPDF4.0	$2.034^{+0.04\%,+0.3\%,+0.9\%}_{-0.04\%,-0.5\%,+0.9\%}$	$9.069^{+0.05\%,+0.9\%,+0.6\%}_{-0.05\%,-0.8\%,-0.6\%}$	$12.194^{+0.05\%,+0.8\%,+0.5\%}_{-0.05\%,-0.9\%,-0.5\%}$
PDF4LHC21	$2.000^{+0.04\%,+0.4\%,+4.6\%}_{-0.04\%,-0.6\%,-4.6\%}$	$8.911^{+0.05\%,+1.0\%,+1.5\%}_{-0.05\%,-1.1\%,-1.5\%}$	$12.012^{+0.05\%,+0.9\%,+1.5\%}_{-0.05\%,-1.0\%,-1.5\%}$
ATLASpdf21	$2.098^{+0.04\%,+0.4\%,+3.2\%}_{-0.04\%,-0.6\%,-4.1\%}$	$9.334^{+0.05\%,+1.1\%,+2.5\%}_{-0.05\%,-1.0\%,-2.9\%}$	$12.465^{+0.05\%,+1.0\%,+2.6\%}_{-0.05\%,-1.0\%,-3.0\%}$
ABMP16	$1.998^{+0.04\%,+0.6\%,+1.5\%}_{-0.04\%,-0.6\%,-1.5\%}$	$8.847^{+0.05\%,+1.0\%,+0.9\%}_{-0.05\%,-0.9\%,-1.0\%}$	$11.974^{+0.05\%,+0.9\%,+0.6\%}_{-0.05\%,-0.9\%,-0.6\%}$

Table 5.7: Single boson production total cross-section results for a series of different PDF sets. The first error which is quoted corresponds to statistical uncertainty, the second to scale error, while the third to PDF error.

PDF set	W^+/W^-	$W^\pm/Z$
CT18	$1.300^{+0.6\%}_{-0.4\%}$	$10.58^{+4.6\%}_{-5.2\%}$
CT18A	$1.284^{+0.6\%}_{-0.5\%}$	$10.34^{+3.1\%}_{-3.0\%}$
MSHT20	$1.285^{+0.7\%}_{-0.7\%}$	$10.27^{+2.1\%}_{-1.7\%}$
NNPDF4.0	$1.286^{+0.8\%}_{-0.8\%}$	$10.32^{+0.7\%}_{-0.7\%}$
PDF4LHC21	$1.283^{+0.5\%}_{-0.5\%}$	$10.36^{+2.4\%}_{-2.4\%}$
ATLASpdf21	$1.291^{+0.5\%}_{-0.4\%}$	$10.32^{+2.5\%}_{-2.2\%}$
ABMP16	$1.280^{+0.3\%}_{-0.3\%}$	$10.34^{+0.9\%}_{-0.9\%}$

Table 5.8: Predictions of the ratios of W^+ to W^- boson and $W^\pm$ to Z boson combined production cross sections in the fiducial region based on different PDF sets. The quoted error is due to PDF uncertainties.

were measured to be

$$\sigma_{Z\to ee} = \frac{N_{ee}^{data} - N_{BKG}}{A_Z^{ee} \cdot C_Z^{ee} \cdot \mathcal{L}} = \frac{N_{ee}}{A_Z^{ee} \cdot C_Z^{ee} \cdot \mathcal{L}} = 1961 \pm 95\,\text{pb} \tag{5.11}$$

$$\sigma_{Z\to \mu\mu} = \frac{N_{\mu\mu}^{data} - N_{BKG}}{A_Z^{\mu\mu} \cdot C_Z^{\mu\mu} \cdot L} = \frac{N_{\mu\mu}}{A_Z^{\mu\mu} \cdot C_Z^{\mu\mu} \cdot L} = 2027 \pm 113\,\text{pb} \tag{5.12}$$

The results in the electron and muon channels are expected to agree, according to the lepton universality predicted by the Standard Model. They are also in agreement with theoretical prediction within uncertainties.

5.9.3 Profile likelihood fit

The first step in the profile likelihood fit is the Asimov fit [74]. The main goals of Asimov fits are the evaluation of the effects of systematics on the fit and check for possible pulled or over constrained NPs. In the Asimov dataset, data are set, in each bin, to the corresponding MC predictions value (signal strength set to 1). In this case, the fit is performed on the Z invariant mass distribution in the window 66 $GeV < m_{ll} <$ 116 GeV with 2 GeV bins in both channels. The systematic uncertainties below the pruning threshold 0.1% are dropped (Fig 5.6 for Z→ee channel and 5.7 for Z→ $\mu\mu$ one).

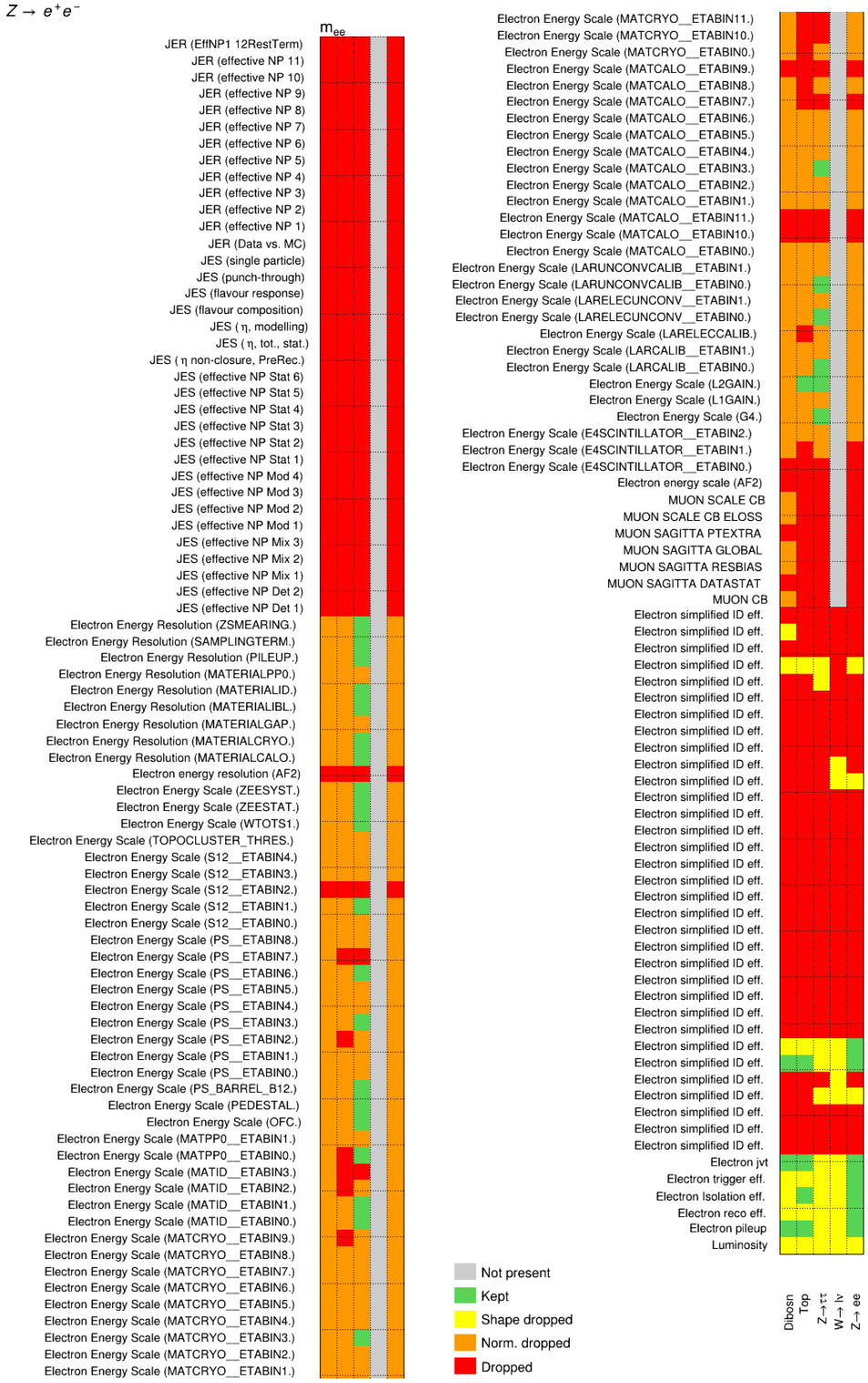

(a) (b)

Figure 5.6: Systematic pruning for $Z \to ee$ channel.

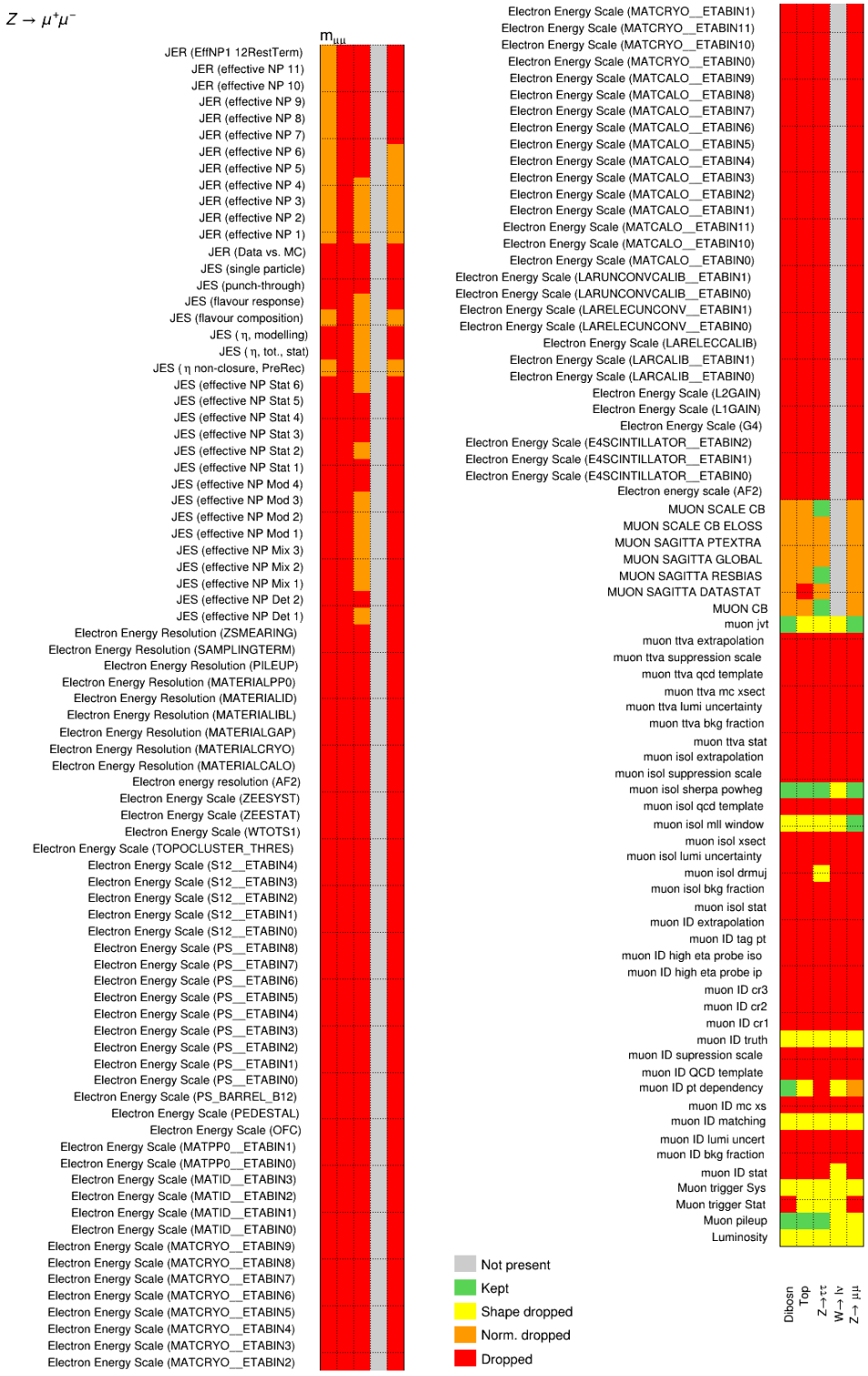

(a) (b)

Figure 5.7: Systematic pruning for $Z \to \mu\mu$ channel.

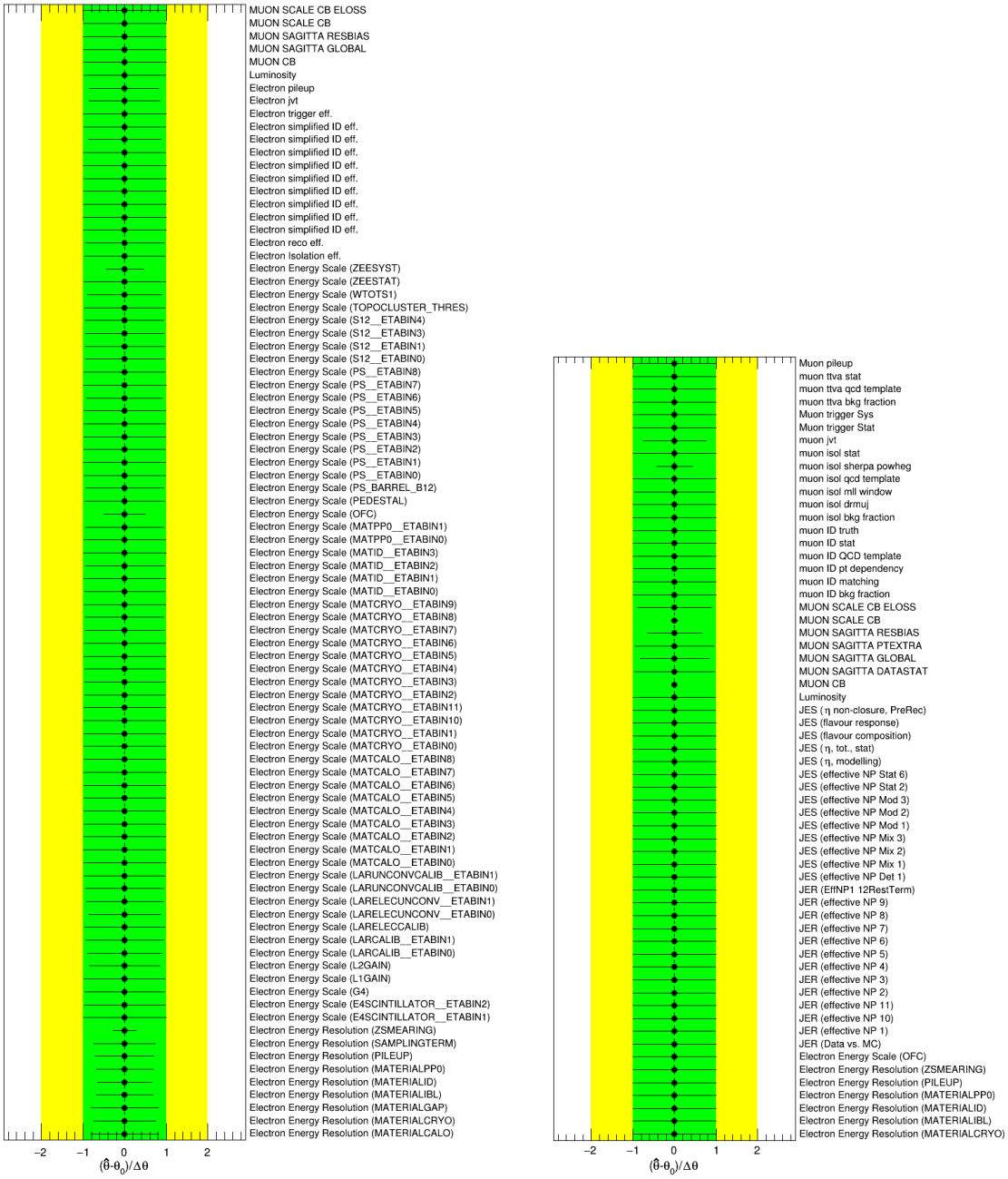

(a) (b)

Figure 5.8: Pulls for $Z \to ee$ channel (on the left) and for $Z \to \mu\mu$ (on the right) when using Asimov dataset.

Fig. 5.8 shows for each systematic θ the difference between its post-fit ($\hat{\theta}$) and pre-fit

(θ_0) value over its pre-fit uncertainty ($\Delta\theta$). For the channel $Z \to ee$, all systematics uncertainty are centered around 1 as expected. Some systematics have an error bar that is smaller than 1 σ after performing the fit, that was expected since this analysis was performed at the beginning of Run-3 with preliminary uncertainties. On the contrary, for channel $Z \to \mu\mu$ 2 systematics (muon energy scale and muon energy resolution) have no error bars. This is due to the fact that the fit is not sensitive to these systematics.

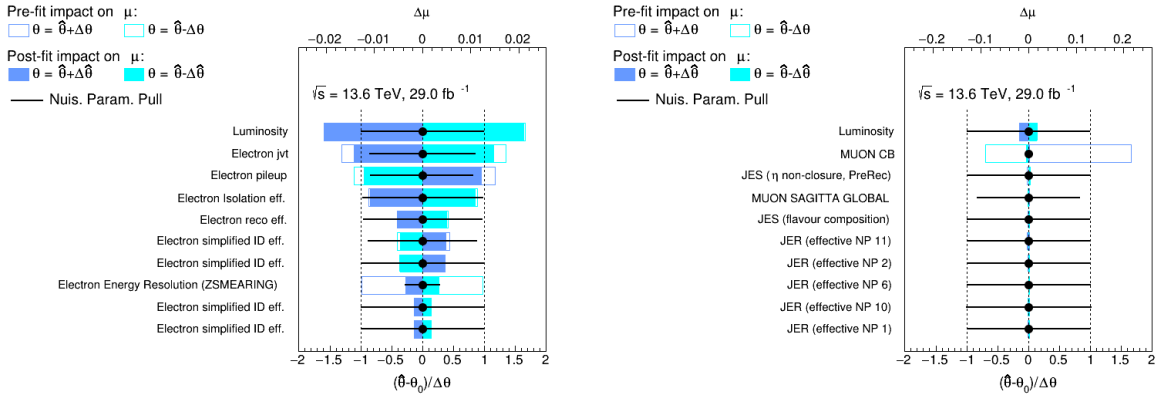

(a) (b)

Figure 5.9: Systematic uncertainties ranked by the impact on the signal strength, before and after the Asimov fit, for $Z \to ee$ channel (on the left) and for $Z \to \mu\mu$ (on the right) when using Asimov dataset.

In both channels, luminosity has the largest impact on the signal strength (Fig 5.9). For the channel $Z \to ee$, the other main systematics are JVT, pileup and isolation. For the $Z \to \mu\mu$ channel, the other main systematics are the muon energy resolution, jet energy scale and the muon sagitta, even though these systematcs have a very low impact on the signal strength.

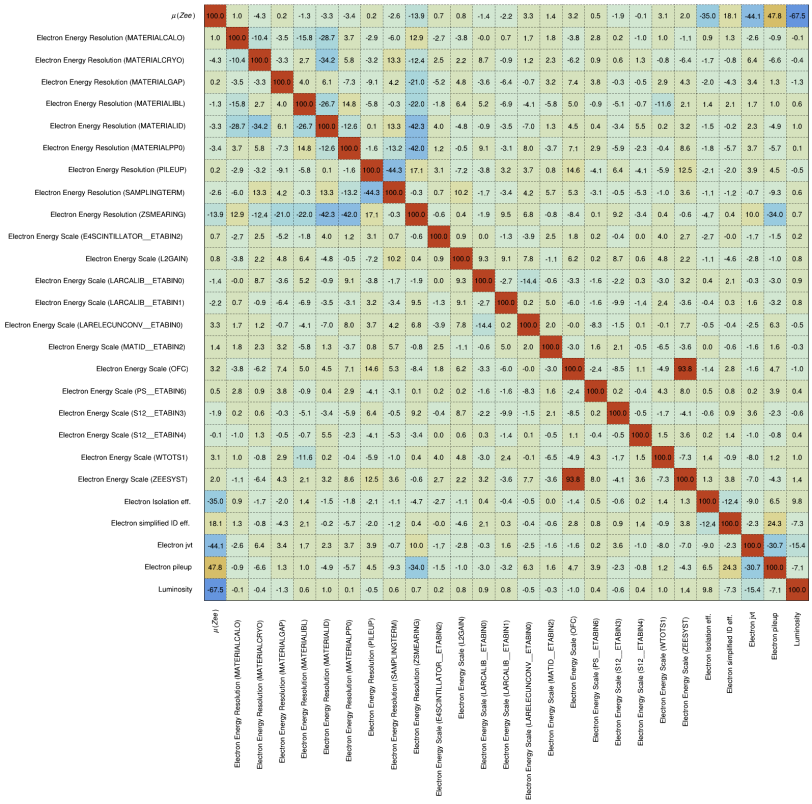

(a)

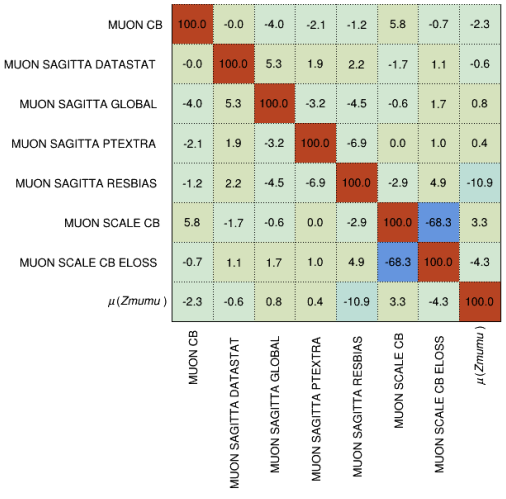

(b)

Figure 5.10: Correlation matrix for $Z \to ee$ channel (on the left) and for $Z \to \mu\mu$ (on the right) when using Asimov dataset.

In Fig 5.10 it is reported the correlation matrix in both channels. A pruning at 20% has been applied.

After checking the performance of the fit with the Asimov dataset, the fit can be performed on data. In Fig 5.11 the pulls for each systematic are reported. Almost all pulls are within 1σ away from the original value. This means that both the central values and uncertainties of each systematics is well estimated. The signal strength is compatible with 1 in both channels, as seen in Fig 5.12. The ranking of the systematic uncertainties on the signal strength is reported in Fig 5.13. As already seen with the Asimov fit, the systematic with largest impact on signal strength is the luminosity. In Fig 5.14 the invariant mass distribution before (left) and after (right) the fit for both channels.

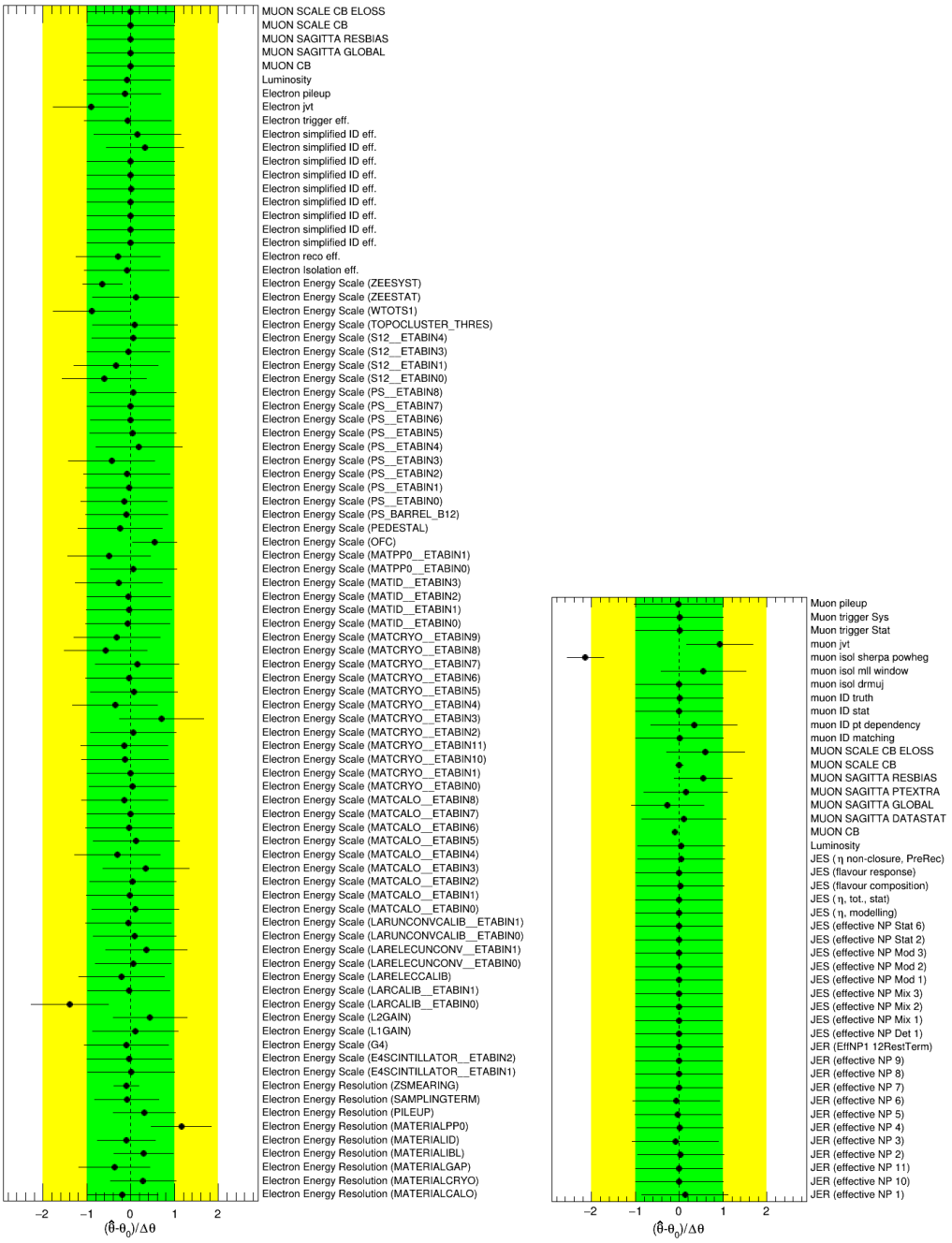

(a) (b)

Figure 5.11: Pulls for $Z \to ee$ channel (on the left) and for $Z \to \mu\mu$ (on the right) when using data.

(a) (b)

Figure 5.12: Signal strenght extracted from channel $Z \to ee$ (on the left) and from $Z \to \mu\mu$ (on the right).

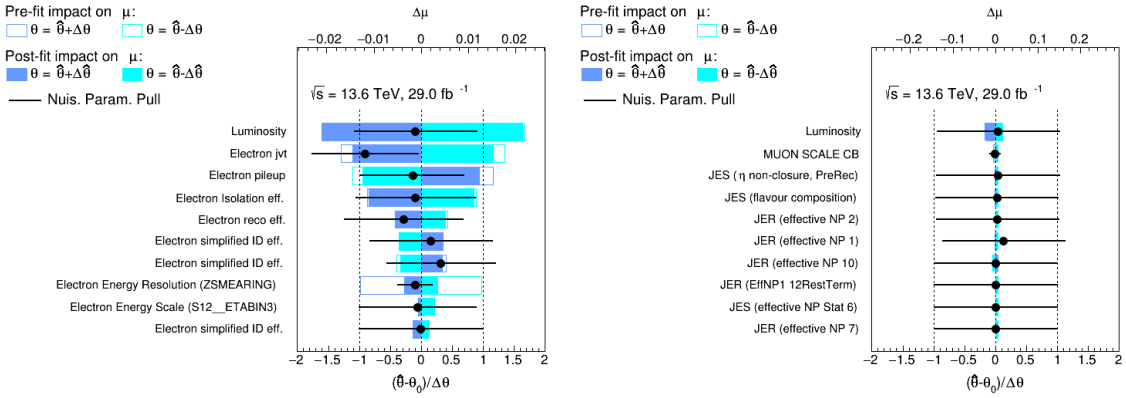

(a) (b)

Figure 5.13: Systematic uncertainties ranked by the impact on the signal strength, before and after the Asimov fit, for $Z \to ee$ channel (on the left) and for $Z \to \mu\mu$ (on the right) when using data.

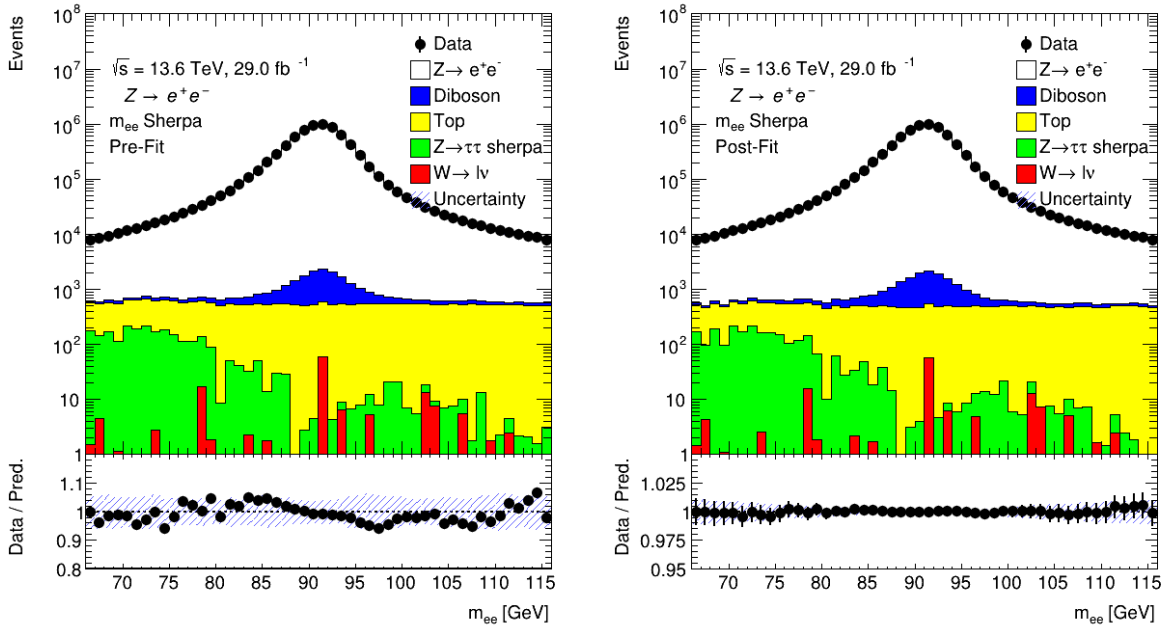

(a)

(b)

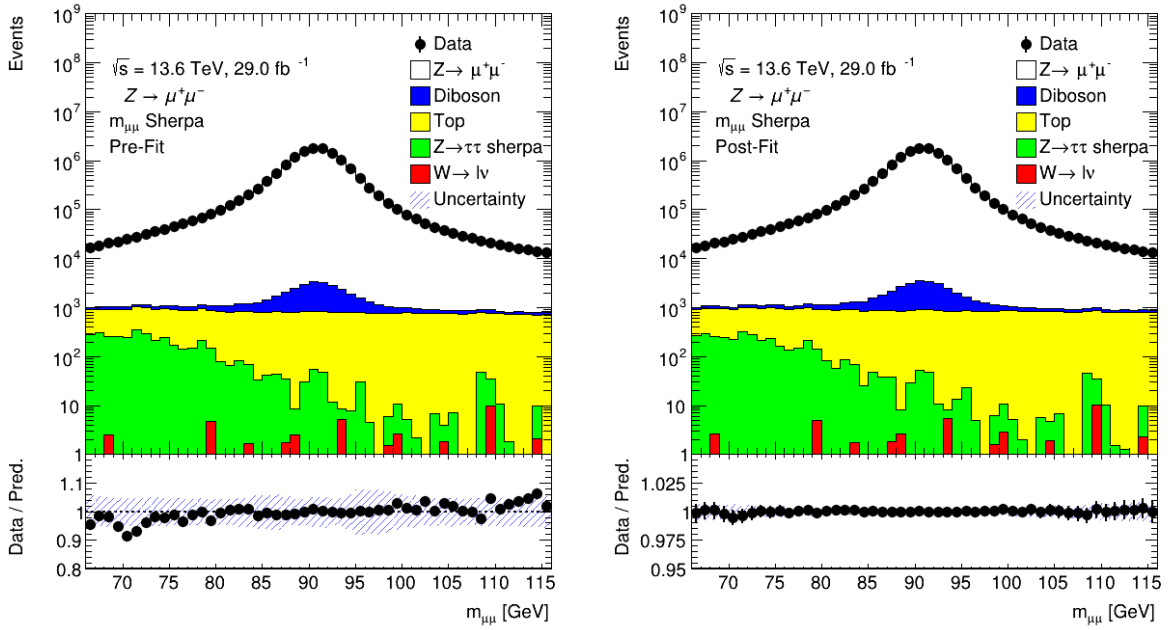

(c)

(d)

Figure 5.14: Invariant mass distribution for $Z \to ee$ channel (on the top) and for $Z \to \mu\mu$ (on the bottom) before (on the left) and after (on the right) the fit.

5.10 Combination with $t\bar{t}$ and W

In a similar way, the fit is performed also on W and $t\bar{t}$, on single bin for each channel. The comparison of data and predictions before and after fits in all regions is shown in Figure 5.15. Good agreement is observed in the single lepton and same flavour dilepton regions while in the $e\mu$ regions the data event yields are slightly lower than the predictions.

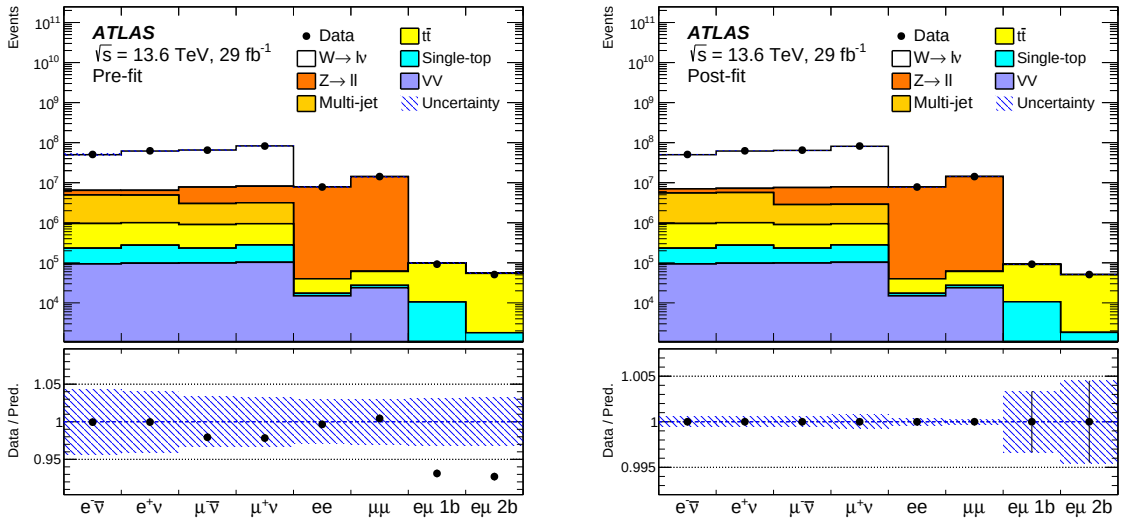

(a) (b)

Figure 5.15: Comparison of the number of data events in each channel (dots) with the predictions (stacked histograms) shown before (a) and after (b) the fits. The dashed error band in the pre-fit figure gives the total systematic uncertainty before the fit, while in the post-fit figure, it represents the statistical uncertainty derived from the fit.

The ratios of the fiducial cross sections are extracted using fits as well. For the W^+/W^--boson cross-section ratio, R_{W^+/W^-}, the W^+-boson signal strength μ_{W^+} is expressed as the product $R_{W^+/W^-}\mu_{W^-}$ thus the likelihood formula for the ratio is written as:

$$
\begin{aligned}
L(\vec{n};\mu_s,\vec{\theta}) = & \prod_{c\in W^+ \text{ channels}} \text{Pois}(n_{\text{data}}|R_{W^+/W^-}\mu_{W^-}S_c(\vec{\theta})+B_c(\vec{\theta}))\times \\
& \prod_{c\in W^- \text{ channels}} \text{Pois}(n_{\text{data}}|\mu_{W^-}S_c(\vec{\theta})+B_c(\vec{\theta}))\times \\
& \prod_{c\in Z \text{ channels}} \text{Pois}(n_{\text{data}}|\mu_Z S_c(\vec{\theta})+B_c(\vec{\theta})) \prod_{i\in \text{NPs}} G(\theta_i)\,.
\end{aligned}
\tag{5.13}
$$

Ratio	$R \pm \delta R_{\text{stat} \oplus \text{syst}}$
W^+/W^-	1.286 ± 0.022
$W^\pm/Z$	10.17 ± 0.25
$t\bar{t}/W^-$	0.256 ± 0.008
$t\bar{t}/W^+$	0.199 ± 0.006
$t\bar{t}/W^\pm$	0.112 ± 0.003

Table 5.9: Ratio of the cross sections measured with the profile likelihood fit.

The ratios $R_{W^\pm/Z}$, $R_{t\bar{t}/W^\pm}$, $R_{t\bar{t}/W^+}$, and $R_{t\bar{t}/W^-}$ are extracted in the same manner. In the latter cases, the $t\bar{t}$ inputs and uncertainties are obtained from the $t\bar{t}$ cross-section analysis at 13.6 TeV [75].

Table 5.9 reports the ratio of all the cross section combination. For the W^+, W^-, and Z boson fiducial cross sections and their ratios, an overall good agreement is observed, while the $t\bar{t}/W$ ratio results are slightly lower than the predictions for most of the PDFs considered. This is consistent with the results of the Run 3 $t\bar{t}$ cross-section measurement [75], where the measured $t\bar{t}$ cross-section is measured to be lower than the predicted value.

5.11 Luminosity measurement with Z counting

As already described in Chapter 2.10, Z boson can also be used for luminosity measurement expecially in the very first stage of a new data taking as a cross check on the calibration of the detectors. By inverting eq 5.1 we get:

$$\mathscr{L} = \frac{N_{ll}^{data} - N_{BKG}}{A_Z^{ll} \cdot C_Z^{ll} \cdot \sigma_Z^{tot} \times BR(Z \to ll)}. \tag{5.14}$$

The cross section used in this case is the mean of the Z cross sections reported in Table 5.7 ($\sigma_Z^{tot} \times BR(Z \to ll) = 2.02 \pm 0.03$ nb). Using the $Z \to ee$ channel data, the measured mluminosity is:

$$\mathscr{L} = 28.2 \pm 1.3\,\text{fb}^{-1}$$

while using $Z \to \mu\mu$

$$\mathscr{L} = 29.2 \pm 1.3\,\text{fb}^{-1}$$

In both cases, the estimated luminosity is compatible with the one provided by LUCID within uncertainties (see Chapter 2.11).

Summary

The luminosity is a fundamental parameter for the LHC, as it allows the performance of the collider to be assessed. Additionally, luminosity is directly related to cross-section processes, making its precise measurement a key aspect of the ATLAS physics program. LUCID-2, the main ATLAS luminometer during Run-2, measured luminosity with a final precision of 0.8%. While LUCID-2 is expected to meet the requirements of the ATLAS physics program for Run-3, it will not be able cope with the challenging running conditions of HL-LHC. The increased luminosity may, in fact, cause algorithm saturation, preventing luminosity measurements. Moreover, the required precision in luminosity measurement must be 1% to fulfill the ATLAS physics program's goals. Therefore, a new detector must be developed. Several detector designs have been proposed, but they need to be tested. To this end, prototypes were installed and are currently being tested during Run-3. Two of these prototypes are based on PMTs, while the third is a fiber detector.

The first PMT prototype consists of four PMTs attached to the JFC-3 shielding, equipped with both Hamamatsu R760 PMTs (LUCID-2) and Hamamatsu R1635 PMTs (new, smaller PMTs) for testing. This prototype exhibits linearity similar to LUCID-2, with no significant differences between the two PMT types. However, in terms of long-term stability, Hamamatsu R760 proved to be much more stable than Hamamatsu R1635. Simulations indicated that a detector using Hamamatsu R760 cannot reach the nominal pileup of 200 due to saturation. Two main strategies are being investigated to improve the prototype's performances:

- increase the Hamamatsu R1635 window thickness to 1.2 mm to match the one of the Hamamatsu R760 window. This solution is expected to improve its long term stability;
- increase the R760 threshold used to define a hit to reduce the detector's acceptance.

The second PMT prototype consists of two Hamamatsu R760 PMTs placed behind the JFC-3 and features very low acceptance. Its linearity is 4-5 times better than that of LUCID-2, but it exhibits larger run-to-run fluctuations, likely due to its low acceptance.

The fiber detector is composed of two independent quartz fiber bundles read out by two Hamamatsu R7459 PMTs. The PMT gain is monitored using ^{207}Bi, like all LUCID

PMTs, and an LED system is used to monitor fiber degradation. A γ-irradiation session showed that fiber transmissivity decreases more rapidly in the UV range than in the visible spectrum. To mitigate radiation damages and improve long-term stability, a Cleartran UV filter was inserted in one of the prototypes. A beam test was conducted to study the production of Cherenkov light inside the fibers. The results of these measurements will be used to develop an algorithm to correct offline the effects of radiation damage on luminosity measurements. The fiber prototype demonstrates perfect linearity both with and without UV filter. The prototype without the UV filter showed a drift in long-term stability due to fiber degradation, while the prototype with the UV filter showed no drift, though it exhibited larger run-to-run fluctuations compared to LUCID-2. The optimal design for LUCID-3 will incorporate all three prototypes: the JF detector, valued for its long-term stability and the direct calibration in vdM scans; the JN detector, with low acceptance suited for reliable online luminosity monitoring; and the fiber detector, offering perfect linearity, ideal for internal μ-correction.

The measurement of the Z boson cross section using early Run-3 data collected by the ATLAS detector at a center-of-mass energy of $\sqrt{s} = 13.6$ TeV is also presented. This analysis is among the first conducted at the start of each data-taking period, as it enables checks of detector calibration, alignment, and luminosity measurement via the Z-counting technique and, in this case, testing theoretical predictions at a new center-of-mass energy. An inconsistency was found in the distribution of the p^t of the Z boson. An additional correction factor was computed to take into account higher order correction. The cross section is measured in the electron and muon decay channels, achieving precision comparable to several NNLO QCD calculations. The measured fiducial and total cross sections are $\sigma^{fid}_{Z\to ee} = 724 \pm 34\,\text{pb}$ and $\sigma_{Z\to ee} = 1961 \pm 95\,\text{pb}$ in the $Z \to ee$ channel, and $\sigma^{fid}_{Z\to\mu\mu} = 749 \pm 41\,\text{pb}$ and $\sigma_{Z\to\mu\mu} = 2027 \pm 113\,\text{pb}$ in the $Z \to \mu\mu$ channel. A profile likelihood fit was performed to validate the results obtained with the event counting. Cross-section ratios with W and $t\bar{t}$ were also computed. The W^+/W^- and $W^\pm/Z$ ratios are in good agreement with theoretical predictions, while the $t\bar{t}/W$ ratio is found to be slightly lower than predictions. Using the same dataset, luminosity was also measured using the Z-counting technique proving to be consistent with the results obtained from LUCID.

Appendices

Appendix A

Activation of the Material close to LUCID

Activation of the material close to LUCID can create signals in the PMTs. Activation impact during physics runs is negligible but it can become relevant in bismuth calibration when the rate of the signals is much lower. A first estimate of the activation can be done by measuring the evolution in time of number of hits in every PMT when there are no beams circulating in LHC. In 2024, a run of this kind was started 2 h after the beam dump when LHC announced that there will be no beam for at least 24 hours. The total number of hit for each 30 s lumiblock is measured as function of the lumiblock and is reported for Bi PMT on side A (Fig. A.1) and side C (Fig. A.2), Bi2 on side A (Fig. A.3) and side C (Fig. A.4), BiM on side A (Fig. A.5) and side C (Fig. A.6) and for prototype detectors on side A (A.7) and on side C (A.8). During this test, hits seen by PMTs may come from two different sources: the ^{207}Bi deposited on the window and the particles generated by the activation of the material. Since the half-life of ^{207}Bi is of the order of 30 years, bismuth rate can be considered constant over the entire run. Almost in all PMTs, hits decrease over time exponentially with similar time constant of 0.8 h. Bi and Bi2 PMTs are less sensitive to activation compared to BiM PMTs (Hamamatsu R1635 placed inside LUCID-2). Probably this difference is due to the different window thickness. The LUCID JN PMT also see more activation compared to LUCID-2 PMTs, probably coming from the activation of the JFC-3 shielding. The amount of activation measured by JF1-A and JF2-A is much less compare to BiM. It is not yet clear if this reduction is due to the position on the JFC-3 shielding or due to the higher threshold. JF1-C hit rate was relatively constant during the entire data taking. JF3-C instead measured a decrease in the hit rate. Since these two PMTs have the same settings, the positioning of the PMT may change the activation measured by the PMT itself. Both fiber prototypes experienced a quite large decrease in hit rate. It was probably caused by the fibers themselves picking up activation.

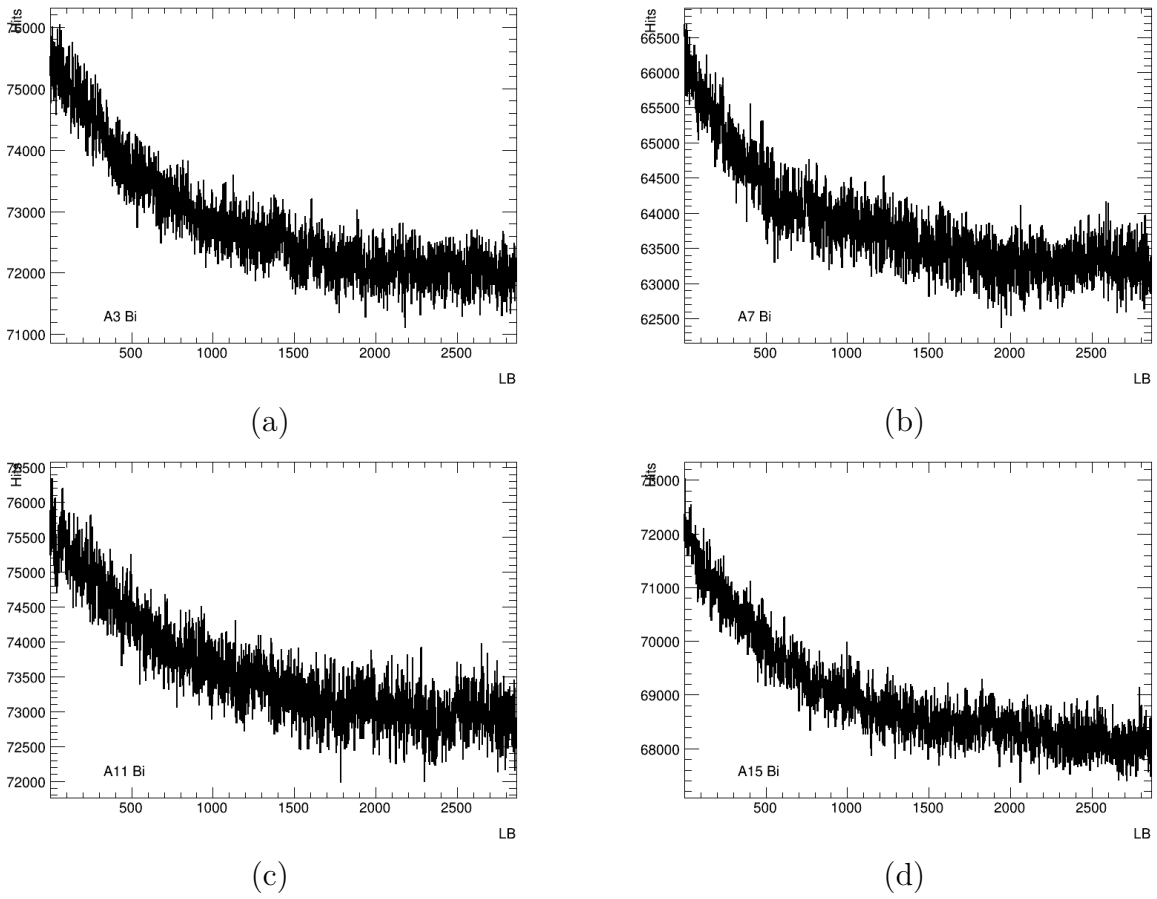

Figure A.1: Hits measured by Bi PMTs on side A as function of the lumiblock.

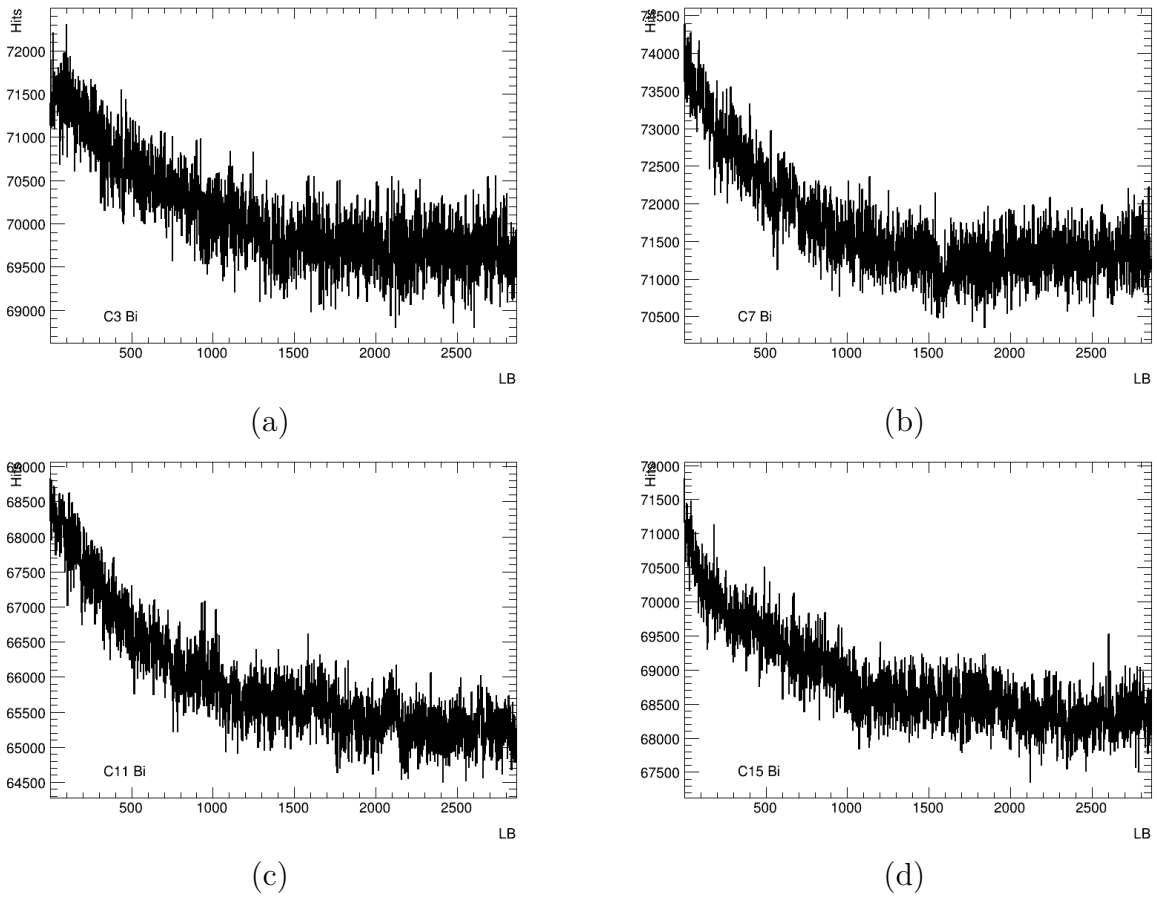

Figure A.2: Hits measured by Bi PMTs on side C as function of the lumiblock.

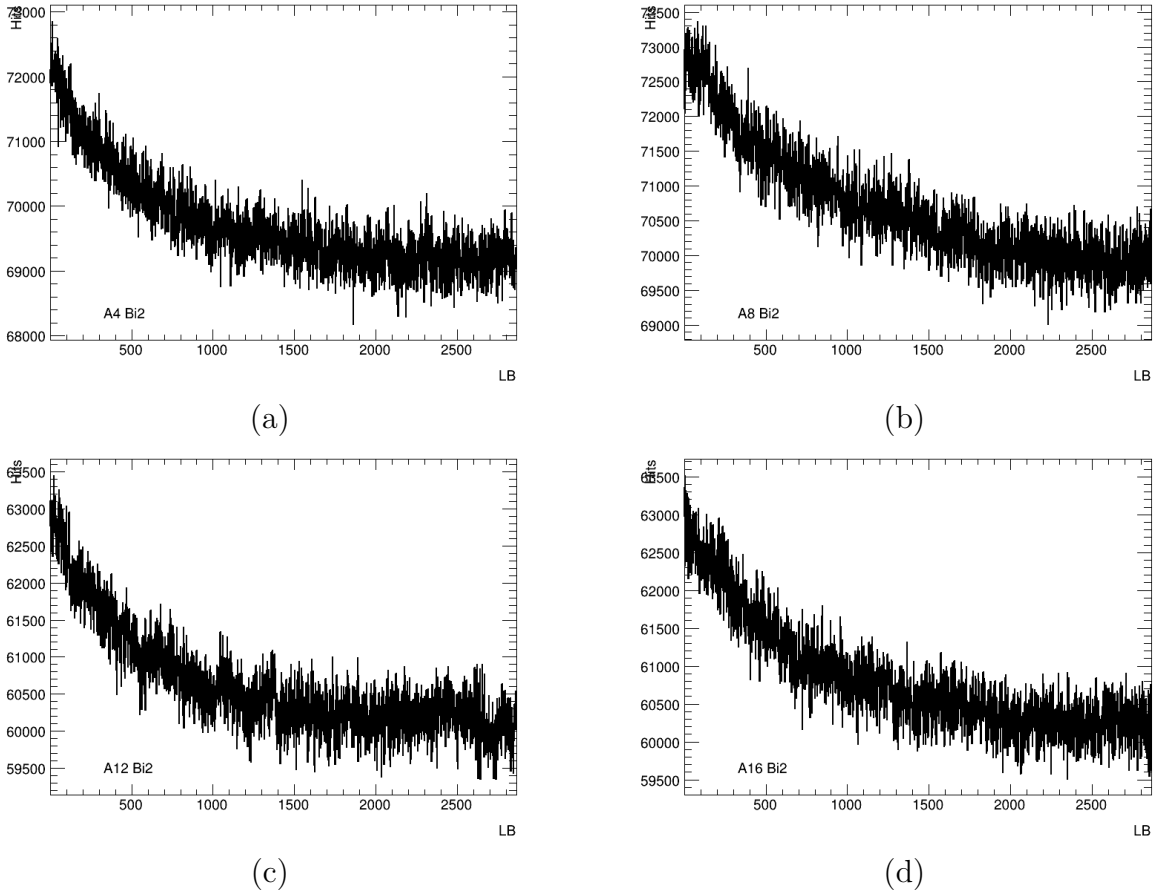

Figure A.3: Hits measured by Bi2 PMTs on side A as function of the lumiblock.

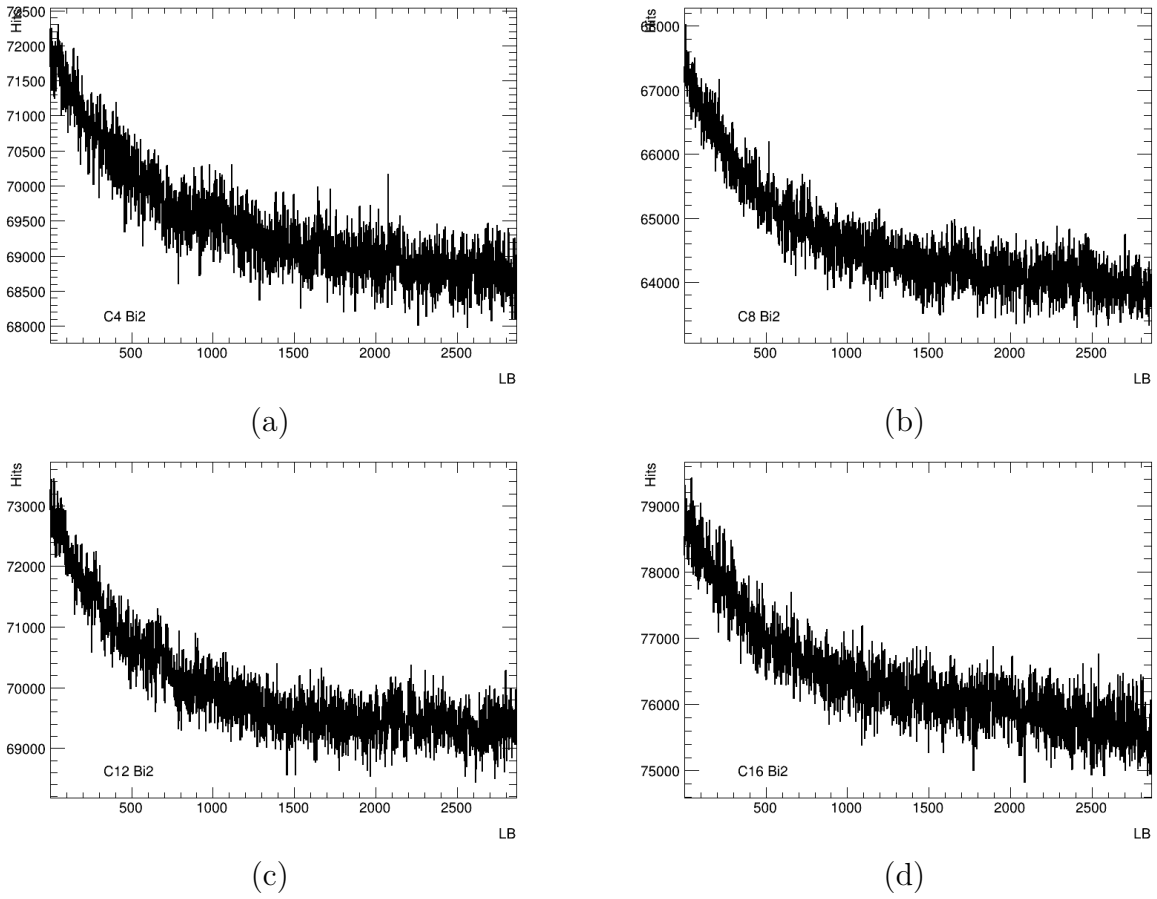

Figure A.4: Hits measured by Bi2 PMTs on side C as function of the lumiblock.

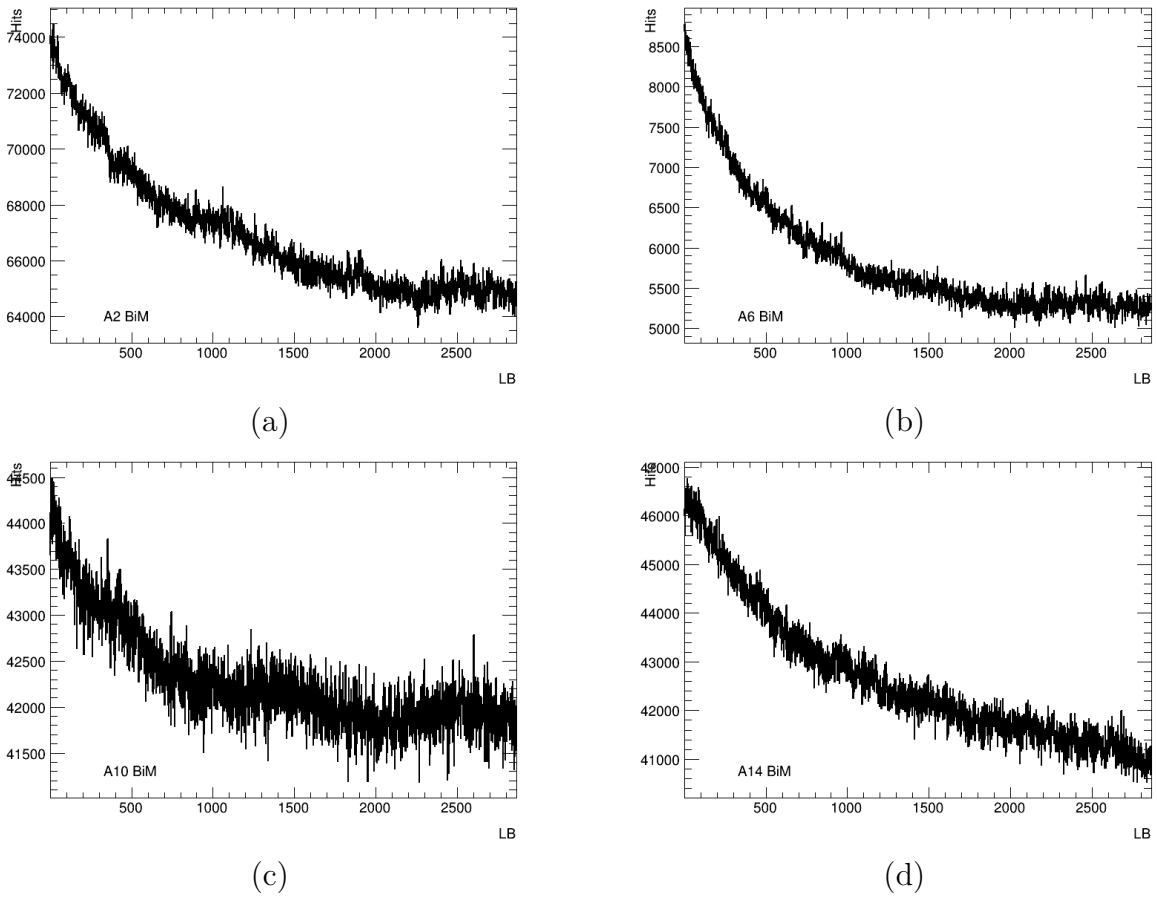

Figure A.5: Hits measured by BiM PMTs on side A as function of the lumiblock.

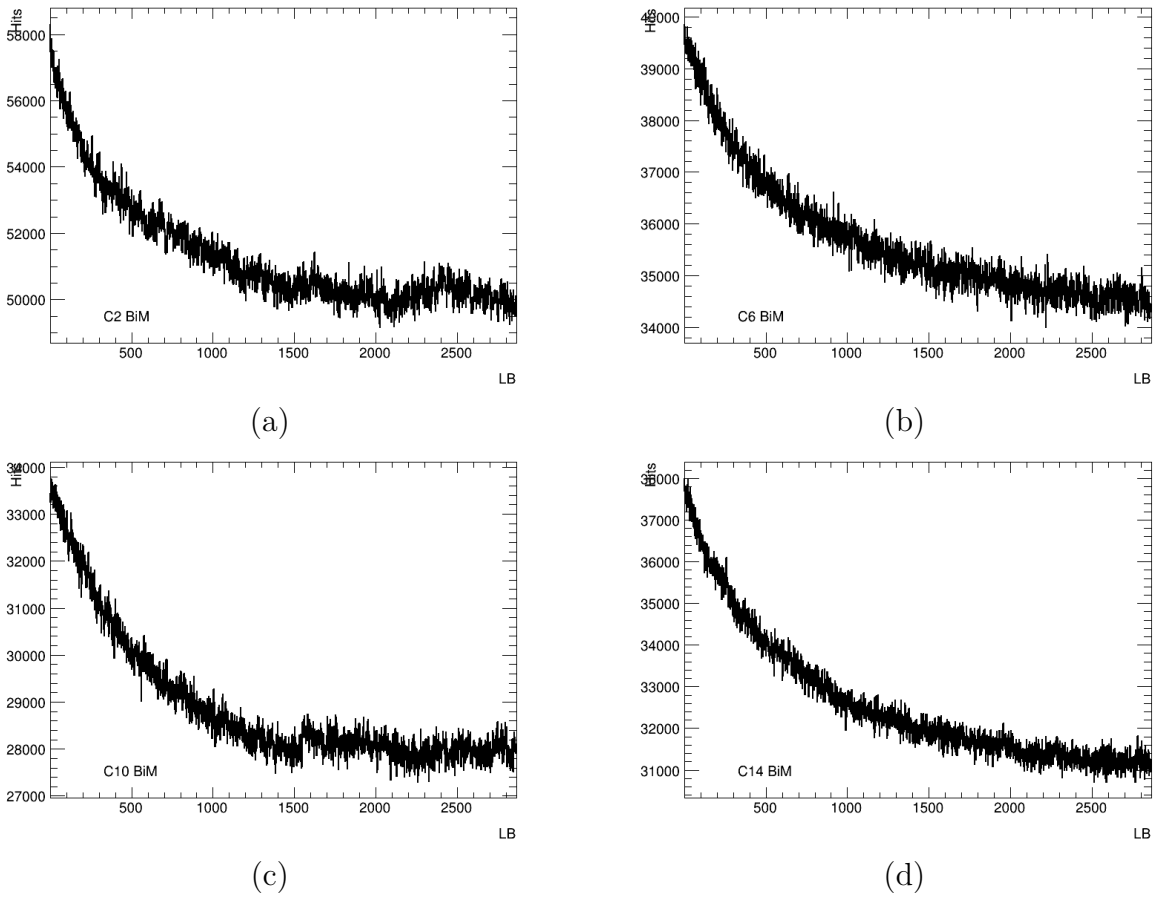

Figure A.6: Hits measured by BiM PMTs on side C as function of the lumiblock.

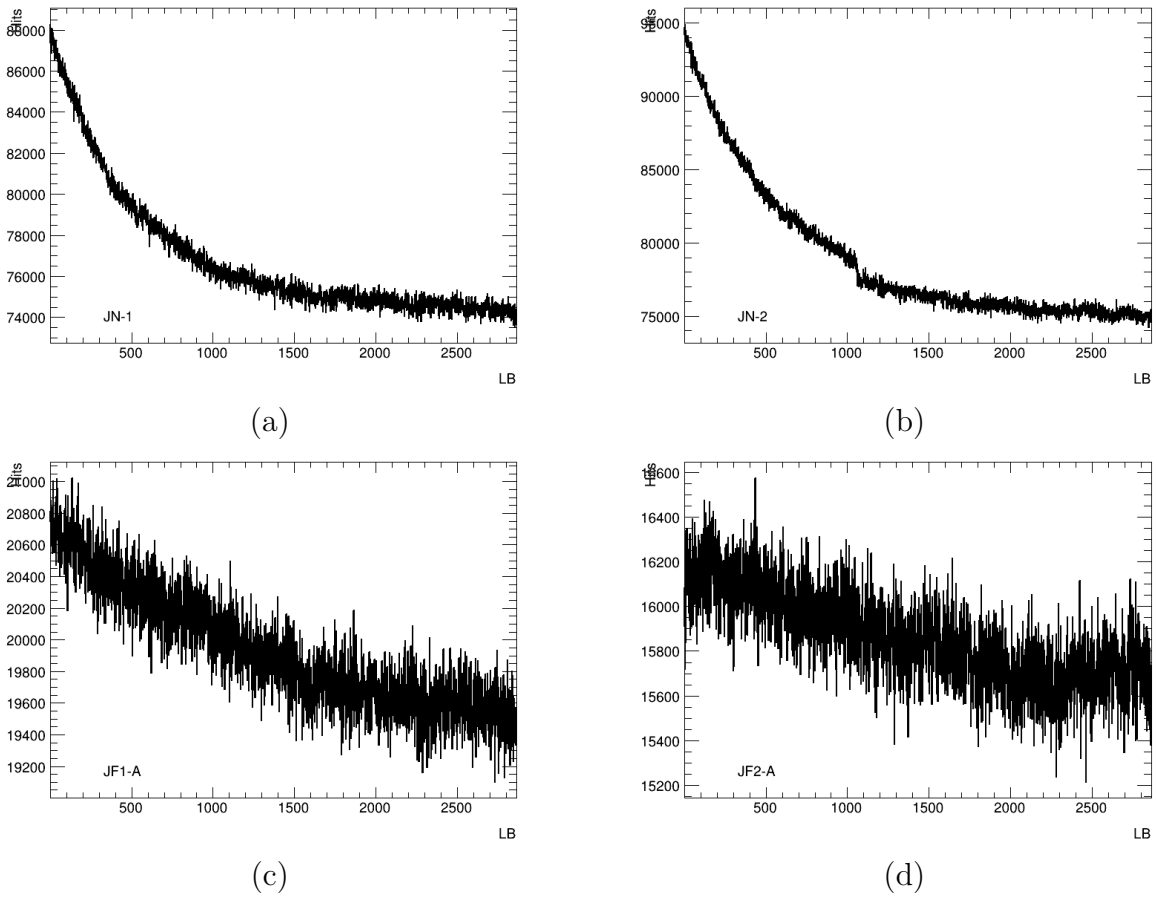

Figure A.7: Hits measured by prototypes PMTs on side A as function of the lumiblock.

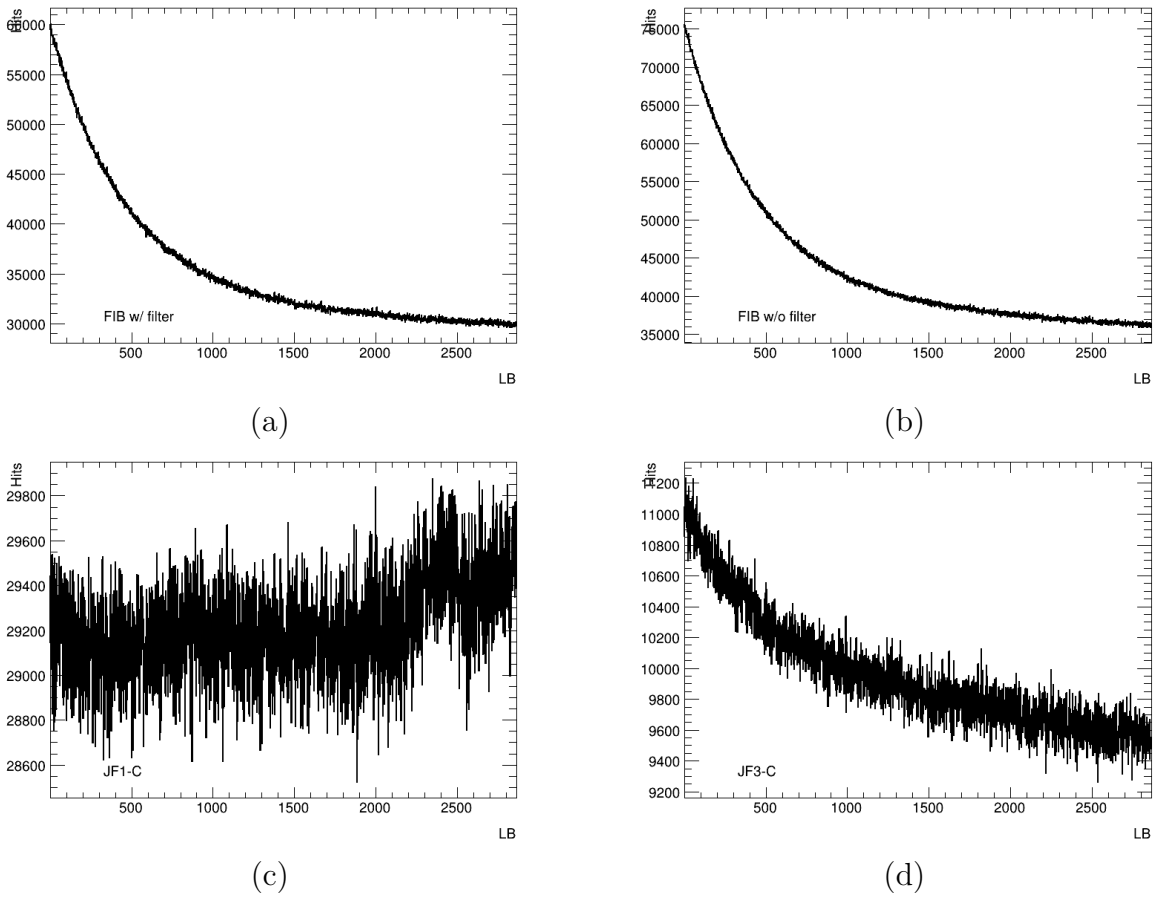

Figure A.8: Hits measured by prototypes PMTs on side C as function of the lumiblock.

Appendix B

PMTs characteristics

	R760	R1635	R7459
Diameter [mm]	13	10	28.2
Photocathode Material	Bialkali	Bialkali	Bialkali
Window Material	Quartz	Quartz	Quartz
Dynode Stages	10	8	11
Max Anode current [μA]	100	30	100

Table B.1: Summary of the main characteristics of the PMTs used in LUCID-2 and LUCID-3 PMTs

Appendix C

$Z \to ll$ control plots

In this section, the kinematic distributions of Z events at detector level, after passing the full selection chain, are presented. Figure C.1 shows the transverse momentum (p_t) of the leading lepton, while Figure C.2 shows the p_t of the sub-leading lepton. The rapidity and transverse momentum (p_t) of the reconstructed Z boson are shown in Figures C.3 and C.4, respectively.

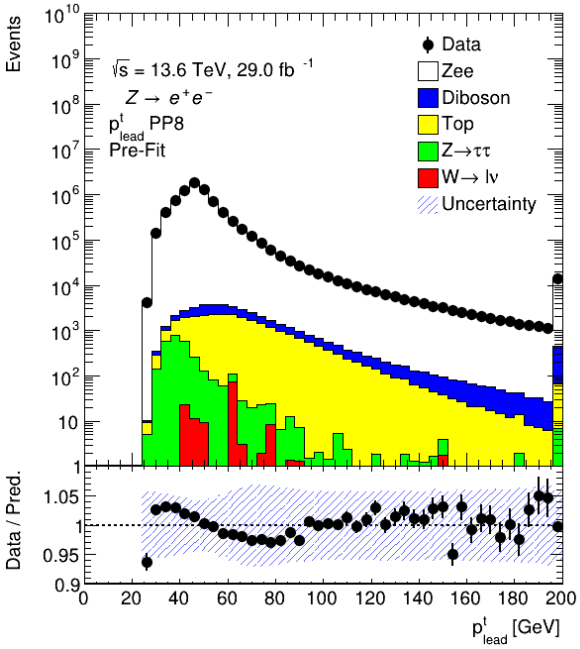

(a) $Z \to ee$, Powheg+Pythia

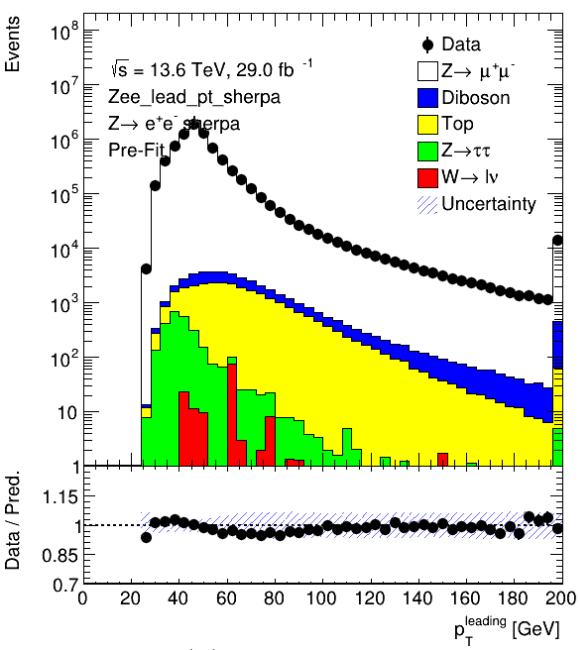

(b) $Z \to ee$, Sherpa

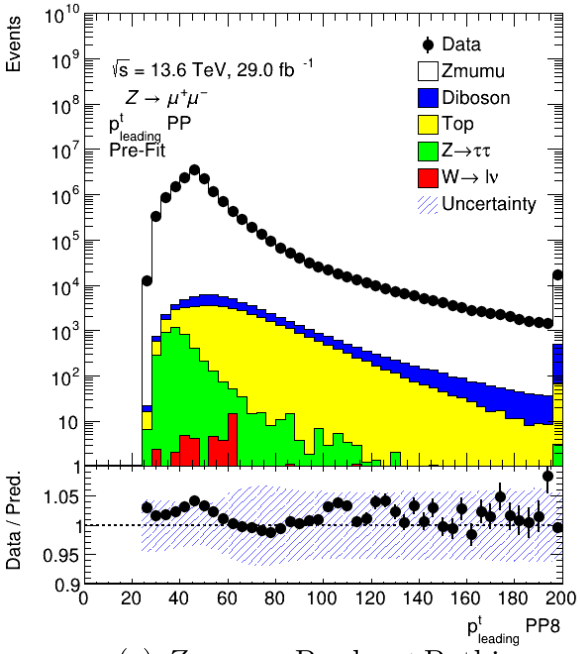

(c) $Z \to \mu\mu$, Powheg+Pythia

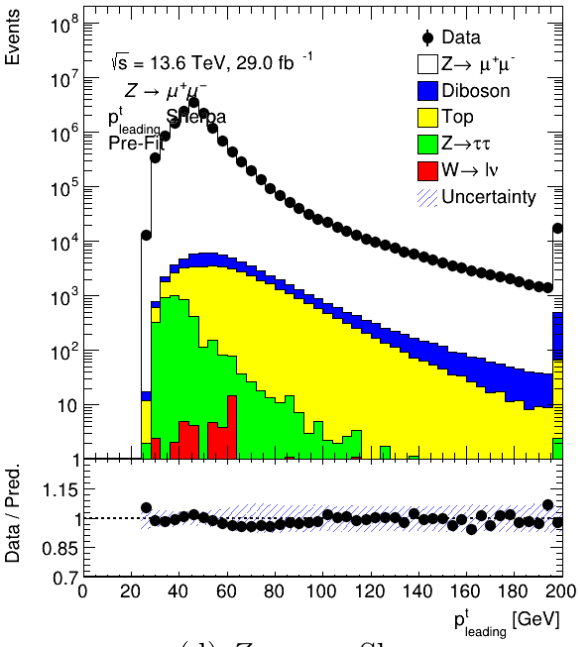

(d) $Z \to \mu\mu$, Sherpa

Figure C.1: Distribution of the p_t for leading lepton using Powheg+Pythia and Sherpa

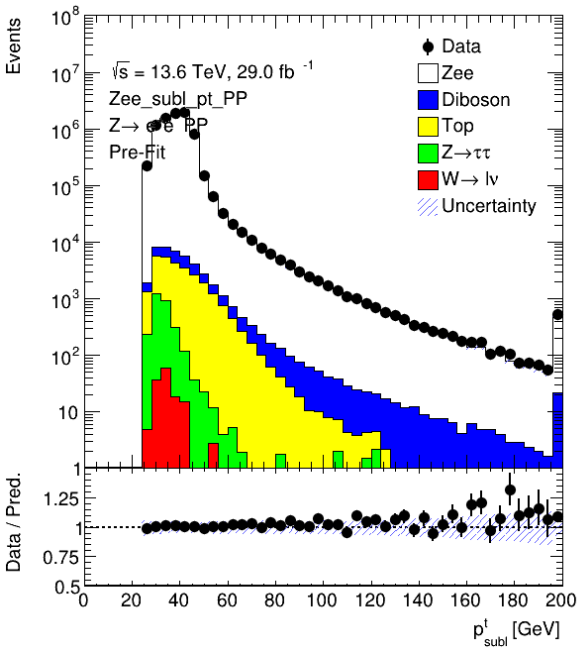

(a)$Z \to ee$, Powheg+Pythia

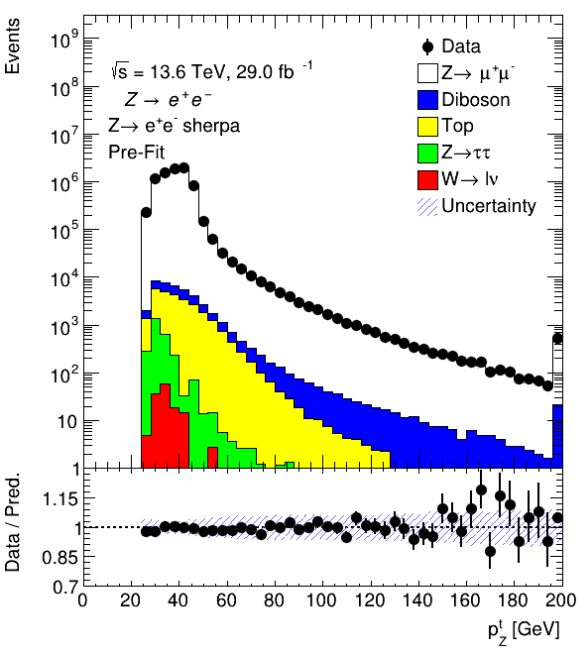

(b)$Z \to ee$, Sherpa

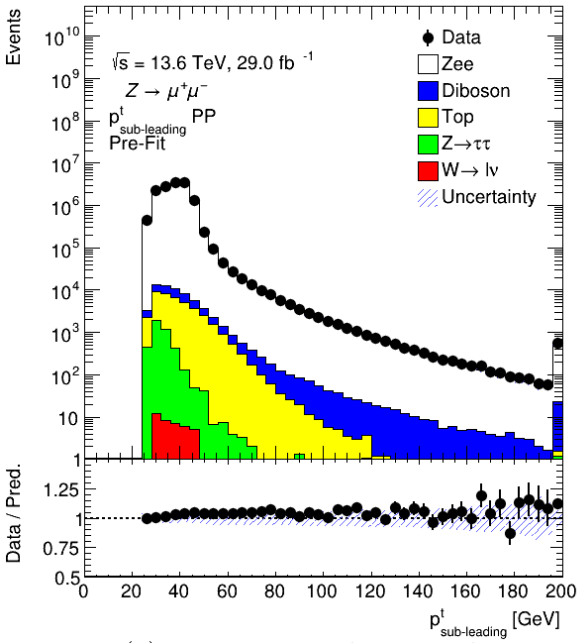

(c)$Z \to \mu\mu$, Powheg+Pythia

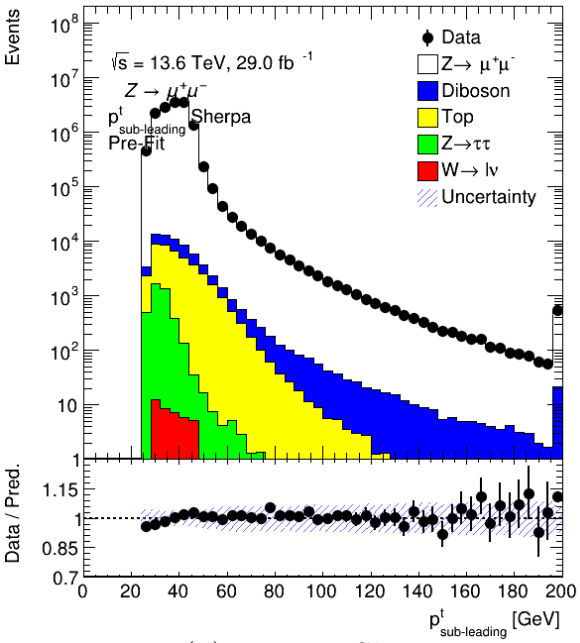

(d)$Z \to \mu\mu$, Sherpa

Figure C.2: Distribution of the p_t for subleading lepton using Powheg+Pythia and Sherpa

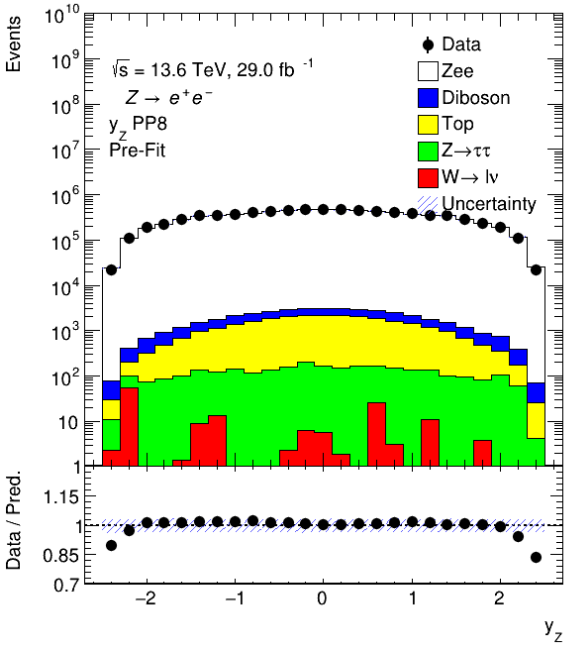

(a)$Z \to ee$, Powheg+Pythia

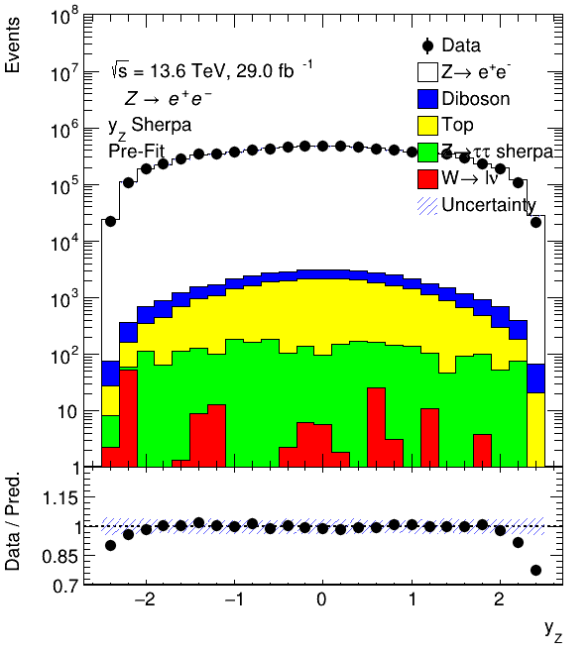

(b)$Z \to ee$, Sherpa

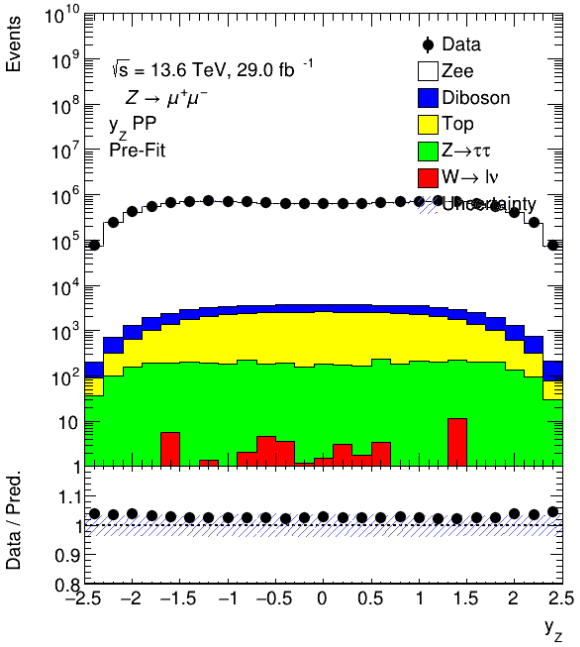

(c)$Z \to \mu\mu$, Powheg+Pythia

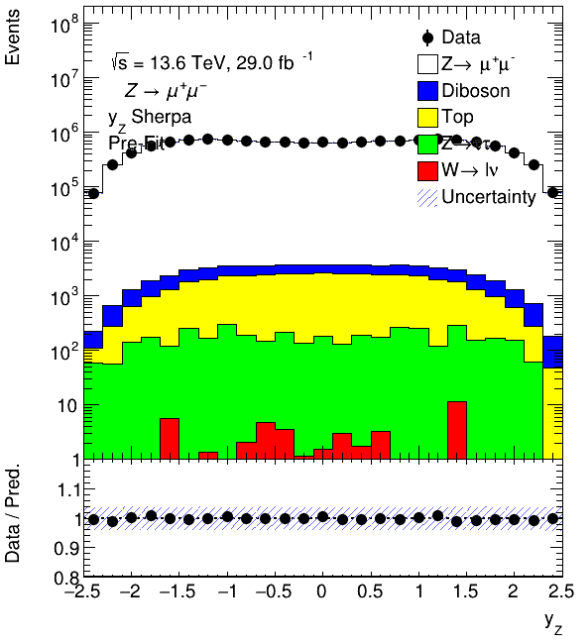

(d)$Z \to \mu\mu$, Sherpa

Figure C.3: Distribution of the y_Z using Powheg+Pythia and Sherpa

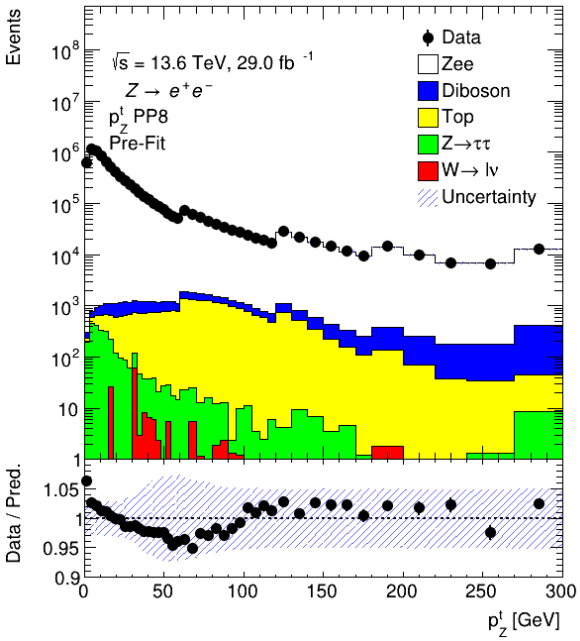

(a)$Z \to ee$, Powheg+Pythia

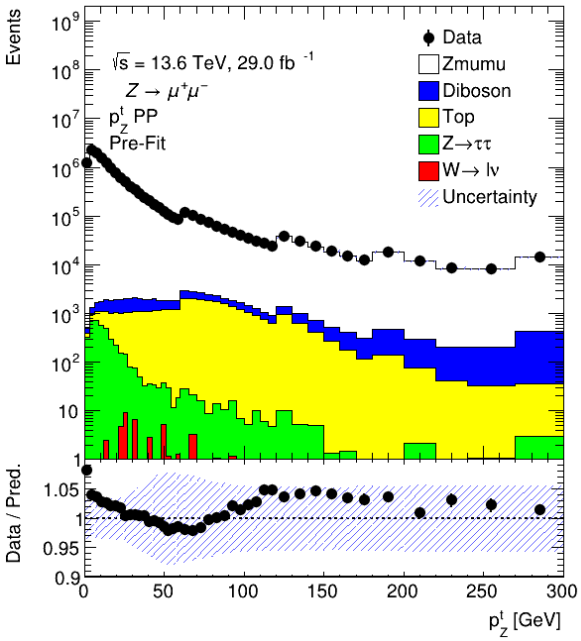

(c)$Z \to \mu\mu$, Powheg+Pythia

Figure C.4: Distribution of the p_Z^t using Powheg+Pythia and Sherpa

Bibliography

[1] J Rossbach and P Schmüser. "Basic course on accelerator optics". In: (1994). DOI: 10.5170/CERN-1994-001.17. URL: https://cds.cern.ch/record/247501.

[2] B.J. Holzer. "Lattice Design in High-energy Particle Accelerators". In: (2014), pp. 61–100. DOI: 10.5170/CERN-2014-009.61. arXiv: 1601.04913. URL: https://cds.cern.ch/record/1982419.

[3] Alexander Wu Chao et al. *Handbook of accelerator physics and engineering*. World scientific, 2023.

[4] P. Grafström and W. Kozanecki. "Luminosity determination at proton colliders". In: *Progress in Particle and Nuclear Physics* 81 (2015), pp. 97–148. ISSN: 0146-6410. DOI: https://doi.org/10.1016/j.ppnp.2014.11.002. URL: https://www.sciencedirect.com/science/article/pii/S0146641014000878.

[5] ATLAS Collaboration. "Luminosity determination in pp collisions at s=7 TeV using the ATLAS detector at the LHC". In: *The European Physical Journal C* 71 (2011), pp. 1–37.

[6] *Luminosity determination in pp collisions at $\sqrt{s}$ = 13 TeV using the ATLAS detector at the LHC*. Tech. rep. All figures including auxiliary figures are available at https://atlas.web.cern.ch/Atlas/GROUPS/PHYSICS/CONFNOTES/ATLAS-CONF-2019-021. Geneva: CERN, 2019. URL: https://cds.cern.ch/record/2677054.

[7] S van der Meer. *Calibration of the effective beam height in the ISR*. Tech. rep. Geneva: CERN, 1968. URL: https://cds.cern.ch/record/296752.

[8] Thomas Sven Pettersson and P Lefèvre. *The Large Hadron Collider: conceptual design*. Tech. rep. 1995. URL: https://cds.cern.ch/record/291782.

[9] D. Acosta et al. "The CDF Cherenkov luminosity monitor". In: *Nuclear Instruments and Methods in Physics Research Section A: Accelerators, Spectrometers, Detectors and Associated Equipment* 461.1 (2001). 8th Pisa Meeting on Advanced Detectors, pp. 540–544. ISSN: 0168-9002. DOI: https://doi.org/10.1016/S0168-9002(00)01294-8. URL: https://www.sciencedirect.com/science/article/pii/S0168900200012948.

[10] G. Avoni et al. "The new LUCID-2 detector for luminosity measurement and monitoring in ATLAS". In: *JINST* 13 (2018), p. 07017.

[11] Takashi Mitani. *Input Mezzanine Board for the Fast Tracker (FTK) at ATLAS*. Tech. rep. ATL-COM-DAQ-2018-154, 2018.

[12] ATLAS Collaboration. *Early Inner Detector Tracking Performance in the 2015 data at $\sqrt{s}$ = 13 TeV*. Tech. rep. Geneva: CERN, 2015. URL: https://cds.cern.ch/record/2110140.

[13] ATLAS Collaboration. "Luminosity determination in pp collisions at s s= 8 TeV using the ATLAS detector at the LHC". In: *The European Physical Journal C* 76 (2016), pp. 1–45.

[14] ATLAS Collaboration. *The LUCID 3 detector for the ATLAS Phase-II Upgrade*. Tech. rep. Geneva: CERN, 2021. URL: https://cds.cern.ch/record/2780604.

[15] R Xiang et al. "Experimental studies of dark current in a superconducting rf photoinjector". In: *Physical Review Special Topics-Accelerators and Beams* 17.4 (2014), p. 043401.

[16] Chris Quigg. *Gauge theories of strong, weak, and electromagnetic interactions*. CRC Press, 2021.

[17] F. Halzen and A.D. Martin. *Quark & Leptons: an Introductory Course in Modern Particle Physics*. Wiley student edition. Wiley India Pvt. Limited, 2008. ISBN: 9788126516568. URL: https://books.google.ch/books?id=ITQy9G62H0gC.

[18] Sheldon L Glashow. "Partial-symmetries of weak interactions". In: *Nuclear physics* 22.4 (1961), pp. 579–588.

[19] Steven Weinberg. "A model of leptons". In: *Physical review letters* 19.21 (1967), p. 1264.

[20] Abdus Salam. "Elementary particle theory". In: *Prog. Of the Nobel Symposium, 1968, Stockholm, Sweden*. Vol. 367. 1968.

[21] R Keith Ellis, W James Stirling, and Bryan R Webber. *QCD and collider physics*. 8. Cambridge university press, 2003.

[22] Martinus Veltman et al. "Regularization and renormalization of gauge fields". In: *Nuclear Physics B* 44.1 (1972), pp. 189–213.

[23] ATLAS Collaboration. "Determination of the strong coupling constant from transverse energy-energy correlations in multijet events at $\sqrt{s}$ = 13 TeV with the ATLAS detector". In: *Journal of High Energy Physics* 2023.7 (July 2023). ISSN: 1029-8479. DOI: 10.1007/jhep07(2023)085. URL: http://dx.doi.org/10.1007/JHEP07(2023)085.

[24] Alan D Martin et al. “Parton distributions for the LHC”. In: *The European Physical Journal C* 63.2 (2009), pp. 189–285.

[25] Guido Altarelli and Giorgio Parisi. “Asymptotic freedom in parton language”. In: *Nuclear Physics B* 126.2 (1977), pp. 298–318.

[26] P. Bagnaia et al. “Evidence for Z0→e+e− at the CERN pp collider”. In: *Physics Letters B* 129.1 (1983), pp. 130–140. ISSN: 0370-2693. DOI: https://doi.org/10.1016/0370-2693(83)90744-X. URL: https://www.sciencedirect.com/science/article/pii/037026938390744X.

[27] Kyle Cranmer et al. *HistFactory: A tool for creating statistical models for use with RooFit and RooStats*. Tech. rep. New York: New York U., 2012. URL: https://cds.cern.ch/record/1456844.

[28] ATLAS Collaboration. “Muon reconstruction and identification efficiency in ATLAS using the full Run 2 pp collision data set at s= 13 TeV”. In: *The European Physical Journal C* 81.7 (2021), p. 578.

[29] ATLAS Collaboration. “Jet reconstruction and performance using particle flow with the ATLAS Detector”. In: *The European Physical Journal C* 77 (2017), pp. 1–47.

[30] Enrico Bothmann et al. “Event generation with Sherpa 2.2”. In: *SciPost Phys.* 7.3 (2019), p. 034. DOI: 10.21468/SciPostPhys.7.3.034. arXiv: 1905.09127 [hep-ph].

[31] Federico Buccioni et al. “OpenLoops 2”. In: *Eur. Phys. J. C* 79.10 (2019), p. 866. DOI: 10.1140/epjc/s10052-019-7306-2. arXiv: 1907.13071 [hep-ph].

[32] Fabio Cascioli, Philipp Maierhöfer, and Stefano Pozzorini. “Scattering Amplitudes with Open Loops”. In: *Phys. Rev. Lett.* 108 (2012), p. 111601. DOI: 10.1103/PhysRevLett.108.111601. arXiv: 1111.5206 [hep-ph].

[33] Ansgar Denner, Stefan Dittmaier, and Lars Hofer. “COLLIER: A fortran-based complex one-loop library in extended regularizations”. In: *Comput. Phys. Commun.* 212 (2017), pp. 220–238. DOI: 10.1016/j.cpc.2016.10.013. arXiv: 1604.06792 [hep-ph].

[34] Steffen Schumann and Frank Krauss. “A parton shower algorithm based on Catani–Seymour dipole factorisation”. In: *JHEP* 03 (2008), p. 038. DOI: 10.1088/1126-6708/2008/03/038. arXiv: 0709.1027 [hep-ph].

[35] Stefan Höche et al. “QCD matrix elements + parton showers. The NLO case”. In: *JHEP* 04 (2013), p. 027. DOI: 10.1007/JHEP04(2013)027. arXiv: 1207.5030 [hep-ph].

[36] Richard D. Ball et al. “Parton distributions for the LHC run II”. In: *JHEP* 04 (2015), p. 040. DOI: 10.1007/JHEP04(2015)040. arXiv: 1410.8849 [hep-ph].

[37] Charalampos Anastasiou et al. “High-precision QCD at hadron colliders: Electroweak gauge boson rapidity distributions at next-to-next-to leading order”. In: *Phys. Rev. D* 69 (2004), p. 094008. DOI: 10.1103/PhysRevD.69.094008. arXiv: hep-ph/0312266.

[38] Paolo Nason. “A new method for combining NLO QCD with shower Monte Carlo algorithms”. In: *JHEP* 11 (2004), p. 040. DOI: 10.1088/1126-6708/2004/11/040. arXiv: hep-ph/0409146.

[39] Stefano Frixione, Paolo Nason, and Carlo Oleari. “Matching NLO QCD computations with parton shower simulations: the POWHEG method”. In: *JHEP* 11 (2007), p. 070. DOI: 10.1088/1126-6708/2007/11/070. arXiv: 0709.2092 [hep-ph].

[40] Simone Alioli et al. “A general framework for implementing NLO calculations in shower Monte Carlo programs: the POWHEG BOX”. In: *JHEP* 06 (2010), p. 043. DOI: 10.1007/JHEP06(2010)043. arXiv: 1002.2581 [hep-ph].

[41] Torbjörn Sjöstrand et al. “An introduction to PYTHIA 8.2”. In: *Comput. Phys. Commun.* 191 (2015), p. 159. DOI: 10.1016/j.cpc.2015.01.024. arXiv: 1410.3012 [hep-ph].

[42] ATLAS Collaboration. “Measurement of the Z/γ^* boson transverse momentum distribution in pp collisions at $\sqrt{s} = 7\,\text{TeV}$ with the ATLAS detector”. In: *JHEP* 09 (2014), p. 145. DOI: 10.1007/JHEP09(2014)145. arXiv: 1406.3660 [hep-ex].

[43] H.-L. Lai et al. “New parton distributions for collider physics”. In: *Phys. Rev. D* 82 (2010), p. 074024. DOI: 10.1103/PhysRevD.82.074024. arXiv: 1007.2241 [hep-ph].

[44] J. Pumplin et al. “New Generation of Parton Distributions with Uncertainties from Global QCD Analysis”. In: *JHEP* 07 (2002), p. 012. DOI: 10.1088/1126-6708/2002/07/012. arXiv: hep-ph/0201195.

[45] Piotr Golonka and Zbigniew Was. “PHOTOS Monte Carlo: A Precision tool for QED corrections in Z and W decays”. In: *Eur. Phys. J. C* 45 (2006), pp. 97–107. DOI: 10.1140/epjc/s2005-02396-4. arXiv: hep-ph/0506026.

[46] N. Davidson, T. Przedzinski, and Z. Was. “PHOTOS Interface in C++: Technical and physics documentation”. In: *Comput. Phys. Commun.* 199 (2016), pp. 86–101. DOI: 10.1016/j.cpc.2015.09.013. arXiv: 1011.0937 [hep-ph].

[47] ATLAS Collaboration. *ATLAS Pythia 8 tunes to 7 TeV data*. ATL-PHYS-PUB-2014-021. 2014. URL: https://cds.cern.ch/record/1966419.

[48] M. Beneke et al. “Hadronic top-quark pair production with NNLL threshold resummation”. In: *Nucl. Phys. B* 855 (2012), pp. 695–741. DOI: 10.1016/j.nuclphysb.2011.10.021. arXiv: 1109.1536 [hep-ph].

[49] Matteo Cacciari et al. "Top-pair production at hadron colliders with next-to-next-to-leading logarithmic soft-gluon resummation". In: *Phys. Lett. B* 710 (2012), pp. 612–622. DOI: 10.1016/j.physletb.2012.03.013. arXiv: 1111.5869 [hep-ph].

[50] Peter Bärnreuther, Michal Czakon, and Alexander Mitov. "Percent-Level-Precision Physics at the Tevatron: Next-to-Next-to-Leading Order QCD Corrections to $q\bar{q} \to t\bar{t} + X$". In: *Phys. Rev. Lett.* 109 (2012), p. 132001. DOI: 10.1103/PhysRevLett.109.132001. arXiv: 1204.5201 [hep-ph].

[51] Michal Czakon and Alexander Mitov. "NNLO corrections to top-pair production at hadron colliders: the all-fermionic scattering channels". In: *JHEP* 12 (2012), p. 054. DOI: 10.1007/JHEP12(2012)054. arXiv: 1207.0236 [hep-ph].

[52] Michal Czakon and Alexander Mitov. "NNLO corrections to top pair production at hadron colliders: the quark-gluon reaction". In: *JHEP* 01 (2013), p. 080. DOI: 10.1007/JHEP01(2013)080. arXiv: 1210.6832 [hep-ph].

[53] Michal Czakon, Paul Fiedler, and Alexander Mitov. "Total Top-Quark Pair-Production Cross Section at Hadron Colliders Through $O(\alpha_S^4)$". In: *Phys. Rev. Lett.* 110 (2013), p. 252004. DOI: 10.1103/PhysRevLett.110.252004. arXiv: 1303.6254 [hep-ph].

[54] Michal Czakon and Alexander Mitov. "Top++: A program for the calculation of the top-pair cross-section at hadron colliders". In: *Comput. Phys. Commun.* 185 (2014), p. 2930. DOI: 10.1016/j.cpc.2014.06.021. arXiv: 1112.5675 [hep-ph].

[55] Nedaa Alexandra Asbah et al. *Measurement of the $t\bar{t}$ cross-section and $t\bar{t}/Z$ cross-section ratio using LHC Run 3 pp collision data at a centre-of-mass energy of $\sqrt{s} = 13.6$ TeV*. Tech. rep. Geneva: CERN, 2023. URL: https://cds.cern.ch/record/2848558.

[56] ATLAS Collaboration. "Measurement of $W^{\pm}$ and Z-boson production cross sections in pp collisions at $\sqrt{s} = 13\,\text{TeV}$ with the ATLAS detector". In: *Phys. Lett. B* 759 (2016), p. 601. DOI: 10.1016/j.physletb.2016.06.023. arXiv: 1603.09222 [hep-ex].

[57] Stefano Camarda et al. "DYTurbo: Fast predictions for Drell-Yan processes". In: *Eur. Phys. J. C* 80.3 (2020). [Erratum: Eur.Phys.J.C 80, 440 (2020)], p. 251. DOI: 10.1140/epjc/s10052-020-7757-5. arXiv: 1910.07049 [hep-ph].

[58] Stefano Camarda, Leandro Cieri, and Giancarlo Ferrera. "Drell–Yan lepton-pair production: qT resummation at N3LL accuracy and fiducial cross sections at N3LO". In: *Phys. Rev. D* 104.11 (2021), p. L111503. DOI: 10.1103/PhysRevD.104.L111503. arXiv: 2103.04974 [hep-ph].

[59] Stefano Camarda, Leandro Cieri, and Giancarlo Ferrera. "Fiducial perturbative power corrections within the $\mathbf{q}_T$ subtraction formalism". In: *Eur. Phys. J. C* 82.6 (2022), p. 575. DOI: 10.1140/epjc/s10052-022-10510-x. arXiv: 2111.14509 [hep-ph].

[60] Stefano Camarda, Leandro Cieri, and Giancarlo Ferrera. "Drell-Yan lepton-pair production: q_T resummation at approximate N^{4}LL+N^{4}LO accuracy". In: (Mar. 2023). arXiv: 2303.12781 [hep-ph].

[61] Renat Sadykov and Vitaly Yermolchyk. "Polarized NLO EW e^+e^- cross section calculations with ReneSANCe-v1.0.0". In: *Comput. Phys. Commun.* 256 (2020), p. 107445. DOI: 10.1016/j.cpc.2020.107445. arXiv: 2001.10755 [hep-ph].

[62] Serge Bondarenko et al. "Hadron-hadron collision mode in ReneSANCe-v1.3.0". In: *Comput. Phys. Commun.* 285 (2023), p. 108646. DOI: 10.1016/j.cpc.2022.108646. arXiv: 2207.04332 [hep-ph].

[63] ATLAS Collaboration. "Precision measurement and interpretation of inclusive W^+, W^- and Z/γ^* production cross sections with the ATLAS detector". In: *Eur. Phys. J. C* 77 (2017), p. 367. DOI: 10.1140/epjc/s10052-017-4911-9. arXiv: 1612.03016 [hep-ex].

[64] Richard D. Ball et al. "The PDF4LHC21 combination of global PDF fits for the LHC Run III". In: (Mar. 2022). arXiv: 2203.05506 [hep-ph].

[65] Tie-Jiun Hou et al. "New CTEQ global analysis of quantum chromodynamics with high-precision data from the LHC". In: *Phys. Rev. D* 103.1 (2021), p. 014013. DOI: 10.1103/PhysRevD.103.014013. arXiv: 1912.10053 [hep-ph].

[66] T. Cridge et al. "An investigation of the α_S and heavy quark mass dependence in the MSHT20 global PDF analysis". In: *Eur. Phys. J. C* 81.8 (2021), p. 744. DOI: 10.1140/epjc/s10052-021-09533-7. arXiv: 2106.10289 [hep-ph].

[67] S. Bailey et al. "Parton distributions from LHC, HERA, Tevatron and fixed target data: MSHT20 PDFs". In: *Eur. Phys. J. C* 81.4 (2021), p. 341. DOI: 10.1140/epjc/s10052-021-09057-0. arXiv: 2012.04684 [hep-ph].

[68] T. Cridge et al. "QED parton distribution functions in the MSHT20 fit". In: *Eur. Phys. J. C* 82.1 (2022), p. 90. DOI: 10.1140/epjc/s10052-022-10028-2. arXiv: 2111.05357 [hep-ph].

[69] Richard D. Ball et al. "The path to proton structure at 1% accuracy: NNPDF Collaboration". In: *Eur. Phys. J. C* 82.5 (2022), p. 428. DOI: 10.1140/epjc/s10052-022-10328-7. arXiv: 2109.02653 [hep-ph].

[70] S. Alekhin et al. "Parton distribution functions, α_s, and heavy-quark masses for LHC Run II". In: *Phys. Rev. D* 96.1 (2017), p. 014011. DOI: 10.1103/PhysRevD.96.014011. arXiv: 1701.05838 [hep-ph].

[71] ATLAS Collaboration. "Determination of the parton distribution functions of the proton using diverse ATLAS data from pp collisions at $\sqrt{s} = 7, 8$ and 13 TeV". In: *Eur. Phys. J. C* 82 (2021), p. 438. DOI: 10.1140/epjc/s10052-022-10217-z. arXiv: 2112.11266 [hep-ex].

[72] Francis Halzen and Alan Martin. *Quarks & Leptons: An introductory course in modern particle physics*. John Wiley & Sons, 1984.

[73] Massimiliano Grazzini, Stefan Kallweit, and Marius Wiesemann. "Fully differential NNLO computations with MATRIX". In: *Eur. Phys. J. C* 78.7 (2018), p. 537. DOI: 10.1140/epjc/s10052-018-5771-7. arXiv: 1711.06631 [hep-ph].

[74] Glen Cowan et al. "Asymptotic formulae for likelihood-based tests of new physics". In: *The European Physical Journal C* 71.2 (Feb. 2011). ISSN: 1434-6052. DOI: 10.1140/epjc/s10052-011-1554-0. URL: http://dx.doi.org/10.1140/epjc/s10052-011-1554-0.

[75] ATLAS Collaboration. "Measurement of the $t\bar{t}$ cross section and its ratio to the Z production cross section using pp collisions at $\sqrt{s} = 13.6$ TeV with the ATLAS detector". In: (). arXiv: 2308.09529 [hep-ex].